This is to certify that the

dissertation entitled

Pulsed Electron Paramagnetic Resonance Studies on Biologically Relevant Ni and Tyrosyl Models

presented by

Gyorgy Filep

has been accepted towards fulfillment
of the requirements for

Ph.D. degree in Chemistry

John L. McCracken
Major professor

Date 9 May 1997

PULSED ELECTRON PARAMAGNETIC RESONANCE STUDIES ON BIOLOGICALLY RELEVANT Ni AND TYROSYL MODELS

By

György Filep

A DISSERTATION

Submitted to
Michigan State University
in partial fulfillment of the requirements
for the degree of

DOCTOR OF PHILOSOPHY

Department of Chemistry

1997

ABSTRACT

PULSED ELECTRON PARAMAGNETIC RESONANCE STUDIES ON BIOLOGICALLY RELEVANT Ni AND TYROSYL MODELS

By

György Filep

Pulsed EPR methods based on Electron Spin Echo (ESE) phenomena, such as Electron Spin Echo Modulation (ESEEM) spectroscopy, are capable of measuring weak hyperfine interactions (of the order of a tenth of a Gauss). In order to expand the capabilities of ESEEM, its 2D variant, Hyperfine Sublevel Correlation Spectroscopy (HYSCORE) was proposed in 1986. Our work has been aimed at exploring the application of HYSCORE in disordered samples of biologically relevant model systems.

The nitrogen ligand hyperfine couplings of $Ni(III)(CN)_4(H_2O)_2^-$ have been measured using a combination of isotopic substitution, orientation selection, and 1- and 2-dimensional Electron Spin Echo Envelope Modulation techniques. The shapes of the contour lines obtained from HYSCORE experiments were analyzed, using the graphical method developed by Dikanov and Bowman (*J. Magn. Reson.* **1995**, *Series A 116*, 125.) for samples prepared with $C^{15}N^-$. The results show an axially symmetric hyperfine

interaction with $|A_{||}|$=1.93 MHz and $|A_{\perp}|$=1.06 MHz (for ^{15}N). The cyanide ^{14}N nuclear quadrupole coupling is characterized by a quadrupole coupling constant, $e^2q_{zz}Q$= 3.67 MHz and an asymmetry parameter, η=0.09, with the principal axis of the NQI tensor being along the C-N bond.

The very slow relaxation of tyrosyl radicals at low temperatures makes pulsed EPR experiments on them rather difficult to perform, because usually we cannot use sampling rate higher than ca. 10 Hz. We have remedied this problem by adding 5 mM Gd^{3+} to the sample. HYSCORE data were analyzed by the graphical method of Dikanov and Bowman mentioned above. The principal values of the HFI tensor are found to be (-0.8, -3.1, -3.6) (MHz), which are reasonably close to the values found by Warncke and McCracken using 1D ESEEM (*J. Chem. Phys.* **1994**, *101*, 1832).

The electronic structure of Ni(III)($H_{-2}G_3$)(terpy) has been studied using 1D ESEEM combined with isotopic substitution. To sort out the contributions of the various nuclei, specific isotopic labeling (with ^{15}N) has been used at the middle pyridine ring. The "product rule" of ESEEM allows one to observe the modulation from this nucleus by dividing the data from the non-labeled sample by that from the ^{15}N-labeled one. The results show no magnetic interaction from this nitrogen. This indicates very low unpaired electron spin density, which may suggest that this nitrogen does not coordinate at all, in contrast to the geometry proposed previously.

Drága Szüleimnek

This Dissertation is dedicated to my beloved parents,

Tóth Róza and Dr. Filep György

Acknowledgment

First of all, I would like to express my greatest respect toward my mentor and teacher, prof. John McCracken, who has given me excellent professional guidance and permanent support during my years at MSU.

I also thank my colleagues, Hong-In Lee, Kurt Warncke, Michelle Mac, Kerry Reidy and Vladimir Bouchev, for their help, support and numerous valuable and open discussions. Special thanks to Andrew Ichimura for his friendship and for being a great colleuague and tennis partner.

Special thanks to some of the members of the community of Eastern European students for their friendship and the fun we had together. Especially to Vladimir F. Bouchev (Vlado), Evstatin T. Krastev (Ati), Branislav Blagojevic (Bane), Marian G. Marinov (Chado), Alexander S. Volya (Sasha). I feel privileged to know all of you. Wish you a happy life and see you back home !

My deepest respect goes to my friend, Dalila G. Kovács, who always stood by me, mostly in difficult times. I thank my good friend Szász Barna for his care and understanding. I also thank my former wife, Gabriella Székely, for her support.

I could never have finished this long journey without my parents' continuous support and faith in me. Thank You, Mom and Dad, for your endless love.

TABLE OF CONTENTS

LIST OF TABLES

LIST OF FIGURES

LIST OF ABBREVIATIONS

Aib	.....	Aminoisobutyrate
bipy	.....	Bipyridine
CW	.....	Continuous wave
C. vinosum	.....	Chromatium vinosum (bacterium)
1D	.....	One dimensional
2D	.....	Two dimensional
D. gigas	.....	Desulfovibrio gigas (bacterium)
dien	.....	Diethylene triamine
DEFENCE	.....	Dead-time free ESEEM by nuclear coherence transfer echoes
en	.....	Ethylene diamine
ENDOR	.....	Electron nuclear double resonance
EPR	.....	Electron paramagnetic resonance
ESE	.....	Electron spin echo
ESEEM	.....	Electon spin echo envelope modulation
EXAFS	.....	Extended x-ray absorption fine structure
FORTRAN	.....	Formula translator (programming language)
FT	.....	Fourier transform
FW	.....	Formula Weight
G_3	.....	Triglycine
GOase	.....	Galactose Oxidase
H_4EDTA	.....	Ethylene diamine tetra-acetic acid
HFI	.....	Hyperfine interaction
$H_{-2}G_3$	.....	trigyline with deprotonated amide groups
HYSCORE	.....	Hyperfine sublevel correlation spectroscopy
MATLAB	.....	Matrix laboratory (programming and visualization software package)
MW	.....	Microwave
NAD	.....	Nicotinamide adenine dinucleotide
NHE	.....	Normal hydrogen electrode
NMR	.....	Nuclear magnetic resonance

NQI	.....	Nuclear quadrupole interaction
PAS	.....	Principal Axis System
PGHS	.....	Prostaglandine H Synthase
PS II	.....	Photosystem II
RNR	.....	Ribonucleotide Reductase
SCE	.....	Saturated calomel electrode
terpy	.....	2,2':6',2'' terpyridine
XANES	.....	X-ray absorption near edge spectroscopy
XAS	.....	X-ray absorption spectroscopy

INTRODUCTION

Electron Spin Echo Envelope Modulation (ESEEM) spectroscopy has become a valuable tool to study weak electron-nuclear hyperfine interactions (HFI) in paramagnetic samples. The analysis of ESEEM in randomly oriented samples is complicated by the fact that the lineshape is determined not only by the principal values of the g- and HFI- tensors but also by the orientation-dependent amplitude factor, k.

Chapter I of this Dissertation covers the basic principles of Electron Spin Echo (ESE) methods, emphasizing the main characteristics, advantages and drawbacks of various one-dimensional ESEEM methods.

To facilitate the interpretation of ESEEM spectra, two-dimensional (2D) versions of the method have recently been introduced. The most widely used 2D ESEEM is Hyperfine Sublevel Correlation Spectroscopy (HYSCORE), which allows one to obtain the principal HFI tensor components via direct analysis of the shape of the 2D correlation patterns rather than via numerical spectral simulations.

Chapter II is devoted to the description of HYSCORE. It presents the principles of the method, followed by general features of 2D data analysis. Then the experimental aspects of HYSCORE are detailed, with an emphasis on disordered systems.

Electronic structure of Ni(III) complexes has been of interest since the discovery of the Ni EPR signal in hydrogenase enzymes. Analysis of the weak

HFI between the unpaired electron of the Ni(III) and the magnetic nuclei of the ligands yields structural information on the Ni center.

Chapter III is a brief review of the relevant properties of hydrogenase enzymes. It focuses on electrochemical and spectroscopic (mainly EPR) results. Questions concerning the coordination of the Ni site in hydrogenases are discussed, using mainly the *D. gigas* hydrogenase as a prototype.

Chapter IV summarizes the literature on the most relevant Ni compounds that have been proposed as structural or functional models for the hydrogenase nickel site.

Chapter V first gives an introduction to the EPR spectroscopy of Ni(III) compounds. It explains the connection between structure and quantities measured by EPR, such as g-values, HFI parameters, Nuclear Quadrupole Interaction (NQI) parameters. The second part presents our study on a Ni(III) complex, Ni(III)(triglycinate)(terpyridine). The results indicate an unusual electron distribution around the Ni center.

Chapter VI presents a HYSCORE study on another Ni(III) model compound, tetracyano nickelate (III). It demonstrates that important hyperfine information can be obtained fairly easily with the aid of this 2D method.

Amino acid radicals have recently been discovered as essential participants in the catalytic mechanisms of some enzymes. Tyrosyl radicals have been intensively studied by EPR, Electron Nuclear Double Resonance (ENDOR) and ESEEM spectroscopies.

Chapter VII gives a short introduction to metallo-radical enzymes, including the review of previous EPR investigations. This is followed by the presentation of our HYSCORE study on a tyrosyl model system. It demonstrates (for the first time) that HYSCORE can effectively be applied to systems with rhombic hyperfine tensor.

Chapter I

Principles of Electron Spin Echo Spectroscopy

I.1. Introduction

Electron Paramagnetic Resonance (EPR) spectroscopy has established itself as an indispensable method in studies of the structure of paramagnetic materials (1-3). EPR in a liquid phase is able to measure isotropic hyperfine interaction (HFI) of magnitude as low as 0.1 G. For paramagnetic species stabilized in disordered solid matrices, i.e. polycrystals, glasses and frozen solutions, the resolution of EPR is reduced to a few Gauss, owing to *inhomogeneous spectral broadening*, which masks the details of EPR spectra. In these cases the hyperfine information can be extracted only if the splittings are larger than the inhomogeneous width (usually 10-100 G). To solve structural problems, however, it is often necessary to obtain information on weak HFI.

In order to make EPR applicable in these cases, various modifications of the method have been proposed. The most widely used of them is Electron Nuclear Double Resonance (ENDOR) spectroscopy (2, 3). ENDOR yields the NMR spectrum of the paramagnetic system by detecting the change in the amplitude of the saturated EPR signal of the sample upon sweeping the frequency of an additional radiofrequency field. This method can often provide HFI and Nuclear Quadrupole Interaction (NQI) parameters of the order of a few Hertz.

Other developments in EPR aimed at resolving small hyperfine splittings in solid samples are the variety of pulsed EPR methods, which are primarily based on Electron Spin Echo (ESE) phenomena (4-8, 12). As compared to Continuous Wave (CW) EPR, which is a frequency domain spectroscopy, ESE is a *time domain method*, in which the evolution of the spin system is directly recorded. In ESE experiments the spins are probed by short (≈ 10-100 ns), high energy resonant pulses, with the static magnetic field being kept constant. Therefore, only *a small portion of the inhomogeneously broadened EPR spectrum is excited* in the ESE experiment. The response of the paramagnetic sample to these pulses is a spontaneous emission of microwave energy called the spin echo, whose magnitude as a function of separation between two of the pulses is measured. The weak hyperfine interactions may manifest themselves as a *modulation of the spin echo envelope* (Electron Spin Echo Envelope Modulation, ESEEM). The periods of these modulations are related to the nuclear transition (NMR) frequencies of the sample.

In this Chapter a qualitative introduction of the ESE phenomenon is given. Vector models explaining the formation of two, three and four pulse echoes are presented, followed by a semiclassical picture of the ESEEM phenomenon.

I.2. Formation of Two-pulse ESE

The simplest pulse sequence to generate a spin echo consists of two consecutive pulses. Two pulse echoes produced by nuclear spins first were

observed by Hahn in 1950, using the pulse sequence $\pi/2$-τ -$\pi/2$ (9), where $\pi/2$ is the turning angle of the pulse. Later, an improved sequence ($\pi/2$-τ -π) was introduced by Carr and Purcell (10). The formation of the two pulse echo will be explained by a simple magnetization vector model.

When the paramagnetic material is placed in a static external magnetic field $\vec{B}_0$, the magnetic moments of the electron spins will form precession cones either parallel or antiparallel with respect to $\vec{B}_0$. For electrons the β spin state has the lower energy, therefore, the higher population (according to Boltzmann's Law). This results in a total macroscopic magnetization ($\vec{M}$), parallel to $\vec{B}_0$. During an ESE experiment a linearly polarized oscillating microwave electromagnetic field is applied, whose magnetic component is perpendicular to $\vec{B}_0$ and can be formulated as $\vec{B}_X(t)=2\vec{B}_1\cos(\omega t)$. The effect of this field is most conveniently analyzed by decomposing it into two circularly polarized components that rotate opposite to one another, denoted $\vec{B}_R$ and $\vec{B}_L$(Figure I-1). They can be expressed as

$$\vec{B}_R=B_1[\underline{i}\cos(\omega t)+\underline{j}\sin(\omega t)] \qquad \text{[I-1a]}$$

$$\vec{B}_L=B_1[\underline{i}\cos(\omega t)-\underline{j}\sin(\omega t)]. \qquad \text{[I-1b]}$$

We notice that under resonance conditions $\vec{B}_R$ will rotate at approximately the angular velocity of the precession of the electron spins, while $\vec{B}_L$ will rotate in the opposite direction and will have little effect on the resonance experiment, thus will be neglected for further discussions.

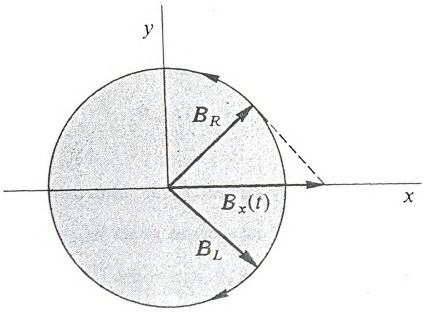

Figure I-1. A linearly polarized oscillating magnetic field, $\mathbf{B_x(t)}$ can be considered as the vectorial sum of two circularly polarized fields that are rotating in opposite directions, namely, clockwise ($\mathbf{B_L}$) and counter-clockwise ($\mathbf{B_R}$).

Let us adopt a reference frame, rotating about the laboratory axis z (the direction of the static magnetic field) at angular velocity ω that is equal to the carrier frequency of the pulse. *In this frame* $\vec{\mathbf{B}}_{\mathbf{R}}$ *appears to be stationary* and we may choose it to lie along the x axis. When the microwave (MW) pulse is applied for a period of time t_p, the $\vec{\mathbf{B}}_1$ field torques the magnetization $\vec{\mathbf{M}}$ about the x-axis by an angle Θ_{flip},

$$\Theta_{flip}=g_e B_1 t_p=\omega_1 t_p. \qquad [I\text{-}2]$$

where g_e is the gyromagnetic ratio of the electron. We choose t_p so that $\Theta_{flip}=90^0$ for the first, 180^0 for the second pulse. The evolution of the spins during the experiment is demonstrated in Figure I-2. Following the first pulse, the magnetization lies in the plane perpendicular to z (c). $\vec{\mathbf{M}}$ consists of a number of spin packets, i.e. groups of spins that have different local magnetic environments, therefore different precession frequencies. Because of this they will fan out during the free precession period τ, leading to the disappearance of the macroscopic magnetization, $\vec{\mathbf{M}}$ (d). Spin packets labeled 2, 3 and 4 have precession frequencies larger than ω_0, so they develop a positive phase angle (with respect to the -y axis) during the free precession period, τ. Packets with an effective local field smaller than $\vec{\mathbf{B}}_0$, for example packets 6, 7 and 8, will accumulate a negative phase angle. The arrows in Figure I-1 indicate the direction of precession of these packets. The second

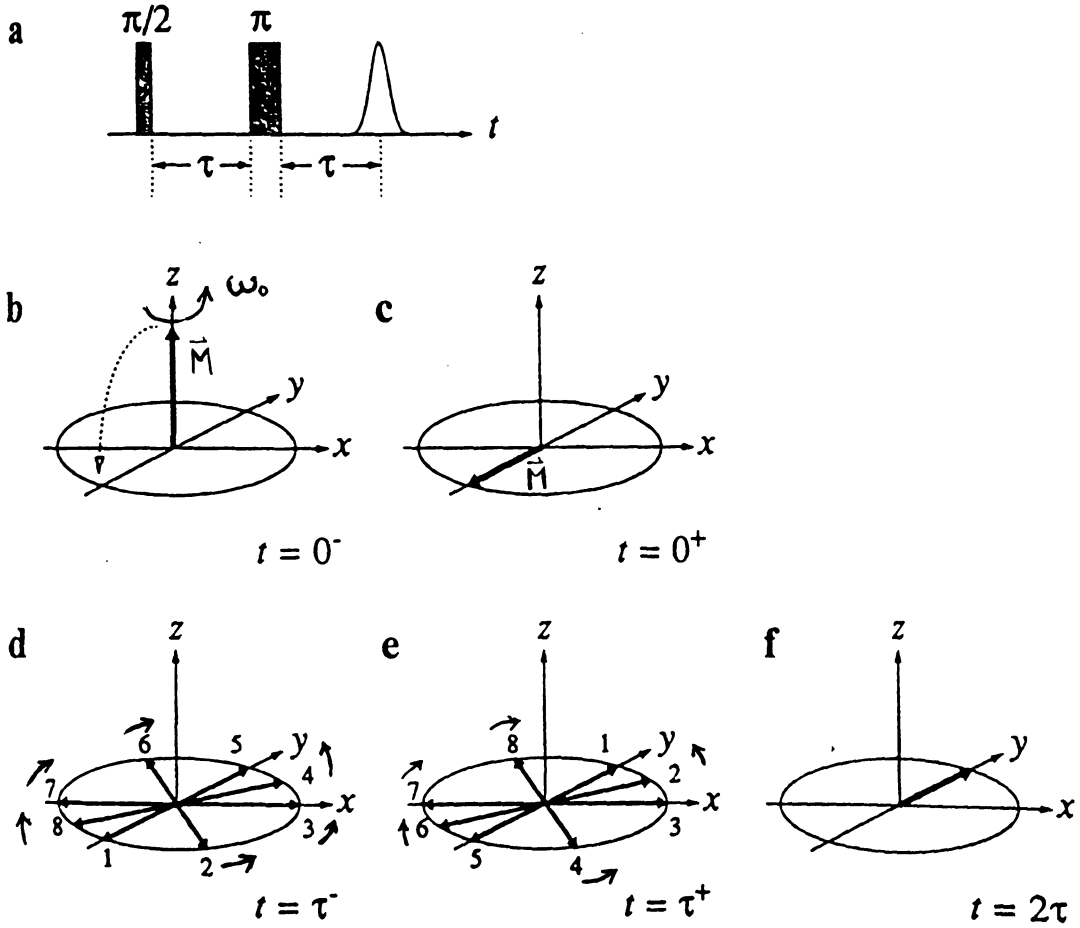

Figure I-2. Vector diagram to explain the formation of the 2-pulse spin echo. (a) the pulse sequence; (b)-(c) the first pulse tilts the magnetization ($\vec{M}$) onto the (xy) plane; (d) the spin packets that comprise $\vec{M}$ dephase due to their different precession frequencies; (e) the second pulse inverts each spin packet around the x-axis; they continue to precess in the (xy) plane; (f) they refocus along y and reform $\vec{M}$ [from Ref. (8)].

pulse torques the magnetization of every spin packet about the x axis by 180^0 (e). Since the spin packets *continue precessing at the same angular velocity,* they rephase along the +y axis after time t following the second pulse (f). This refusing of the magnetization components leads to an *emission of MW radiation by the sample and is called the spin echo.* When a short MW irradiation of fixed wavelength (pulse) is applied only a portion of the inhomogeneous line is excited (Fig. I-3). The excitation bandwidth ($\Delta\nu$) is determined by the length of the pulse, namely, $\Delta\nu=1/t_p$. This can be understood quantitatively from taking the Fourier transform of the finite wave train of length t_p, and is discussed elsewhere (11). For a fixed flip angle, one may increase t_p by decreasing B_1 (decreasing the MW power), making the excitation bandwidth of the pulse smaller (making the pulse more selective); or vice versa, t_p may be decreased by increasing B_1, making the pulse less selective. In the latter case limitations are imposed by the performance of the MW electronics (how fast switches one can have) as well as by the threshold of the MW power (limit of the amplifier).

I.3. Three-pulse echo (Stimulated Echo)

The 3-pulse sequence ($\pi/2$-τ -π /2-T-$\pi/2$) creates a stimulated echo at time τ after the third pulse (9). The dynamics of the spin system is shown in Fig. I-4 [from Ref. (8)]. The first pulse rotates the magnetization about the x axis (b), so it lies along the -y axis (c). Then dephasing of the magnetization in the xy plane follows, in the same way as described above for the primary echo (d).

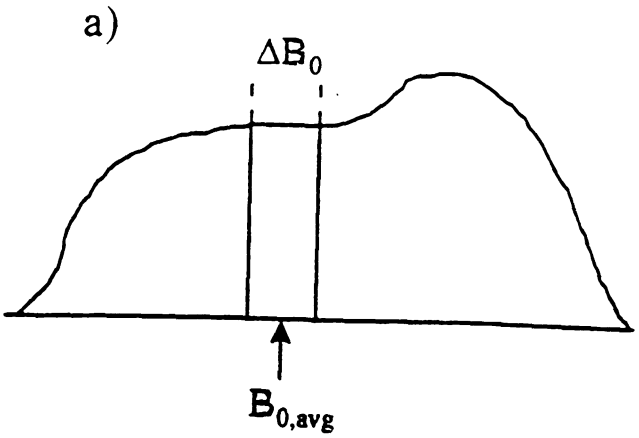

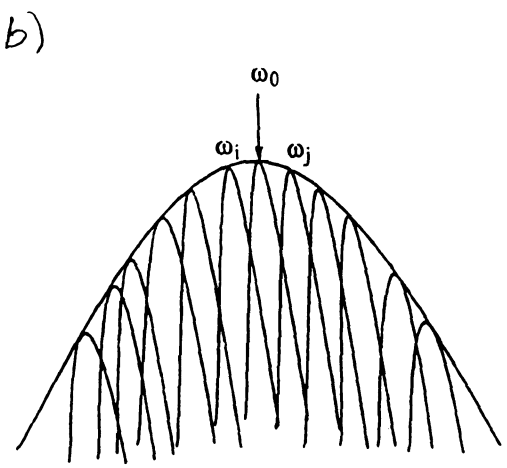

Figure I-3. The inhomogeneously broadened EPR lineshape. (a) $\mathbf{B}_{0,\,avg}$ is the mean value of the resonant magnetic field, $\Delta\mathbf{B}_0$ is the linewidth of the portion of the spectrum excited by a pulse. (b) the magnified view of the portion excited by the pulse, with the resonant lines corresponding to individual spin packets. ω_0, ω_i, ω_j are the precession frequencies of the spin packet magnetization components.

The second pulse rotates the y components of the spin packets along the z axis (e). If the condition $T_{2e}<<T<T_{1e}$ holds (T_{2e} and T_{1e} are the transversal and longitudinal relaxation times of the electron, respectively), the magnetization in the (xy) plane will fully decay during the free precession period T and only the magnetization along the z axis survives (f). At time T the third $\pi/2$ pulse is applied which transfers this polarization pattern to magnetization in the (xy) plane (g), which, after time τ following the third pulse refocuses along the y axis, yielding the stimulated echo (h).

I.4. Four-pulse Echo

The four-pulse echo sequence is basically the stimulated echo sequence *with one additional mixing pulse* (a π-pulse) *inserted* between the second and third $\pi/2$ pulses (Figure II-1a). The role of this pulse is to invert the magnetization, while interchanging spin packets belonging to the opposite electronic manifolds. We focus on a spin packet δM_z located along the -z axis after the second $\pi/2$-pulse (Figure I-5, (a)). By applying the π-pulse with the $\vec{B}_1$ field along x axis, δM_z is inverted onto the +z axis (b), then the last $\pi/2$-pulse torques the spin-packet onto the -y axis (c), where it starts precessing about $\vec{B}_0$ immediately after the fourth pulse. In analogy to the formation of the stimulated echo, the total magnetization along the -y axis is maximized at time τ after the fourth pulse.

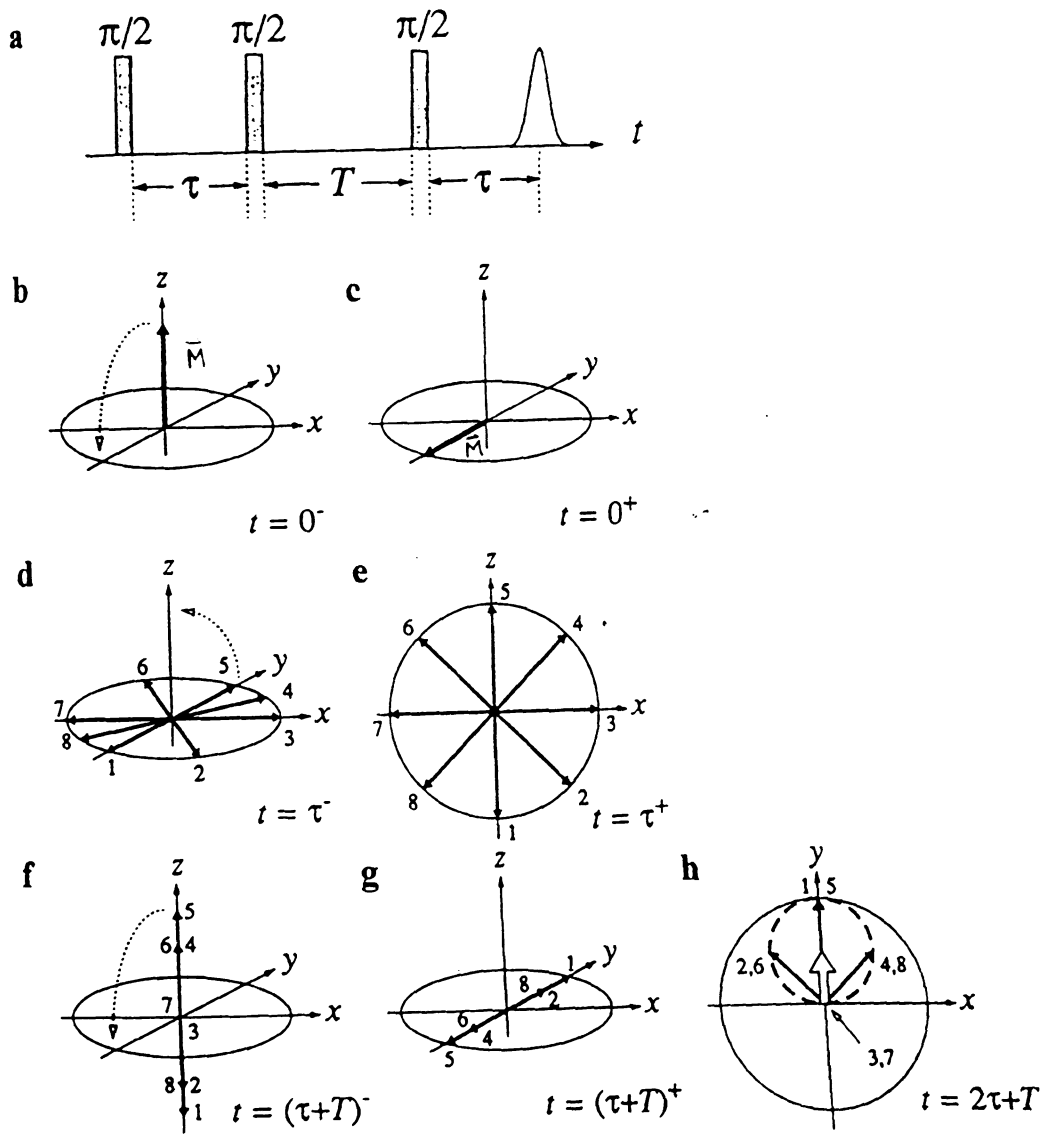

Figure I-4. Vector model to explain the formation of the 3-pulse echo. (a) the pulse sequence; (b), (c) same events as in Figure I-1. (d) the second pulse torques the magnetization along z; (e) the magnetization components precess about z; (f, g) the surviving magnetization components (directed along z) are flipped onto the (xy) plane by the third pulse; (h) the spin packets refocus along y, forming the echo [from Ref. (8)].

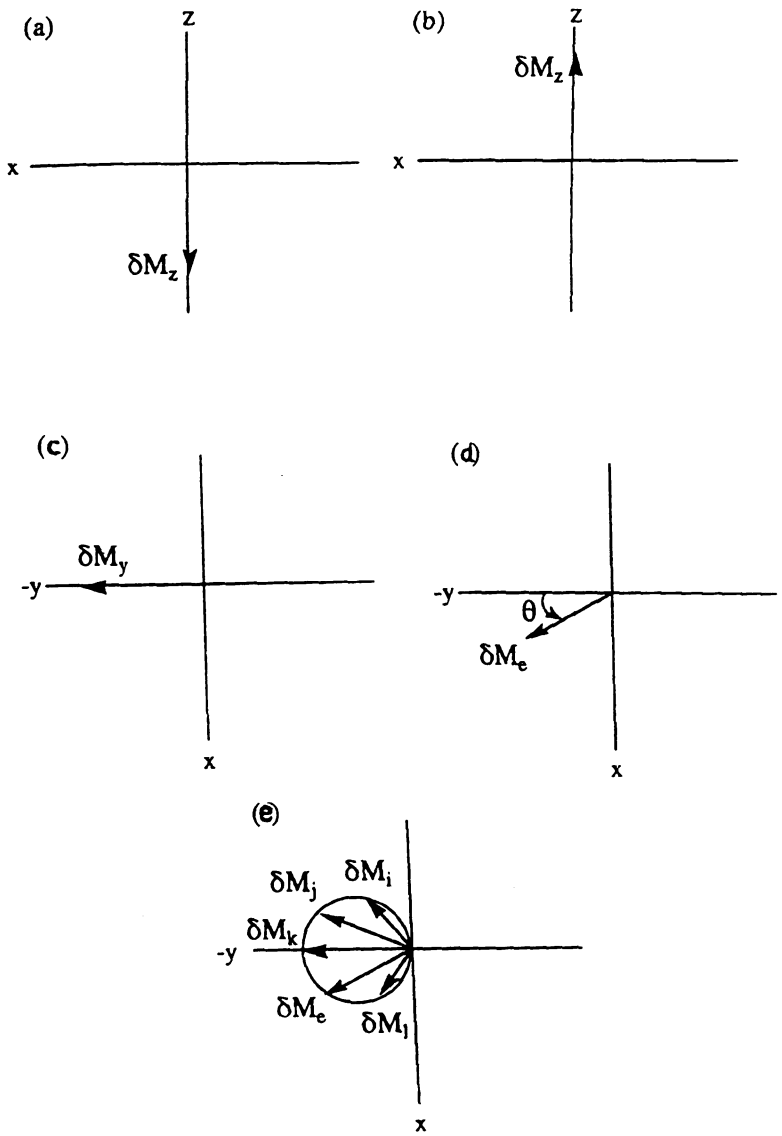

Figure I-5. Illustration of the formation of the 4-pulse echo. (a) Position of spin packet δM_z after the second pulse; (b) the inverting π-pulse reorients δM_z; (c) the third pulse torques δM_z onto the (xy) plane; (d) spin packets start precess about z; (e) by the time τ after the last pulse various spin packets assume the position shown, which creates the echo along the -y axis.

I.5. Semiclassical Description of ESEEM

One can gain qualitative understanding of the modulation phenomenon when combining the classical picture of spin echo formation with the quantum mechanical treatment of an unpaired electron spin coupled to a spin 1/2 nucleus (12). The spin Hamiltonian for such a spin system (S=1/2, I=1/2) consists of electronic Zeeman, nuclear Zeeman and electron-nuclear hyperfine interaction terms and it is given (in angular units) as

$$\frac{\hat{\mathcal{H}}}{\hbar} = \omega_S \hat{S}_Z + A_{ZZ}\hat{S}_Z\hat{I}_Z + A_{XZ}\hat{S}_Z\hat{I}_X - \omega_I \hat{I}_Z \qquad [I\text{-}3]$$

where $A_{ZZ}=A=A_{||}\cos^2\Theta+A_{\perp}\sin^2\Theta$, $A_{XZ}=B=(A_{||}-A_{\perp})\cos\Theta\sin\Theta$, $\omega_s=g\beta B_0/h$ and $\omega_I=g_n\beta_n B_0/h$ (12). $A_{||}$ and $A_{\perp}$ are the principal values of the axially symmetric HFI tensor, which can be described in terms of a Fermi contact coupling, A_{iso}, and a dipole-dipole coupling term, $T=gg_n\beta\beta_n/r^3$, with $A_{||}=A_{iso}+2T$ and $A_{\perp}=A_{iso}-T$. The angle Θ describes the orientation of the principal axis of the hyperfine tensor with respect to the laboratory field. The remaining terms are g, the electron g-factor; g_n, the nuclear g-value; β, the Bohr magneton; β_n, the nuclear magneton. The Hamiltonian matrix is easily constructed in the *uncoupled basis set* consisting of electron and nuclear spin product states, $|m_s, m_I\rangle$. Diagonalization to yield the eigenvalues and eigenvectors of Eq. [I-3] can be managed independently for the two electron spin manifolds as the only term in the operator that gives rise to off-diagonal elements is that involving I_X.

The results are summarized in the energy level scheme of Fig. I-6, where the normalized probability amplitudes for the EPR transitions marked |u| and |v| are given by

$$|u| = \frac{\langle 2|\hat{S}_X|3\rangle}{0.5g\beta B_1} = \sin\left[\frac{\varphi_\alpha - \varphi_\beta}{2}\right] \qquad \text{[I-4a]}$$

$$|v| = \frac{\langle 1|\hat{S}_X|3\rangle}{0.5g\beta B_1} = \cos\left[\frac{\varphi_\alpha - \varphi_\beta}{2}\right] \qquad \text{[I-4b]}$$

The angles φ_α and φ_β define the axes of quantization for the a and b electron spin manifolds, respectively, and are given by $\sin\varphi_\alpha = B/2\omega_\alpha$ and $\sin\varphi_\beta = B/2\omega_\beta$. In general, *all four of the possible EPR transitions for the S=1/2, I=1/2 spin system of Fig. I-6 are allowed.* These transitions will be excited simultaneously in a pulsed EPR experiment, provided that the MW pulses have sufficient bandwidth.

To illustrate the modulation effect the rotating reference frame used in the explanation of spin echoes will again be applied (Figure I-7). The four partially allowed transitions are designated by letters **A**, **B**, **C** and **D**. The discussion will focus on transition **A**. After the first ($\pi/2$) pulse, the transverse magnetization that corresponds to transition **A** will precess more slowly than ω_0 ($\omega_A < \omega_0$). Thus in the rotating coordinate system it will acquire a negative phase angle, $(\omega_A - \omega_0)\tau$ during the free precession period. Application of the second pulse will excite transition **A**, and because the MW pulse excites *all transitions simultaneously*, the corresponding semi-forbidden transition **C** will be excited as well. So, as shown in Fig. I-7b, the effect of the second pulse

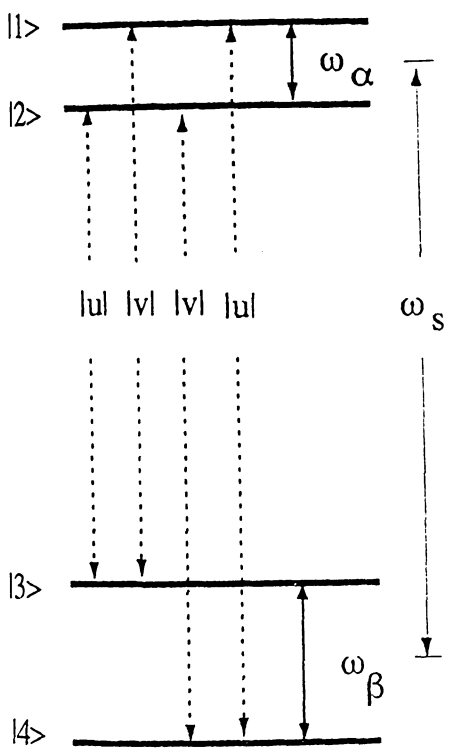

Eigenvectors:

$$|1\rangle = \cos(\varphi_\alpha/2)\,|+\,+\rangle + \sin(\varphi_\alpha/2)\,|+\,-\rangle$$

$$|2\rangle = -\sin(\varphi_\alpha/2)\,|+\,+\rangle + \cos(\varphi_\alpha/2)\,|+\,-\rangle$$

$$|3\rangle = \cos(\varphi_\beta/2)\,|-\,+\rangle + \sin(\varphi_\beta/2)\,|-\,-\rangle$$

$$|4\rangle = -\sin(\varphi_\beta/2)\,|-\,+\rangle + \cos(\varphi_\beta/2)\,|-\,-\rangle$$

$$\omega_\alpha = \sqrt{(\omega_I - A/2)^2 + B^2/4}$$

$$\omega_\beta = \sqrt{(\omega_I + A/2)^2 + B^2/4}$$

Figure I-6. Energy level diagram of an S=1/2, I=1/2 spin system in the solid state, described by the Hamiltonian of Eq. [I-3].

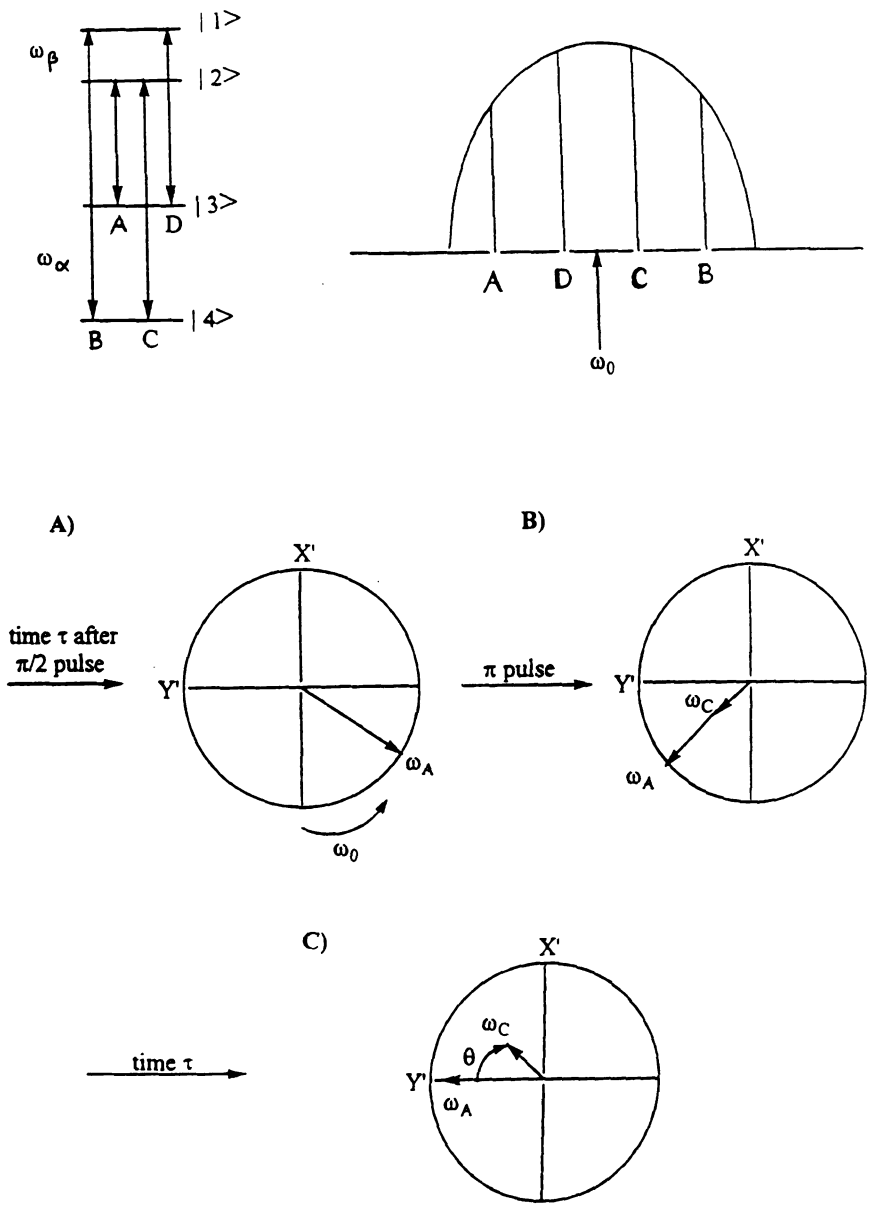

Figure I-7. Schematic illustration of the origin of spin echo modulation. The upper left insert shows the scheme of the four-level energy level diagram of Fig. I-6, while the upper right insert shows the spin packets in the inhomogeneous line. **A), B), C)** show the branching of the transitions, which leads to the modulation phenomenon (see text).

is not only flipping the magnetization component ω_A, but also inducing "branching" of the spin packet into two portions, precessing at ω_A and ω_C. Spin packet **C** has a precession frequency greater than ω_0, and while spin packet **A** will refocus along Y after time t following the second pulse, **C** will be at an angle Θ with respect to Y (Fig. I-7c), due to the difference in their precession frequencies. The echo amplitude is given by the projections of all the spin packet magnetizations onto axis Y. While **A** contributes fully to the echo, the contribution of **C** can be written as $c \cdot \cos\Theta$, where **c** is the length of the magnetization vector **C**. One can immediately see that $\Theta = |\omega_A - \omega_C| \cdot \tau$ or $\Theta = \omega_\alpha \tau$, where ω_α is the hyperfine frequency (NMR frequency) in the $|\alpha\rangle$ electron spin manifold (the difference between levels $|3\rangle$ and $|4\rangle$). If we designate the portion of magnetization split from spin packet **A** upon the second pulse (i.e. the "branching") as k, we may write the expression for the echo amplitude as

$$E(\tau) = k \cdot \cos(\omega_\alpha \tau) \cdot E_0 \qquad [I\text{-}5]$$

where E_0 is the full echo amplitude (i.e. amplitude observed with no modulation). Equation [I-5] shows that the echo amplitude as a function of t indeed is modulated by ω_α and dependent on the modulation depth k (which is determined by the extent of the "branching"). The same reasoning may be expanded to the other pair of transitions **B** and **D**, which are simultaneously excited during the pulse experiment. Thus, we expect to have ω_β as a modulation frequency as well. The quantitative quantum mechanical

treatment outlined later shows that the echo amplitude is modulated by frequencies ω_α, ω_β, $\omega_\alpha+\omega_\beta$ and $\omega_\alpha-\omega_\beta$ (13, 14).

I.6. Two-pulse ESEEM

In this experiment the amplitude of the primary echo is measured as a function of pulse separation, τ. The echo decay is primarily determined by spin-spin relaxation (characterized by relaxation time T_2). The weak HFI with nearby nuclei manifests itself as modulation of the echo envelope. The total time dependence of the echo amplitude thus can be expressed as

$$E(\tau)=E_{dec}(\tau)\cdot E_{mod}(\tau) \qquad [I\text{-}6]$$

where E_{mod} is the modulation, E_{dec} is the decay of the echo envelope.
The exact expression for the modulation function for S=1/2, I=1/2 spin system (13) is

$$E_{mod}(\tau)=1-\frac{k}{4}[2-2\cos\omega_\alpha\tau-2\cos\omega_\beta\tau+\cos(\omega_\alpha+\omega_\beta)\tau+\cos(\omega_\alpha-\omega_\beta)\tau] \qquad [I\text{-}7]$$

Thus, the echo intensity is modulated by the basic nuclear transition (ENDOR) frequencies, ω_α, ω_β, and their combinations, $\omega_\alpha+\omega_\beta$, $\omega_\alpha-\omega_\beta$. These modulation frequencies can be resolved by *Fourier transform* of the full echo envelope function $E(\tau)$. Note that the combination frequencies have opposite phase to the basic frequencies (cf. Eq. [I-7]), thus negative components also appear in the 2-pulse ESEEM spectrum. Prior to Fourier transform it is customary to perform a dead-time reconstruction first suggested by Mims (15)

to reduce the line-shape distortion introduced by the instrumental dead-time (usually ca. 150 ns).

I.7. Three-pulse ESEEM

In the three pulse ESEEM experiment usually T is varied while τ is kept constant. Thus the amplitude of the spin echo is measured as a function of T (or T+τ). The modulations can be observed for longer periods than in the 2-pulse ESEEM ($T_1 >> T_2$), which results in a better frequency resolution. With the introduction of $\tau` = \tau + T$, the explicit form of $E_{mod}(\tau, T)$ for the 3-pulse echo (13, 14) is

$$E_{mod}(\tau, T) = 1 - \frac{k}{4}\{[1-\cos(\omega_\alpha \tau)][1-\cos(\omega_\beta \tau`)] + [1-\cos(\omega_\beta \tau)][1-\cos(\omega_\alpha \tau`)]\} \qquad [I\text{-}8]$$

This equation clearly shows two important features of the 3-pulse experiment. One that only the fundamental hyperfine frequencies contribute to the modulation. The other that depending on the actual τ, certain frequencies can be enhanced, while others can be partially or fully suppressed. This leads to *blind spots* in the 3-pulse ESEEM spectra, which results in lineshape distortion in disordered systems (6, 14, 18).

I.5. Four-pulse ESEEM

Two basic versions of the 4-pulse echo experiment have been used: the two-dimensional 4-pulse ESEEM (HYSCORE) and the 1D version. HYSCORE is dealt with in Chapter II. Here we mention a few characteristics of the 1D 4-

pulse ESEEM. This is carried out in such a way that the two time variables (t_1 and t_2) of the pulse sequence (Figure II-1a) are incremented simultaneously, so that $t_1=t_2=T/2$, while τ is kept constant. In this case the modulation formula, Eq. [II-8] takes the following form (16-18):

$$S(\tau, T)=1-\frac{k}{4}\Big[C_0+2C_\alpha\cos[\frac{\omega_\alpha}{2}(\tau+T)]+2C_\beta\cos[\frac{\omega_\beta}{2}(\tau+T)] +2C_c\{c^2\cos[\frac{\omega_+}{2}(\tau+T)]-s^2\cos[\frac{\omega_-}{2}(\tau+T)]\}\Big] \quad [I\text{-}9]$$

where C_0, C_α, C_β, s, c, k, ω_+, ω_- are defined by Eq. [II-9]. It can be seen that apart from a scaling factor of 1/2, the frequencies of the two-pulse and four-pulse ESEEM are the same. The four-pulse sequence, however, has the advantage that during the variable time intervals nuclear spin coherence evolves which decays much more slowly than electron spin coherence (6, 8). This results in a pronounced reduction of line widths (i.e. in a better spectral resolution) and is particularly important in studies of *sum peaks (ω_+) in spectra of disordered systems* (17, 21-23), where the frequency of these peaks is closely related to the dipolar part of the hyperfine coupling (19).

A novel application of the 4-pulse sequence has been proposed by Ponti and Schweiger (20) to exploit undistorted ESEEM spectra. This experiment is termed DEFENCE (deadtime free ESEEM by nuclear coherence transfer echoes) and is shown to yield *the distortion free absorption powder lineshape*. A DEFENCE spectrum essentially is the projection of the two-dimensional HYSCORE spectrum on its ω_2 axis.

I.6. Density Matrix Description of ESEEM

The density operator formalism has proven particularly useful to describe the evolution of the spin ensemble in magnetic resonance (2, 24, 25). It can be shown easily that the expectation value <A> of an observable represented by operator $\hat{A}$ can be obtained as

$$<A>(t)=Tr\{\hat{\rho}(t)\cdot\hat{A}\} \qquad [I\text{-}10]$$

where $\hat{\rho}(t)$ is the matrix representation of the time-dependent density operator. The "equation of motion" for $\hat{\rho}$ can be derived from the time-dependent Schrödinger equation, and takes the form:

$$\frac{d}{dt}\hat{\rho}(t) = \frac{1}{i\hbar}[\hat{\mathbf{H}},\hat{\rho}], \qquad [I\text{-}11]$$

where the Hamiltonian $\hat{\mathbf{H}}$ may be time-dependent. In a spin-echo experiment the expectation value of interest is the magnetization along the y axis, which is proportional to $\hat{S}_Y$. The normalized echo amplitude in the two-pulse experiment is then:

$$E(\tau)=\frac{Tr\{\hat{\rho}(2\tau)\cdot\hat{S}_Y\}}{Tr\{\hat{\rho}(0)\cdot\hat{S}_Y\}} \quad . \qquad [I\text{-}12]$$

The Hamiltonian in the electron spin echo experiment consists of a time-dependent and a time-independent part,

$$\hat{\mathbf{H}}_{TOT} = \hat{\mathbf{H}}_0 + \hat{\mathbf{H}}_1(t) \qquad [I\text{-}13]$$

where $\hat{\mathbf{H}}_0$ describes the static interactions in the sample (electronic and nuclear Zeeman, nuclear hyperfine and quadrupolar interaction), while $\hat{\mathbf{H}}_1$ expresses the interaction between the spins and the MW pulse. Here we outline the derivation of the modulation formula for the two-pulse ESEEM, following Mims (13).

The time-dependence of $\hat{\mathbf{H}}_1$ can be removed by transforming the problem into a reference frame rotating at the MW carrier frequency, ω. The entire derivation will be cast in this rotating coordinate system. The evolution of the density matrix can be expressed as

$$\hat{\rho}(2\tau) = \mathbf{R} \cdot \hat{\rho}(0) \cdot \mathbf{R}^{\dagger}, \qquad \text{[I-14]}$$

where

$$R = R_{\tau} \cdot R_{2P} \cdot R_{\tau} \cdot R_{1P}, \qquad \text{[I-15]}$$

with

$$\mathbf{R}_t = \exp[-i\hat{\mathbf{H}}_0 t/\hbar], \qquad \text{[I-16]}$$

$$\mathbf{R}_{iP} = \exp[-i\hat{\mathbf{H}}_{TOT} t_{iP}/\hbar]. \qquad \text{[I-17]}$$

$\mathbf{R}_t$ and $\mathbf{R}_{iP}$ are the propagators during free precession and nutation periods, t_{iP} is the duration of the i^{th} pulse. It is convenient to carry out these matrix manipulations in a representation in which $\hat{\mathbf{H}}_0$ is diagonal ("interaction representation") (13). The unitary transformation which diagonalizes $\hat{\mathbf{H}}_0$ is represented in a sub-matrix form as

$$\hat{\mathcal{H}}_0 = \begin{pmatrix} M_\alpha & 0 \\ 0 & M_\beta \end{pmatrix} \cdot \hat{\mathbf{H}}_0 \cdot \begin{pmatrix} M_\alpha^\dagger & 0 \\ 0 & M_\beta^\dagger \end{pmatrix}, \qquad \text{[I-18]}$$

where M_α and M_β are matrices of dimension 2I+1 (I is the nuclear spin). $\hat{\mathbf{H}}_0$ is the matrix representation of the Hamiltonian in a state space with basis vectors $|\alpha, m_I\rangle$, and $|\beta, m_I\rangle$ (m_I is the nuclear quantum number). In this representation $\hat{\mathbf{H}}_0$ is block diagonal (high-field approximation). Thus, M_α and M_β are matrices diagonalizing these blocks. In the "interaction representation" the matrices of our interest will take the following form (26):

$$\mathbf{R}_t = \begin{pmatrix} P_t^\dagger & 0 \\ 0 & Q_t^\dagger \end{pmatrix}, \qquad \text{[I-19]}$$

$$\mathbf{R}_{1P} = \frac{\sqrt{2}}{2} \begin{pmatrix} E & -iM \\ -iM^\dagger & E \end{pmatrix}, \qquad \text{[I-20]}$$

$$\mathbf{R}_{2P} = \begin{pmatrix} 0 & -iM \\ -iM^\dagger & 0 \end{pmatrix}, \qquad \text{[I-21]}$$

$$\hat{S}_Y = \begin{pmatrix} 0 & -iM/2 \\ iM^\dagger/2 & 0 \end{pmatrix}, \qquad \text{[I-22]}$$

$$\hat{\rho}(0) = \begin{pmatrix} aE & 0 \\ 0 & bE \end{pmatrix}, \qquad \text{[I-23]}$$

where E is the *einheit* operator, $M = M_\alpha^\dagger \cdot M_\beta$, a and b are the initial populations of the α and β electronic spin states, respectively. $P_t^\dagger$ and $Q_t^\dagger$ are diagonal matrices, with elements $P_{ii}^\dagger = \exp(-i\omega_{\alpha i}t)$ and $Q_{ii}^\dagger = \exp(-i\omega_{\beta i}t)$, where $\omega_{\alpha i}$ and $\omega_{\beta i}$ are the nuclear transition (ENDOR) frequencies in the α and β electronic

manifolds, respectively. Computing the echo amplitude using Eq. [I-3] leads to (13):

$$E(\tau) = \frac{1}{2I+1}\mathrm{Re}\{\mathrm{Tr}(Q_\tau^\dagger M^\dagger P_\tau^\dagger M Q_\tau M^\dagger P_\tau M)\}. \qquad \text{[I-24]}$$

When I=1/2, M has a simple form (13):

$$M = \begin{pmatrix} v & u \\ -u^* & v^* \end{pmatrix} \qquad \text{[I-25]}$$

and the normalized echo modulation function will take the form

$$E(\tau) = |v|^4 + |u|^4 + |v|^2 \cdot |u|^2 \cdot \{2\cos(\omega_\alpha \tau) + 2\cos(\omega_\beta \tau) - \\ -\cos[(\omega_\alpha - \omega_\beta)\tau] - \cos[(\omega_\alpha + \omega_\beta)\tau]\} \qquad \text{[I-26]}$$

This is the familiar formula for the two-pulse echo for S=1/2, I=1/2 (cf. Eq. [I-7]).

References

1. Wertz, J. E.; Bolton, J. R. *Electron Spin Resonance, Elementary Theory and Practical Applications*, Chapman and Hall: New York, 1986.

2. Atherton, N. M. *Principles of Electron Spin Resonance*, Ellis-Harwood PTR Prentice Hall: New York, 1993.

3. Pilbrow, J. R. *Transition Ion Electron Paramagnetic Resonance* Clarendon Press: Oxford, 1990.

4. Keijzers, C. D.; Reijerse, E. J.; Schmidt, J. *Pulsed EPR: A New Field of Applications*, North Holland: Amsterdam, 1989.

5. Kevan, L.; Bowman, M. K., eds., *Modern Pulsed and Continuous Wave Electron Spin Resonance*, Wiley-Interscience: New York, 1990.

6. Schweiger, A. *Angew. Chem. Int. Ed. Engl.* **1991**, *30*, 265.

7. Dikanov, S. A.; Tsvetkov, Yu. D. *Electron Spin Echo Envelope Modulation (ESEEM) Spectroscopy* CRC Press: Boca Raton, 1992.

8. Ponti, A.; Schweiger, A., *Appl. Magn. Reson.* **1994**, *7*, 363.

9. Hahn, E. L. *Phys. Rev.* **1950**, *80*, 580.

10. Carr, H. Y.; Purcell, E. M. *Phys. Rev*, **1954**, *84*, 630.

11. Arfken, G. *Mathematical Methods for Physicists* , 3rd edition, Academic Press: San Diego, 1985; pp. 801-803.

12. McCracken, J. In *Handbook of Electron Spin Resonance*, Vol II., Poole, C. P.; Farach, H. A., eds., in press.

13. Mims, W. B. *Phys. Rev.* **1972**, *B 5*, 2409.

14. Mims, W. B. *Phys. Rev.* **1972**, *B 6*, 3543.

15. Mims, W. B. *J. Magn. Reson.* **1984**, *59*, 291.

16. Gemperle, C.; Aebli, G.; Schweiger, A.; Ernst, R. R. *J. Magn. Reson.* **1990**, *88*, 241.

17. Tyryshkin, A. M.; Dikanov, S. A.; Goldfarb, D. *J. Magn. Reson.* **1993**, *Series A 105*, 271.

18. Schweiger, A. In *Modern Pulsed and Continuous-Wave Electron Spin Resonance*, Kevan, L.; Bowman, M. K., eds., Wiley-Interscience: New York, 1990; Chapter 2.

19. Reijerse, E. J.; Dikanov, S. A. *J. Chem. Phys.* **1991**, *95*, 836.

20. Ponti, A.; Schweiger, A. *J. Chem. Phys.* **1995**, *102*, 5207.

21. Lee, H-I.; McCracken, J. *J. Phys. Chem.* **1994**, *98*, 12861.

22. Dikanov, S. A.; Spoyalov, A. P.; Hüttermann, J. *J. Chem. Phys.* **1994**, *100*, 7973.

23. Dikanov, S. A.; Burgard, C.; Hüttermann, J. *Chem. Phys. Lett.* **1993**, *212*, 493.

24. Cohen-Tannoudji, C.; Diu, B.; Laloë, F. *Quantum Mechanics*, John Wiley & Sons: New York, 1977. p. 295ff.

25. Slichter, C. P. *Principles of Magnetic Resonance*, 3rd ed., Springer Verlag: Berlin, 1989. p. 157ff.

26. Lee, H.-I. *Ph. D. Dissertation*, Michigan State University, 1994.

D ESEEM techniques prov

pectra, correlating pairs of

upling and determining

The first variant of 2D ESE

s based on the three-pulse

ESEEM patterns (functions

urier Transform (FT) wi

pectrum in which, for a S

pected: (0, 0), (ω_α, 0), (0, ω_β

pectrum is symmetrical

nidulus FT spectrum, al

mplitude and a *suppres*

SEEM is *absent*.

The disadvantage

f the primary echo deca

As a result, the resolutio

rders of magnitude, esp

by using autoregression

the larger linewidth, as

Chapter II

HYSCORE

2D ESEEM techniques provide a means of disentangling complicated ESEEM spectra, correlating pairs of ESEEM lines belonging to a certain hyperfine coupling and determining the relative sign of different hyperfine couplings. The first variant of 2D ESEEM spectroscopy proposed by Merks and de Beer (1) is based on the three-pulse sequence. It involves collecting sets of stimulated ESEEM patterns (functions of T) at different values of τ. Subsequent 2D Fourier Transform (FT) with respect to τ and T yields a two-dimensional spectrum in which, for a S=1/2, I=1/2 spin system, the following peaks are expected: (0, 0), (ω_α, 0), (0, ω_α), (ω_β, 0), (0, ω_β), (ω_α, ω_β), (ω_β, ω_α); note that the spectrum is symmetrical relative to the diagonal, $\omega_1=\omega_2$ (1, 10). In the modulus FT spectrum, all six peaks with non-zero coordinates have the same amplitude and a *suppression effect typical of the one-dimensional stimulated ESEEM is absent.*

The disadvantage of this 3-pulse 2D ESEEM, however, is that the time of the primary echo decay is much shorter than that of the stimulated echo. As a result, the resolution along the different frequency axes may differ by orders of magnitude, especially in single crystals. This problem can be solved by using autoregression methods for the spectral analysis along the axis with the larger linewidth, as in Ref. (2).

overcome these drawbac

pulse sequence was pro

the correlation betw

spin manifolds. Th

spectroscopy or E

pulse stimulated echo

First, t_1 is varied w

domain data set. Ther

ure II-1b). The linewid

spin-lattice relax

ESCORE spectrum) is o

can be represented as

uence there are three t

stitute the axis of the 2

usted according to spe

3).

In this Chapter, a b

are presented. First, a ge

important features of the

review of the experimen

disordered samples is dis

To overcome these drawbacks of the 3-pulse 2D ESEEM a new method using a four-pulse sequence was proposed by Höfer et al. (3) (Figure II-1a), which also reveals the correlation between hyperfine sublevels belonging to the opposite electron spin manifolds. Therefore it was termed *hyperfine sublevel correlation spectroscopy or* HYSCORE. In this experiment the amplitude of the 4-pulse stimulated echo is measured as a function of the two time periods t_1 and t_2. First, t_2 is varied while t_1 is kept constant to obtain one "slice" of the time-domain data set. Then t_1 is incremented until all the slices are collected (Figure II-1b). The linewidth in both dimensions is determined by the electronic spin-lattice relaxation time, T_1. The frequency-domain data (HYSCORE spectrum) is obtained by 2D Fourier Transformation (Figure II-1c) and can be represented as a contour plot (Figure II-1d). In the four-pulse sequence there are three time variables (τ, t_1 and t_2). Two of them (t_1 and t_2) constitute the axis of the 2D ESEEM spectrum and the third one (τ) has to be adjusted according to spectral properties and desired information (see Section II.3).

In this Chapter, a brief overview of some relevant aspects of HYSCORE are presented. First, a general description of the method is given, then some important features of the 2D data analysis are examined, followed by a short review of the experimental aspects. Finally, the application of HYSCORE to disordered samples is discussed.

igure II-1. Scheme of obta

he amplitude of the 4-p

Time-domain data matr

presentation of the freq

pectrum) obtained by 2D

ata matrix and taking th

ontour plot of the abov

Figure II-1. Scheme of obtaining a HYSCORE contour plot. (a) Measurement of the amplitude of the 4-pulse echo as a function of t_2 and t_1. (b) The resulting 2D time-domain data matrix, with only 33 of all the 128 t_1-slices shown. (c) 3D representation of the frequency-domain data (HYSCORE magnitude spectrum) obtained by 2D Fast Fourier Transformation of the time domain data matrix and taking the absolute value of the resulting complex matrix. (d) Contour plot of the above spectrum.

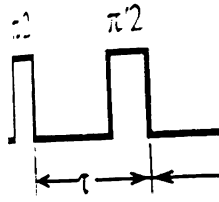
π/2
τ
Preparation

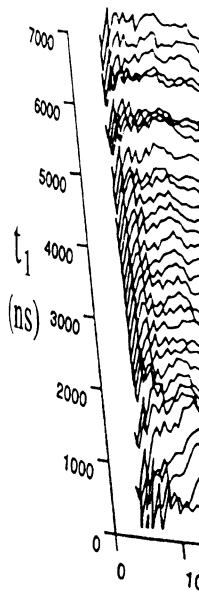
7000
6000
5000
t_1
4000
(ns)
3000
2000
1000
0
0

(a)

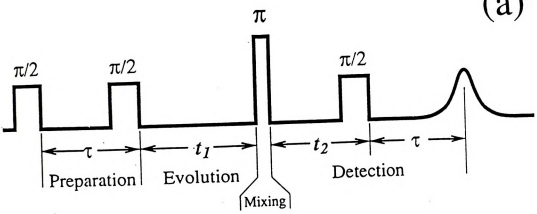
π
π/2
π/2
π/2
τ
t_1
t_2
τ
Preparation
Evolution
Mixing
Detection

(b)

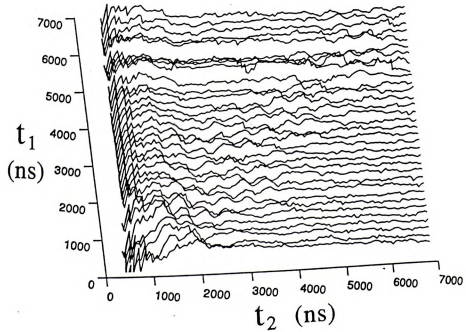
7000
6000
5000
t_1 4000
(ns) 3000
2000
1000
0
0
1000
2000
3000
4000
5000
6000
7000
t_2 (ns)

(c)

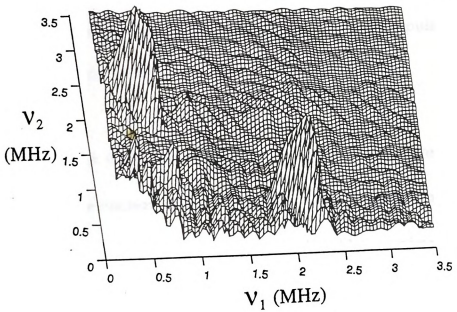
3.5
3
2.5
ν_2
2
(MHz)
1.5
1
0.5
0
0
0.5
1
1.5
2
2.5
3
3.5
ν_1 (MHz)

(d)

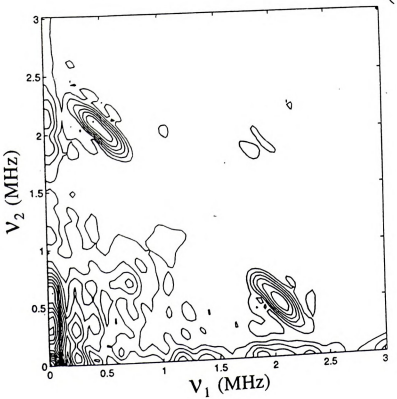
3
2.5
2
1.5
1
0.5
0
ν_2 (MHz)
0
0.5
1
1.5
2
2.5
3
ν_1 (MHz)

Int

e H

rivec

nsid

here

β

ensor

nside

with

E is

the

m

II.1. Introduction to HYSCORE

The HYSCORE modulation formula for the S=1/2, I=1/2 case has been derived by Gemperle et al. (4). Nonselective, ideal $\pi/2$ and π pulses were considered. The spin system is described by the Hamiltonian

$$\hat{\mathcal{H}} = \omega_S \hat{S}_Z + \hat{I}\mathbf{A}\hat{S} - \omega_I \hat{I}_Z \qquad \text{[II-1]}$$

where $\omega_S = g_e \beta_e B_0 / \hbar$ (isotropic g-tensor) is the electron Larmor frequency, $\omega_I = g_n \beta_n B_0 / \hbar$ is the nuclear Larmor frequency, **A** is the (anisotropic) hyperfine tensor. By neglecting the $\hat{S}_X$ and $\hat{S}_Y$ terms (high field approximation), the two nuclear transition frequencies, ω_α and ω_β, associated with electronic spin states $m_S=+1/2$ and $m_S=-1/2$, respectively are given by

$$\omega_\alpha = (\hat{I}\mathbf{A}_+\hat{I})^{1/2} \qquad \text{[II-2a]}$$

$$\omega_\beta = (\hat{I}\mathbf{A}_-\hat{I})^{1/2} \qquad \text{[II-2b]}$$

with

$$\mathbf{A}_\pm = \pm\mathbf{A}/2 + \omega_I \mathbf{E}. \qquad \text{[II-3]}$$

E is the 3x3 unit matrix and $\hat{I}$ is the unit vector along $\mathbf{B}_0$. The amplitude of the four-pulse echo is obtained in the following form, using the density matrix approach described in Chapter I:

$$S(t_1, t_2) = \mathrm{Tr}\{\hat{S}_X U(t) P_{p/2} U(t_2) P_p U(t_1) P_{p/2} U(t) P_{p/2} \hat{S}_Z P_{\pi/2}^{-1} U(t)^{-1} P_{\pi/2}^{-1} U(t_1)^{-1} P_\pi^{-1} U(t_2)^{-1} P_{\pi/2}^{-1} U(t)^{-1}\}, \qquad \text{[II-4]}$$

with the propagators U, P for the free precession and nutation periods, respectively:

$$U(t)=\exp\{-i\,\hat{\mathcal{H}}t\} \qquad [II\text{-}5]$$

$$P_{\pi/2}=\exp\{-i(\pi/2)\hat{S}_X\} \qquad [II\text{-}6]$$

$$P_{\pi}=\exp\{-i(\pi)\hat{S}_X\} \qquad [II\text{-}7]$$

An evaluation of Equation [II-4] was performed by the algebraic computer program MACSYMA(4, 5) and lead to the result

$$S(t_1, t_2)=1-\frac{k}{4}\{C_0+C_\alpha[\cos(\omega_\alpha t_1+\frac{\omega_\alpha\tau}{2})+\cos(\omega_\alpha t_2+\frac{\omega_\alpha\tau}{2})]+$$

$$+C_\beta[\cos(\omega_\beta t_1+\frac{\omega_\beta\tau}{2})+\cos(\omega_\beta t_2+\frac{\omega_\beta\tau}{2})]+$$

$$+C_c[c^2\cos(\omega_\alpha t_1+\omega_\beta t_2+\frac{\omega_+\tau}{2})+c^2\cos(\omega_\beta t_1+\omega_\alpha t_2+\frac{\omega_+\tau}{2})+$$

$$+s^2\cos(\omega_\alpha t_1-\omega_\beta t_2+\frac{\omega_-\tau}{2})+s^2\cos(\omega_\beta t_1-\omega_\alpha t_2+\frac{\omega_-\tau}{2})]\}. \qquad [II\text{-}8]$$

with amplitudes

$$C_0=3-\cos(\omega_\beta\tau)-\cos(\omega_\alpha\tau)-s^2\cos(\omega_+\tau)-c^2\cos(\omega_-\tau)$$

$$C_\alpha=c^2\cos(\omega_\beta\tau-\frac{\omega_\alpha\tau}{2})+s^2(\omega_\beta\tau+\frac{\omega_\alpha\tau}{2})-\cos(\frac{\omega_\alpha\tau}{2})$$

$$C_\beta=c^2\cos(\omega_\alpha\tau-\frac{\omega_\beta\tau}{2})+s^2\cos(\omega_\alpha\tau+\frac{\omega_\beta\tau}{2})-\cos(\frac{\omega_\beta\tau}{2})$$

$$C_c=-2\sin(\frac{\omega_\alpha\tau}{2})\sin(\frac{\omega_\beta\tau}{2}), \qquad [II\text{-}9]$$

the sum and difference frequencies $\omega_+=\omega_\alpha+\omega_\beta$ and $\omega_-=\omega_\alpha-\omega_\beta$, amplitude factors $s^2=\sin^2(\delta/2)$ and $c^2=\cos^2(\delta/2)$, and the depth parameter $k=4\sin^2(\delta/2)\cos^2(\delta/2)$. δ is the angle between the two effective magnetic fields at the nucleus,

corresponding to the two electron spin alignments ($m_S=\pm 1/2$) and can be expressed as

$$\sin^2(\delta/2)=\frac{\left|\omega_I^2-\frac{1}{4}(\omega_\alpha+\omega_\beta)^2\right|}{\omega_\alpha\omega_\beta} \qquad \text{[II-10a]}$$

$$\cos^2(\delta/2)=\frac{\left|\omega_I^2-\frac{1}{4}(\omega_\alpha-\omega_\beta)^2\right|}{\omega_\alpha\omega_\beta} \qquad \text{[II-10b]}$$

The constant term C_0 in Eq. [II-8] depends on τ only and does not contribute to the echo modulation. The second and third terms proportional to C_α and C_β contain the modulation frequencies ω_α and ω_β either in the t_1 or t_2 time domain. In the frequency domain this will result in peaks at $(0, \omega_\alpha)$, $(\omega_\alpha, 0)$, $(0, \omega_\beta)$, $(\omega_\beta, 0)$. The last term with coefficient C_c contains cosine functions with both time variables *simultaneously* in the argument. It produces *cross peaks* in the 2D spectrum at $(\omega_\alpha, \omega_\beta)$, $(\omega_\beta, \omega_\alpha)$. Thus, for a S=1/2, I=1/2 spin system, the HYSCORE spectrum, $S(\omega_1, \omega_2)$ will consist of six peaks as shown schematically in Fig. II-2 by the solid squares. Two pairs of axial peaks with frequencies ω_α and ω_β appear along the axes ω_1 and ω_2, and form two identical 1D spectra. The two cross peaks are related by reflection symmetry relative to the diagonal $\omega_1=\omega_2$. Note that since ideal pulses are assumed, *peaks along the diagonal do not occur*. In real experiments the pulses are never ideal and diagonal peaks do occur (Fig. II-2, empty squares). From Eq. [II-8] it can be inferred that the

peaks appear as a mixture of absorption and dispersion type signals (6) with a variable phase shift that depends on τ. Phasing is normally impossible and it is advisable to plot the magnitude spectrum. The peak amplitudes in this case (4), are expected to be

$$A(\omega_\alpha, 0)=A(0, \omega_\alpha)=\frac{k}{4}\left| c^2\cos(\omega_\beta\tau-\frac{\omega_\alpha\tau}{2})+s^2\cos(\omega_\beta\tau+\frac{\omega_\alpha\tau}{2})-\cos(\frac{\omega_\alpha\tau}{2}) \right| \quad [II\text{-}11a]$$

$$A(\omega_\beta, 0)=A(0, \omega_\beta)=\frac{k}{4}\left| c^2\cos(\omega_\alpha\tau-\frac{\omega_\beta\tau}{2})+s^2\cos(\omega_\alpha\tau+\frac{\omega_\beta\tau}{2})-\cos(\frac{\omega_\beta\tau}{2})\right| \quad [II\text{-}11b]$$

$$A(\omega_\alpha, \omega_\beta)=\frac{k}{4}\left| \sin(\frac{\omega_\alpha\tau}{2})\sin(\frac{\omega_\beta\tau}{2})\right| \ (2c^4+2s^4)^{1/2}. \quad [II\text{-}11c]$$

Depending on the actual values of ω_α, ω_β, t, s^2 and c^2, *blind spots* may occur, at which the intensity of some peaks drops to zero. If the condition of complete excitation ($\omega_1 >> \omega_\alpha, \omega_\beta$, where ω_1 is the MW field strength of the pulses) is not fulfilled, the two allowed and two forbidden transitions are no longer equally excited. This has the following consequences: (a) the Hamiltonian of Eq. [II-1] must be taken into account also *during the pulses* (7, 8). (b) The coherence exchange between the two nuclear transitions ω_α and ω_β is incomplete for non-ideal mixing π-pulse; this leads to the *appearance of two diagonal peaks* $(\omega_\alpha, \omega_\alpha)$, $(\omega_\beta, \omega_\beta)$. (c) The peak intensities are no longer described by Eqs. [II-11] and the formula for the modulation depth parameter, k, is not valid anymore. (d) All possible two-, three- and four-pulse echoes are created (Fig. II-3a), of which, however, the unwanted ones can be eliminated by *phase-cycling* (4) (Fig. II-3b). In our HYSCORE experiments a 4-step phase-cycling

igure II-2

: spir

a

b

Figure I

non-idea

phase-cy

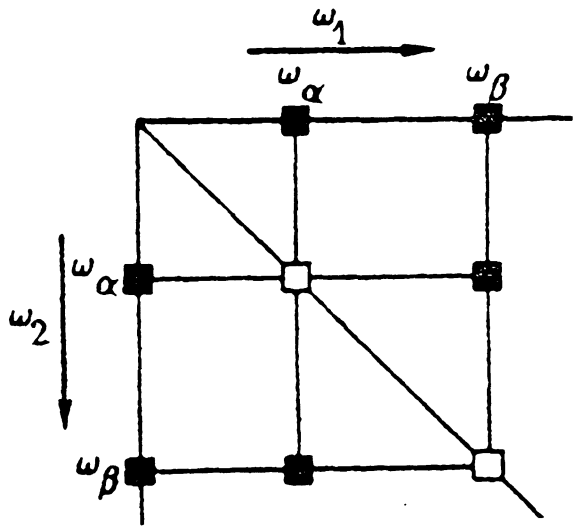

Figure II-2. Schematic of the expected peaks in HYSCORE spectrum of S=1/2, I=1/2 spin system [from Ref. (4)].

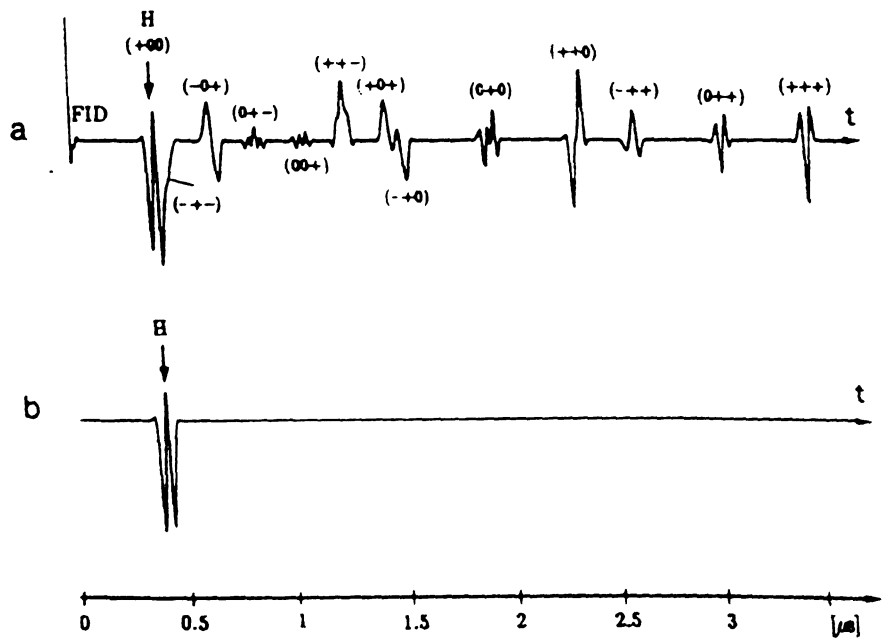

Figure II-3. Computer simulated spin echoes generated by a sequence of four non-ideal pulses (τ=400 ns, t_1=2μs, t_2=1.1μs); (a) without phase-cycling; (b) with phase-cycling according to the cycling scheme of Table II-1 [from Ref. (4)].

was used (see Chapter VI). It should be mentioned that the 3-pulse stimulated echo always coincides with the 4-pulse echo and *cannot be eliminated* by phase cycling. Since cross peaks between nuclear transitions for the same m_s state do not appear, HYSCORE may not only be used to assign peaks to particular sites but it also allows one to determine *the relative sign of the hyperfine coupling* constants within each site (4).

II.2. HYSCORE data analysis

As mentioned above, the HYSCORE correlation spectrum, $S(\omega_1, \omega_2)$ is obtained via a 2D Fourier Transform (FT) of the time-domain data, $S(t_1, t_2)$. 2D FT simply means taking the Fourier Transform (9) of $S(t_1, t_2)$ with respect to t_2, leading to $S(t_1, \omega_1)$, then the FT of $S(t_1, \omega_1)$ is performed with respect to t_1, resulting in $S(\omega_1, \omega_2)$. The order of FT's with respect to t_1 and t_2 may be interchanged. The *complex Fourier Transformation* of the data set can be performed in different ways leading to different spectral representations as well as different spectral densities (10). Therefore, it may be of interest to give a brief introduction to certain relevant aspects of 2D FT.

Amplitude- and Phase-Modulation of 2-D ESEEM Signals

In a 2D experiment, a signal observed during a time t_2 is modulated as a function of a previous time interval t_1. This history can either affect the phase or the amplitude, or both (6). If we consider *non-quadrature detected* signals, as is normally the case in ESEEM experiments, an exemplary 2D time-domain signal can be described as

$$S(t_1, t_2)=\cos(\omega_A t_1)\cos(\omega_D t_2+\omega_P t_1), \qquad \text{[II-12]}$$

which is represented in Fig. II-4a. For the sake of simplicity, all relaxation and amplitude factors have been neglected. Also, constant phase shifts arising from the spectrometer deadtime are not important here and are therefore omitted. The signal $S(t_1, t_2)$ contains a frequency ω_D detected during t_2 and is modulated by the two frequencies ω_A and ω_P as a function of t_1 where ω_A affects the amplitude while ω_P modulates the phase of the signal. A FT performed in the t_2 domain will generate a real- and imaginary part spectrum $F(\omega_2)=A(\omega_2)$ + $iD(\omega_2)$, containing the absorption (A) and dispersion (D) line-shapes, respectively. For a phase modulated signal, this assignment is only valid for the first slice in the t_1 domain ($t_1=0$). The signal $S(t_1, \omega_2)$ then becomes:

$$S(t_1, \omega_2)=\cos(\omega_A t_1)\exp(i\omega_P t_1)F(\omega_2=\omega_D) =$$

$$\frac{1}{2}\{\exp(i(\omega_A+\omega_P)t_1) + \exp(i(\omega_P-\omega_A)t_1)F(\omega_2=\omega_D). \qquad \text{[II-13]}$$

From this equation we can derive the *special cases* of exclusive amplitude or phase modulation. If the signal $S(t_2)$ is only modulated in amplitude ($\omega_P=0$), no information about the sign of the modulation frequency is present. Thus, a complex FT in the t_1 domain results in a pair of lines at the positions (ω_A, ω_D) and $(-\omega_A, \omega_D)$. As *only the real part signal in t_2 is recorded,* the complex FT in the ω_2 domain also generates two lines at $+\omega_D$ and $-\omega_D$ and the calculation of

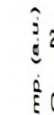

Figure I

followin

The tim

(+, +) q

$S(\omega_1, \omega_2$

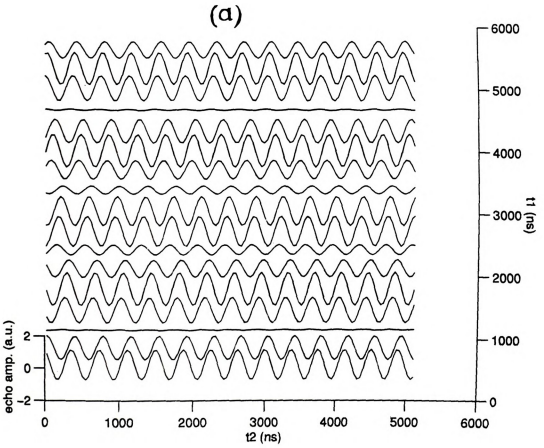

Figure II-4. Graphical representation of Eq. [II-12], calculated with the following parameters: $\omega_A/2\pi$=2.00 MHz, $\omega_P/2\pi$=1.33 MHz, $\omega_D/2\pi$=2.66 MHz. (a) The time domain data matrix, $S(t_1, t_2)$, with only 13 of the 128 slices shown. (b) (+, +) quadrant of the absolute value spectrum, $S(\omega_1, \omega_2)$, (c) (-, +) quadrant of $S(\omega_1, \omega_2)$.

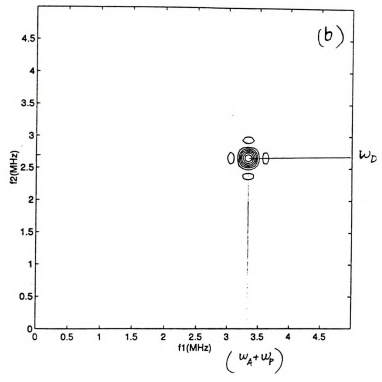
(b)
f2(MHz)
f1(MHz)
ω_D
$(\omega_A + \omega_P)$

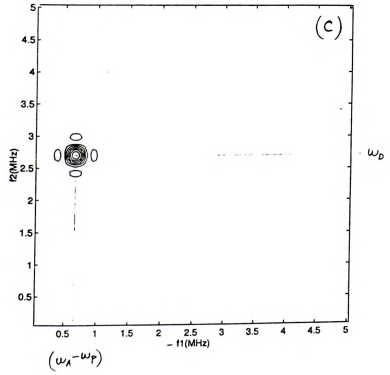
(c)
f2(MHz)
f1(MHz)
ω_D
$(\omega_A - \omega_P)$

the 2D-FT results in 4 lines, each of which *contain the same information*. In the case of an amplitude modulated real part signal, it is therefore sufficient to consider only the frequency range $\omega_1 > 0$, $\omega_2 > 0$. If only the phase modulation is present (ω_A=0), the complex FT in the t_1 domain preserves the sign of the modulation frequency resulting in a single line at (ω_P, ω_2).

If both amplitude and phase are modulated, the second FT again results in a pair of lines, now at the positions (ω_A+ω_P, ω_D) and (ω_P-ω_A, ω_D). In contrast to the amplitude modulation, we now have to consider *positive and negative frequencies in the ω_1 domain*, while it is still sufficient to deal only with the positive ω_2 frequencies (Figure II-4b, c). In general, the line shapes obtained after a 2D-FT are a mixture of absorption and dispersion lines (6). Therefore, the *absolute value (magnitude) spectrum* defined by

$$S(\omega_1, \omega_2)=[Re^2(\omega_1, \omega_2) + Im^2(\omega_1, \omega_2)]^{1/2} \qquad \text{[II-14]}$$

is normally used for evaluation and presentation purposes.

2D-FT of HYSCORE Data

Here we examine only those parts of the HYSCORE modulation formula (Eq. [II-8]) which produce cross peaks after 2D-FT, namely:

$$S(t_1, t_2)=C[c^2\cos(\omega_\alpha t_1+\omega_\beta t_2+\Phi_+)+c^2\cos(\omega_\beta t_1+\omega_\alpha t_2+\Phi_+)+$$
$$+s^2\cos(\omega_\alpha t_1-\omega_\beta t_2+\Phi_-)+s^2\cos(\omega_\beta t_1-\omega_\alpha t_2+\Phi_-)] \qquad \text{[II-15]}$$

The amplitude factor C and the phase constants $\Phi_\pm$ are independent of t_1 and t_2 and depend on t only. The t_1 dependence we are interested in acts only on

the phase of the signal. A most interesting situation arises from the factors c^2 and s^2 defined by Eqs. [II-10]. If we consider weak anisotropic HFI we can *approximate* the nuclear transition frequencies by

$$\omega_{\alpha\beta} = |\omega_I \pm A/2| \qquad \text{[II-16]}$$

where A denotes the hyperfine coupling for a particular crystal orientation, ω_I is the nuclear Larmor frequency. Using [II-16] we get

$$c^2 = \frac{\left|\omega_I^2 - \frac{A^2}{4}\right|}{\omega_\alpha \omega_\beta} \text{ and } \quad s^2=0 \qquad \text{[II-17]}$$

for $\omega_I > A/2$ (relatively weak HFI), while

$$c^2 = 0 \quad \text{and} \quad s^2 = \frac{\left|\omega_I^2 - \frac{A^2}{4}\right|}{\omega_\alpha \omega_\beta} \qquad \text{[II-18]}$$

for $\omega_I < A/2$ (relatively large HFI). FT of Eq. [II-15] with respect to t_2 then results in

$$S(t_1, \omega_2)=\exp(i\omega_\alpha t_1)\cdot F(\omega_2=\omega_\beta) + \exp(i\omega_\beta t_1)\cdot F(\omega_2=\omega_\alpha) \qquad \text{[II-19a]}$$

for $\omega_I > A/2$, and

$$S(t_1, \omega_2)=\exp(-i\omega_\alpha t_1)\cdot F(\omega_2=\omega_\beta) + \exp(-i\omega_\beta t_1)\cdot F(\omega_2=\omega_\alpha) \qquad \text{[II-19b]}$$

for $\omega_I < A/2$.

The contribution from the time independent phase shift in Eq. [II-15] has been omitted. *The sign of the phase modulation in t_1 depends here on the relation of the hyperfine coupling to the nuclear Larmor frequency.* Carrying out the FT in the second dimension and calculating the absolute value spectrum

results in a pair of cross peaks at $(\omega_\alpha, \omega_\beta)$, $(\omega_\beta, \omega_\alpha)$ if $\omega_1 > A/2$, while in the case of $\omega_1 < A/2$, the cross peaks are in the negative ω_1 region, at $(-\omega_\alpha, \omega_\beta)$ and $(-\omega_\beta, \omega_\alpha)$. This is verified by an experimental example shown in Figure II-5 [from Ref. (10)], showing both (+, +) and (-, -) regions of the HYSCORE spectrum of the malonic acid radical. At this particular crystal orientation $A_1 < 2\omega_I$, while $A_2 > 2\omega_I$. So, A_1 is expected to give rise to cross-peaks in the (+, +) region, while cross peaks corresponding to A_2 are expected to be in the (-, +) region. This indeed is observed, except that cross peaks that correspond to A_2 also appear in the (+, +) region, though not as intensely as in the (-, +) region. This is due to the fact that Eq. [II-16] is an approximation, only. With the exact expressions for the nuclear transition (ENDOR) frequencies, factors *s^2 and c^2 will not drop to zero*. Therefore, there will always be a contribution from a positive phase modulation for every negative phase modulation in t_1 and vice versa. It is also interesting to note that the diagonal peaks, which are due to an incomplete inversion by the π-pulse (4), are mainly confined to the positive ω_1 region. Thus, the modulation that leads to the diagonal peaks is a *phase modulation in t_1 with a positive sign*.

II.3. Experimental aspects

In the HYSCORE experiment, two important parameters have to be adjusted to achieve optimum results. The first step is to find a τ value so that the

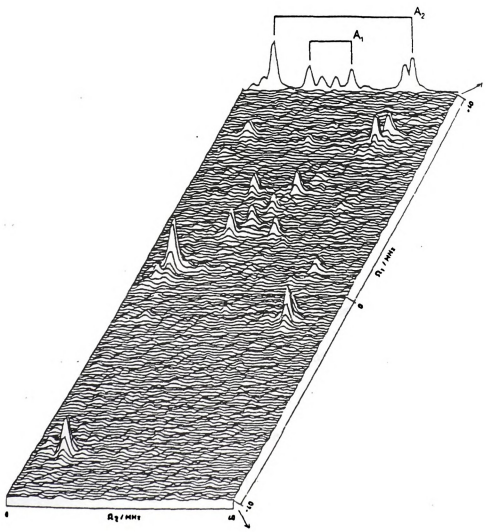

Figure II-5. HYSCORE absolute value spectrum of irradiated malonic acid [from Ref. (10)].

suppression effect of the cross peaks is minimized and in the second step, the π-pulse is adjusted in width and amplitude to obtain the best inversion of the stimulated echo.

A method of finding the optimum t value is to record a series of 3-pulse experiments with increasing τ (separation between the first and second pulses) then Fourier Transform them with respect to T and calculate the absolute value spectrum. Choose τ for the HYSCORE at which the least suppression is observed in the frequency region of interest (10). In single crystals with a limited number of lines there may be several τ values fulfilling this condition. *In disordered systems*, however, it is important to use the smallest τ at which all lines are present to minimize line-shape distortions. In practice, τ values in the range of 120-200 ns are used (10, 14). This approach is justified by the formula for the amplitude of the cross peaks in the absolute value mode (Eq. [II-11c]), which may be rewritten in the following form,

$$A(\omega_\alpha, \omega_\beta)=\frac{k}{8}[(1-\cos\omega_\alpha\tau)(1-\cos\omega_\beta\tau)]^{1/2}(2c^4+2s^4)^{1/2}. \qquad \text{[II-20]}$$

This shows that the cross peak amplitude is mainly determined by the amplitudes of the corresponding line-pair measured in the 3-pulse experiment. Therefore, if one pair of lines are suppressed in the 3-pulse experiment, the corresponding cross peaks in the HYSCORE experiment should also be suppressed. This is not exactly observed in the experiments, however (10).

The next aspect of the optimization procedure is to increase the amplitude ratio of the cross peaks to undesired diagonal peaks. It has been pointed out (4) that the diagonal peaks result from an incomplete mixing by the inverting π-pulse. For perfect mixing this pulse should be much shorter than the $\pi/2$-pulses. In the case of relatively high frequency proton lines, this condition cannot be fulfilled because of the limited MW power available. The degree of inversion obtained for certain pulse widths and amplitudes can be estimated from the appearance of the HYSCORE echo. Fig. II-6 compares the results of two experiments (10). In (a) the π and $\pi/2$ pulses had the same amplitude and their width was 20 ns and 10 ns respectively. Under these conditions, the diagonal peaks dominate the spectrum. The spectrum in (b) was obtained with a pulse width of 14 ns for the π-pulse and 10 ns for the $\pi/2$ pulses. Correspondingly, the power of the π-pulse was 3 dB higher than that of the $\pi/2$-pulses, which leads to significant improvement of the ratio of cross peak amplitudes to diagonal peak amplitudes.

II.4. HYSCORE on disordered samples

In disordered samples (glasses, frozen solutions, powders) the analysis of 1D ESEEM spectra may become complex. Part of the reason for this complexity is illustrated in Figure II-7, where part (a) shows the simulated ENDOR powder spectrum for an S=1/2, I=1/2 spin system with an axial hyperfine tensor. In this case the principal values of the tensor can readily be determined from the

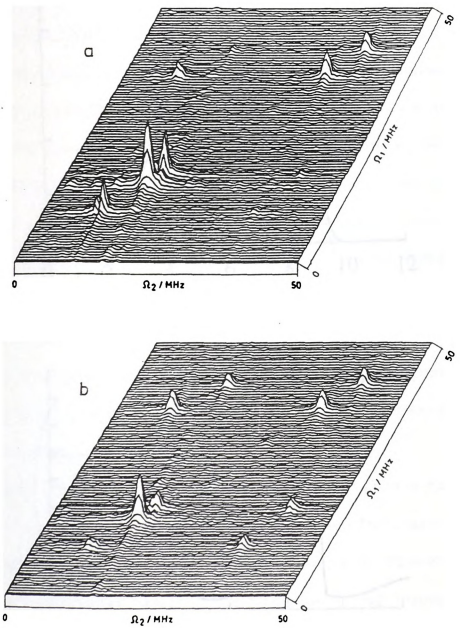

Figure II-6. HYSCORE absolute value spectrum of irradiated succinic acid. (a) Width of the $\pi/2$ pulses 10 ns, that of the π-pulse 20 ns; (b) width of $\pi/2$ pulses 10 ns, that of π-pulse 14 ns (power of the π-pulse is +3dB higher than that of $\pi/2$ pulses) [from Ref. (10)].

Figure II.

system. P

The corre

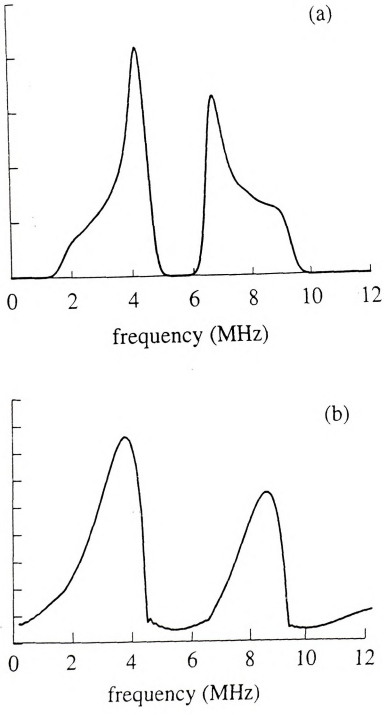

Figure II-7. (a) Simulated powder ENDOR spectrum for an S=1/2, I=1/2 system. Parameters: g_n=2.261 (^{31}P), $A_{||}$=7.1 MHz, $A_{\perp}$=2.4 MHz, B_0=3200 G. (b) The corresponding simulated 3-pulse ESEEM spectrum.

frequencies of the turning points and lineshape singularities (12). The corresponding ESEEM simulation is shown in Fig. II-7b. Here the lineshape features are absent, because the intensity of the ESEEM is determined by the *product* of the orientation dependent coupling parameter (which gives rise to the classical powder lineshape seen in (a)) with the modulation depth parameter, k, which is also orientation dependent; k goes to zero at the canonical orientations, so the turning points and singularities are missing. Due to the absence of these characteristic features, *computer simulation* is typically required to extract the principal values of the HFI tensor from ESEEM. Some of these limitations can be overcome by HYSCORE. The contour plots of the cross peaks carry information about the hyperfine tensor (11, 14). This is illustrated in Figure II-8, where (a) and (b) correspond to the weak and strong coupling cases,
respectively. The contours will be parallel and perpendicular to the diagonal only in the case of small anisotropy in the HFI, where the nuclear transition (ENDOR) frequencies may be approximated by Eq. [II-16]. When the anisotropy is increased (greater T), the cross peaks develop a *curvature*. This effect is demonstrated in Fig. II-9. These simulations were done by a MATLAB program, "hysline1.m" (see Appendix).

Recently, Dikanov and Bowman have derived simple analytical expressions for cross-peak contours for disordered S=1/2, I=1/2 systems (13). They have proposed a simple graphical method to obtain the principal elements of the hyperfine tensor. Here we outline their approach. First,

Figure II-8. Schematic

gon system with a sm

$\langle A_{\parallel}/2$.

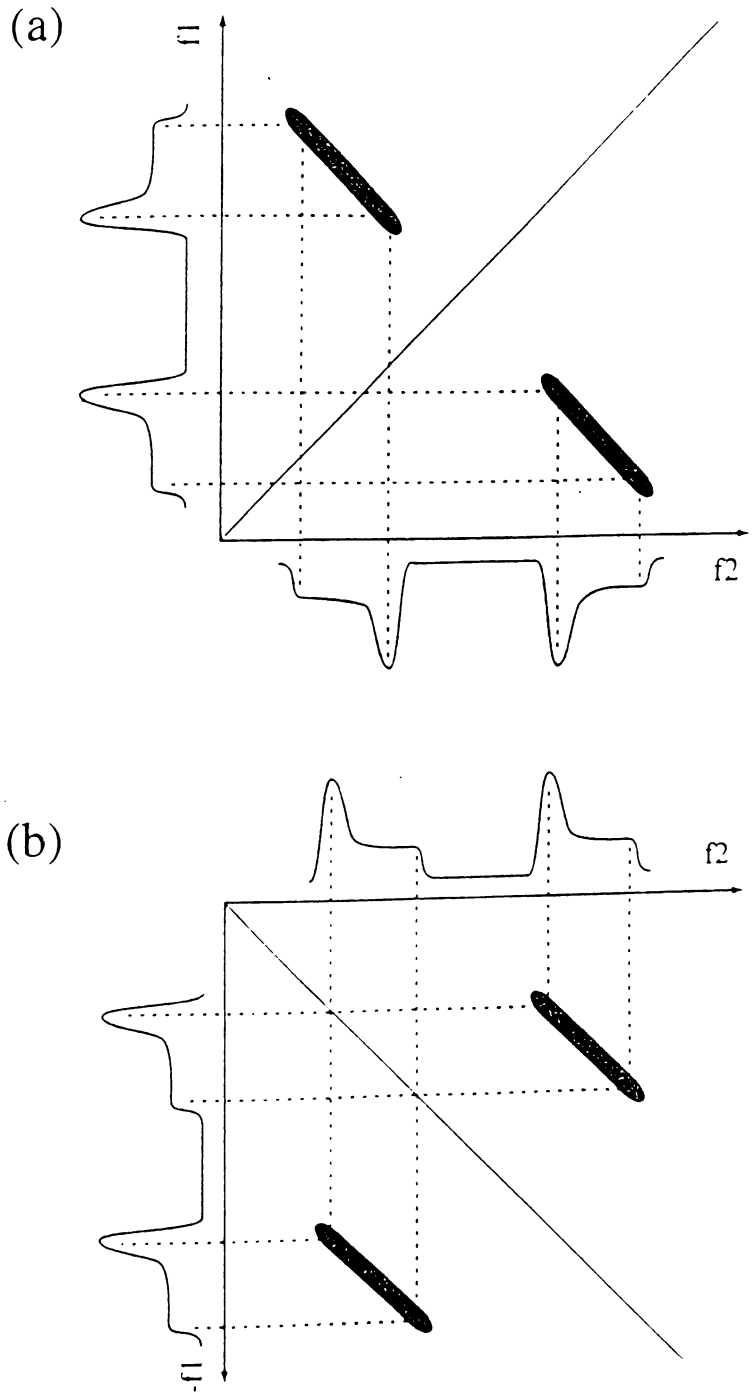

Figure II-8. Schematic HYSCORE contour plots arising from an S=1/2, I=1/2 spin system with a small anisotropic hyperfine interaction. (a) $\omega_I > A_{||}/2$, (b) $\omega_I < A_{||}/2$.

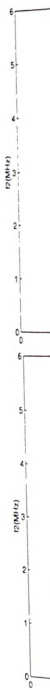

figure II-9. Simulated

=1/2, I=1/2 system. P

linewidth=0.1 MHz, T=

(d). Simulation was pe

Appendix).

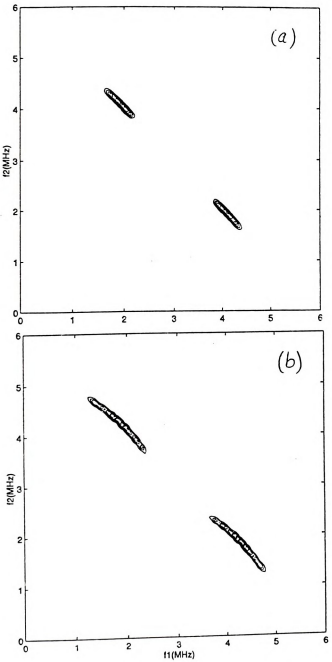

Figure II-9. Simulated HYSCORE contour plots arising from axial HFI from an S=1/2, I=1/2 system. Parameters: $\omega_I/2\pi$=3 MHz, A_{iso}=2 MHz, Gaussian linewidth=0.1 MHz, T=0.4 MHz (a), T=0.8 MHz (b), T=1.2 MHz (c), T=1.6 MHz (d). Simulation was performed with the MATLAB program "hysline1.m" (see Appendix).

6
5
4
3
2
1
0
0
f2(MHz)

6
5
4
3
2
1
0
0
f2(MHz)

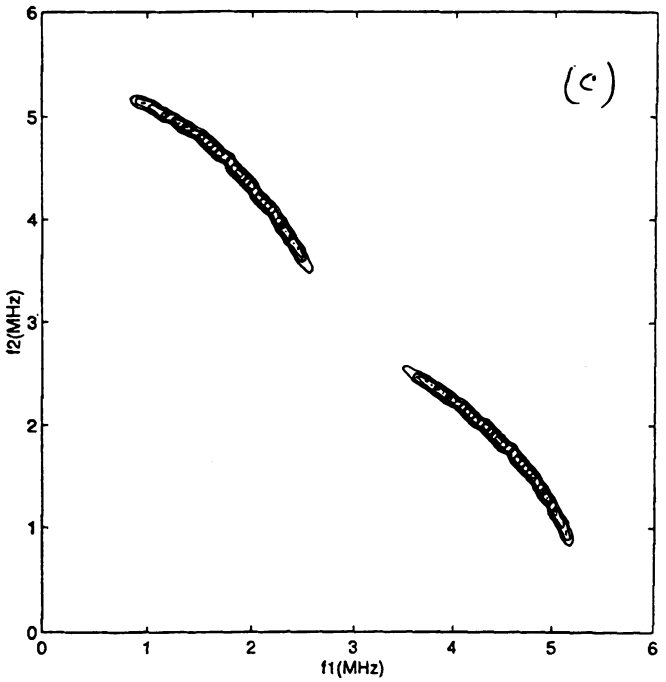
(c)
f2(MHz)
f1(MHz)
0
1
2
3
4
5
6

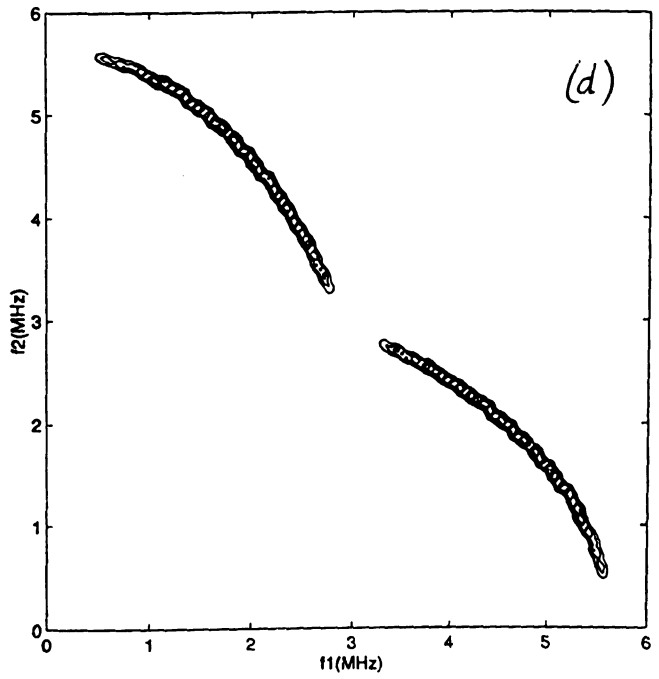
(d)
f2(MHz)
f1(MHz)
0
1
2
3
4
5
6

nsider an *axial HFI ten*

nisotropic part, with pr

nd the unique principa

n written as

where $\omega_{\alpha\beta}=-\omega_I \pm A/2$

ensor are $A = A_{iso}+2T$

n angular units). Eqs.

tarting point of the de

etween the ENDOR fr

which means that in th

requencies form *two a*

f the HFI parameters

G_{α}

This suggests a straigh

xperimental 2D spec

consider an *axial HFI tensor*, consisting of an isotropic component, A_{iso} and anisotropic part, with principal values (-T, -T, 2T). If Θ is the angle between $\mathbf{B}_0$ and the unique principal axis of the HFI tensor, the ENDOR frequencies can be written as

$$\omega_\alpha{}^2 = \omega_{||\alpha}{}^2\cos^2\Theta + \omega_{\perp\alpha}{}^2\sin^2\Theta \qquad \text{[II-21a]}$$

$$\omega_\beta{}^2 = \omega_{||\beta}{}^2\cos^2\Theta + \omega_{\perp\beta}{}^2\sin^2 \qquad \text{[II-21b]}$$

where $\omega_{||\alpha(\beta)} = -\omega_I \pm A_{||}/2$, $\omega_{\perp\alpha(\beta)} = -\omega_I \pm A_\perp/2$; the principal values of the HFI tensor are $A_{||} = A_{iso} + 2T$ and $A_\perp = A_{iso} - T$, and ω_I is the nuclear Larmor frequency (in angular units). Eqs. [II-21] are equivalent to Eq. [1] in Ref. (20), which is the starting point of the derivation. It can easily be shown that the relation between the ENDOR frequencies has the following form:

$$(\omega_\alpha)^2 = Q_\alpha(\omega_\beta)^2 + G_\alpha \qquad \text{[II-22a]}$$

$$(\omega_\beta)^2 = Q_\beta(\omega_\alpha)^2 + G_\beta \qquad \text{[II-22b]}$$

which means that in the 2D HYSCORE contour plot the correlated ω_α and ω_β frequencies form *two arcs*, whose geometrical parameters, Q_α and Q_β depend of the HFI parameters A_{iso} and T. It can be shown that

$$Q_{\alpha(\beta)} = \frac{T + 2A_{iso} \mp 4\omega_I}{T + 2A_{iso} \pm 4\omega_I} \qquad \text{[II-23a]}$$

$$G_{\alpha(\beta)} = \frac{\pm 2\omega_I(4\omega_I^2 - A_{iso}^2 + 2T^2 - A_{iso}\cdot T)}{T + 2A_{iso} \pm 4\omega_I} \qquad \text{[V-23b]}$$

This suggests a straightforward way to extract A_{iso} and T from the experimental 2D spectrum: obtain a set of correlated ω_α and ω_β frequencies

rom the cross peak con

straight line will have a

2] for A_{ac} and T will yi

This analysis can

nisotropic part [-T(1+d

ze

$$\omega_\alpha^2 = \omega_{zz}^2 c$$

$$\omega_\beta^2 = \omega_{z\beta}^2 c$$

where $\omega_{z\alpha(\beta)}$ are the EN

rientation of $\mathbf{B}_0$ with r

be expressed as $\omega_{z\alpha(\beta)}$=-

angles specifying the o

the HFI tensor. Eqs. [II

$$\omega_{\alpha(\beta)}=[[\omega$$

where $\omega_{T\alpha(\beta)}$ designate

plane and are defined

$$\omega_{T\alpha(\beta)}=\omega$$

Note that Eq. [II-25] h

the axial case, except

25] corresponds to ar

incrementing Φ betw

from the cross peak contour, plot ω_α^2 vs. ω_β^2 (or vice versa), the resulting straight line will have a slope of $Q_{\alpha(b)}$ and an intercept of $G_{\alpha(\beta)}$. Solving Eqs. [II-23] for A_{iso} and T will yield two equivalent sets of parameters (13).

This analysis can easily be extended to a rhombic HFI tensor, with an anisotropic part [-T(1+d), -T(1-d), +2T]. The ENDOR frequencies in this case are

$$\omega_\alpha^2 = \omega_{z\alpha}^2\cos^2\Theta + \omega_{y\alpha}^2\sin^2\Theta\sin^2\Phi + \omega_{x\alpha}^2\sin^2\Theta\cos^2\Phi \qquad \text{[II-24a]}$$

$$\omega_\beta^2 = \omega_{z\beta}^2\cos^2\Theta + \omega_{y\beta}^2\sin^2\Theta\sin^2\Phi + \omega_{x\beta}^2\sin^2\Theta\cos^2\Phi \qquad \text{[II-24b]}$$

where $\omega_{i\alpha(\beta)}$ are the ENDOR frequencies corresponding to the canonical orientation of $\mathbf{B_0}$ with respect to the principal axes of the HFI tensor and can be expressed as $\omega_{i\alpha(\beta)}=-\omega_I\pm A_{ii}/2$; i=x, y, z. Θ and Φ are the polar and azimuthal angles specifying the orientation of $\mathbf{B_0}$ in the principal axis system (PAS) of the HFI tensor. Eqs. [II-24] can be rewritten in the following form,

$$\omega_{\alpha(\beta)}=\{[\omega_{z\alpha(\beta)}^2 - \omega_{T\alpha(\beta)}^2]\cos^2\Theta + \omega_{T\alpha(\beta)}^2]\}^{1/2} \qquad \text{[II-25]}$$

where $\omega_{T\alpha(\beta)}$ designate the effective ENDOR frequencies in the transverse (xy) plane and are defined as (compare to Eq. [10] in Ref. (13)),

$$\omega_{T\alpha(\beta)}=\omega_{x\alpha(\beta)}^2\cos^2\Phi + \omega_{y\alpha(\beta)}^2\sin^2\Phi. \qquad \text{[II-26]}$$

Note that Eq. [II-25] has the same form as Eq. [1] of Ref. (13), which describes the axial case, except for the Φ-dependence of $\omega_{T\alpha(\beta)}$. Thus at a certain Φ, Eq. [II-25] corresponds to an axial tensor, yielding an *arc-shaped* correlation pattern. Incrementing Φ between 0 and $\pi/2$ produces a series of arcs, which form a

arm-shaped cross peak

grows a result of a num

"SpinEchoRom.m" (see A

Despite its growi

ize. It has been utilized

nitrogens from those of

photosynthetic reaction

of ESEEM frequencies

[8]. Analysis of the co

histidine complexes of

contributing to the hy

previously. Pilbrow's g

method (19). It is base

increase the modulati

the intensity of cross p

enhanced. Höfer has

disordered samples ir

possible τ is the most

appears to be useful i

eliminate the suppre

used HYSCORE to a

broadening effects of

horn-shaped cross peak pattern. This is illustrated in Figure II-10, which shows a result of a numerical calculation done by the MATLAB program "hyslineRom.m" (see Appendix).

Despite its growing popularity, HYSCORE has had few applications so far. It has been utilized to isolate the ESEEM contributions of weakly coupled nitrogens from those of the more strongly coupled ones in a bacterial photosynthetic reaction center (15) and also to correlate unambiguously pairs of ESEEM frequencies belonging to certain ^{14}N couplings in a Fe-S protein (16). Analysis of the contour line shapes in HYSCORE of imidazole and histidine complexes of VO^{2+} was carried out by Dikanov and coworkers (18), contributing to the hyperfine information obtained on these complexes previously. Pilbrow's group have proposed a new six-pulse 2D ESEEM method (19). It is based on augmenting the five-pulse sequence proposed to increase the modulation depth (21) with an additional π-pulse. As a result, the intensity of cross peaks relative to that of diagonal peaks is significantly enhanced. Höfer has examined the suppression effect in HYSCORE in disordered samples in detail (14). He has shown that generally the shortest possible τ is the most beneficial. Thus HYSCORE with remote detection (15) appears to be useful in some cases, and proposed a 3D version of ESEEM to eliminate the suppression effect completely (14). Pöppl and coworkers have used HYSCORE to analyze the inhomogeneous and homogeneous line-broadening effects of proton ESEEM signals in single crystals (17).

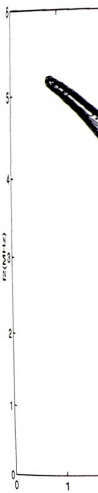

Figure II-10. Simulate

hyperfine interaction

MHz, A_{zz}=2 MHz, T=

Simulation was calcu

Appendix).

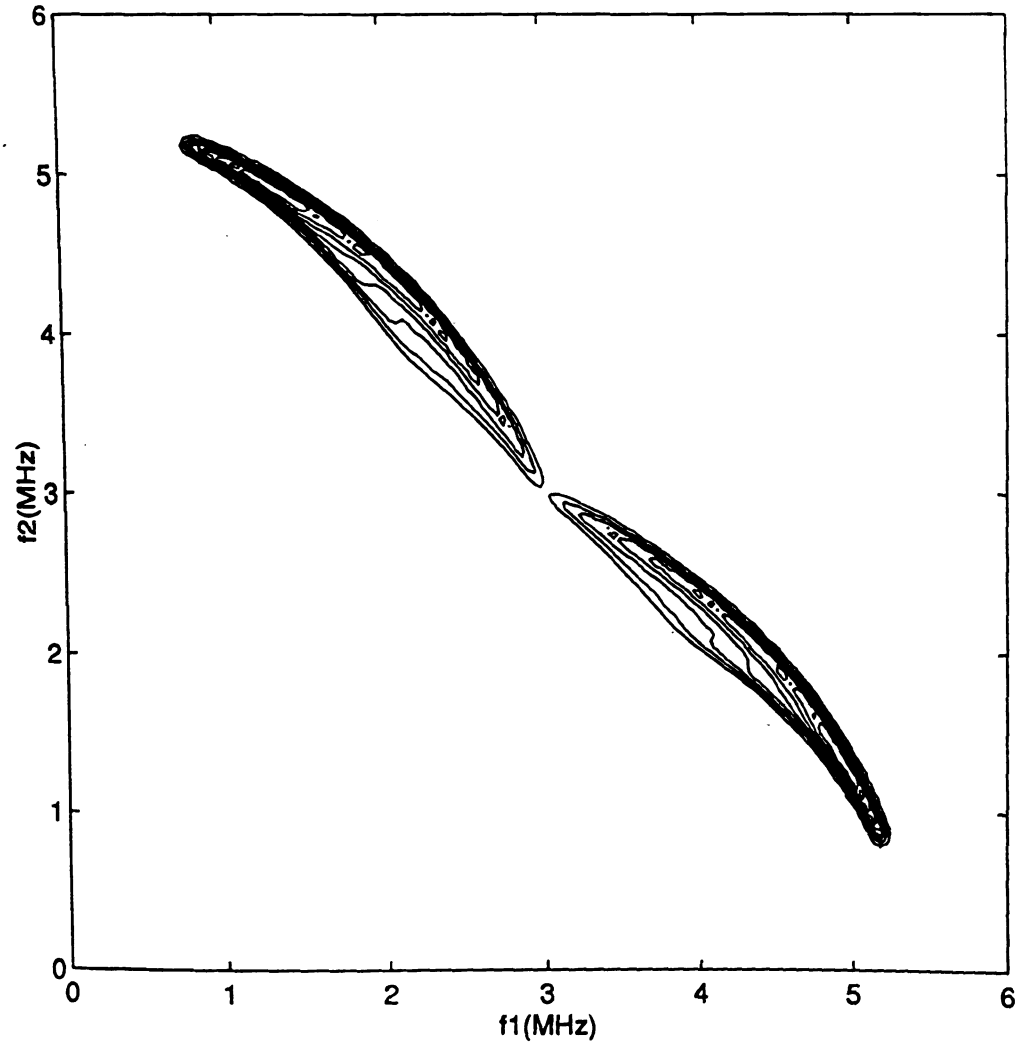

Figure II-10. Simulated HYSCORE contour plot arising from a rhombic hyperfine interaction in an S=1/2, I=1/2 spin system. Parameters: $\omega_I/2\pi$=3 MHz, A_{iso}=2 MHz, T=1.2 MHz, δ=0.7, Gaussian linewidth=0.1 MHz. Simulation was calculated with the MATLAB program "hyslineRom.m" (see Appendix).

1. Merks, R. P. J.; d

2. Barkhuijsen, H.;
Reson. **1982**, *50*,

3. Höfer, P.; Grupp
1986, *132*, 279.

4. Gemperle, C.; A
88, 241.

5. MACSYMA, Int

6. Ernst, R. R.; Bo
Magnetic Reson
Oxford, 1987.

7. Barkhuijsen, H
Reson. **1985**, *61*

8. Astashkin, A.
Chem. Phys. Le

9. Arfken, Mathe
Press: San Die

10. Höfer, P. In *I*
EMARDIS-91
pp. 1-15.

References

1. Merks, R. P. J.; de Beer, R. *J. Phys. Chem.* **1979**, *83*, 3319.

2. Barkhuijsen, H.; de Beer, R.; de Wild, E. L.; van Ormondt, D. *J. Magn. Reson.* **1982**, *50*, 299.

3. Höfer, P.; Grupp, A.; Nebenführ, H.; Mehring, M. *Chem. Phys. Lett.* **1986**, *132*, 279.

4. Gemperle, C.; Aebli, G.; Schweiger, A.; Ernst, R. R. *J. Magn. Reson.* **1990**, *88*, 241.

5. MACSYMA, Interactive Computer System, Mathlab Group, MIT, 1983.

6. Ernst, R. R.; Bodenhausen, G.; Wokaun, A. *Principles of Nuclear Magnetic Resonance in One and Two Dimensions*, Clarendon Press: Oxford, 1987.

7. Barkhuijsen, H.; de Beer, R.; Pronk, B. J.; van Ormondt, D. *J. Magn. Reson.* **1985**, *61*, 284.

8. Astashkin, A. V.; Dikanov, S. A.; Kurshev, V. V.; Tsvetkov, Yu. D. *Chem. Phys. Lett.* **1987**, *136*, 335.

9. Arfken, Mathematical methods for physicist, 3rd Edition, Academic Press: San Diego, 1985; pp. 794-823.

10. Höfer, P. In *Electron Magnetic Resonance of Disordered Systems EMARDIS-91*; Yordanov, N. D., Ed.; World Scientific: Singapore, 1991; pp. 1-15.

11. Shane, J. J.; Höfer
99, 596.

12. Blinder, S. M. J.

13. Dikanov, S. A.;

14. Höfer, P. *J. Mag*

15. Käss, H.; Rautt
1995, *99*, 436.

16. Shergill, J. K.; J
1995, *34(51)*, 165

17. Pöppl, A.; Bött
214.

18. Dikanov, S. A.
Chem. Soc. **199**

19. Song, R.; Zhor
Phys. Lett. **199**

20. Cho, H.; Pfer
Chem. Phys. L

21. Gemperle, C.
565.

11. Shane, J. J.; Höfer, P.; Reijerse, E. J.; de Boer, E. J. *J. Magn. Reson.* **1992**, *99*, 596.

12. Blinder, S. M. *J. Chem. Phys.* **1960**, *33(3)*, 748.

13. Dikanov, S. A.; Bowman, M. K. *J. Magn. Reson.* **1995**, *Series A 116*, 125.

14. Höfer, P. *J. Magn. Reson.*, **1994**, *Series A 111*, 77.

15. Käss, H.; Rautter, J.; Bönigk, B.; Höfer, P.; Lubitz, W. *J. Phys. Chem.* **1995**, *99*, 436.

16. Shergill, J. K.; Joannou, C. L.; Mason, J. R.; Cammack, R. *Biochemistry* **1995**, *34(51)*, 16533.

17. Pöppl, A.; Böttcher, R.; Völkel, G. *J. Magn. Reson.* **1996**, *Series A 120*, 214.

18. Dikanov, S. A.; Samoilova, R. I.; Smieja, J. A.; Bowman, M. K. *J. Am. Chem. Soc.* **1995**, *117*, 10579.

19. Song, R.; Zhong, Y. C.; Noble, C. J.; Pilbrow, J. R.; Hutton, D. R. *Chem. Phys. Lett.* **1995**, *237*, 86.

20. Cho, H.; Pfenninger, S.; Gemperle, C.; Schweiger, A.; Ernst, R. R. *Chem. Phys. Lett.* **1989**, *160*, 391.

21. Gemperle, C.; Schweiger, A.; Ernst, R. R. *Chem. Phys. Lett.* **1991**, *178*, 565.

II. Introduction

ince the identification

ave been intensively

olecular and catalytic

ast two *major groups*

hose that contain only

Desulfovibrio vulgaris

I), while the *Desulfo*

prototype of the (Ni,

enzyme is to catalyze

is expressed by the fo

Understanding the

gain insight into the

hydrogen oxidizing

the study of the me

efficient means of p

In this Chap

are summarized. R

described briefly.

Chapter III

Ni-containing Hydrogenases

III.1. Introduction

Since the identification of the Ni-centers in hydrogenases, these enzymes have been intensively studied from various types of biochemical approach: molecular and catalytic properties, spectroscopy and genetics. There are at least *two major groups*: the Ni-Fe-S type (with the subgroup Ni-Fe-S-Se) and those that contain only [Fe-S] clusters. The hydrogenase from the bacterium *Desulfovibrio vulgaris* is the most extensively studied Fe-only hydrogenase (1), while the *Desulfovibrio gigas* hydrogenase may be considered as a prototype of the (Ni, Fe)-hydrogenases (2). The function of the hydrogenase enzyme is to catalyze the production or consumption of hydrogen gas, which is expressed by the following equation:

$$H_2 \Leftrightarrow 2H^+ + 2e^- \qquad \text{[III-1]}$$

Understanding the catalytic mechanism of these enzymes is of importance to gain insight into the H-metabolism of certain bacteria (sulfate reducing, hydrogen oxidizing, etc.). Since hydrogenases are strikingly effective catalysts, the study of the mechanism of action is also motivated by the need for efficient means of producing hydrogen gas (3).

In this Chapter some relevant results of previous hydrogenase research are summarized. Redox and spectroscopic properties of these enzymes are described briefly. Experimental approaches in the study of the Ni-center in

Ni Fe) hydrogenases a

tructure of the Ni bind

udies on the *D. gigas*

II.1. Evidence for the

The history of the iden

rogressed through se

Alcaligenes *eutrophus* (

growth (4). In 1981, it

the *A. eutrophus* was

is present in hydroge

mplex was found to be

the hydrogenases fro

reported by Lancaste

assignment was conf

signals were observe

(11). In 1984 a secon

reported in the NAI

III.3. Structural Con

Some general featu

conceptual model o

crystallographic st

(Ni, Fe) hydrogenases are presented. Results and questions concerning the structure of the Ni binding site are discussed, with the emphasis on EPR studies on the *D. gigas* hydrogenase.

III.2. Evidence for the Involvement of Ni in Hydrogenases

The history of the identification of Nickel in certain hydrogenases has progressed through several stages. In 1965 it was observed that the bacterium *Alcaligenes eutrophus* (strains H1 and H16) required Ni for their autotrophic growth (4). In 1981, it was demonstrated that the synthesis of hydrogenase in the *A. eutrophus* was dependent on the presence of Ni. It was shown that Ni is present in hydrogenase. In 1973, the activity of hydrogenase from *Nocardia opaca* was found to be stimulated by nickel (5). In 1981, nickel was found in the hydrogenases from various bacteria (6). The EPR signal from Ni(III) was reported by Lancaster in 1980 (7) in membranes of methanogenic bacteria. The assignment was confirmed by isotopic substitution with ^{61}Ni (8). Similar signals were observed in hydroganases from *D. gigas* (9, 10) and *C. vinosum* (11). In 1984 a secondary role for nickel in the binding of subunits was reported in the NAD linked hydrogenase from *N.opaca* (12).

III.3. Structural Components of Hydrogenases - General Model

Some general features of the hydrogenase molecule are summarized in the conceptual model of Fig. III-1. This picture is mainly based on the x-ray crystallographic structure of the *D. gigas* hydrogenase determined recently

Figure III-1. Schem

(13)].

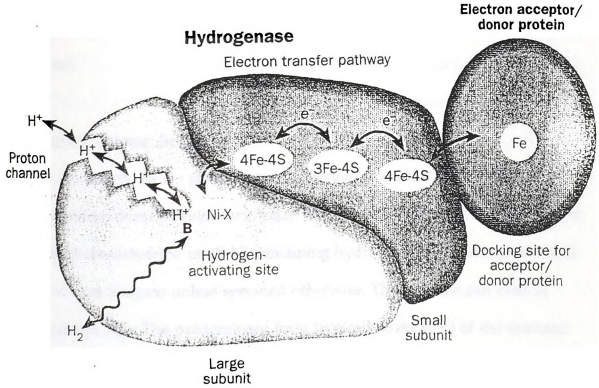

Figure III-1. Schematic general structure of (Ni, Fe) hydrogenases [from Ref. (13)].

(4). Most hydrogenase
imetallic center, see b
athway comprises thr
ontaining active site t
otential docking site
electrons. The propose
mino acid residues le
being a small, diffusib
channel.

II.4 Hydrogenase Ac
From this point on w
hydrogenase from *D*
and best characterize
efer to this enzyme
three states (15). The
enzyme after isolati
inactive toward hyd
hydrogen/tritium e
to the EPR signal N
10%) is in the *'read*
signal Ni-B) is also

(14). Most hydrogenases consist of two subunits. The active site (a Ni-Fe dimetallic center, see below) is buried inside the large subunit. The electron pathway comprises three Fe-S clusters, arranged in a line from the Ni-containing active site to the surface of the small subunit, where there is a potential docking site for a c-type cytochrome, which acts as a source or sink of electrons. The proposed proton channel consists of a chain of H^+-carrying amino acid residues leading to the surface of the large subunit. Hydrogen, being a small, diffusible molecule probably does not require any special channel.

III.4. Hydrogenase Activity

From this point on we shall focus our discussion on the water soluble hydrogenase from *Desulfovibrio gigas*, which is the most extensively studied and best characterized of all Ni containing hydrogenases. All statements will refer to this enzyme unless specified otherwise. This enzyme can exist in three states (15). The predominant form (typically over 90%) of the oxidized enzyme after isolation is termed the *'unready'* state. This is completely inactive toward hydrogen as shown by hydrogen uptake (15) and hydrogen/tritium exchange studies (16). This state of the enzyme is assigned to the EPR signal Ni-A (see below). Most of the rest of the enzyme (less than 10%) is in the *'ready'* state. This form of the enzyme (giving rise to the EPR signal Ni-B) is also inactive but can rapidly be reduced to the active state by

ong reducing agents.

e 'ready' state but slo

Figure III-2 show

ected during the rec

mosphere. The spect

gnals of Fe-S clusters

where Ni signals are

disappearance of the

shown), followed by

An EPR silent state is

pically observed w

develops (C, D). Afte

obtained (E). At low

4S] clusters can be ob

III.5. EPR Spectra fro

EPR spectra recorde

activation (2, 18) ar

state was correlated

The hyperfine patt

that Ni-A arises fr

to room temperatu

(g= 2.33, 2.16, 2.02

strong reducing agents. The *'active'* state is produced rapidly by reduction of the *'ready'* state but slowly by reduction of the *'unready'* state.

Figure III-2 shows EPR spectra representing a typical sequence of events detected during the reduction of *D. gigas* hydrogenase exposed to a H_2 atmosphere. The spectra were recorded at 77 K. At this temperature EPR signals of Fe-S clusters are not observable (they become dominant below 30 K, where Ni signals are not discernible due to saturation). The first event is the disappearance of the g=2.02 signal arising from the [3Fe-xS] cluster (not shown), followed by the disappearance of signals Ni-A and Ni-B (Fig. III-2A). An EPR silent state is attained, at which a low intensity radical type signal is typically observed whose origin is unknown (B). Next, the Ni-C signal develops (C, D). After a long incubation under H_2 another EPR silent state is obtained (E). At low temperatures (below 15 K) EPR signals from reduced [4Fe-4S] clusters can be observed at this stage (2).

III.5. EPR Spectra from Hydrogenases

EPR spectra recorded for the *D. gigas* hydrogenase at various states of activation (2, 18) are shown in Fig. III-3. As already mentioned, the *'unready'* state was correlated with a signal named Ni-A (g= 2.31, 2.23, 2.02) (Fig. III-3a.). The hyperfine pattern observed upon substitution with ^{61}Ni (I=3/2) indicates that Ni-A arises from a single Ni ion (8, 10). The signal remains detectable up to room temperature. The *'ready'* state appears to correlate with signal Ni-B (g= 2.33, 2.16, 2.02), which is present to a small proportion (less than 10%) in

Figure III-2. X-band
incubation under H
of the EPR spectra
Ref. (17)].

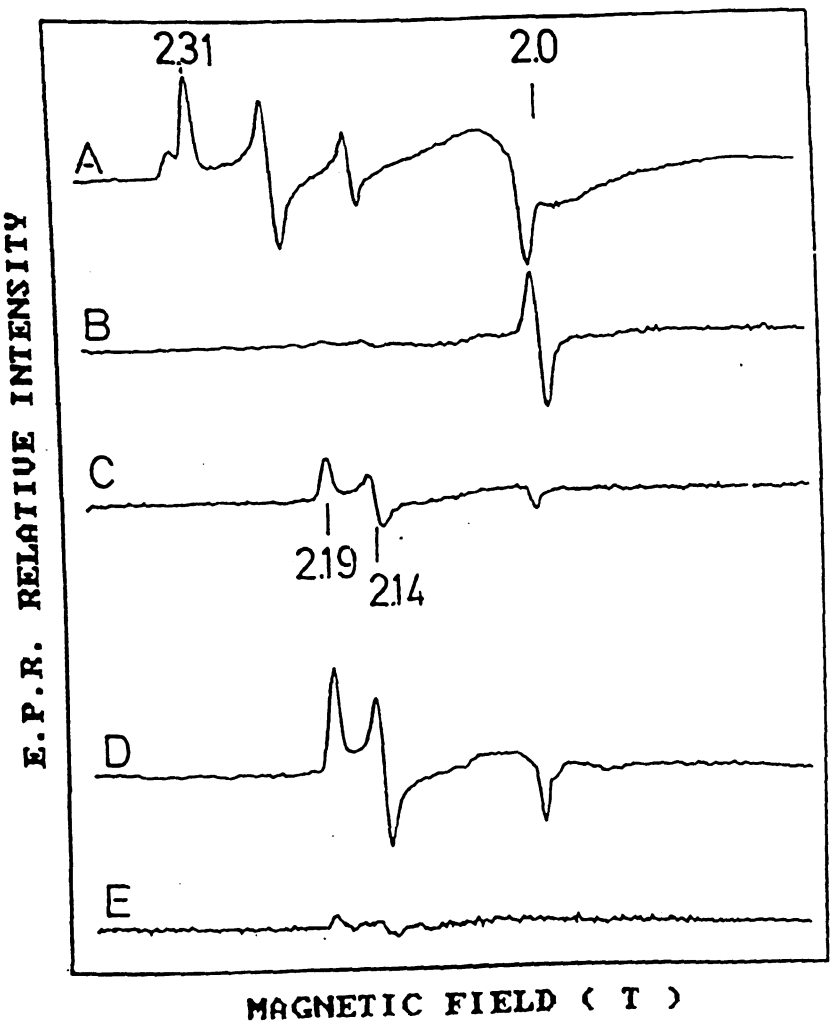

Figure III-2. X-band EPR spectra of *D. gigas* hydrogenase at different stages of incubation under H_2. Spectra taken at 77 K. A: Native enzyme. B-E: Evolution of the EPR spectra upon increasing the time of incubation under H_2. [from Ref. (17)].

Figure III-3. Various

hydrogenase. (a) Ni

recorded at 8 K; (e)

treated with CO, 10

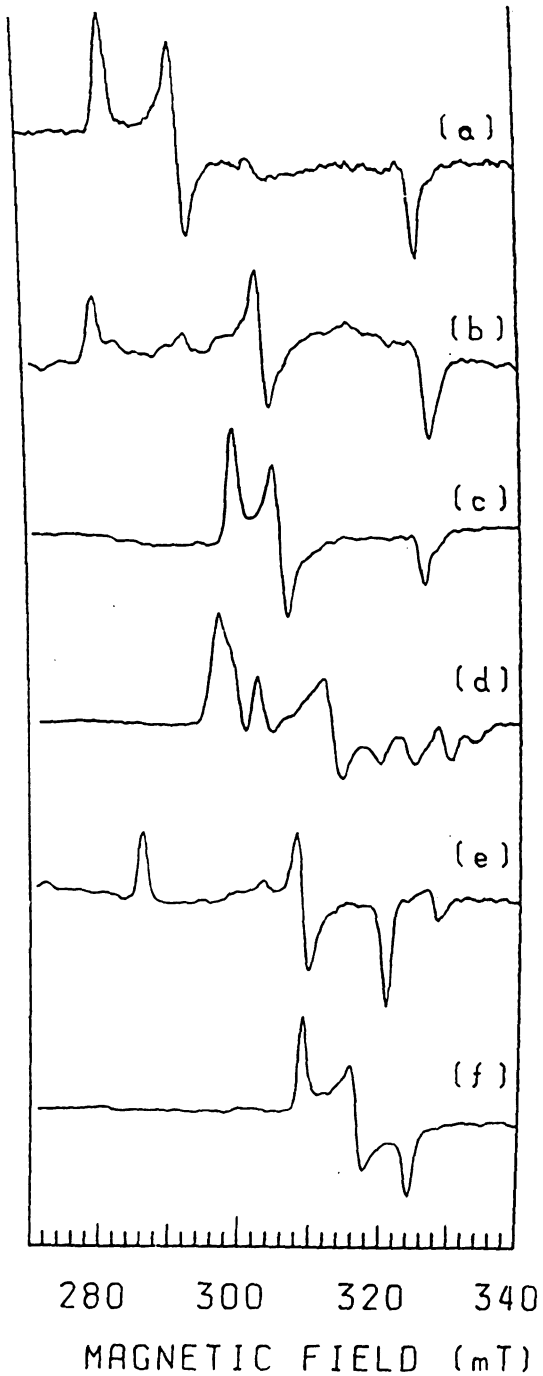

Figure III-3. Various X-band EPR spectra displayed by the *D. gigas* hydrogenase. (a) Ni-A at 105 K; (b) Ni-B at 105 K; (c) Ni-C at 30 K; (d) as (c) recorded at 8 K; (e) as (c) after illumination, at 30 K; (f) reduced with H_2 and treated with CO, 105 K. [from Ref. (17)].

the isolated enzyme. B

II][III] oxidation state

A third type of

been observed and is

'unready' state, the act

studies on the Ni-C sp

oxidation and reduc

the *enzyme* (2, 19, 20)

An important

21). Irradiation with

in the EPR spectrum

coordination site. Th

200 K in the dark. Th

kinetic isotope *effect*,

monoxide (CO) is a

H_2. Addition of CO

spectrum assigned t

species of *C. vinosu*

identical to that of t

the isolated enzyme. Both Ni-A and Ni-B are postulated to represent the Ni(III) oxidation state (see below).

A third type of EPR signal, termed Ni-C (g= 2.19, 2.14, 2.02), has also been observed and is shown in Fig. III-3c. During the slow activation of the *'unready'* state, the activity correlated with the appearance of Ni-C (18). Redox studies on the Ni-C species (see below) show that it disappears upon both oxidation and reduction, thus *it represents an intermediate oxidation state of the enzyme* (2, 19, 20).

An important property of this Ni-C species is that it is light sensitive (21). Irradiation with visible light at temperatures below 100 K causes a change in the EPR spectrum (Fig. III-3e), which indicates a structural change in the Ni coordination site. This process is reversed by raising the temperature to about 200 K in the dark. The rate of this photochemical reaction shows a strong *kinetic isotope effect*, being nearly 6 times slower in D_2O than in H_2O. Carbon monoxide (CO) is a strong inhibitor for most hydrogenases, competitive with H_2. Addition of CO to the hydrogen reduced enzyme produces a transient spectrum assigned to a carbonyl species (22) (Fig. III-3f). Irradiation of the CO species of *C. vinosum* hydrogenase produces an EPR spectrum almost identical to that of the irradiated Ni-C species (Fig. III-3e).

1. Coordination of

The lineshape of the N

with Ni-C being the 'r

suggest a distorted oc

Ni-A, Ni-B and Ni-C

EPR could detect wea

D. gigas hydrogenase

accessible to the solv

replacement of H_2O b

signal (5 G) was obse

which indicates wea

EPR studies o

Albracht et al. (25) i

This number is sign

coordination sphere

(EXAFS) spectrosco

hydrogenases, respe

The understa

enhanced by the re

the hydrogenase fr

subunits of the het

various redox cofa

entirely within the

III.6. Coordination of the Ni-site

The lineshape of the Ni EPR signals all reveal a rhombic g-tensor anisotropy, with Ni-C being the 'most axial'. The g values (g_1, $g_2 > g_3$, while $g_3 \cong 2$) may suggest a distorted octahedral geometry for the Ni coordination sphere. The Ni-A, Ni-B and Ni-C signals show no hyperfine splitting. However, pulsed EPR could detect weak hyperfine interaction with one nitrogen nucleus in the *D. gigas* hydrogenase (23). This ESEEM study also reveals that Ni ion is accessible to the solvent only when the protein is in its Ni-C form. On replacement of H_2O by D_2O a small decrease in the linewidth of the Ni-C signal (5 G) was observed in *C. vinosum* and *D. gigas* hydrogenases (21, 24), which indicates weak interaction with exchangeable protons.

EPR studies on ^{33}S-enriched *Wolinella succinogenes* hydrogenase by Albracht et al. (25) indicated hyperfine interaction with one sulfur nucleus. This number is significantly lower than three or four sulfurs located in the Ni coordination sphere, estimated by Extended X-ray Absorption Fine Structure (EXAFS) spectroscopy for *M. thermoautotrophicum* and *D. gigas* hydrogenases, respectively (26, 27).

The understanding of the structure of the Ni site has been greatly enhanced by the recent publication of a crystal structure at 2.8 Å resolution of the hydrogenase from *D. gigas* by Volbeda et al. (14). It shows that the two subunits of the heterodimer are associated with each other, and that the various redox cofactors are widely separated. The Fe-S clusters are located entirely within the small subunit, while the Ni site lies entirely within the

arge subunit. The Fe-

d 1 [4Fe-4S] clusters a

linear fashion spaced

The Ni center lies abo

farthest from the Ni s

ligands is a histidine

arrangement of the Fe

n or from the Ni cer

One of the mo

revelation that the N

and Fe (Figure III-4).

on the metal analysis

(distinct from Ni) an

appropriate for a fit

ligated by the four c

these cysteines are b

two cysteines bridge

can be described as

four cysteine residu

appears to be five-c

modeled as H_2O m

large subunit. The Fe-S clusters found in the *D. gigas* enzyme are comprised of 2 [4Fe-4S] clusters and a [3Fe-4S] cluster. These clusters are arranged in a linear fashion spaced ca. 10 Å apart with the [3Fe-4S] cluster in the middle. The Ni center lies about 10 Å from the proximal [4Fe-4S] cluster. The [4Fe-4S] farthest from the Ni site (the distal cluster) is unique in that one of the Fe ligands is a histidine imidazole. The surface exposed histidine plus the linear arrangement of the Fe-S clusters suggest an electron transfer pathway leading to or from the Ni center.

One of the most interesting aspects of the crystal structure is the revelation that the Ni center is actually a dimetallic cluster composed of Ni and Fe (Figure III-4). The assignment of the second metal as an Fe was based on the metal analysis, the strong anomalous scattering of Cu-K^{α} radiation (distinct from Ni) and the electron density associated with the metal center (appropriate for a first row transition metal) (14). The dimetallic cluster is ligated by the four conserved cysteines found in the large subunit. Two of these cysteines are bound as terminal ligands to the Ni center. The remaining two cysteines bridge between the Ni and Fe atoms. The structure of the Ni site can be described as a highly distorted trigonal-pyramidal arrangement of the four cysteine residues. The Fe center lies ca 2.7 Å from the Ni atom and appears to be five-coordinate with three exogenous ligands, which were modeled as H_2O molecules. Recent IR data, however, identified bands in the

figure III-4. The str

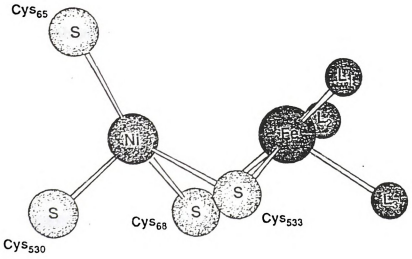

Figure III-4. The structure of the Ni-Fe cluster in the *D. gigas* hydrogenase.

2000 cm^{-1} region of the

r(CO (28).

The information

act that the crystals e

tates of the enzyme (

have contributed to a

crystallographic struc

obtained from X-ray

from a number of di

enzymes from photo

sulfate reducing bac

performed (30). The

(XANES) data provi

(31).

The EXAFS d

presence of S-scatte

exhibit evidence for

best by a set of four

roseopersicina., whi

(32).

2000 cm^{-1} region of the spectrum that suggest triply bonded species such as CN^- or CO (28).

The information obtained from the crystal structure suffers from the fact that the crystals employed were a mixture of at least three different redox states of the enzyme (50% SI, 36% A and 14% B as defined below). This may have contributed to a large amount of disorder in the Ni-Fe site. The crystallographic structure of the Ni site can be compared with information obtained from X-ray Absorption Spectroscopy (XAS) on redox poised enzymes from a number of different species (29). A recent comparison involving enzymes from photosynthetic bacteria (*T. roseopersicina.* and *C. vinosum*), sulfate reducing bacteria (*D. gigas* and *D. desulfuricans*) and *E. coli* has been performed (30). The Ni K-edge X-ray Absorption Near Edge Spectroscopy (XANES) data provide a useful predictor of coordination number/geometry (31).

The EXAFS data from all of these hydrogenases is dominated by the presence of S-scattering atoms at 2.22(1) Å. Oxidized enzymes frequently exhibit evidence for O, N ligation, but the reduced enzymes are most often fit best by a set of four S-donor ligands. One exception is the enzyme from *T. roseopersicina.*, which exhibits evidence of O, N ligation at all redox levels (32).

III. Interaction Betwe

In addition to signals

type EPR signals from

hydrogenase the sign

EPR spectrum below

discernible and readil

and Magnetic Circula

of the [3Fe-4S] type.

No magnetic i

[Fe-4S] clusters are

low temperatures is

appears to be a redu

indicates that the re

facilitate electron tra

III.8. Redox Properti

It has been found th

Nernst type relation

behave quite differ

The E_m/pH value f

involves one proto

of the maximal act

III.7. Interaction Between Nickel and [Fe-S] clusters

In addition to signals arising from nickel, many of the (Ni, Fe) hydrogenases give EPR signals from oxidized [Fe-S] clusters (6, 17, 33). In the case of *D. gigas* hydrogenase the signal is almost isotropic, at g=2.02, which dominates the EPR spectrum below 30 K. At this temperature the Ni-A signal is barely discernible and readily saturated. It has been demonstrated by Mössbauer (34) and Magnetic Circular Dichroism (35) spectroscopies that the [Fe-S] cluster is of the [3Fe-4S] type.

No magnetic interactions of the Ni-A or Ni-B species with the oxidized [3Fe-4S] clusters are detected. On the other hand, splitting of the Ni-C signal at low temperatures is observed (Fig. III-3d) (2). The interacting paramagnet appears to be a reduced [4Fe-4S] cluster (20). This spin-spin interaction indicates that the redox centers are located close enough in the enzyme to facilitate electron transfer.

III.8. Redox Properties of Hydrogenases

It has been found that the rate of H_2 production by hydrogenases follows a Nernst type relationship with the applied redox potential. Hydrogenases behave quite differently, some being pH dependent, others pH independent. The E_m/pH value for the *D. gigas* hydrogenase indicates that the redox process involves one proton and one electron (E_m is the redox potential at which half of the maximal activity is observed).

These E_m values must

the redox centers pres

potential correspondi

and refers to the situa

terms are equal. Thes

"EPR redox titration"

species is followed as

changed stepwise by

enzyme (2, 20, 36, 37

pylori hydrogenase is

-70 mV midpoint po

with a redox proces

was shown to be pH

with the Nernst equ

associated with the

develops at a poten

-380 mV and comp

The redox cl

Figure III-6. The p

Electrode (NHE).

understood irreve

and/or incorporat

These E_m values must be related in some way to the midpoint potentials of the redox centers present in the enzyme. Midpoint potential is defined as the potential corresponding to the inflection point of the S-shaped titration curve and refers to the situation when the amounts of the oxidized and reduced forms are equal. These midpoint potentials can be obtained by the method of "EPR redox titration". This means that the intensity of the EPR signal of the species is followed as a function of the redox potential of the system, which is changed stepwise by adding the reducing agent (dithionite or H_2) to the enzyme (2, 20, 36, 37). The result of such an experiment performed with *D. gigas* hydrogenase is displayed in Fig. III-5 (9, 17, 38). The 3Fe center titrated at -70 mV midpoint potential. The disappearance of the Ni-A signal is associated with a redox process with the midpoint potential of -220 mV. This process was shown to be pH dependent (-60 mV per pH unit) and the data were fitted with the Nernst equation for a one-electron reduction (9). Redox processes associated with the Ni-C signal were also studied by titrimetry (2). Ni-C develops at a potential of about -270 mV, reaches maximum intensity at about -380 mV and completely disappears below -450 mV.

The redox chemistry associated with the Ni site is summarized in Figure III-6. The potential values are relative to the Normal Hydrogen Electrode (NHE). The slow conversion of form Ni-B to form Ni-A is a poorly understood irreversible process, which may involve a conformational change and/or incorporation of O_2. The presence of O atoms in the oxidized forms

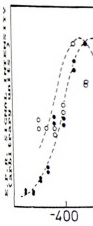

Figure III-5. EPR re

g=2.02 signal, 4 K;

K; open circles: Ni-

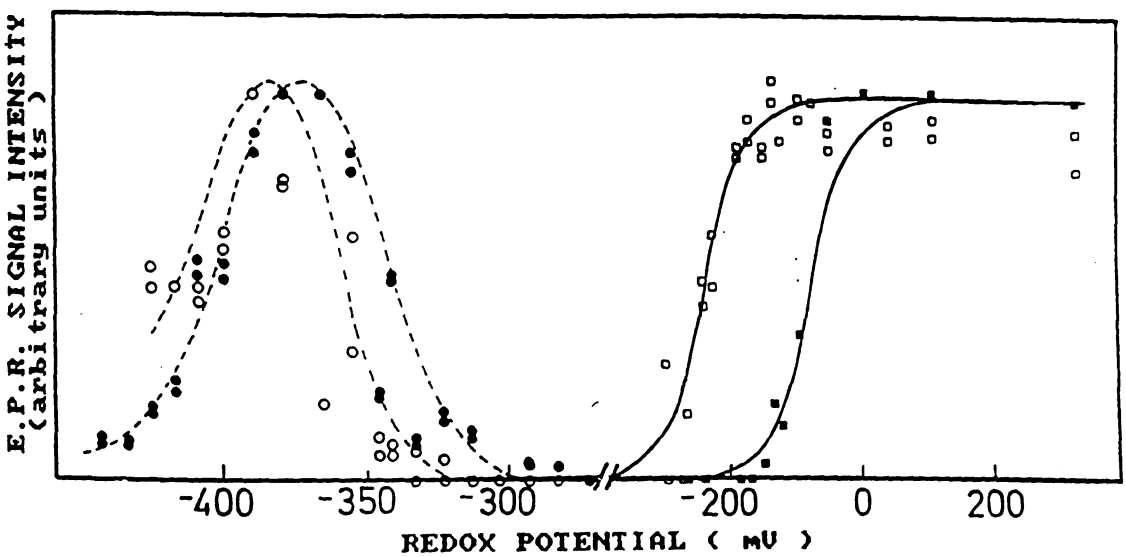

Figure III-5. EPR redox titrations of the *D. gigas* hydrogenase. Full squares: g=2.02 signal, 4 K; open squares: Ni-A signal, 77 K; full circles: Ni-C signal, 20 K; open circles: Ni-C signal, 4 K [from Ref. (17)].

Figure III-6. Schem

cluster in hydroger

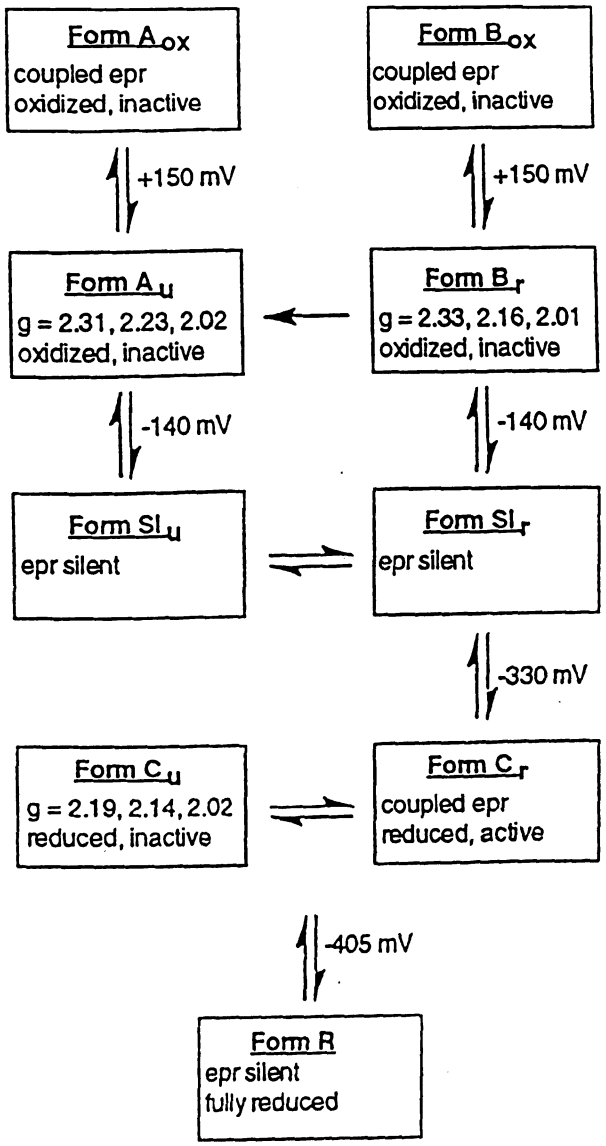

Figure III-6. Scheme describing the redox chemistry associated with the Ni-Fe cluster in hydrogenases.

as been directly obs

f $^{18}O_2$ (39). Oxidativ

he native species Ni

enzyme (40). At mor

reated that is coupl

signal of the oxidize

by one-electron to p

existence of active a

supported by a stud

B (41). When form A

form A is observed

and the resulting SI

produced upon oxi

SI samples produce

Several redo

proposed, example

provide simple exp

of S=1/2 Ni EPR s

the Ni center, whe

+3 to 0). *Scheme A*

for Ni, and that th

by thiolate ligatio

has been directly observed via line broadening of EPR signals in the presence of $^{17}O_2$ (39). Oxidative titrations of the *C. vinosum* hydrogenase revealed that the native species Ni-A and Ni-B are not the fully oxidized forms of the enzyme (40). At more positive potentials (+150 mV) a new S=1/2 center is created that is coupled to the EPR signals Ni-A and Ni-B as well as to the EPR signal of the oxidized [3Fe-4S] cluster. Both species Ni-A and Ni-B are reduced by one-electron to produce an EPR Silent Intermediate (SI) (41, 42). The existence of active and inactive conformations of the enzyme is further supported by a study of the reductive interconversion of species Ni-A and Ni-B (41). When form A is reduced at 4 ^{0}C to the SI level and reoxidized, only form A is observed as a product. However, when the reduction is carried out and the resulting SI state is allowed to equilibrate at 30 ^{0}C, form B is also produced upon oxidation. A similar temperature dependence is observed for SI samples produced from form B.

Several redox schemes to explain these observations have been proposed, examples of which are summarized in Table III-1. *Schemes A* and *B* provide simple explanations for the sequential appearance and disappearance of S=1/2 Ni EPR signals. *Scheme A* utilizes one-electron redox chemistry at the Ni center, whereas *Scheme B* reduces Ni through four redox states (from +3 to 0). *Scheme A* has the advantage that it utilizes only two oxidation states for Ni, and that the unusual oxidation state involved (+3) is the one favored by thiolate ligation.*Scheme B* implies unprecedented redox chemistry for a

TABLE III-1. Redox schemes proposed for the Ni-Fe cluster in hydrogenases.

TABLE III-1. Redox schemes proposed for the Ni-Fe cluster in hydrogenases.

Sample	*77 K epr Signal*	*Scheme A*	*Scheme B*	*Scheme C*	*Scheme D*
Form A	g = 2.31, 2.23, 2.02	Ni(III)	Ni(III)	Ni(I), Fe(II)	Ni(III), Fe(IV)
Form B	g = 2.33, 2.16, 2.01	Ni(III)	Ni(III)	Ni(I), Fe(II)	Ni(III), Fe(IV)
SI	none	Ni(II)	Ni(II)	Ni(I), Fe(I)	Ni(III), Fe(III)
Form C	g = 2.19, 2.14, 2.02	Ni(III)	Ni(I)	Ni(I), Fe(II)	Ni(III), Fe(II)
R	none	Ni(II)	Ni(0)	Ni(I), Fe(I)	Ni(II), Fe(II)

single Ni center that

ompress the Ni(III/

eparated by about 2

is provided by a mo

eduction of Ni(III)

The redox act

Measurement of the

redox levels provid

density on the Ni c

a shift of ca. 2 eV ir

investigated was th

reduced samples g

description of the

However, EXAFS c

function of redox p

three electrons to g

delocalized over s

Another po

responsible for th

(*Scheme C*) or Ni(

vary the Ni oxida

coupled antiferro

silent states. The

single Ni center that must involve considerable structural change in order to compress the Ni(III/II) and Ni(II/I) redox couples, which are normally separated by about 2 V, into a ≈250 mV range. This kind of structural change is provided by a model system where Ni-S bonds lengthen by 0.14 Å upon reduction of Ni(III) to Ni(II) (43).

The redox activity of the Ni center has been examined by XAS. Measurement of the differences in the Ni K-edge energy between the various redox levels provides a sensitive method for detecting changes in the charge density on the Ni center (44). For a one-electron metal-centered redox process, a shift of ca. 2 eV in the edge energy is expected. In none of the cases investigated was the edge energy shift between the fully oxidized and fully reduced samples greater than 1.5 eV, *ruling out Scheme B* as a realistic description of the redox chemistry. *Scheme A* cannot be ruled out entirely. However, EXAFS data reveal no significant changes in the Ni-S distances as a function of redox poise. Thus, the redox chemistry, which requires at least three electrons to go from the oxidized to the reduced enzyme is likely to be delocalized over several atomic centers in the Ni-Fe cluster.

Another possibility is that the Fe atom in the Ni-Fe cluster is primarily responsible for the redox chemistry (Table III-1). These schemes feature Ni(I) (*Scheme C*) or Ni(III) (*Scheme D*) to account for the EPR signal, but do not vary the Ni oxidation state. Instead, the S=1/2 Ni centers are proposed to be coupled antiferromagnetically to S=1/2 Fe centers to account for the EPR silent states. These schemes have several advantages over the ones involving

clusively Ni. First,
edox center in biol
ata in that the stru
much. They are also
below). Neverthele
states for Ni and ha
example, they also
hyperfine splittings
Fe center in labeled
simply transfer the

A third poss
n the redox proces
and not a particula
dithiolato dinickel
ligation (44-46).

III.9. The Role of

Another aspect of
the use of Ni as th
CO). Such a role i
photochemical re
hyperfine couplir

exclusively Ni. First, Fe has a facile redox chemistry and is widely found as a redox center in biology. Second, these schemes are consistent with the XAS data in that the structure and charge density of the Ni center need not change much. They are also consistent with a role for Fe as a CO binding site (see below). Nevertheless, both *Scheme C* and *D* still suggest unusual oxidation states for Ni and have many of the problems found in *Scheme A* and *B*. For example, they also provide no compelling explanation for the absence of ^{57}Fe hyperfine splittings or line broadening in the EPR spectra arising from the Ni-Fe center in labeled hydrogenase samples (34). In essence, *Scheme C* and *D* simply transfer the redox processes from Ni to Fe.

A third possibility is that the thiolate ligands are "intimately involved" in the redox process and that the redox chemistry is a property of the cluster and not a particular metal center. This possibility is supported by studies of μ-dithiolato dinickel(II) model complexes that also feature terminal thiolate ligation (44-46).

III.9. The Role of Ni as a Binding Site

Another aspect of many hypothetical reaction mechanisms for hydrogenase is the use of Ni as the binding site for substrate (H_2 or H^-) and inhibitors (e.g. CO). Such a role is suggested by two properties of the enzyme: the photochemical reactivity of Ni-C (see above) and the observation of ^{13}C hyperfine coupling in the Ni-C signal at 77 K in the presence of ^{13}CO (39).

However, recent in

site for H_2, or at leas

The photoche

of a ligand photodi

mechanism involve

observation of the l

photodissociation o

ENDOR and XAS s

viridopersicina (47).

in the enzyme corr

with a coupling co

and a more strong

exchangeable with

exchangeable prot

reappear. This ob

and recombinatio

CO as a ligand gi

C distance and a

EXAFS spectrum

with a ligand en

the hydrogenase

second coordina

EXAFS spectru

However, recent investigations suggest that *Ni may not serve as the binding site for H_2,* or at least is not the only binding site.

The photochemical behavior of the Ni-C species has the characteristics of a ligand photodissociation and recombination reaction. One possible mechanism involves an S=1/2 Ni-H^- complex, which is consistent with the observation of the large isotope effect mentioned earlier. The photodissociation of a Ni-H species has been examined by a combination of ENDOR and XAS studies of the reaction using hydrogenase from *T. roseopersicina* (47). The ^{1}H-ENDOR spectrum reveals two sets of resonances in the enzyme corresponding to protons that were not solvent exchangeable with a coupling constant of 12-14 MHz (assigned to cysteine β-CH_2 protons), and a more strongly coupled (20 MHz) proton resonance arising from protons exchangeable with D_2O. Exposure to light causes the resonance due to the exchangeable proton to vanish, and annealing causes the resonance to reappear. This observation is consistent with the photochemical dissociation and recombination of a Ni-H species, but do not exclude other mechanisms. CO as a ligand gives rise to a rich EXAFS spectrum that arises from a short M-C distance and a second coordination sphere O atom. Examination of the EXAFS spectrum of a crystallographically characterized Ni-CO complex (47) with a ligand environment similar (with respect to EXAFS) to that found for the hydrogenase Ni center clearly showed the short Ni-C interaction and the second coordination sphere O atom. No such features can be observed in the EXAFS spectrum of hydrogenases. *These observations implicate the Fe center*

f the Ni-Fe cluster a

urther supported by

ydrogenase (30).

Because CO is

inding site for H_2 o

he unique IR featur

ydrogenases (48).

sotope effect. On th

omplex, because w

orm C, the EPR sig

is not a reactive int

presence of water,

of H_2. It is more li

n enzyme substrat

he Ni-Fe cluster.

III.10. Summary

The crystal structu

heterodimetallic N

which have been

reassessed. The b

hydrogenases ob

of the Ni-Fe cluster as the binding site for the CO ligand. This conclusion is further supported by recent Mössbauer studies of reduced *C. vinosum* hydrogenase (30).

Because CO is a competitive inhibitor, the Fe atom is also a likely binding site for H_2 or H^-. This suggestion is supported by the discovery that the unique IR features associated with the Fe site are also found in Fe-only hydrogenases (48). An Fe-H_2(H^-) complex is also consistent with the observed isotope effect. On the other hand, it is unlikely that species Ni-C is an H_2 or H^- complex, because when H_2 is carefully removed from a sample containing form C, the EPR signal Ni-C is *stable indefinitely* (49). This proves that form C is not a reactive intermediate, since the hydride should convert to H_2 in the presence of water, while an H_2 adduct should dissociate at low partial pressure of H_2. It is more likely that form C is an *enzyme product complex, rather than an enzyme substrate complex;* in other words it has protons associated with the Ni-Fe cluster.

III.10. Summary

The crystal structure obtained from *D. gigas* hydrogenase reveals a heterodimetallic Ni-Fe active site. The interpretation of the Ni EPR data, which have been based on the assumption of an isolated Ni center, have to be reassessed. The basic structural features seem to be similar in several hydrogenases obtained from a variety of bacteria. The largest difference is the

resence of O, N liga

ydrogenase, in whi

The redox che

echniques, none of

edox chemistry. EN

with cysteinate met

forms A, B and C,

oxidation state of th

Several expla

including redox act

thiolate ligands. A

by IR studies, in w

on the redox poter

supported by the r

μ-dithiolato and te

substrate and inhi

the existence of N

hydrogenase impl

Given that

hydrogenases is t

that one of the fu

irreversibly inact

fact that Fe-only

presence of O, N ligation in many enzymes as opposed to the *D. gigas* hydrogenase, in which the active site shows pure S-coordination.

The redox chemistry of hydrogenases has been probed by several techniques, none of which provide unambiguous evidence for Ni centered redox chemistry. ENDOR spectroscopy reveals that the resonances associated with cysteinate methylene protons exhibit the same coupling constant in forms A, B and C, suggesting that *all three of these forms feature the same oxidation state of the Ni-Fe cluster,* in agreement with XAS experiments.

Several explanations for the redox chemistry of the cluster are possible including redox activity at the Fe center and/or redox processes involving the thiolate ligands. A participation of Fe in the redox chemistry is also suggested by IR studies, in which the frequencies of bands from the Fe ligands depend on the redox potential. Mechanisms involving thiolate redox chemistry are supported by the redox behavior of a series of dinickel model complexes with μ-dithiolato and terminal thiolate ligation. Studies on the role of Ni as a substrate and inhibitor binding site fail to provide unequivocal evidence for the existence of Ni-H or Ni-CO complexes. Recent studies on CO complexes of hydrogenase implicate Fe as a potential binding site for CO.

Given that one of the outstanding properties of the Ni-containing hydrogenases is their stability to irreversible oxidation by O_2, it seems possible that one of the functions of Ni is to modify the catalytic site so that it is not irreversibly inactivated upon exposure to O_2. This notion is supported by the fact that Fe-only hydrogenases are much better catalysts of H_2 redox chemistry,

hd are irreversibly d

ocessed further by

elenocysteinate.

but are irreversibly deactivated by O_2. The stability toward O_2 seems to be increased further by the substitution of a terminal Ni-cysteinate ligand by selenocysteinate.

1. Huynh, B. H.; V.; Peck, H. D

2. Teixeira, M.; D. V.; Peck, H *260*, 8942.

3. Benemann, J. Beach, Florid

4. Bartha, R.; O

5. Aggag, M.; S

6. Cammack, R *Chemistry of* Chapter 8.

7. Lancaster, J.

8. Albracht, S.

9. Cammack, **1982**,*142*, 28

10. Moura, J. J. DuVarney, LeGall, J. E

11. Albracht, S **1983**, *724*, 3

12. Schneider,

13. Cammack,

14. Volbeda, A Fontecilla-

15. Fernandez *Biophys. A*

16. Hallahan, *Biochim.*

References

1. Huynh, B. H.; Czechowski, M. H.; Krüger, H.-J.; DerVartanian, D. V.; Peck, H. D., Jr.; LeGall, J. *Proc. Natl. Acad. Sci, USA* **1984**, *81*, 3728.

2. Teixeira, M.; Moura, I.; Xavier, A. V.; Huynh, B. H.; DerVartanian, D. V.; Peck, H. D., Jr.; LeGall, J.; Moura, J. J. G. *J. Biol. Chem.* **1985**, *260*, 8942.

3. Benemann, J. R. *Proc. 10th World Hydrogen Energy Conf.* (Cocoa Beach, Florida; 1994).

4. Bartha, R.; Ordal, E. J. *J. Bacteriol.* **1965**, *89*, 1015.

5. Aggag, M.; Schlegel, H. G. *Arch. Microbiol.* **1973**, *88*, 299.

6. Cammack, R.; Fernandez, V. M.; Schneider, K. In *The Bioinorganic Chemistry of Nickel*, Lancaster, J. R., Jr., Ed., VCH: New York, 1988; Chapter 8.

7. Lancaster, J. R. *FEBS Lett.* **1980**, *115*, 285.

8. Albracht, S. P. J.; Graf, E.-G.; Thauer, R. K. *FEBS Lett.* **1982**, *140*, 311.

9. Cammack, R.; Patil, D. S.; Aguirre, R.; Hatchikian, E. C. *FEBS Lett.* **1982**,*142*, 289.

10. Moura, J. J. G.; Moura, I.; Huynh, B. K.; Krüger, H.-J.; Teixeira, M.; DuVarney, R. C.; DerVartanian, D. V.; Xavier, A. V.; Peck, H. D., Jr.; LeGall, J. *Biochem. Biopys. Res. Commun.* **1982**, *408*, 1388.

11. Albracht, S. P. J.; Kalkman, M. L.; Slater, E. C. *Biochim. Biophys. Acta* **1983**, *724*, 309.

12. Schneider, K.; Schlegel, H. G.; Jochim, K. *Eur. J. Biochem.* **1984**,*138*, 533.

13. Cammack, R. *Nature* **1995**, *373*, 556.

14. Volbeda, A.; Charon, M-H.; Piras, C.; Hatchikian, E. C.; Frey, M.; Fontecilla-Camps, J. C. *Nature* **1995**, *373*, 580.

15. Fernandez, V. M.; Hatchikian, E. C.; Cammack, R. *Biochim. Biophys. Acta* **1985**, *832*, 69.

16. Hallahan, D.; Fernandez, V. M.; Hatchikian, E. C.; Cammack, R. *Biochim. Biophys. Acta* **1986**, *874*, 72.

17. Moura, J. J. G. *Chemistry of N* Chapter 9.

18. Fernandez, V. *Biochim. Biop*

19. Kojima, N.; F W. H.; Walsh

20. Cammack, R. *Biochim. Biop*

21. van der Zwa *FEBS Lett.* **19**

22. van der Zwa *Biochim. Bio*

23. Chapman, A *FEBS Lett.* **19**

24. DerVartania *Quim.* **1985**,

25. Albracht, S. Böcher, R.; 116.

26. Lindahl, P. Walsh, C.

27. Scott, R. A LeGall, J.;

28. Bagley, K. W. H. *Bioc*

29. Eidsness, *Chemistry* Chapter 4

30. Maroney, Zh. In *Tr* K., Eds.;

17. Moura, J. J. G.; Teixeira, M.; Moura, I.; LeGall, J. In *The Bioinorganic Chemistry of Nickel*, Lancaster, J. R., Jr., Ed., VCH: New York, 1988; Chapter 9.

18. Fernandez, V. M.; Hatchikian, E. C.; Patil, D. S.; Cammack, R. *Biochim. Biophys. Acta* **1986**, *883*, 145.

19. Kojima, N.; Fox, J. A.; Hausinger, R. P.; Daniels, L.; Orme-Johnson, W. H.; Walsh, C. *Proc. Natl. Acad. Sci. USA* **1983**, *80*, 378.

20. Cammack, R.; Patil, D. S.; Hatchikian, E. C.; Fernandez, V. M. *Biochim. Biophys. Acta* **1987**, *912*, 98.

21. van der Zwaan, J. W.; Albracht, S. P. J.; Fontijn, R. D.; Slater, E. C. *FEBS Lett.* **1985**, *179*, 271.

22. van der Zwaan, J. W.; Albracht, S. P. J.; Fontijn, R. D.; Roelofs, Y. B. M. *Biochim. Biophys. Acta* **1986**, *872*, 208.

23. Chapman, A.; Cammack, R.; Hatchikian, C. E.; McCracken, J.; Peisach, J. *FEBS Lett.* **1988**, *242*, 134.

24. DerVartanian, D. V.; Krüger, H.-J.; Peck, H. D., Jr.; LeGall, J. *Rev. Port. Quim.* **1985**, *27*, 70.

25. Albracht, S. P. J.; Kröger, A.; van der Zwaan, J. W.; Unden, G.; Böcher, R.; Mell, H.; Fontijn, R. D. *Biochim. Biophys. Acta* **1986**, *874*, 116.

26. Lindahl, P. A.; Kojima, N.; Hausinger, R. P.; Fox, J. A.; Teo, B. K.; Walsh, C. T.; Orme-Johnson, W. H. *J. Am. Chem. Soc.* **1984**, *106*, 3062.

27. Scott, R. A.; Wallin, S. A.; Czechowski, M.; DerVartanian, D. V.; LeGall, J.; Peck, H. D., Jr.; Moura, I. *J. Am. Chem. Soc.* **1984**, *106*, 6864.

28. Bagley, K. A.; Duin, E. C.; Roseboom, W.; Albracht, S. P. J.; Woodruff, W. H. *Biochemistry* **1995**, *34*, 5527.

29. Eidsness, M. K.; Sullivan, R. J.; Scott, R. A. In *The Bioinorganic Chemistry of Nickel*, Lancaster, J. R., Jr., Ed.; VCH: New York, 1988; Chapter 4.

30. Maroney, M. J.; Allan, C. B.; Chohan, B. S.; Choudhury, S. B.; Gu, Zh. In *Transition Metal Sulfur Chemistry*, Stiefel, E. I.; Matsumoto, K., Eds.; ACS Symposium Series 653, 1996; Chapter 4.

33. Colpas, G. J.; M
S.; Suib, S. L.;

32. Bagyinka, C.;
115, 3576.

33. Cammack, R.;
Transport and
Holland: New

34. Krüger, H.-J.;
DerVartanian
Moura, J. J. G

35. Johnson, M. I
DerVartaniar
Chemistry, X

36. Lissolo, T.; I

37. Mege, R.-M.

38. Teixeira, M.;
J.; Peck, H. I
130, 481.

39. van der Zw
Albracht, S.

40. Surerus, K.
M.; Duin, E
4980.

41. Albracht, S

42. Roberts, R.

43. Krüger, H.

44. Maroney,
Gurbiel, R

45. Colpas, G
29, 4779.

31. Colpas, G. J.; Maroney, M. J.; Bagyinka, C.; Kumar, M.; Willis, W. S.; Suib, S. L.; Mascharak, P. K.; Baidya, N. *Inorg. Chem.* **1991**,*30*, 920.

32. Bagyinka, C.; Whitehead, J. P.; Maroney, M. J. *J. Am. Chem. Soc.* **1993**, *115*, 3576.

33. Cammack, R.; Lalla-Maharajh, W. V.; Schneider, K. In *Electron Transport and Oxygen Utilization*, Ho, C., Ed.; Elsevier North Holland: New York, 1982; pp. 411-415.

34. Krüger, H.-J.; Huynh, B. H.; Ljungdahl, L. O.; Xavier, A. V.; DerVartanian, D. V.; Moura, I.; Peck, H. D., Jr.; Teixeira, M.; Moura, J. J. G.; LeGall, J. *J. Biol. Chem.* **1982**, *257*, 14620.

35. Johnson, M. K.; Zambrano, I. C.; Czechowski, M. H.; Peck, H. D., Jr.; DerVartanian, D. V.; LeGall, J. In *Frontiers in Bioinorganic Chemistry*, Xavier, A. V., Ed., VCH: Weinheim, 1986; pp. 36-44.

36. Lissolo, T.; Pulvin, S.; Thomas, D. *J. Biol. Chem.* **1984**, *259*, 11725.

37. Mege, R.-M.; Bourdillon, C. *J. Biol. Chem.* **1985**, *260*, 14701.

38. Teixeira, M.; Moura, I.; Xavier, A. V.; DerVartanian, D. V.; LeGall, J.; Peck, H. D., Jr.; Huynh, B. H.; Moura, J. J. G. *Eur. J. Biochem.* **1983**, *130*, 481.

39. van der Zwaan, J. W.; Coremans, J. M. C. C.; Bouwens, E. C. M.; Albracht, S. P. J. *Biochim. Biophys. Acta* **1990**, *1041*, 101.

40. Surerus, K. K.; Chen, M.; van der Zwaan, J. W.; Rusnak, F. M.; Kolk, M.; Duin, E. C.; Albracht, S. P. J. Muenck, E. *Biochemistry* **1994**, *33*, 4980.

41. Albracht, S. P. J. *Biochim. Biophys. Acta* **1994**, *1188*, 167.

42. Roberts, R. M.; Lindahl, P. A. *J. Am. Chem. Soc.* **1995**, *117*, 2565.

43. Krüger, H.-J.; Holm, R. H. *J. Am. Chem. Soc.* **1990**, *112*, 2955.

44. Maroney, M. J.; Pressler, M. A.; Mirza, S. A.; Whitehead, J. P.; Gurbiel, R. J.; Hoffman, B. M. *Adv. Chem. Ser.* **1995**, *246*, 21.

45. Colpas, G. J.; Kumar, M.; Day, R. O.; Maroney, M. J. *Inorg. Chem.* **1990**, *29*, 4779.

Mirza, S. A.; Pre
Inorg. Chem. **199**

Whitehead, J. P.
Maroney, M. J.

van der Spek, T
Bagley, K. A.; S
Biochem. **1996**,

Barondeau, D.
1994, *116*, 3442.

46. Mirza, S. A.; Pressler, M. A.; Kumar, M.; Day, R. O.; Maroney, M. J. *Inorg. Chem.* **1993**, *32*, 977.

47. Whitehead, J. P.; Gurbiel, R. J.; Bagyinka, C.; Hoffman, B. M.; Maroney, M. J. *J. Am. Chem. Soc.* **1993**, *115*, 5629.

48. van der Spek, T. M.; Arendsen, A. F.; Happe, R. P.; Yun, S.; Bagley, K. A.; Stufkens, D. J.; Hagen, W. R.; Albracht, S. P. J. *Eur. J. Biochem.* **1996**, *237*, 629.

49. Barondeau, D. P.; Roberts, L. M.; Lindahl, P. A. *J. Am. Chem. Soc.* **1994**, *116*, 3442.

V.1. Introduction

Synthetic compoun
the active site of hy
structure and funct
considered as a mo
It shows similar sp
reproduces the rec
similar to that of
structural models,
as functional mod

Before X-ra
ogas hydrogenas
the (Ni, Fe) hydr
There are still u
while the mecha
the oxidation st
binuclear cluste
results in hype
line broadenin
peculiar unpai

Chapter IV

Synthetic Models for the Ni-site of Hydrogenases

IV.1. Introduction

Synthetic compounds that mimic the chemical and/or physical properties of the active site of hydrogenases have contributed to the understanding of the structure and function of the catalytic site. A particular Ni-complex may be considered as a model if it fulfills at least one of the following conditions: (a) it shows similar spectroscopic properties to those of the enzyme; (b) it reproduces the redox properties of the enzyme; (c) it has catalytic activity similar to that of hyrogenases. Compounds with properties (a) are called structural models, while those which have properties (b) or (c) are referred to as functional models (1-3).

Before X-ray crystallographic data showed that the active site of the *D. gigas* hydrogenase was most likely a Ni-Fe cluster (4), the catalytic center in the (Ni, Fe) hydrogenases had been postulated to be a mononuclear Ni-site. There are still unanswered questions concerning the nature of the active site, while the mechanism of the catalysis is unclear. One fundamental problem is the oxidation states of the ions involved and electronic structure of the binuclear cluster. Interesting, that while ^{61}Ni enrichment in the protein results in hyperfine splitting in the EPR signal ($\cong$ 20 G), no splitting or even line broadening is observed upon ^{57}Fe enrichment (5), which suggests a peculiar unpaired electron distribution involving mostly the Ni metal and

oordinated cystein

he determined nati

educed species (e.g

his far on the assu

paramagnet, must b

Ni(III) complexes m

studies of which co

state. Synthetic mo

binuclear Ni-Fe or

IV.2. Polynuclear

Only two thiolato

namely the tetran

DACO)H_2 = N,N'

[Ni(dmpn)]$_2$Fe]^2

mercaptoethyl)-1

to compare the N

complexes with

lack of structura

drawing firm co

Ni - Fe distance

distances obser

organization o

coordinated cysteinyl S atoms. Another problem is the relationship between the determined native structure of the active site and the structure of the reduced species (e.g. Ni-C). Certainly, EPR and other spectroscopic data, based thus far on the assumption of the active site being an isolated Ni(III) or Ni(I) paramagnet, must be reinterpreted. On the other hand, some mononuclear Ni(III) complexes may still be considered as relevant models, spectroscopic studies of which could provide useful information on this unusual oxidation state. Synthetic modeling strategies in the future will probably focus on binuclear Ni-Fe or Ni-Ni thiolate complexes.

IV.2. Polynuclear Ni complexes

Only two thiolato-bridged Ni-Fe complexes have appeared in the literature, namely the tetranuclear species, $[\{Ni(BME\text{-}DACO)FeCl\}_2(\mu\text{-}Cl)_2]$, where (BME-DACO)$H_2$ = N,N'-bis(mercaptoethyl)-1,5-diazacyclooctane (Figure IV-1A) and $[\{Ni(dmpn)\}_3Fe]^{2+}$, where (dmpn)H_2 = N,N'-dimethyl-N,N'-bis(2-mercaptoethyl)-1,3-diaminopropane (Figure IV-1B) (6, 7). While it is tempting to compare the Ni-S and Fe-S bond lengths in these and other Ni and Fe complexes with those of the Ni-Fe cluster in the hydrogenase structure, the lack of structural data on relevant Ni(III) model complexes prevents us from drawing firm conclusions about the electronic character of the Ni-Fe site. The Ni - Fe distance of 2.7 Å is at the low end of the 2.6 - 3.9 Å range of Ni - Ni distances observed for synthetic $[Ni_2(\mu\text{-}SR)_2]^{2+}$ complexes (1) and suggests pre-organization of the Ni-Fe center for the inclusion of a third bridging ligand.

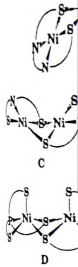

Figure IV-1. Sche

A: [(Ni(BME-DA

bis(mercaptoethy

(dmpn)H_2 = N,N

C: $[Ni_2(memta)_2$

$SC_2H_4)_3]_2]^-$; E: [N

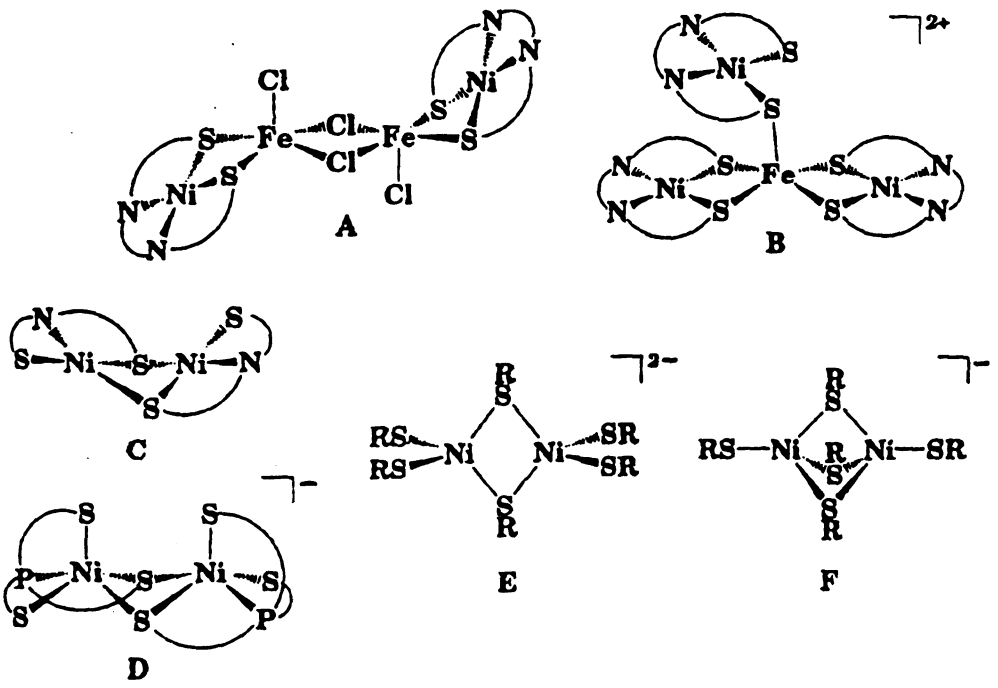

Figure IV-1. Schematic structures of model complexes referred to in the text. A: $[\{Ni(BME\text{-}DACO)FeCl\}_2(\mu\text{-}Cl)_2]$, where $(BME\text{-}DACO)H_2$ = N,N′-bis(mercaptoethyl)-1,5-diazacyclooctane; B: $[\{Ni(dmpn)\}_3Fe]^{2+}$, where $(dmpn)H_2$ = N,N′-dimethyl-N,N′-bis(2-mercaptoethyl)-1,3-diaminopropane; C: $[Ni_2(memta)_2]$, where $(memta)H_2 = (HSC_2H_4)_2NC_2H_4SMe$; D: $[Ni_2\{P(2\text{-}SC_6H_4)_3\}_2]^-$; E: $[Ni_2(SC_4H_9)_6]^{2-}$; F: $[Ni_2(S\text{-}2,4,5\text{-}i\text{Pr}_3C_6H_2)_5]^-$. [From Ref. (3)].

A large number of

square-planar coord

ative (1). In particu

$[Ni_2(memta)_2]$, whe

n Figure IV-2) exhi

0.35 V versus the f

valence species [Ni

oxidized form is co

spectra of mononu

suggested that oxi

bound sulfur atom

electrochemical ox

21 in Figure IV-2

simulations only

oxidation of **21** b

derivative of **21** b

samples of a clos

$[Ni_2^{2.5}]^+$ electroni

By contra

related [Ni(pdm

a chemically re

a valence-deloc

in behavior be

A large number of dimers with two thiolato bridges and Ni(II) ions with square-planar coordination have been reported, some of which are redox active (1). In particular, Maroney and coworkers have reported that $[Ni_2(memta)_2]$, where $(memta)H_2 = (HSC_2H_4)_2NC_2H_4SMe$ (Figure IV-1C and **21** in Figure IV-2) exhibits a chemically reversible one-electron oxidation at $E_{1/2}$ = -0.35 V versus the ferrocene/ferrocenium (+0.05 V vs. SCE) to form a mixed-valence species $[Ni_2(memta)_2]^+$ (8). Moreover, the EPR spectrum of this oxidized form is comparable to the Ni-A and Ni-B signals, unlike the EPR spectra of mononuclear Ni(III) thiolates (9). Maroney et al. also have suggested that oxidation of the Ni site in the hydrogenase occurs at a Ni-bound sulfur atom as opposed to the Ni-center (8, 10). They have shown that electrochemical oxidation of the dimeric alkyl thiolate-ligated Ni(II) complex (**21** in Figure IV-2) affords a radical in which, according to their EPR simulations only ca. 20% of the spin density resides on the Ni. Chemical oxidation of **21** by I_2 results in **22**, while oxidation of the monomeric cyanide derivative of **21** by O_2 yields **23** (Figure IV-2). Experiments with ^{61}Ni-enriched samples of a closely related oxidized product indicate a valence-delocalized $[Ni_2^{2.5}]^+$ electronic structure (11).

By contrast, Krüger and Holm have reported that the structurally related $[Ni(pdmt)_2]$, where $(pdmt)H_2$ = 2,6-bis(mercaptomethyl)pyridine shows a chemically reversible one-electron reduction at $E_{1/2}$=-1.21 V vs. SCE to form a valence-delocalized species $[Ni_2^{1.5}(pdmt)_2]^-$ (12). The reason for the difference in behavior between these two complexes is unclear, and it is therefore

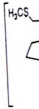

Figure IV-2. An
S-based oxidatio
Chemical oxidat
derivative of **21**

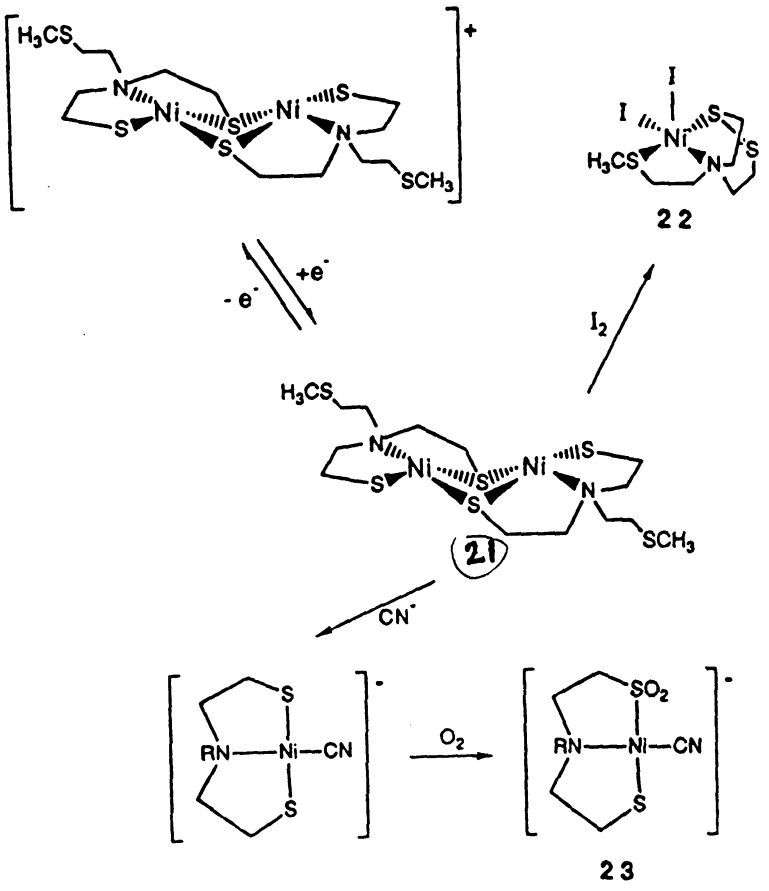

Figure IV-2. An example of an alkyl-thiolate Ni(II) complex which undergoes S-based oxidation. Electrochemical oxidation of **21** affords a Ni(II) thiyl radical. Chemical oxidation with I_2 yields **22**. Oxidation of the monomeric cyanide derivative of **21** with O_2 leads to **23** [from Ref. (8)].

mpossible to predic

the hydrogenase.

Perhaps the r

valence-delocalized

workers (13). It con

S_2 = 2.251-2.260 Å a

coordinated by one

S_{eq} = 2.373 Å) and

compound demon

poor model for th

the parent comple

spanned by arms

Also relev

and $[Ni_2(S\text{-}2,4,5\text{-}$

with distorted te

ligands, respecti

Ni(II) thiolates

II.3. Mononuc

Millar and cow

monomeric tet

oxidized in air

impossible to predict the redox chemistry for the Ni-Fe thiolate complex of the hydrogenase.

Perhaps the most relevant structural model for the Ni-Fe center is the valence-delocalized complex, $[Ni_2\{P(2\text{-}SC_6H_4)_3\}_2]^-$, described by Millar and co-workers (13). It contains a double thiolato bridge, $[Ni_2^{2.5}(\mu\text{-}SR)_2]^{3+}$, with Ni - ($\mu$-S) = 2.251-2.260 Å and Ni···Ni = 2.501 Å. The square-pyramidal Ni ions are also coordinated by one basal and one apical thiolato ligand (Ni - S_{ba} = 2.115, Ni - S_{ap} = 2.373 Å) and one basal phosphano ligand (Figure IV-1D). While this compound demonstrates the viability of a binuclear $[Ni(\mu\text{-}S)_2Fe]$ cluster, it is a poor model for the reductive activation of the hydrogenase Ni-Fe site, since the parent complex $[Ni_2\{P(2\text{-}SC_6H_4)_3\}_2]^-$ is a dimer of square-planar Ni(II) ions spanned by arms of the tris(2-mercaptophenyl)phosphano ligands.

Also relevant models are the complexes $[Ni_2(SC_4H_9)_6]^{2-}$ (Figure IV-1E) and $[Ni_2(S\text{-}2,4,5\text{-}i\text{Pr}_3C_6H_2)_5]^-$ (Figure IV-1F), which are dimers of Ni(II) ions with distorted tetrahedral coordination bridged by two and three thiolato ligands, respectively (14). The redox behavior of these and other tetrahedral Ni(II) thiolates is irreversible, however.

IV.3. Mononuclear Ni complexes

Millar and coworkers have synthesized and structurally characterized a monomeric tetrathiolate Ni(II) complex, $[Ni(nbdt)_2]^{2-}$, which is readily oxidized in air to form the corresponding stable Ni(III) complex at biologically

evant redox poten

(III) can be attaine

vironment by inco

ctors (15, 16). The

ability and the ch

ost stabilizing en

N are anionic and

and coworkers (17

be particularly

work follow later

properties of a se

of this group of c

coworkers have

synthesizing rea

rich coordinatio

structurally cha

incorporate a re

site in the hydr

ligated Ni(II) c

ligated Ni(II) c

glassy carbon

H_2 (19).

relevant redox potentials (9). Holm and coworkers have demonstrated that Ni(III) can be attained in a sulfur-containing multidentate ligand environment by incorporating carboxyl or amidate groups adjacent to the sulfurs (15, 16). They have investigated the relationship between Ni(III) stability and the character of its local ligand environment and found that the most stabilizing environment is one in which the atoms coordinated to the Ni are anionic and polarizable. In the comprehensive studies by Margerum and coworkers (17) deprotonated oligopeptides (amidates) have been shown to be particularly effective in stabilizing Ni(III) (more details on Margerum's work follow later in this Chapter). Holm has studied the electrochemical properties of a series of thiolate/amidate complexes (16). The redox properties of this group of compounds are summarized in Figure IV-3. Kovacs and coworkers have focused on functional model systems by designing and synthesizing reactive mononuclear Ni complexes which contain Ni in a S-rich coordination environment (2). Mascharak and coworkers have structurally characterized two mononuclear Ni thiolate complexes that incorporate a reactive site which is able to mimic some functions of the active site in the hydrogenase (18). Crabtree et al. have discovered a labile sulfur-ligated Ni(II) complex, which promotes H/D exchange and a macrocyclic N-ligated Ni(II) complex, which displays proton-coupled electron transfer at a glassy carbon electrode and that ultimately results in the reaction $2H^+ + 2e^- \rightarrow H_2$ (19).

Figure IV-3. Su

thiolate/amida

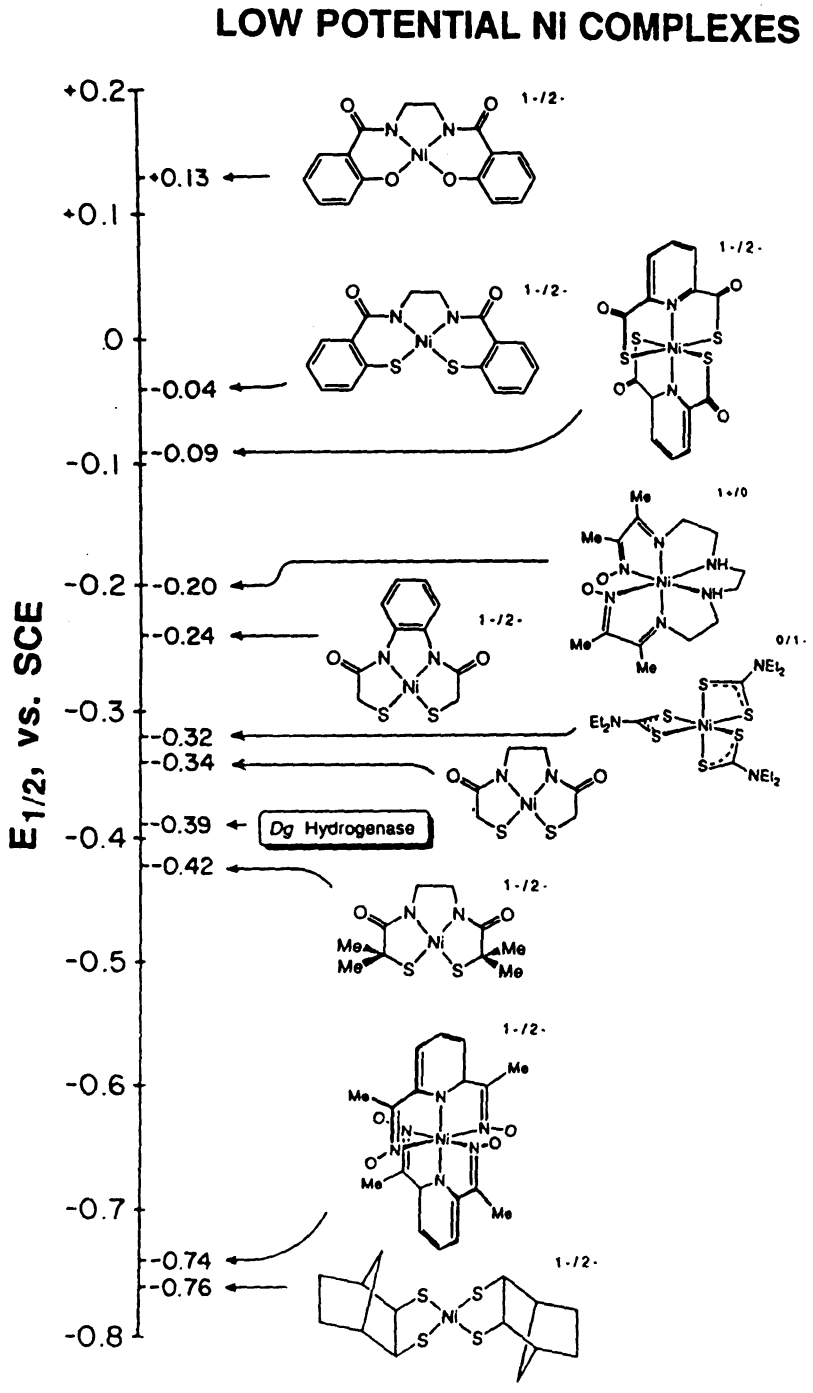

Figure IV-3. Summary of redox properties of synthetic tetrathiolate and thiolate/amidate Ni-complexes [from Ref.(16)].

7.4 Complexes bas

Ni III complexes o

synthesized by Mar

Ni site in hydroger

stable (half-life of

to be 28 min., cf. R

substitution is sim

these complexes a

The prepar

can be oxidized re

K[Ni(III)$(CN)_4$(H

can be replaced b

spectra feature a

tetragonally elon

unpaired electro

the equatorial p

nitrogens, not

interactions ma

VI). Samples n

the CW EPR s

HFI, resulting

broadening in

IV.4. Complexes based on tetracyano nickelate(III)

Ni(III) complexes of general structure shown in Figure IV-4 have been synthesized by Margerum et al. (20, 21) and served as magnetic models for the Ni site in hydrogenases for the following reasons: (1) the Ni(III) is relatively stable (half-life of tetracyano-Ni(III) in solution at low pH values is reported to be 28 min., cf. Ref. (17)); (2) hyperfine splitting generated by ^{61}Ni isotopic substitution is similar to those observed in proteins; (3) the EPR spectra of these complexes are similar to the protein's Ni signals Ni-A, Ni-B and Ni-C.

The preparation of these complexes starts from $K_2[Ni(II)(CN)_4]$, which can be oxidized readily by $K_2S_2O_5$ or excess HOCl, yielding $K[Ni(III)(CN)_4(H_2O)_2]$ (20, 21). The axially coordinated water molecules then can be replaced by other ligands, yielding mixed ligand complexes, whose EPR spectra feature axial g-tensor with $g_\perp > g_{||}$, $g_{||} \cong 2.00$. This is consistent with a tetragonally elongated ligand field with a $(d_{z^2})^1$ ground state (Chapter V). The unpaired electron being mainly in the d_{z^2} orbital creates low spin density in the equatorial plane of these complexes, leading to small HFI with the CN^- nitrogens, not resolved in the CW EPR spectrum. These hyperfine interactions may readily be measured by pulsed EPR techniques (see Chapter VI). Samples made with $^{13}CN^-$, on the other hand, show large HFI splitting in the CW EPR spectrum. Axially coordinated nitrogen also gives rise to large HFI, resulting in HFI splitting only in the $g_{||}$ region of the spectrum and line broadening in the $g_\perp$ region.

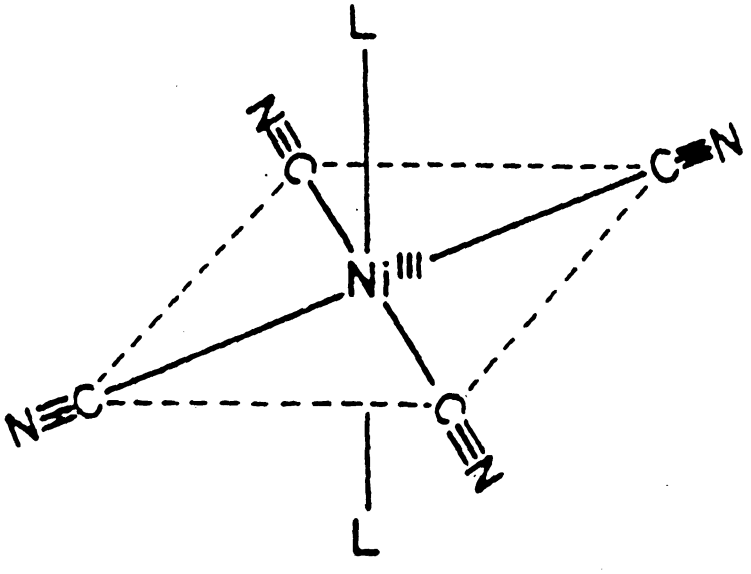

Figure IV-4. Structure of $[Ni(III)(CN)_4L_2]^-$.

1.3 Monopeptide

As early as 1971, M

reacts spontaneous

intermediate that

proposed to be a N

behavior (23). A d

proportional to th

deprotonated ami

catalyzed the rea

Tripeptide

amides form Ni(

IV-3. These comp

oxidation of the

deprotonated pe

help to stabilize

EPR stud

of these Ni(III)

molecules by N

EPR spectrum;

was observed,

positions (26).

pyridine, imid

IV.5. Monopeptide Complexes of Ni(III)

As early as 1971, Margerum and coworkers discovered that Ni(II) tetraglycine reacts spontaneously with O_2 to give a species absorbing at 350 nm and an intermediate that oxidizes iodide to I_2 (22). The intermediate was later proposed to be a Ni(III) complex, based on its EPR spectrum and redox behavior (23). A detailed study (24) showed that the rate of O_2 uptake was proportional to the rate of decomposition of Ni(III)($H_{-3}G_4$) (H_{-3} denotes the 3 deprotonated amide groups in the peptide, G refers to glycine), and that Ni(III) catalyzed the reaction.

Tripeptides, tetrapeptides, pentapeptides and the corresponding peptide amides form Ni(III) complexes with the general structure shown in Figure IV-5. These complexes are readily prepared by electrochemical or chemical oxidation of the corresponding square-planar Ni(II) complexes (23-25). The deprotonated peptide nitrogen groups (*amidate*) are very strong σ-donors that help to stabilize trivalent oxidation states of Cu as well as of Ni.

EPR studies gave strong evidence for the elongated tetragonal structure of these Ni(III) complexes (26). Replacement of one of the axial water molecules by NH_3 results in a three line (1:1:1) splitting in the $g_{||}$ region of the EPR spectrum; at higher concentrations of NH_3 a five line splitting (1:3:5:3:1) was observed, consistent with two equivalent NH_3 molecules at the axial positions (26). Monopeptide Ni(III) complexes form adducts also with pyridine, imidazole, and azide ion (N_3^-) (27). Extended X-ray Absorption Fine

H

H

A
B
C

Figure IV

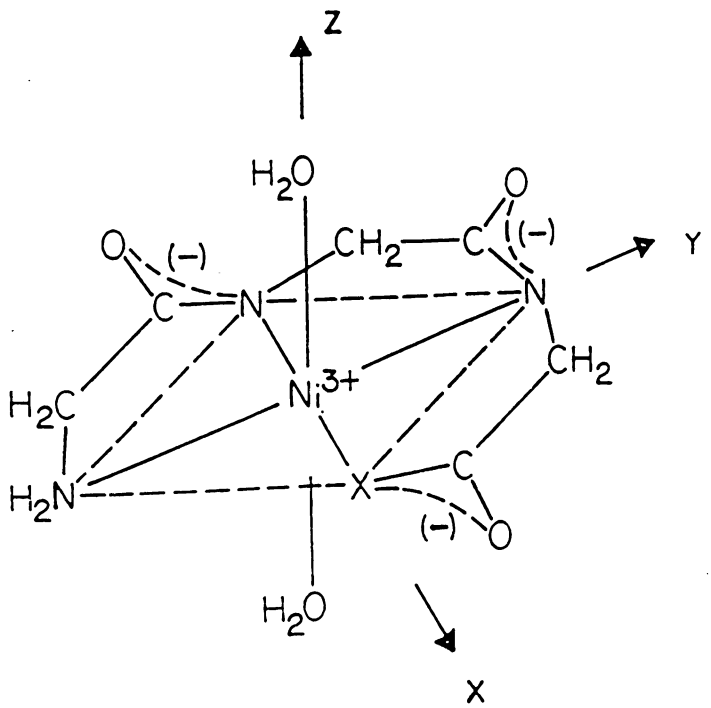

A $Ni(III)(H_{-2}G_3)$, $X = O$
B $Ni(III)(H_{-3}G_4)^-$, $X = NCH_2COO^-$
C $Ni(III)(H_{-3}G_4a)$, $X = NCH_2CONH_2$

Figure IV-5. General structure of Ni(III) monopeptide complexes.

Structure (EXAFS

six coordinate stru

IV.6. Bis(peptido)

At high pH and v

corresponds to th

a six-coordinate s

octahedron with

oxidized electroc

violet-black colo

features $g_{11}>g_{\perp}$

monopeptide co

rather than elon

shown by the A

complex forms

species conver

this complex is

The inductive

thus the ligan

high-spin six-

in the Aib_2 lig

Structure (EXAFS) data also confirm the assignment of tetragonally distorted six coordinate structure for these Ni(III) complexes (17).

IV.6. Bis(peptido) complexes of nickel (III)

At high pH and with excess diglycine (GG) Ni(II) forms a blue complex that corresponds to the formula $Ni(II)(H_{-1}GG)_2^{2-}$ (28). X-ray crystallography reveals a six-coordinate structure, which can be described as a tetragonally distorted octahedron with a compressed N^--Ni(II)-N^- axis (29). This complex can be oxidized electrochemically to form the corresponding Ni(III) complex with a violet-black color (Figure IV-6) (30). The EPR spectrum of this Ni(III) species features $g_{||}>g_{\perp}$, which is in marked contrast to the EPR spectra of the monopeptide complexes (Chapter V), due to the tetragonal compression rather than elongation of the octahedral ligand field. Interesting behavior is shown by the Aib_2 complex of Ni(II) (Aib=aminoisobutyrate). Initially a blue complex forms, but as the pH is increased this high-spin $Ni(II)(H_{-1}Aib_2)(Aib_2)^-$ species converts to an orange low-spin $Ni(II)(H_{-1}Aib_2)_2^{2-}$ complex (17). When this complex is oxidized it forms the tetragonally compressed Ni(III) species. The inductive effect of $-CH_3$ groups in Aib_2 increases the bond strength to Ni thus the ligand field strength will now be sufficient to convert the normally high-spin six-coordinate Ni(II) to a low-spin form. The strong donor groups in the Aib_2 ligand also stabilize the +3 oxidation state. As a result, the E^0 value

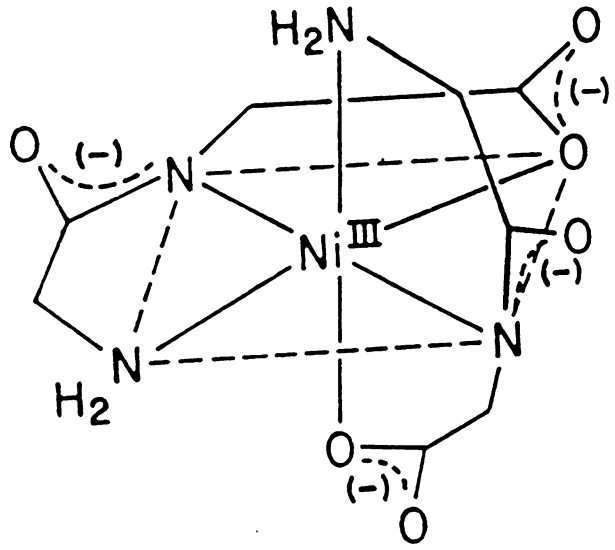

Figure IV-6. Structure of $[Ni(III)(H_{-2}GG)_2]^-$.

f this complex is

table *indefinitely*

Tripeptide

and do not readil

mono(tripeptido)

form bis(tripepti

The bis complexe

orresponding N

II.7. Ni(III) Mix

By mixed ligan

which at least o

other than wat

midazole, azid

tripeptide and

adducts vary

pyridine (17).

Bipyrid

mono(tripept

(31). The EPI

the bipy com

the g_{11} regio

of this complex is remarkably low (+0.34 V vs. SCE), and Ni(III)$(H_{-1}Aib_2)_2^-$ is *stable indefinitely* at pH 8-12 at room temperature.

Tripeptides form stable low-spin square-planar complexes with Ni(II) and do not readily add a second tripeptide ligand. On the other hand, mono(tripeptido)Ni(III) complexes react readily with a second tripeptide to form bis(tripeptido) nickel(III) complexes. Hence, the mode of preparation of the bis complexes is to first oxidize the mono-peptido-Ni(II) to the corresponding Ni(III) complex and then add excess tripeptide.

IV.7. Ni(III) Mixed Ligand Complexes

By mixed ligand complexes we mean those Ni(III)monopeptide complexes, in which at least one of the two axial coordination sites is occupied by a ligand other than water. Axial ammonia adducts have already been mentioned. Imidazole, azide (N_3^-) and pyridine also form axial adducts with Ni(III) tripeptide and tripeptide amide complexes. The stability constants of the adducts vary from 1100 to 50 M^{-1}, in the order: imidazole > $NH_3 \approx N_3^-$ > pyridine (17).

Bipyridine (bipy) and terpyridine (terpy) will react with mono(tripeptido)-Ni(III) complexes to form stable mixed ligand complexes (31). The EPR spectra of these complexes are given in Figure IV-7. The EPR of the bipy complex shows a triplet, while the terpy adduct a quintet of peaks in the g_{11} region due to one and two axially coordinated nitrogens, respectively.

Figur

[Ni(III)(

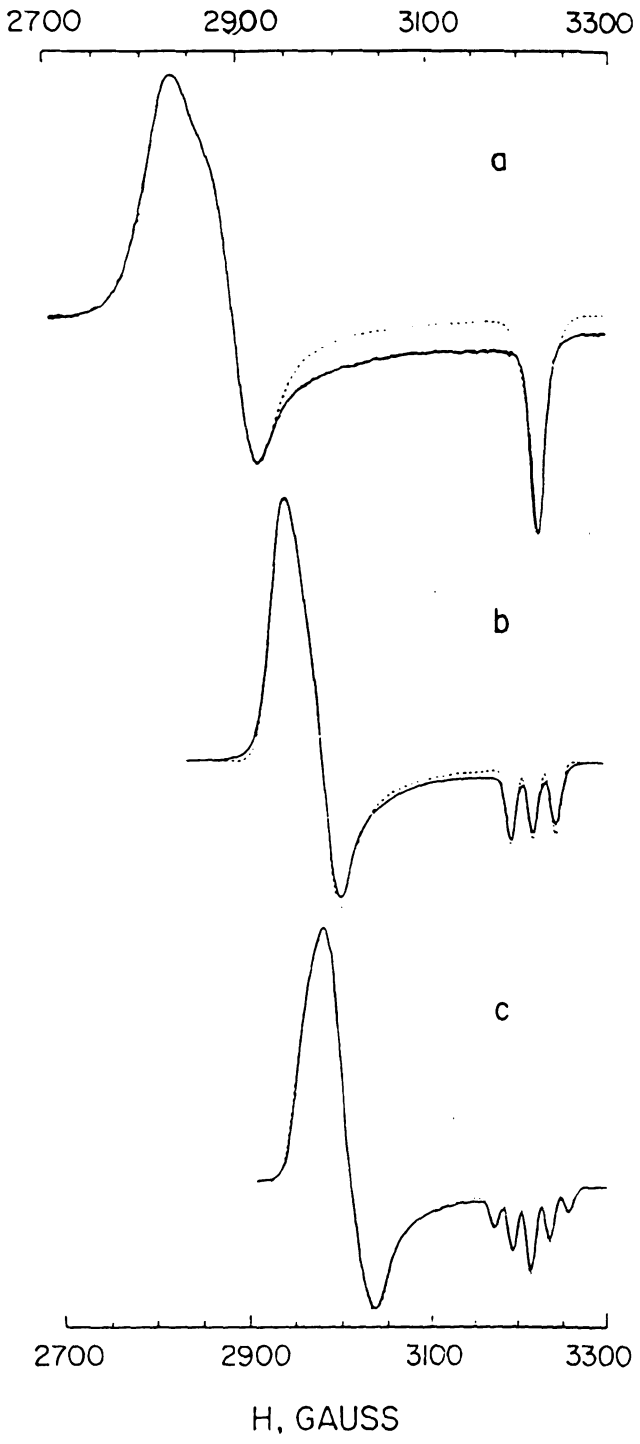

Figure IV-7. EPR spectra of the monopeptide Ni(III) complex, $[Ni(III)(H_{-2}GAG)(H_2O)_2]^+$ (a), and of its bipy (b) and terpy (c) adducts. [from Ref. (17)]

Ethylenediamin

ripeptide as mo

they act as l

coordination sit

frozen solution

indicative of tw

conditions

molecules as

Cyanide i

monoadduct, N

EPR spectrum s

used, a large sp

splitting is grea

isotropic HFI c

ligand orbital (

of the unpaire

new species to

species showi

ligated nitrog

$C^{15}N^-$ is used

one of the Ai

the z-axis. Th

shown in Fig

Ethylenediamine (en) and diethylene triamine (dien) can add to a Ni(III) tripeptide as monodentate ligands at low pH, coordinating axially. At pH 7 they act as bidentate ligands, occupying additionally one equatorial coordination site, replacing the COO^- (carboxylate) group. Above pH 11, the frozen solution EPR of the dien complex shows a quintet in the $g_{||}$ region, indicative of two axially coordinated nitrogens. This means that under these conditions dien acts as a tridentate ligand, replacing both axial water molecules as well as the equatorially coordinated carboxylate group (31).

Cyanide ion reacts with $Ni(III)(H_{-2}Aib_3)(H_2O)_2$ to form an axial monoadduct, $Ni(III)(H_{-2}Aib_3)(H_2O)(CN)^-$ (Figure IV-8A). The frozen solution EPR spectrum shows a single peak in the $g_{||}$ region. When $^{13}CN^-$ (I=1/2) is used, a large splitting occurs in both $g_\perp$ and $g_{||}$ regions (17). The hyperfine splitting is greater than that observed for the $^{14}NH_3$ adduct, because the isotropic HFI constant (A_{iso}) is larger and because the greater s character of the ligand orbital (sp for CN^- versus sp_3 for NH_3) allows for a stronger interaction of the unpaired electron with the nucleus. Addition of more CN^- causes a new species to form that has an EPR spectrum typical for an elongated Ni(III) species showing a triplet splitting in the $g_{||}$ region, indicating one axially ligated nitrogen donor. This spectrum does not change when either $^{13}CN^-$ or $C^{15}N^-$ is used to make the sample. Thus, the triplet splitting must come from one of the Aib_3 nitrogens and the CN^- ions are no longer coordinated along the z-axis. These observations can be explained by assuming the structure shown in Figure IV-8B (17). Excess cyanide results in the displacement of the

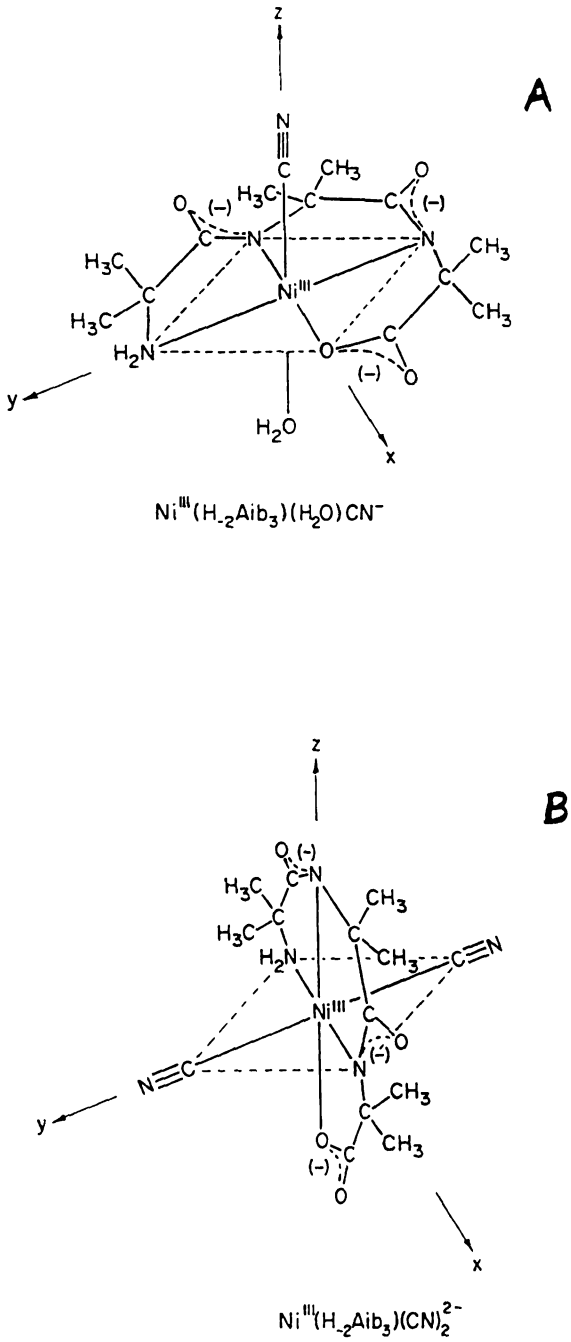

Figure IV-8. Structure of $[Ni(III)(H_{-2}Aib_3)(H_2O)(CN)]^-$ (A) and $[Ni(III)(H_{-2}Aib_3)(CN)_2]^-$ (B); where Aib=aminoisobutyrate.

peptide and the

be prepared by t

omplex present

yanides become

peptide and the formation of $Ni(III)(CN)_6^{3-}$. Hexacyanonickelate(III) can also be prepared by the oxidation of $Ni(II)(CN)_4^{2-}$ followed by addition of CN^-. This complex presents an example of dynamic Jahn-Teller distortion, where the six cyanides become equivalent because of vibrational interchange (20).

1. Halcrow,
2. Kovacs, J.
3. Halcrow,
4. Volbeda, Fonticella
5. Krüger, H DerVarta G.; LeGal
6. Mills, D. Darensbo
7. Colpas,
8. Kumar, 1989, *111*
9. Fox, S.;
10. Maroney *Transitio* Stiefel, E 1996.
11. Choudh J. *Inorg.*
12. Krüger,
13. Franoli 6587.
14. Silver,
15. Krüger
16. Krüger
17. Marge *Nickel;*

References

1. Halcrow, M. A.; Christou, G. *Chem. Rev.* **1994**, *94*, 2421.

2. Kovacs, J. in *Advances in Inorganic Biochemistry* **1994**, *Vol. 9*, 173.

3. Halcrow, M. A. *Angew. Chem. Int. Ed. Engl.* **1995**, *34(11)*, 1193.

4. Volbeda, A.; Charon, M.-H.; Piras, C.; Hatchikian, E. C.; Frey, M.; Fonticella-Camps, J. C. *Nature* **1995**, *373*, 580.

5. Krüger, H.-J.; Huynh, B. H.; Ljungdahl, P. O.; Xavier, A. V.; DerVartanian, D. V.; Moura, I.; Peck, H. D., Jr.; Teixeira, M.; Moura, J. J. G.; LeGall, J. *J. Biol, Chem.* **1982**, *257*, 14620.

6. Mills, D. K.; Hsiao, Y. M.; Farmer, P. J.; Atnip, E. V.; Reibenspies, J. H.; Darensbourg, M. Y. *J. Am. Chem. Soc.* **1991**, *113*, 1421.

7. Colpas, G. J.; Day, R. O.; Maroney, M. J. *Inorg. Chem.* **1992**, *31*, 5053.

8. Kumar, M.; Day, R. O.; Colpas, G. J.; Maroney, M. J. *J. Am. Chem. Soc.* **1989**, *111*, 5974.

9. Fox, S.; Eang, Y.; Silver, A.; Millar, M. *J. Am. Chem. Soc.* **1990**, *112*, 3218.

10. Maroney, M. J.; Allan, C. B.; Chohan, B. S.; Choudhury, S. B.; Gu, Z. in *Transition Metal Sulfur Chemistry; ACS Symposium Series Vol. 653*, Stiefel, E. I.; Matsumoto, K., Eds.; ACS Publication: Washington, D. C. 1996.

11. Choudhury, S. B.; Pressler, M. A.; Mirza, S. A.; Day, R. O.; Maroney, M. J. *Inorg. Chem.* **1994**, *33*, 4831.

12. Krüger, H.-J.; Holm, R. H. *Inorg. Chem.* **1989**, *28*, 1148.

13. Franolic, J. D.; Wang, W. Y.; Millar, M. *J. Am. Chem. Soc.* **1992**, *114*, 6587.

14. Silver, A.; Millar, M. J. *Chem. Soc. Commun.* **1992**, 948.

15. Krüger, H.-J.; Holm, R. H. *J. Am. Chem. Soc.* **1990**, *112*, 2955.

16. Krüger, H.-J.; Peng, G.; Holm, R. H. *Inorg. Chem.* **1991**, *30*, 734.

17. Margerum, D. W.; Anliker, S. L., in *The Bioinorganic Chemistry of Nickel*; Lancaster, J. R., Jr., Ed.; VCH: New York, 1988; Chapter 2.

18. Baidya, M
19. Efros, L. I
Chem. **199**
20. Pappenha
21. Wang, Y.
Chem. **198**
22. Paniago,
1971, 1427
23. Bossu, F.
24. Bossu, F.
L. *Inorg.*
25. Bossu, F.
26. Lappin,
1630.
27. Murray,
28. Brookes,
29. Freeman
30. Jacobs, S
31. Pappen
Inorg. C

18. Baidya, M.; Olmstead, M.; Mascharak, P. K. *Inorg. Chem.* **1991**, *30*, 929.

19. Efros, L. L.; Thorp, H. H.; Brudvig, G. W. W.; Crabtree, R. H. *Inorg. Chem.* **1992**, *31*, 1722.

20. Pappenhagen, T. L.; Margerum, D. W. *J. Am. Chem. Soc.* **1985**, *107*, 4576.

21. Wang, Y. L.; Beach, M. W.; Pappenhagen, T. L.; Margerum, D. W. *Inorg. Chem.* **1988**, *27*, 4464.

22. Paniago, E. B.; Weatherburn, D. C.; Margerum, D. W. *Chem. Commun.* **1971**, 1427.

23. Bossu, F. P.; Margerum, D. W. *J. Am. Chem. Soc.* **1976**, *98*, 4003.

24. Bossu, F. P.; Paniago, E. B.; Margerum, D. W.; Kirksey, S. T., Jr.; Kurtz, J. L. *Inorg. Chem.* **1978**, *17*, 1034.

25. Bossu, F. P.; Margerum, D. W. *Inorg. Chem.* **1977**, *16*, 1210.

26. Lappin, A. G.; Murray, C. K.; Margerum, D. W. *Inorg. Chem.* **1978**, *17*, 1630.

27. Murray, C. K.; Margerum, D. W. *Inorg. Chem.* **1982**, *21*, 3501.

28. Brookes, G.; Pettit, L. P. *J. Chem. Soc. Dalton Trans.* **1975**, 2106.

29. Freeman, H. C.; Sinclair, R. L. *Acta Crystallogr.* **1978**, *B34*, 2451.

30. Jacobs, S. A.; Margerum, D. W. *Inorg. Chem.* **1984**, *23*, 1195.

31. Pappenhagen, T. L.; Kennedy, W. R.; Bowers, C. P.; Margerum, D. W. *Inorg. Chem.* **1984**, *23*, 1345.

V.I. Abstract

The goal of this

structure of Ni(

equatorially coo

center. To sort

(with ^{15}N) has b

ring of the terp

observe the mo

labeled sample

surprisingly, in

may suggest th

geometry prop

Chapter V

ESEEM Study on Ni(III)(triglycinate)(terpy)

V.1. Abstract

The goal of this investigation is to gain information on the electronic structure of Ni(III)($H_{-2}G_3$)(terpy) (Figure V-6). This complex features four equatorially coordinated nitrogens, which are weakly coupled to the Ni(III) center. To sort out the contributions of these nuclei specific isotopic labeling (with ^{15}N) has been used, by substituting the nitrogen in the middle pyridine ring of the terpyridine chelate. The "product rule" of ESEEM allows one to observe the modulation from this nucleus by dividing the data from the non-labeled sample by that from the ^{15}N-labeled one. The result, quite surprisingly, indicated no contribution from this particular nitrogen. This may suggest that this nitrogen does not coordinate at all, in contrast to the geometry proposed earlier [see Ref.(16)].

V2. Theory of El

EPR spectra of N

(d^9) and Ni^+ (d^8)

and d^7 ions are

under appropri

therefore it is n

absence of exte

Ni(III) is

identical to the

to make compl

magnitude of t

all Ni(III) studi

opposite reaso

conditions. Ni(

and those with

elongated octa

The g-tensor

The anisotrop

orbitals prima

momentum to

orbit coupling

The g-tensor

V.2. Theory of EPR of Ni(III) Complexes

EPR spectra of Ni are observable in at least three redox states: Ni^{3+} (d^7), Ni^{2+} (d^8) and Ni^{+} (d^9) ions are all paramagnetic in at least some complexes. the d^7 and d^9 ions are classical Kramers systems, which must be EPR detectable under appropriate experimental conditions. Ni^{2+} has an integral spin (S=1) therefore it is not guaranteed to have a doubly degenerate ground state in the absence of external magnetic field.

Ni(III) is isoelectronic with Co(II) and Fe(I), but is far from being identical to them in its behavior. The larger positive charge on the Ni tends to make complexes with negatively charged ligands tighter. This increases the magnitude of the crystal field terms and favors the low-spin state. As a result all Ni(III) studied thus far have low-spin electron configuration. For just the opposite reason Fe^{+} prefers high-spin ground state under all reasonable conditions. Ni(III) complexes fall into two major classes; those with $g_{\perp} > g_{||}$ and those with $g_{||} > g_{\perp}$. The former have been recognized as tetragonally elongated octahedral complexes, the latter as square planar complexes (1, 2).

The g-tensor

The anisotropy of the g-tensor of d^7 ions results from the admixture of the d-orbitals primarily by spin-orbit coupling, which contributes orbital angular momentum to the electronic Zeeman interaction. In the absence of the spin-orbit coupling the orbital angular momentum would be quenched out (3). The g-tensor can be calculated by using appropriate ligand-field terms and

additional matri

Hamiltonian car

eigenstates of L_z

Zeeman term is

is always true fo

onsidered in th

orbitals are muc

perturbation the

widely been use

symmetry of th

Figure V-

system with the

The diagram ir

electron prima

g-values in this

$\frac{2\lambda}{\Delta E_{xy-xz}}$, $g_{zz}=2$

epresents the

Thus, the squa

In the c

unpaired elect

additional matrix elements provided by the spin-orbit coupling. The Hamiltonian can be written in terms of the free ion orbitals that are eigenstates of $\mathbf{L}_z$ (z-component of the angular momentum). If the electronic Zeeman term is much smaller than either the field or spin-orbit terms (which is always true for fields of ca. 3000 G), only the lowest doublet need be considered in the calculation. If the ligand-induced separations of the d orbitals are much greater than the important spin-orbit matrix elements, *perturbation theory* can be used to calculate the g-values. This method has widely been used in an attempt to relate the observed g-tensor to the symmetry of the complex (4-7).

Figure V-1 shows a simple energy level diagram for a low-spin d^7 system with the relative energies of the d orbitals in different ligand fields. The diagram indicates that in a square-planar arrangement the unpaired electron primarily resides in an orbital which is mainly d_{xy} in character. The g-values in this case are predicted by the following expressions (9): $g_{xx}=g_{yy}=2-\frac{2\lambda}{\Delta E_{xy-xz}}$, $g_{zz}=2-\frac{2\lambda}{\Delta E_{xy-(x^2-y^2)}}$, where λ is the spin-orbit coupling constant, $\Delta E_{xy\text{-}xz}$ represents the energy difference between the *xy* and*xz* unperturbed states. Thus, the square-planar geometry leads to $g_{\parallel} > g_{\perp}$.

In the case of a tetragonally distorted octahedral ligand field the unpaired electron is located in the d_{z^2} orbital.

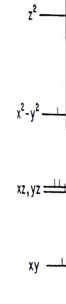

Tetrago
compre

Figure V-1. E

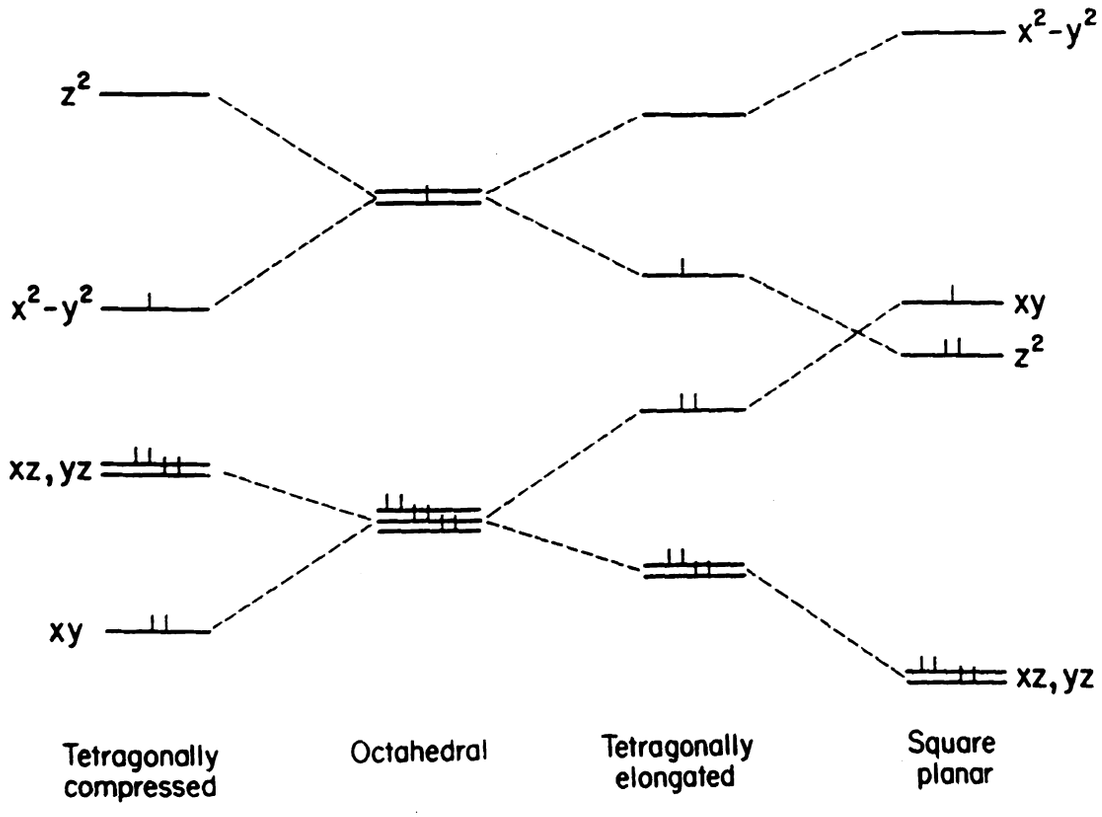

Figure V-1. Energy level diagram for d-orbitals in various ligand fields [from Ref. (8)].

The g-values no

tensor has been

complexes and

The nuclear hy

Two kinds of h

complexes. One

nucleus (I=3/2

The measured

the Ni(III) cent

CW EPR.

The oth

electron and th

("superhyperf

and usually n

measured by

parameters, e

constant, repr

nature of the

which we de

proportional

The g-values now are $g_{xx}=g_{yy}=2-\frac{6\lambda}{\Delta E_{z^2-xz}}$, $g_{zz}=2$, so $g_{\perp} > g_{||}$ (9). This kind of g-tensor has been the most commonly observed for mononuclear Ni(III) complexes and in hydrogenases.

The nuclear hyperfine interaction

Two kinds of hyperfine interactions (HFI) have been studied in Ni(III) complexes. One is the HFI between the unpaired electron and the ^{61}Ni nucleus (I=3/2). These measurements require ^{61}Ni enrichment in the sample. The measured HFI tensor yields information on the electronic structure of the Ni(III) center. These interactions are large and can readily be measured by CW EPR.

The other kind of HFI is the magnetic coupling between the unpaired electron and the magnetic nuclei (such as ^{1}H, ^{2}H, ^{14}N, etc.) of the ligand ("superhyperfine interactions"). These are of small magnitude (few Gauss) and usually not resolved in frozen solution EPR spectra. They can be measured by ENDOR or ESEEM. In general, the HFI tensor provides three parameters, each of which carries structural information. A_{iso}, the isotropic constant, reports on the unpaired electron spin density as well as on the nature of the molecular wavefunctions. The anisotropic portion of the HFI, which we designate T, provides geometric information, since its magnitude is proportional to $1/r^3$, where r is the effective distance between the electron and

e nucleus. The

gramagnetic spe

Nuclear *Quadrup*

Nuclei with I≥1

agnetic mome

electric field (Fig

electronic struct

quadrupole par

nuclear spin (th

field determine

moment in tur

field gradient.

quadrupole m

and may mani

measured dire

(12). Owing to

spin angular

terms of nucl

the nucleus. The rhombicity parameter, δ, is related to the symmetry of the paramagnetic species (10).

Nuclear Quadrupolar Interaction (NQI)

Nuclei with $I \geq 1$ possess a quadrupole moment, which is collinear with the magnetic moment. The quadrupole moment interacts with a non-uniform electric field (Figure V-2). The electric field gradient is determined by the electronic structure of the paramagnetic species, therefore, measuring the quadrupole parameters can yield useful structural information (3, 11-13). The nuclear spin (through its magnetic moment) is quantized along the effective field determined by the magnet and nearby electrons. The quadrupole moment in turn orients the nucleus in the direction of the largest electric field gradient. This competition between the magnetic moment and quadrupole moment alters the energy of the nuclei placed in a magnetic field and may manifest itself in the result of the EPR experiment. NQI can also be measured directly, using Nuclear Quadrupole Resonance (NQR) spectroscopy (12). Owing to the collinearity of the quadrupole moment with the nuclear spin angular momentum, the Hamiltonian of the NQI can be expressed in terms of nuclear spin operators (3, 11),

$$\hat{\mathcal{H}}_{NQI} = \kappa[3\hat{I}_Z^2 - I^2 + \eta(\hat{I}_X^2 - \hat{I}_Y^2)],$$

Figure V-2.

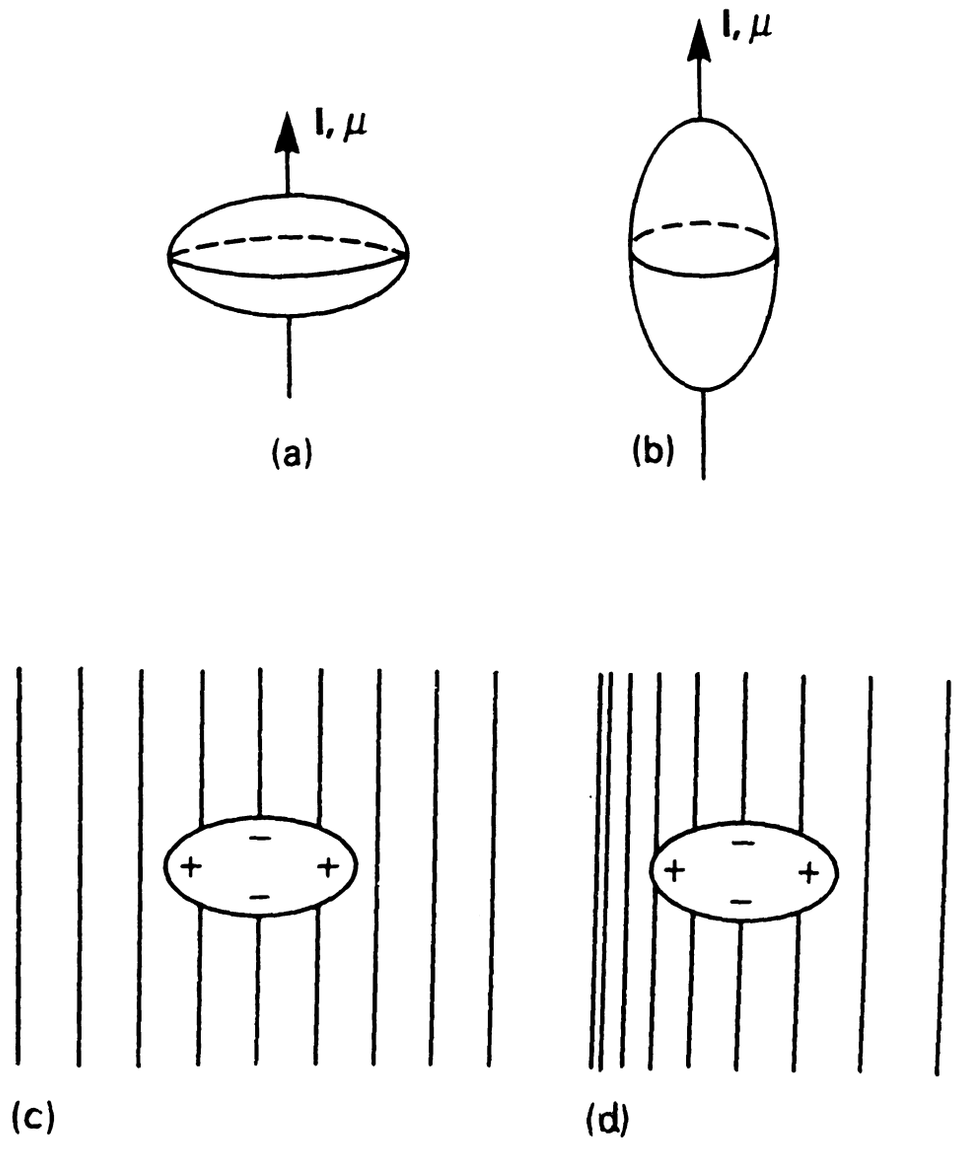

Figure V-2. Oblate (a) and prolate (b) shape of quadrupolar nuclei. Schematic representation of the interaction of the quadrupolar nucleus in a uniform electric field (c), and in a field gradient (d).

where κ is the qu

parameter define

electric field gra

The effect

which shows a s

exactly twice th

leads to the col

appearance of p

The observed f

appear as sharp

feature located

about the hyp

where κ is the quadrupole coupling constant, $\kappa=\frac{e^2qQ}{4\hbar}$, η is the asymmetry parameter defined as $\eta=|q_{xx}-q_{yy}|/q_{zz}$, where q_{ii} are the principal values of the electric field gradient tensor.

The effect of $\hat{\mathcal{H}}_{NQI}$ on ENDOR and ESEEM is illustrated in Figure V-3, which shows a special case for S=1/2, I=1, where the isotropic nuclear HFI is exactly twice the nuclear Larmor frequency. This "exact cancellation" (14) leads to the collapse of energy levels in one spin manifold and results in the appearance of pure quadrupole frequencies in the ESEEM (or ENDOR) spectra. The observed frequencies (3) are $\nu_+=(3+\eta)\kappa$, $\nu_-=(3-\eta)\kappa$, $\nu_0=2\eta\kappa$ (Figure V-3) they appear as sharp peaks. The other electron spin manifold gives rise to a broad feature located at higher frequency (15); this peak contains all information about the hyperfine interaction.

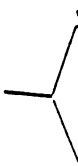

Figure V-3.

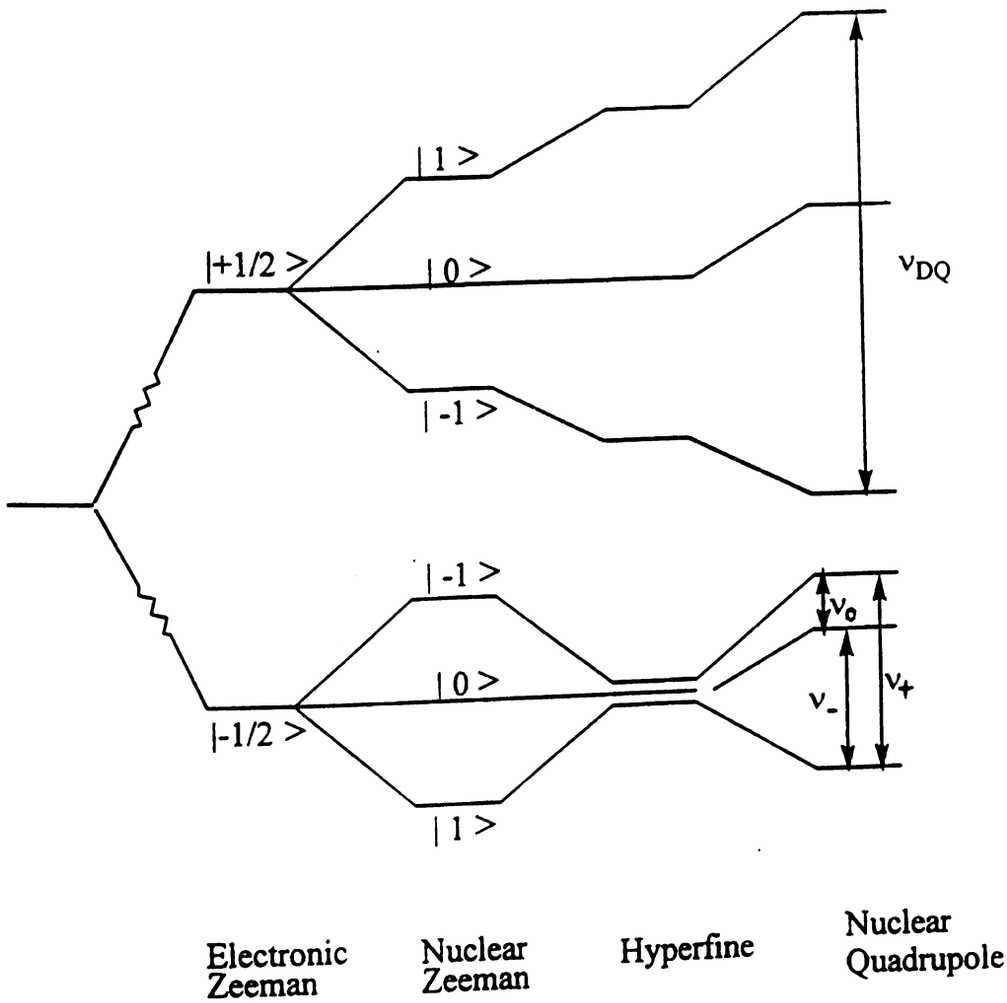

Figure V-3. Energy level diagram for S=1/2, I=1/2 spin system at "exact cancellation".

V.3. Sample Pr

The procedure

Preparation of

366 mg of Ni(C

flask. Also pre

tryglicine (Sig

ca. 0.4 M "OX

"OXONE" is a

g/mol. All the

Combine 5 m

mL beaker eq

M NaOH solu

NaOH). The

formation of

the amide pr

Preparation o

terpyridine (

mL of aceto

mL of the N

NaOH (for

to make Ni

solution of

V.3. Sample Preparation

The procedure follows the one published in the literature (16).

Preparation of Ni(II)($H_{-2}G_3$): Make up 0.1 M Ni(II) stock solution by dissolving 366 mg of $Ni(ClO_4)_2.6H_2O$ (Aldrich, FW=365.70 g/mol) in a 10 mL volumetric flask. Also prepare 0.14 M triglycine (G_3) solution by dissolving 265 mg tryglicine (Sigma, FW=189.2 g/mol) in a 10 mL volumetric flask. Also make a ca. 0.4 M "OXONE" stock solution, using 1.23 g "OXONE" in 5 mL water. "OXONE" is a trademark of Aldrich for $2KHSO_5.KHSO_4.K_2SO_4$, FW=614.78 g/mol. All these solutions should be freshly prepared.

Combine 5 mL of the Ni(II) stock solution with 5 mL of the G_3 solution in a 50 mL beaker equipped with a magnetic stirrer and a pH electrode. Slowly add 1 M NaOH solution to it to raise the pH to ca. 10 (it takes about 1 mL of the NaOH). The color of the solution changes to deep yellow, indicating the formation of the Ni(II)($H_{-2}G_3$) complex ($H_{-2}G_3$ denotes triglycine with two of the amide protons lost). The Ni concentration in this solution is 45 mM.

Preparation of Ni(III)($H_{-2}G_3$)(terpy): Prepare 0.3 M solution of 2,2′:6′,2″ terpyridine (terpy) by dissolving 699 mg terpy (Sigma, FW=233 g/mol) in 10 mL of acetone. Mix 300 μL of this solution with 3 mL of ethylene glycol. Mix 1 mL of the Ni(II)($H_{-2}G_3$) stock solution with 1 mL of H_2O and 0.1 mL of 0.1 M NaOH (for pH adjustment). While stirring, add 300 μL of "OXONE" solution to make Ni(III)($H_{-2}G_3$)$(H_2O)_2$ in situ. Then quickly add the ethylene glycol solution of the terpy just prepared. Put an aliquot of this solution into an EPR

ube, freeze it w

M, with a 2-fo

Preparation of t

acetyl pyridine

consists of thre

ntroduce ^{15}N

$^{15}NH_4OAC$ (Ca

of the product

V.4. Results a

The CW-EPR

spectra of the

small HFI co

spectrum dis

identical wit

consistent w

V.1). The res

spectrum re

(Figure V-6)

of

tube, freeze it with liquid N_2. The sample has a Ni concentration of ca. 10 mM, with a 2-fold excess of terpy.

Preparation of the ^{15}N-labeled terpy: the synthesis of terpy starting from 2-acetyl pyridine is described in *Org. Synth.* **1986**, *Vol. 64*, 189. The procedure consists of three major steps summarized in Figure V-4. Our goal is to introduce ^{15}N only into the middle ring. This can be done conveniently using $^{15}NH_4OAC$ (Cambridge Isotopes) in step B of the synthesis. The identification of the product was done by using ^{13}C and ^{1}H-NMR and mass spectrometry.

V.4. Results and Discussion

The CW-EPR spectrum of the $Ni(H_2G_3)$(terpy) is shown in Figure V-5. The spectra of the all-^{14}N and of the ^{15}N-labeled samples are identical, because the small HFI coupling is masked by the inhomogeneous line broadening. The spectrum displays a quasi-axial HFI tensor with $g_{\perp}$=2.154, $g_{||}$=2.011 and is identical with the one published in the literature (2, 16). These g-values are consistent with a tetragonally distorted octahedral ligand field (see Section V.1). The resolved hyperfine splittings observed in the $g_{||}$ region of the spectrum result from the two axially coordinated (equivalent) nitrogens (Figure V-6). This strong coupling is due to the fact that the unpaired electron of

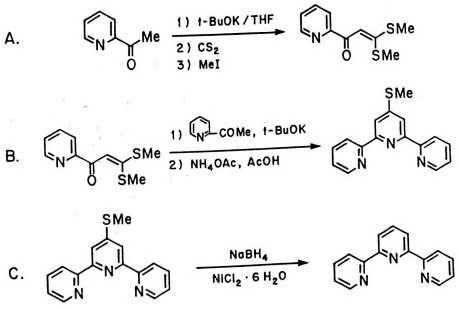

Figure V-4. The synthesis of terpyridine.

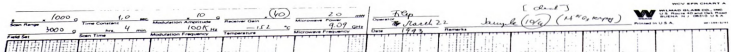

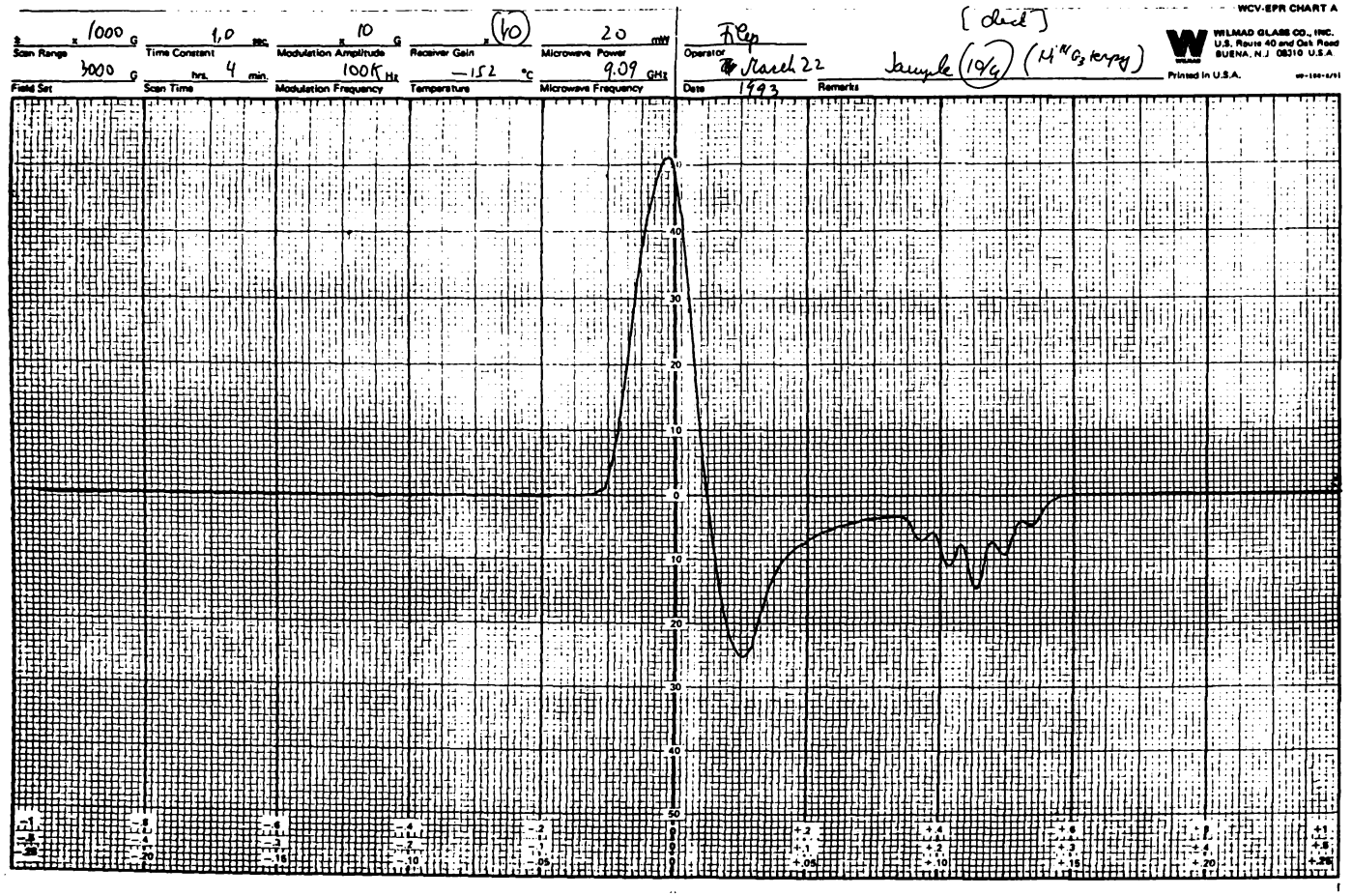

Figure V-5. CW-EPR spectrum of Ni(III)($H_{-2}G_3$)(terpy).

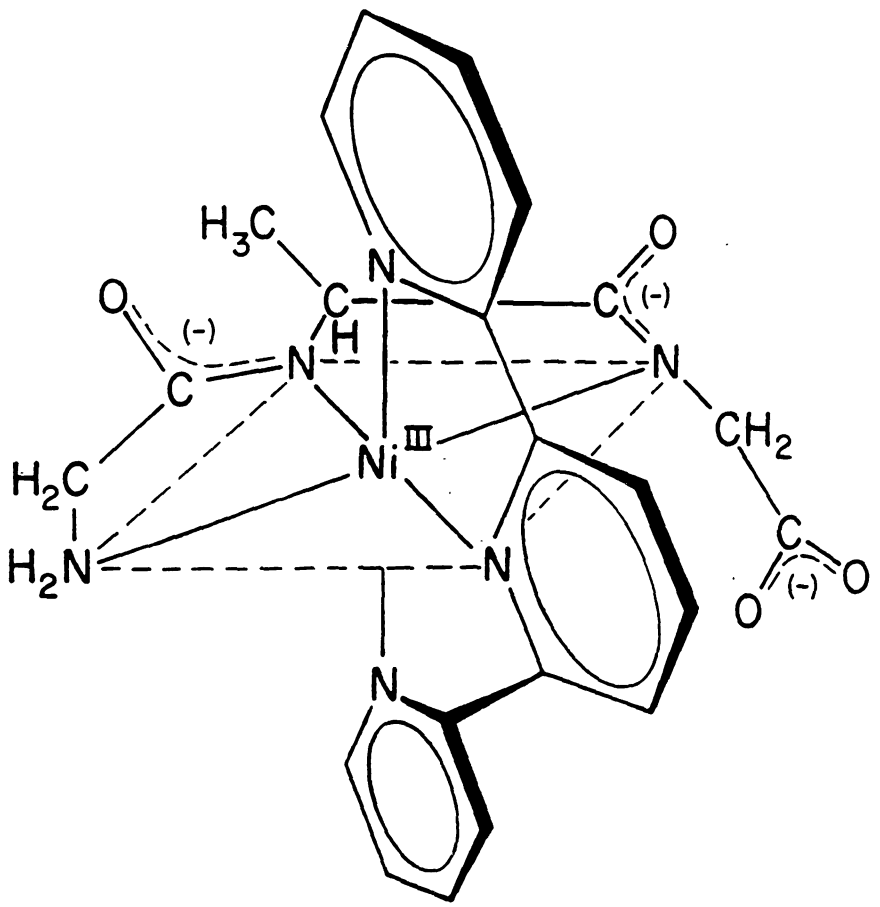

Figure V-6. Proposed structure of Ni(III)($H_{-2}G_3$)(terpy).

Ni(III) mainly

axis (and low

coordinated n

ESEEM. The s

because the n

MW pulse, sc

simultaneous

to sort out th

replacing one

function of s

individual nu

correct only

disordered s

where E(t) is

ith nitrogen.

terpy, the ot

ESEEM func

where f_4 is

position, f_4'

NQI of ^{15}N

Ni(III) mainly resides in the d_{z^2} orbital, creating high spin density along the z axis (and low spin density in the equatorial plane). The equatorially coordinated nitrogens in turn are weakly coupled and can be studied by ESEEM. The strongly coupled axial nitrogens do not contribute to the ESEEM, because the magnitude of their HFI exceeds the excitation bandwidth of the MW pulse, so the corresponding branching transitions cannot be excited simultaneously (Chapter I). One approach to analyze complex ESEEM data is to sort out the contributions from the various nitrogens by specifically replacing one ^{14}N by ^{15}N. This is made possible by the fact that the modulation function of several nuclei is the product of the modulation functions of individual nuclei ["product rule", see Ref(17)]. Though this rule strictly is correct only for 2-pulse single crystal ESEEM, it has been found applicable to disordered samples to a good approximation. In our case,

$$E(t)=\prod_{i=1}^{4} f_i(t)$$

where E(t) is the experimental ESEEM function, f_i is the modulation from the i^{th} nitrogen. We have prepared two samples, one with ordinary (non-labeled) terpy, the other with terpy labeled with ^{15}N in the middle ring. Dividing the ESEEM functions we obtain

$$E_{div}(t)=f_4/f_4^*$$

where f_4 is the modulation function from the ^{14}N nucleus at the middle position, f_4^* is the corresponding ^{15}N modulation function. Due to the lack of NQI of ^{15}N (I=1/2), f_4^* features very small modulation depth, so E_{div} to a good

approximation

analyzed by n

Figure

ESEEM data. T

and (f) have b

and (e)-(f) hav

respectively.

^{14}N and ^{15}N d

ESEEM traces

be concluded

to be equato

of Ni(III)(H_{-2}

measuremen

not shown).

nitrogens, p

This

directly coo

center in te

be to propo

Ni(III) but

nitrogens w

unlikely, h

complexes

approximation is identical to the ^{14}N modulation function, and can be analyzed by numerical simulation.

Figure V-7 summarizes our results by showing 3 pairs of 3-pulse ESEEM data. Traces (a), (c), (e) arise from non-labeled samples, while (b), (d) and (f) have been obtained from the ^{15}N-labeled sample. Data (a)-(b), (c)-(d) and (e)-(f) have been collected at g=2.175 ($g_{\perp}$), g=2.100 (g_{im}) and g=2.014 ($g_{||}$), respectively. *No detectable difference can be seen* between the corresponding ^{14}N and ^{15}N data. This has been confirmed by dividing the corresponding ESEEM traces, as described above. The results are shown in Figure V-8. It can be concluded that the *nitrogen of the middle pyridine ring* of terpy (proposed to be equatorially coordinated*) has no significant contribution to the ESEEM* of Ni(III)($H_{-2}G_3$)(terpy). Identical conclusions have been drawn from measurements performed at 11 and 13 GHz resonance frequency range (data not shown). The ESEEM in this complex is apparently due to the other three nitrogens, probably primarily to the two negatively charged amidate groups.

This result is rather unexpected, especially knowing that equatorial, not directly coordinated CN^- nitrogens show significant coupling to the Ni(III) center in tetracyano-nickelate(III) (Chapter VI). A possible explanation would be to propose that the middle nitrogen of terpy is not coordinated directly to Ni(III) but assumes a bidentate coordination by terpy, involving the two axial nitrogens with the middle pyridine ring rotated away from the Ni(III). This is unlikely, however, since terpy usually acts as a tridentate chelate, making complexes of extremely high stability. The other possible explanation

Figure V-7.

Figure V-7. Three-pulse ESEEM on Ni(III)(H_2G_3)(terpy): traces (a), (c) and (e) are from the non-labeled complex, traces (b), (d) and (f) are from complex containing ^{15}N in the middle pyridine ring. (a), (b) taken at g=2.175; (c), (d) at g=2.100; (e), (f) at g=2.014.

echo amplitude
5

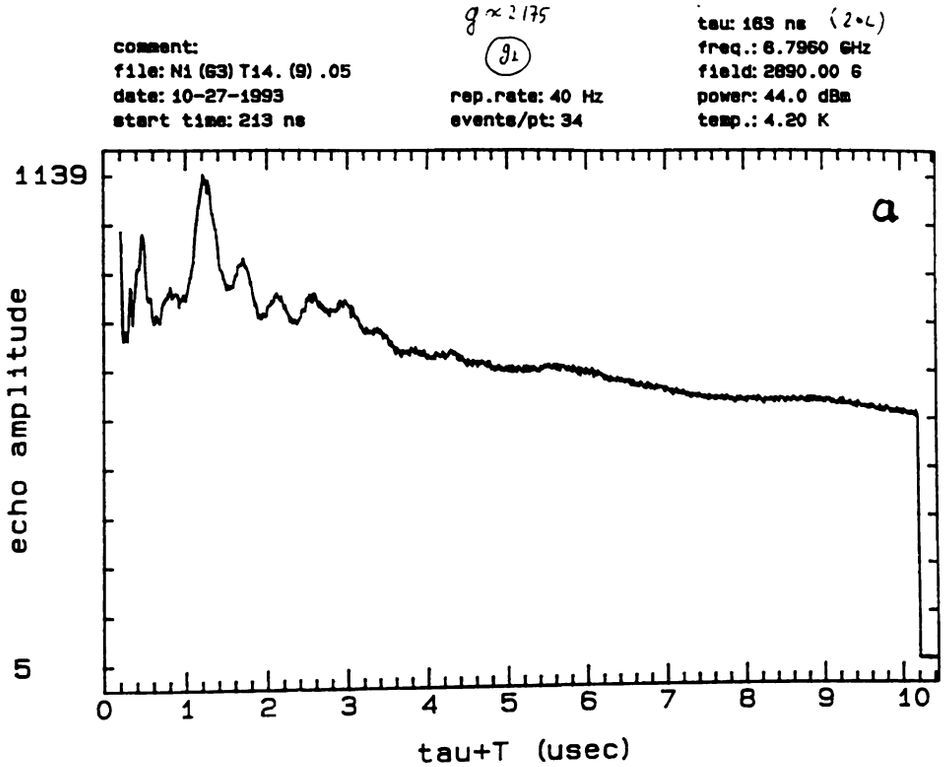
g ≈ 2.175
(g1)
comment:
file: Ni (63) T14. (9) .05
date: 10-27-1993
start time: 213 ns
rep.rate: 40 Hz
events/pt: 34
tau: 163 ns (2*L)
freq.: 8.7960 GHz
field: 2890.00 G
power: 44.0 dBm
temp.: 4.20 K
1139
5
a
echo amplitude
0 1 2 3 4 5 6 7 8 9 10
tau+T (usec)

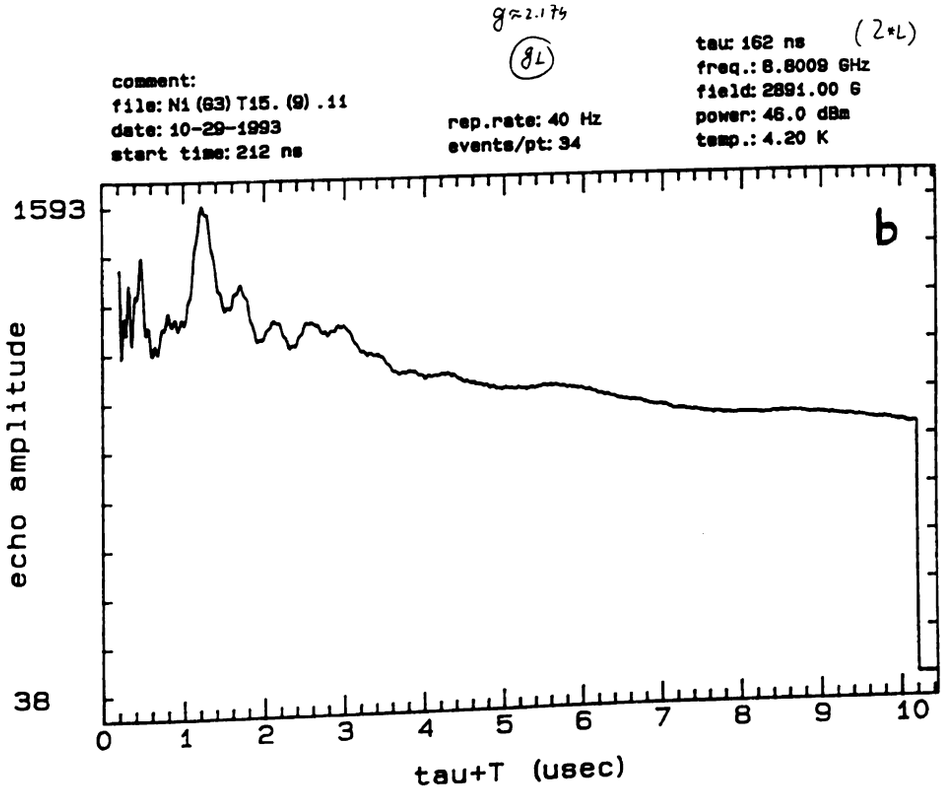
g ≈ 2.175
(g1)
comment:
file: Ni (63) T15. (9) .11
date: 10-29-1993
start time: 212 ns
rep.rate: 40 Hz
events/pt: 34
tau: 162 ns (2*L)
freq.: 8.8009 GHz
field: 2891.00 G
power: 46.0 dBm
temp.: 4.20 K
1593
38
b
echo amplitude
0 1 2 3 4 5 6 7 8 9 10
tau+T (usec)

878

echo amplitude

1

119

echo amplitude

31

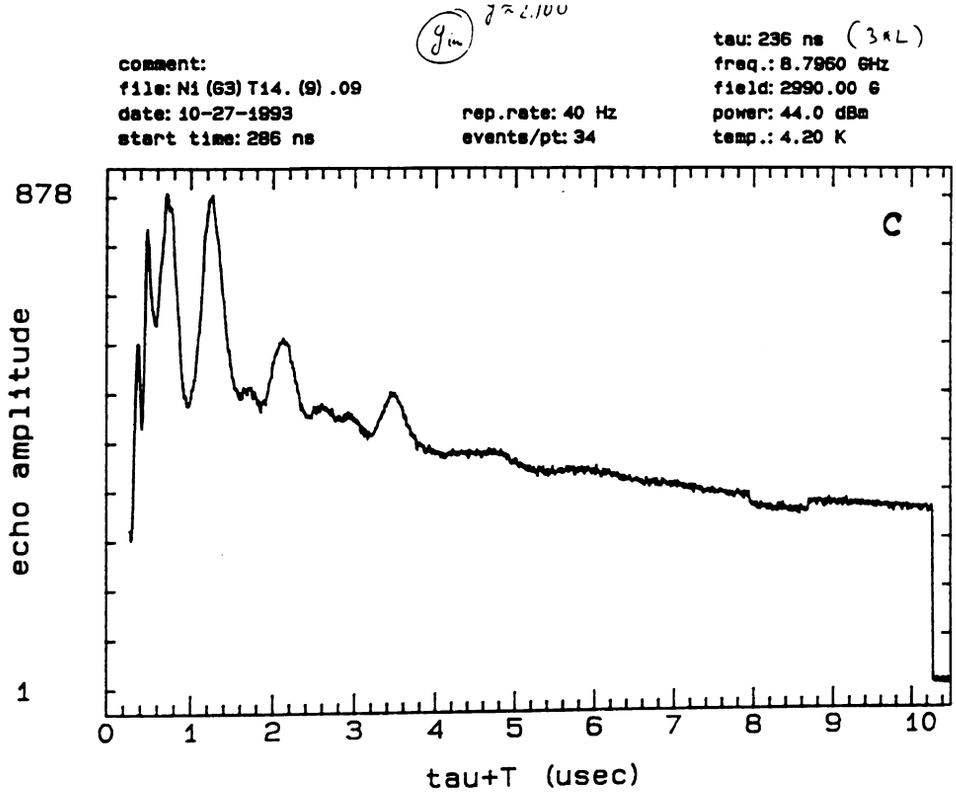
comment:
file: Ni (63) T14. (9) .09
date: 10-27-1993
start time: 286 ns
rep.rate: 40 Hz
events/pt: 34
tau: 236 ns (3*L)
freq.: 8.7960 GHz
field: 2990.00 G
power: 44.0 dBm
temp.: 4.20 K
878
1
c
echo amplitude
0 1 2 3 4 5 6 7 8 9 10
tau+T (usec)

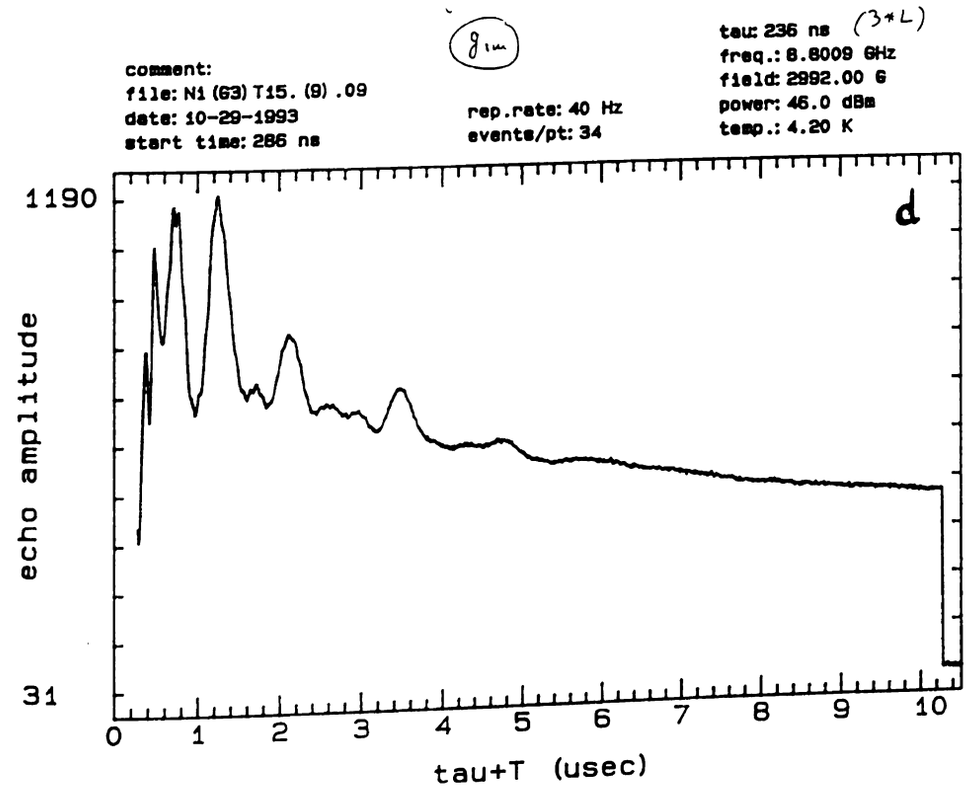
comment:
file: Ni (63) T15. (9) .09
date: 10-29-1993
start time: 286 ns
rep.rate: 40 Hz
events/pt: 34
tau: 236 ns (3*L)
freq.: 8.8009 GHz
field: 2992.00 G
power: 46.0 dBm
temp.: 4.20 K
1190
31
d
echo amplitude
0 1 2 3 4 5 6 7 8 9 10
tau+T (usec)

137

echo amplitude

-5

10

echo amplitude

31

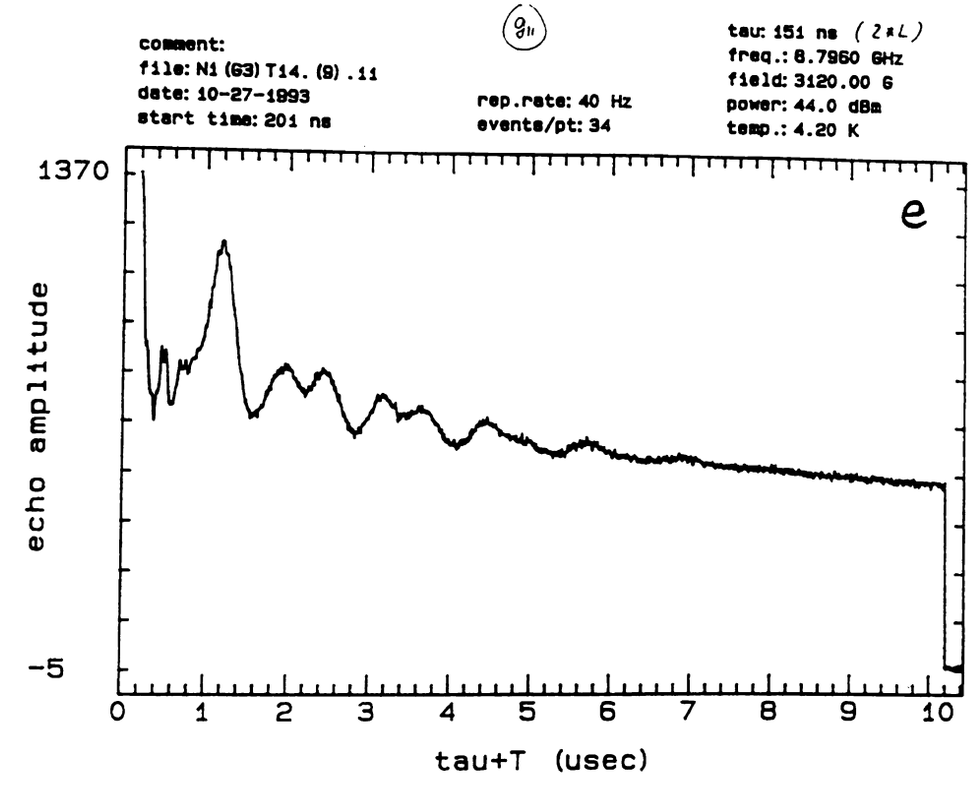
comment:
file: N1 (G3) T14. (9) .11
date: 10-27-1993
start time: 201 ns
$g_{\perp}$
rep.rate: 40 Hz
events/pt: 34
tau: 151 ns (2*L)
freq.: 8.7960 GHz
field: 3120.00 G
power: 44.0 dBm
temp.: 4.20 K
1370
-5
echo amplitude
e
0 1 2 3 4 5 6 7 8 9 10
tau+T (usec)

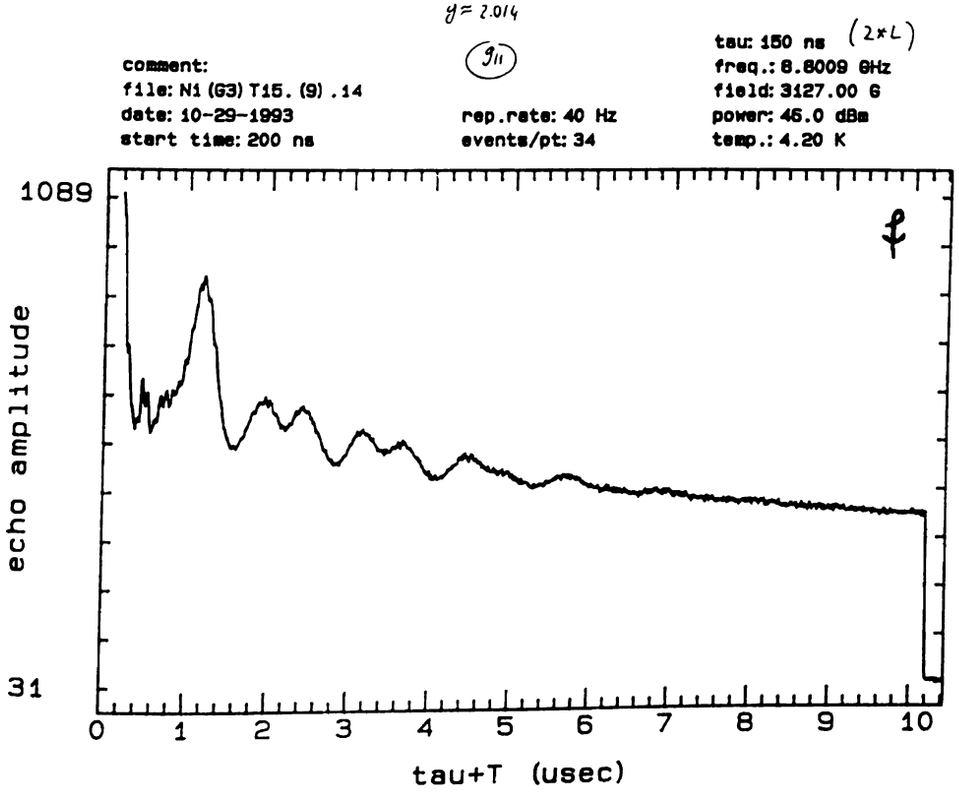
$g = 2.014$
comment:
file: N1 (G3) T15. (9) .14
date: 10-29-1993
start time: 200 ns
$g_{\perp}$
rep.rate: 40 Hz
events/pt: 34
tau: 150 ns (2*L)
freq.: 8.8009 GHz
field: 3127.00 G
power: 46.0 dBm
temp.: 4.20 K
1089
31
echo amplitude
f
0 1 2 3 4 5 6 7 8 9 10
tau+T (usec)

102

echo amplitude

5

Figure V-8.

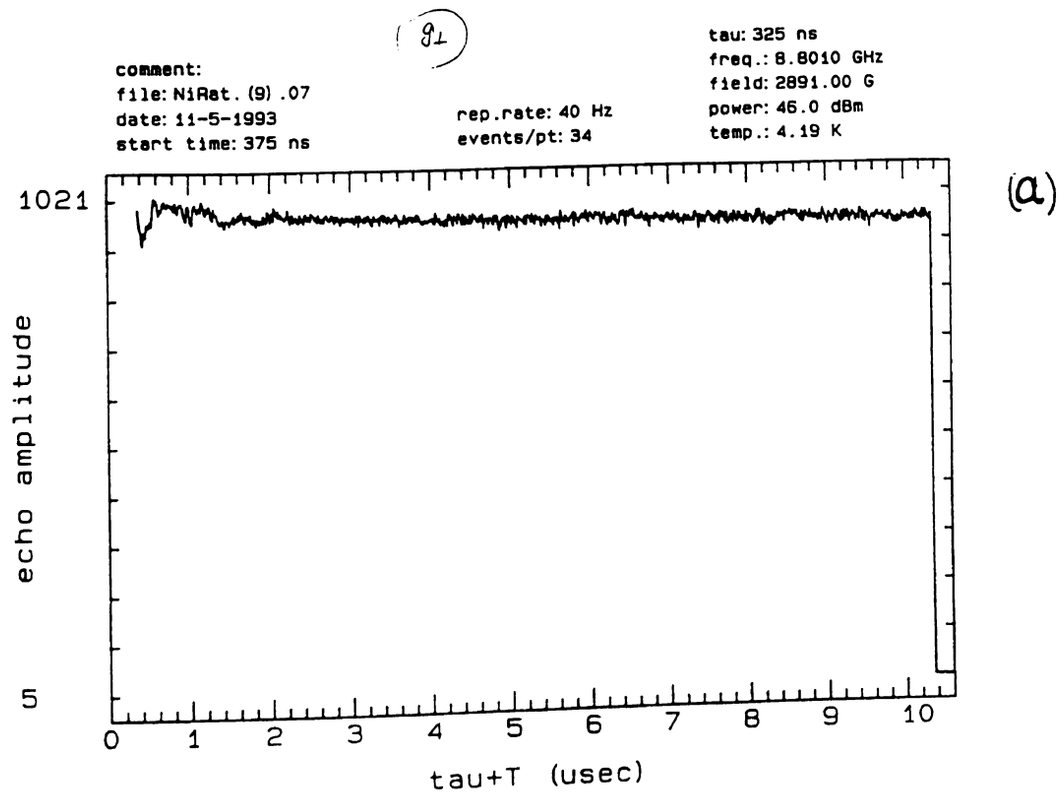

Figure V-8. ESEEM functions obtained after dividing the all-^{14}N traces by the corresponding ^{15}N traces; (a) g=2.175; (b) g=2.100; (c) g=2.014.

1065

echo amplitude

10

echo amplitude

0

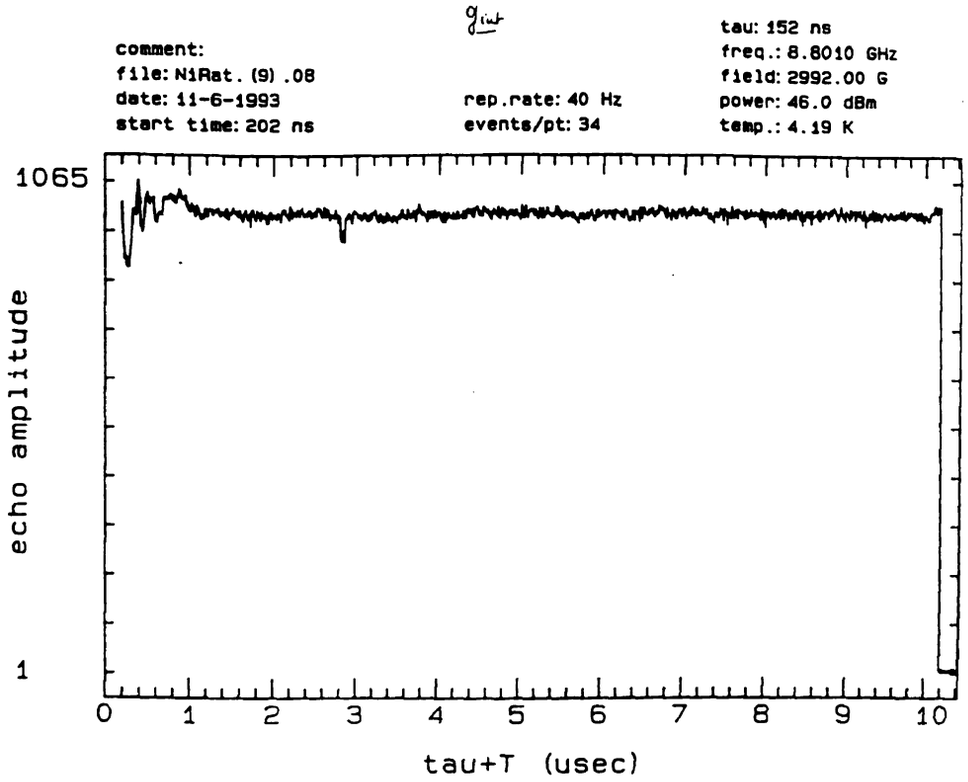
comment:
file: NiRat. (9) .08
date: 11-6-1993
start time: 202 ns
rep.rate: 40 Hz
events/pt: 34
tau: 152 ns
freq.: 8.8010 GHz
field: 2992.00 G
power: 46.0 dBm
temp.: 4.19 K
1065
1
echo amplitude
0 1 2 3 4 5 6 7 8 9 10
tau+T (usec)

(b)

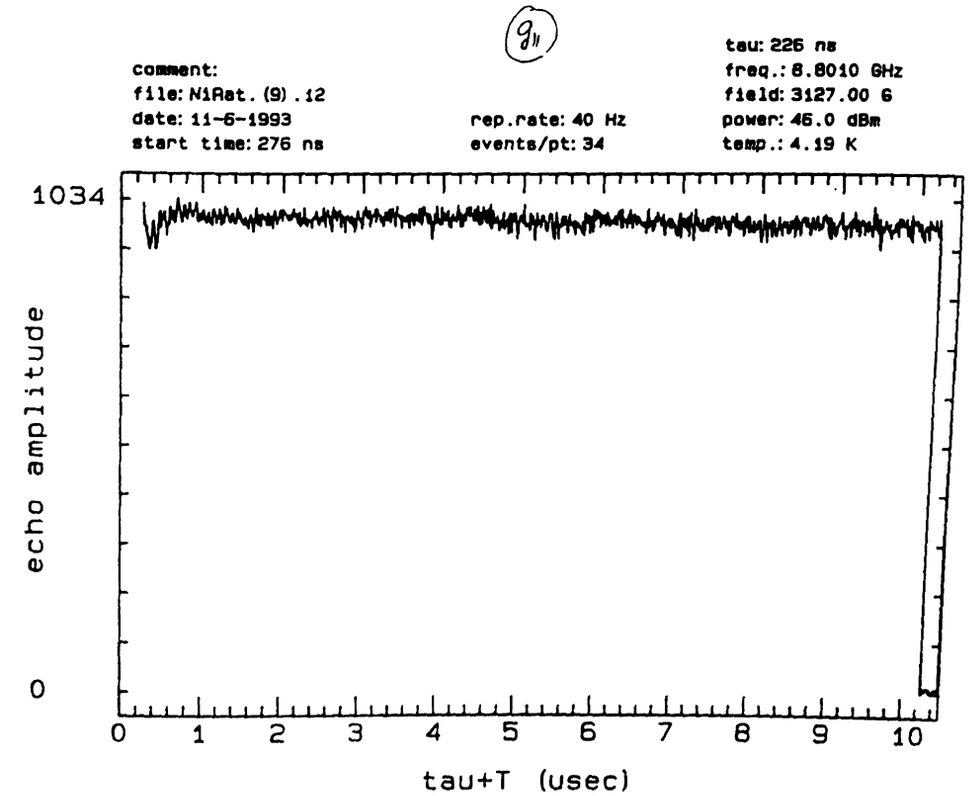
comment:
file: NiRat. (9) .12
date: 11-6-1993
start time: 276 ns
rep.rate: 40 Hz
events/pt: 34
tau: 226 ns
freq.: 8.8010 GHz
field: 3127.00 G
power: 46.0 dBm
temp.: 4.19 K
1034
0
echo amplitude
0 1 2 3 4 5 6 7 8 9 10
tau+T (usec)

(c)

is that the spi

equatorial ter

ligands. The s

in the case of

between the l

on Ni(III) ele

is that the spin density in the equatorial plane is too small at the site of the equatorial terpy nitrogen, in spite of the presence of two anionic amidate ligands. The substantial spin density (therefore strong hyperfine interaction) in the case of equatorial CN^- may be due mainly to back-bonding interaction between the ligand and the d_{z^2} orbital of Ni(III). The lack of experimental data on Ni(III) electronic structure prevents further conclusions being drawn.

1. Salerno
Jr., Ed.,
2. Marge
Nickel,
3. Slichte
Verlag
4. Lappin
1630.
5. Bossu,
6. Desid
7. Bernst
8. Jacobs
9. Maki,
1964,
10. Gord
Appli
York,
11. Ather
PTR
12. Luck
Press
13. Chap
14. Mim
15. Gerf
16. Papp
Inorg
17. Mim
Bioc

References

1. Salerno, J. C. In *The Bioinorganic Chemistry of Nickel*, Lancaster, J. R., Jr., Ed., VCH: New York, 1988; Chapter 3.

2. Margerum, D. W.; Anliker, S. L. In *The Bioinorganic Chemistry of Nickel*, Lancaster, J. R., Jr., Ed., VCH: New York, 1988; Chapter 2.

3. Slichter, C. P. *Principles of Magnetic Resonance*, 3rd ed., Springer Verlag: Berlin, 1989.

4. Lappin, A. G.; Murray, C. K.; Margerum, D. W. *Inorg. Chem.* **1978**, *17*, 1630.

5. Bossu, F. P.; Margerum, D. W. *J. Am. Chem. Soc.* **1976**, *98*, 4003.

6. Desideri, A.; Raynore, J. B. *J. Chem. Soc. Dalton Trans.* **1977**, *19*, 2051.

7. Bernstein, D. K.; Gray, H. *Inorg. Chem.* **1972**, *11*, 3035.

8. Jacobs, S. A.; Margerum, D. W. *Inorg. Chem.* **1984**, *23*, 1195.

9. Maki, A. H.; Edelskin, N.; Davison, A.; Holm, R. H. *J. Am. Chem. Soc.* **1964**, *86*, 4580.

10. Gordy, W. In *Techniques in Chemistry, Vol. XV: Theory and Applications of Electron Spin Resonance;* West, W., Ed.; Wiley: New York, 1980.

11. Atherton, N. M. *Principles of Electron Spin Resonance*, Ellis-Harwood PTR Prentice Hall: New York, 1993.

12. Lucken, E. A. C. *Nuclear Quadrupole Coupling Constants*, Academic Press: New York, 1969.

13. Chapter VI of this Dissertation.

14. Mims, W. B.; Peisach, J. *J. Chem. Phys.* **1978**, *69*, 4921.

15. Gerfen, G. J.; Singel, D. J. *J. Chem. Phys.* **1994**, *100*, 4127.

16. Pappenhagen, T. L.; Kennedy, W. R.; Bowers, C. P.; Margerum, D. W. *Inorg. Chem.* **1985**, *24*, 4356.

17. Mims, W. B.; Peisach, J. In *Advanced EPR: Applications in Biology and Biochemistry*, A. Hoff, Ed.; Elsevier: New York, 1988; Chapter 1.

Structural

VI.1. Abstra

The nitroge

measured u

and 1- and

techniques.

correlation

graphical m

prepared w

interaction

stimulated

determine

the electron

octahedral

characteriz

asymmetry

along the C

Chapter VI

Structural Characterization of Bis(aquo)tetracyano-nickelate(III), using one- and two-dimensional pulsed EPR methods

VI.1. Abstract

The nitrogen ligand hyperfine couplings of $Ni(III)(CN)_4(H_2O)_2^-$ have been measured using a combination of isotopic substitution, orientation selection, and 1- and 2-dimensional Electron Spin Echo Envelope Modulation techniques. The shapes of the contour lines obtained from hyperfine sublevel correlation spectroscopy (HYSCORE) experiments were analyzed, using the graphical method developed by Dikanov and Bowman [Ref. (25)] for samples prepared with $C^{15}N^-$. The results show an axially symmetric hyperfine interaction with $|A_{||}|=1.93$ MHz and $|A_{\perp}|=1.06$ MHz (for ^{15}N). Conventional stimulated echo experiments on ^{14}N-containing samples were done to determine the nuclear quadrupole parameters and gain further insight into the electronic structure of a Ni(III) complex in a tetragonally elongated octahedral ligand field. The cyanide ^{14}N nuclear quadrupole coupling is characterized by a quadrupole coupling constant, $e^2q_{zz}Q= 3.67$ MHz and an asymmetry parameter, $\eta=0.09$, with the principal axis of the NQI tensor being along the C-N bond.

VI.2. Introd

Hydrogena

of microorg

mechanism

biologist's p

means of p

based on th

hydrogenas

Base

spectroscop

of the H_2-b

show a cor

isotopic su

and have b

catalyticall

chemically

'unready' f

hours; Ni-

reduced to

observed a

rhombic E

VI.2. Introduction

Hydrogenases are enzymes responsible for hydrogen metabolism in a variety of microorganisms by catalyzing the reaction $H_2 \Leftrightarrow 2H^+ + 2e^-$ (1-5). The mechanism of the catalytic cycle presents an interest not only from the biologist's point of view but also in the scope of a search for an efficient means of producing hydrogen gas (6). These enzymes have been classified based on their metal content as 'iron only', Ni-Fe, and Ni-Fe-Se hydrogenases, with the Ni-Fe hydrogenases representing the largest group.

Based primarily on Electron Paramagnetic Resonance (EPR) spectroscopic data, the Ni-site in these enzymes has been postulated to be part of the H_2-binding site (1). At ambient redox potentials Ni-Fe hydrogenases show a composite of two EPR signals, which have been shown by ^{61}Ni isotopic substitution studies to originate from a Ni-based paramagnetic center and have been termed Ni-A and Ni-B (7). This oxidized state of the enzyme is catalytically inactive. To become active, the protein must be reduced chemically or by incubation under H_2. The Ni-A signal corresponds to the 'unready' form of the enzyme, whose complete activation may take several hours; Ni-B has been assigned to the 'ready' state, which can be quickly reduced to the active form. Upon reduction, a new EPR signal termed Ni-C is observed and has been attributed to a hydride complex of the Ni-center. The rhombic EPR signals Ni-A, Ni-B and Ni-C differ considerably, which

indicates ma

Ni upon rec

This

(ESEEM) stu

was accessib

same study

nucleus in t

basis of the

postulated

A rec

hydrogenas

cluster cont

data togeth

Se hydroge

shows the t

cysteinyl-su

cysteine sic

second met

molecules i

significant

revealed a

for oxidize

the nitroge

indicates major structural changes in the coordination environment of the Ni upon reduction and subsequent substrate binding.

This was demonstrated by an Electron Spin Echo Envelope Modulation (ESEEM) study on the hydrogenase of *D. gigas* showing that the nickel site was accessible to solvent only when the protein was in its Ni-C form (8). The same study showed weak magnetic hyperfine coupling with a nitrogen nucleus in the vicinity of the Ni in both the Ni-A and Ni-C forms. On the basis of the nuclear quadrupole interaction (NQI) parameters it was postulated that this nitrogen might be due to a histidine moiety.

A recent X-ray crystallographic study on the native structure of the hydrogenase from the bacterium *Desulfovibrio gigas* suggests a binuclear cluster containing Ni and Fe at the active site (9). Consideration of the X-ray data together with the results of EXAFS studies on this enzyme and on Ni-Fe-Se hydrogenases (10-12) led to a proposed structure for this binuclear site that shows the two metal ions separated by about 2.7 Å and bridged by two cysteinyl-sulfur ligands. The terminal ligands for the Ni are also provided by cysteine side chains resulting in a four-sulfur coordination for the metal. The second metal ion is most likely Fe and is bound by three putative H_2O molecules in addition to the bridging cysteines. The X-ray data also show a significant amount of disorder at this site and the EPR spectra of the crystals revealed an 85%/15% composite of the Ni-A and Ni-B signals, typically found for oxidized, inactive proteins. Although the X-ray data show no evidence for the nitrogen-based Ni ligand suggested by previous ESEEM studies of Ni-A

and Ni-C, t

be hydroge

binuclear c

The

Ni-center s

relevant st

with the m

(HFI) and

nitrogens c

methods.

hydrogena

with $g_{-} > g$

those obse

the axially

previously

ligand hyp

can be use

hydrogena

VI.3. Mate

Bis(aquo)

procedure

acid (HO

and Ni-C, the side chain of a highly conserved histidine residue, His 72, may be hydrogen bonded to one of the bridging cysteinyl sulfur atoms of the binuclear center (9), giving rise to the observed echo modulation.

The lack of knowledge of the electronic structure of the hydrogenase Ni-center serves to motivate the systematic spectroscopic investigation of relevant structural model compounds (5, 7). The present work is concerned with the measurement of nitrogen electron-nuclear hyperfine interaction (HFI) and nuclear quadrupole interaction (NQI) parameters of the ligand nitrogens of Bis(aquo)tetracyano nickelate(III) by 1- and 2-dimensional ESEEM methods. Although this compound lacks the binuclear structure of the hydrogenase Ni-site, it provides a good magnetic model for this metal center, with $g_{\perp} > g_{||}$, $g_{||}=2.01$, and ^{61}Ni hyperfine coupling constants consistent with those observed for the protein (13-16). The HFI parameters of the protons of the axially coordinated water molecules in this complex were determined previously (17, 18). These results will contribute to a foundation upon which ligand hyperfine couplings obtained by ESEEM and ENDOR spectroscopies can be used to gain insight into the electronic structure of the Ni-Fe hydrogenase active site.

VI.3. Materials and Methods

Bis(aquo) tetracyano nickelate(III) has been prepared according to literature procedures by oxidation of $Ni(II)(CN)_4$, using a 10-fold excess of hypochlorous acid (HOCl) (13, 19). After the addition of HOCl the sample was mixed with

equal volum

immediately

of the sampl

CW-EPR sp

obtained fro

Cont

Varian E-4

instrument

carried out

frequency

to calibrate

respectivel

Hyp

dimension

hyperfine

(21, 22). Fo

shape is d

an S=1/2,

of the cor

(25).

A

time-don

employe

equal volume of ethylene glycol to enhance glass formation, then frozen immediately in 4 mm outer diameter quartz EPR tubes. Ni(III) concentration of the sample was estimated to be 2mM, as judged from the intensity of its CW-EPR spectrum. $KC^{15}N$ for preparation of the ^{15}N-containing samples was obtained from Cambridge Isotope Laboratories, Ltd.

Continuous Wave (CW) EPR spectra were obtained on an X-band Varian E-4 spectrometer. Pulsed EPR studies were performed on a home-built instrument described in detail previously (20). The pulsed experiments were carried out at 4.2 K in a cryogenic immersion dewar. An EIP Model 25B frequency counter and a Micro-Now Model 515B NMR gaussmeter were used to calibrate the microwave frequency and magnetic field strength, respectively.

Hyperfine Sublevel Correlation Spectroscopy (HYSCORE) is a two dimensional ESEEM technique that reveals the correlation between the hyperfine frequencies of the opposite electron spin manifolds as cross peaks (21, 22). For disordered samples HYSCORE contour spectra show ridges whose shape is determined by the hyperfine (HFI) and NQI parameters (23, 24). For an S=1/2, I=1/2 spin system the quantitative relationship between the shape of the contour lines and principal values of the HFI tensor has been derived (25).

A four-pulse ($\pi/2$-τ-$\pi/2$-t_1-π-t_2-$\pi/2$) sequence was used to collect the 2-D time-domain HYSCORE data set. A second microwave pulse channel was employed for the π-pulse so that its width and amplitude could be controlled

independent

was 32 ns, th

being 8 time

appeared to

and maximi

step phase c

eliminate u

In th

measured a

Then t_i is i

collected (s

128x128 po

Fourier Tra

points, wit

resulting co

map (see C

using MA

also writte

Cus

out on the

data was

each possi

independently. The length (full width at half maximum) of the $\pi/2$ pulses was 32 ns, that of the π-pulse was 16 ns, with the peak power of the π-pulse being 8 times that of the $\pi/2$ pulses. The application of the narrow π-pulse appeared to be necessary to achieve efficient mixing of the hyperfine states and maximize the intensity of the cross peaks in the spectrum (22, 26). A four step phase cycle, +(0,0,0,0), +(π,π,0,0), +(0,0,π,0), +(π,π,π,0), was used to eliminate unwanted spin echoes.

In the HYSCORE experiment the amplitude of the 4-pulse echo is measured as a function of t_2, yielding one row (or "slice") of the data matrix. Then t_1 is incremented and the subsequent slices of the time-domain data are collected (see Chapter II). Time domain data presented in this paper are of size 128x128 points. The correlation contour plots have been obtained by 2-D Fast Fourier Transformation of the time-domain data with zero-filling to 512 points, without dead-time reconstruction. The absolute values of the resulting complex matrix may be represented as a 3-D plot or as a contour map (see Chapter 5). These calculations and the associated graphics were done using MATLAB. The HYSCORE simulation program called "hysline1.m" was also written in MATLAB and is included in the APPENDIX.

Customary 3-pulse (stimulated echo) ESEEM experiments were carried out on the ^{14}N-containing sample. Numerical simulation of the time domain data was based on the diagonalization of the spin Hamiltonian matrix for each possible orientation of the external field with respect to the molecule

then summ

frequency

function w

similar to t

pulse exper

graphical t

VI.4. Resul

The CW-EI

identical to

axial g-tens

splitting. H

nitrogen ar

inhomogen

Fig.

sample obt

of the EPR

perpendicu

ESEEM spe

to be along

^{14}N HFI ter

characteris

then summing all the contributions to obtain the powder average. To get frequency domain information (ENDOR like spectra), the modulation function was Fourier transformed using a dead-time reconstruction routine similar to that described by Mims (27). The simulation program for the 3-pulse experiments was written in FORTRAN and linked to MATLAB's graphical toolbox for output display and manipulation.

VI.4. Results and Discussion

The CW-EPR spectrum of a frozen solution sample of $Ni(III)(CN)_4(H_2O)_2^-$ is identical to that reported previously (13) (Figure VI-1.). The spectrum reveals axial g-tensor anisotropy with $g_\perp$=2.20, $g_{||}$=2.01 and no resolved hyperfine splitting. Hyperfine interactions between the unpaired electron and the nitrogen and hydrogen nuclei of the ligands are masked by the inhomogeneous broadening of the resonance lineshape.

Fig. VI-2a shows the 4-pulse HYSCORE spectrum of the ^{15}N-containing sample obtained at a static magnetic field value corresponding to the $g_\perp$ edge of the EPR spectrum. In this case all molecules with their $g_{||}$ axes perpendicular to the external magnetic field vector will contribute to the ESEEM spectrum (28). Taking the principal axes of the cyanide ^{15}N HFI tensors to be along their corresponding Ni-C bonds, all possible orientations of the ^{15}N HFI tensor will be sampled. The observed contour lineshape is characteristic of an axial HFI tensor (24, 25). The inhomogeneous broadening

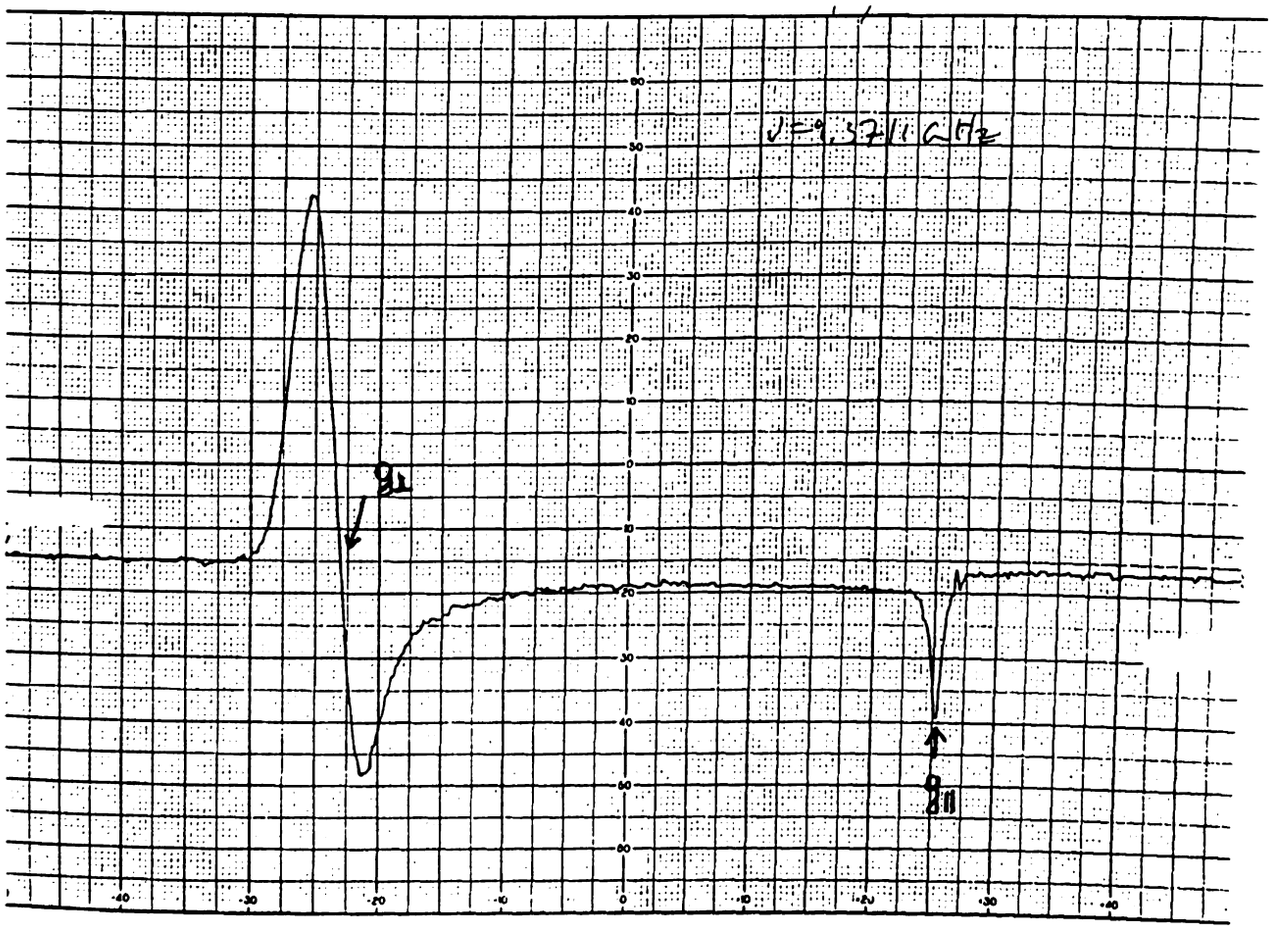

Figure VI-1. CW-EPR spectrum of $Ni(III)(CN)_4(H_2O)_2^-$.

due to the

peaks only

homogene

directions

diagonal is

Dikanov a

Fermi cont

These auth

HYSCORE

consists of

where ν_α a

spin manif

with ν_t beir

that if one

HYSCORE

due to the spread of the nuclear frequencies results in a broadening of the peaks only in the direction perpendicular to the diagonal, while the homogeneous broadening mechanism widens the lines equally in all directions (29). Thus, the linewidth of the cross-section parallel to the diagonal is purely due to homogeneous broadening. The formulas derived by Dikanov and Bowman (25) were used to extract the HFI parameters, i.e. the Fermi contact constant (A_{iso}) and the dipolar interaction constant, $T=\frac{\mu_e\mu_n}{r^3}$. These authors have shown (cf. Chapter II) that the expected lineshape of a HYSCORE contour for an S=1/2, I=1/2 spin system with an axial HFI tensor consists of two arcs, described by the equations:

$$\nu_\alpha^2=Q_\alpha\nu_\beta^2+G_\alpha \qquad \text{[VI-1a]}$$

$$\nu_\beta^2=Q_\beta\nu_\alpha^2+G_\beta \qquad \text{[VI-1b]}$$

where ν_α and ν_β are the nuclear coupling frequencies in the α and β electron spin manifolds, respectively and

$$Q_{\alpha(\beta)} = \frac{T + 2A_{iso} \mp 4\nu_L}{T + 2A_{iso} \pm 4\nu_L} \qquad \text{[VI-2a]}$$

$$G_{\alpha(\beta)} = \frac{\pm 2\nu_L (4\nu_L^2 - A_{iso}^2 + 2T^2 - A_{iso} \cdot T)}{T + 2A_{iso} \pm 4\nu_L} \qquad \text{[VI-2b]}$$

with ν_L being the nuclear Larmor frequency. It is readily seen from Eqs. [VI-1] that if one selects points along one of the two correlation ridges of the HYSCORE contour map and plots the square of frequencies ν_2 versus the

square of t

intercept o

along the r

Fig. VI-2b.

+1.317. Sol

G_y yields t

A_{iso}=±1.65

frequency-

3b). Both p

well with

independe

position. F

obtained a

absorption

the static

spectrum

inhomoger

direction p

perpendic

experimen

HFI tenso

the two pe

square of the corresponding ν_1's, a straight line with a slope of $\mathbf{Q}_\alpha$ and intercept of $\mathbf{G}_\alpha$ should be obtained. In Fig. VI-2a we show six points selected along the ridge, marked by +. The corresponding $(\nu_2)^2$ vs. $(\nu_1)^2$ plot is shown in Fig. VI-2b. The slope of the resulting straight line is -0.251, the intercept is +1.317. Solving equations [VI-2a] and [VI-2b], using these values for $\mathbf{Q}_\alpha$ and $\mathbf{G}_\alpha$ yields two possible sets of HFI parameters: $A_{iso}=\pm 1.35$ MHz, $T=\pm 0.29$ MHz; $A_{iso}=\pm 1.65$ MHz, $T=\mp 0.29$ MHz. To confirm these values we have carried out a frequency-domain numerical simulation of the HYSCORE contours (Fig. VI-3b). Both parameter sets give rise to identical simulation results that agree well with experiment (Fig. VI-3a). To distinguish between these sets, an independent HYSCORE measurement was made at a second magnetic field position. Fig. VI-3c shows the contour plot of the HYSCORE spectrum obtained at a magnetic field value corresponding to the $g_{||}$ edge of the EPR absorption envelope. In this case *only molecules with their $g_{||}$ axis parallel to the static magnetic field vector, $\mathbf{B}_0$, contribute to the "single crystal like" spectrum* (28). Indeed, the HYSCORE contour plot shows no significant inhomogeneous broadening, that is, no extra peak broadening in the direction perpendicular to the diagonal (29). Because the orientation of $\mathbf{B}_0$ is perpendicular to the hyperfine axis of the nitrogens at this field value, this experiment only measures $A_\perp=A_{iso}-T$, i.e. the perpendicular component of the HFI tensor. The observed coupling (the separation between the projections of the two peaks on either axis) is 1.05 MHz, which fixes the actual HFI

Figure VI-2

Figure VI-2. (a) HYSCORE contour plot obtained from the $g_{\perp}$ region of the $Ni(III)(C^{15}N)_4(H_2O)_2^-$ EPR spectrum. (b) Plot of the square of the correlating frequencies of the six points on the ridge, marked by +'s. The slope and intercept of the resulting straight line are explicit functions of the HFI parameters, A_{iso} and T.

$(\nu_2)^2$ (MHz^2)

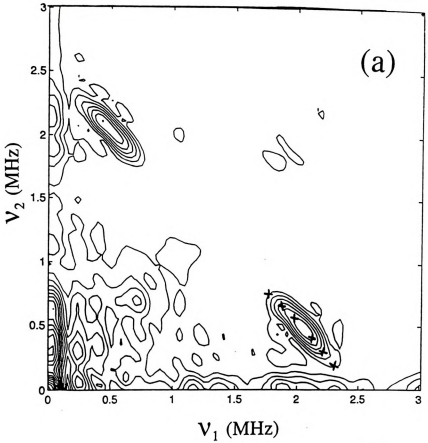
(a)
ν_2 (MHz)
ν_1 (MHz)
0
0.5
1
1.5
2
2.5
3

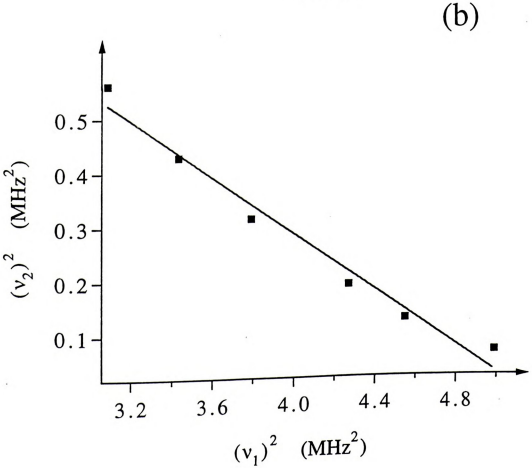
(b)
$(\nu_2)^2$ (MHz^2)
$(\nu_1)^2$ (MHz^2)
0.1
0.2
0.3
0.4
0.5
3.2
3.6
4.0
4.4
4.8

Figure VI-

Figure VI-3. (a) HYSCORE contour plot obtained at the $g_{\perp}$ edge of the EPR spectrum of Ni(III)($C^{15}N)_4(H_2O)_2^-$. Experimental conditions: resonance frequency, ν_0= 8.862 GHz; static magnetic field, $\mathbf{B_0}$=2890 G; τ=200 ns; 128x128 echo amplitudes were collected; time increment was 50 ns (b) The result of the corresponding numerical simulation. Simulation parameters: Larmor frequency of ^{15}N, ν_L=1.25 MHz; isotropic HFI constant, A_{iso}=1.35 MHz; anisotropic HFI constant, T=+0.29 MHz corresponding to an effective dipole-dipole distance, r_{eff}=3.10 Å (A_{iso}=1.65 MHz with T=-0.29 MHz gives the same result); Gaussian linewidth, 0.12 MHz. (c) HYSCORE contour plot at $g_{||}$. ν_0=8.905 GHz; $\mathbf{B_0}$=3170 G; τ=200 ns; size of data matrix, 128x128; time increment between pulses, 50 ns. (c) Simulation using ν_L=1.35 MHz; the other parameters are the same as in (b).

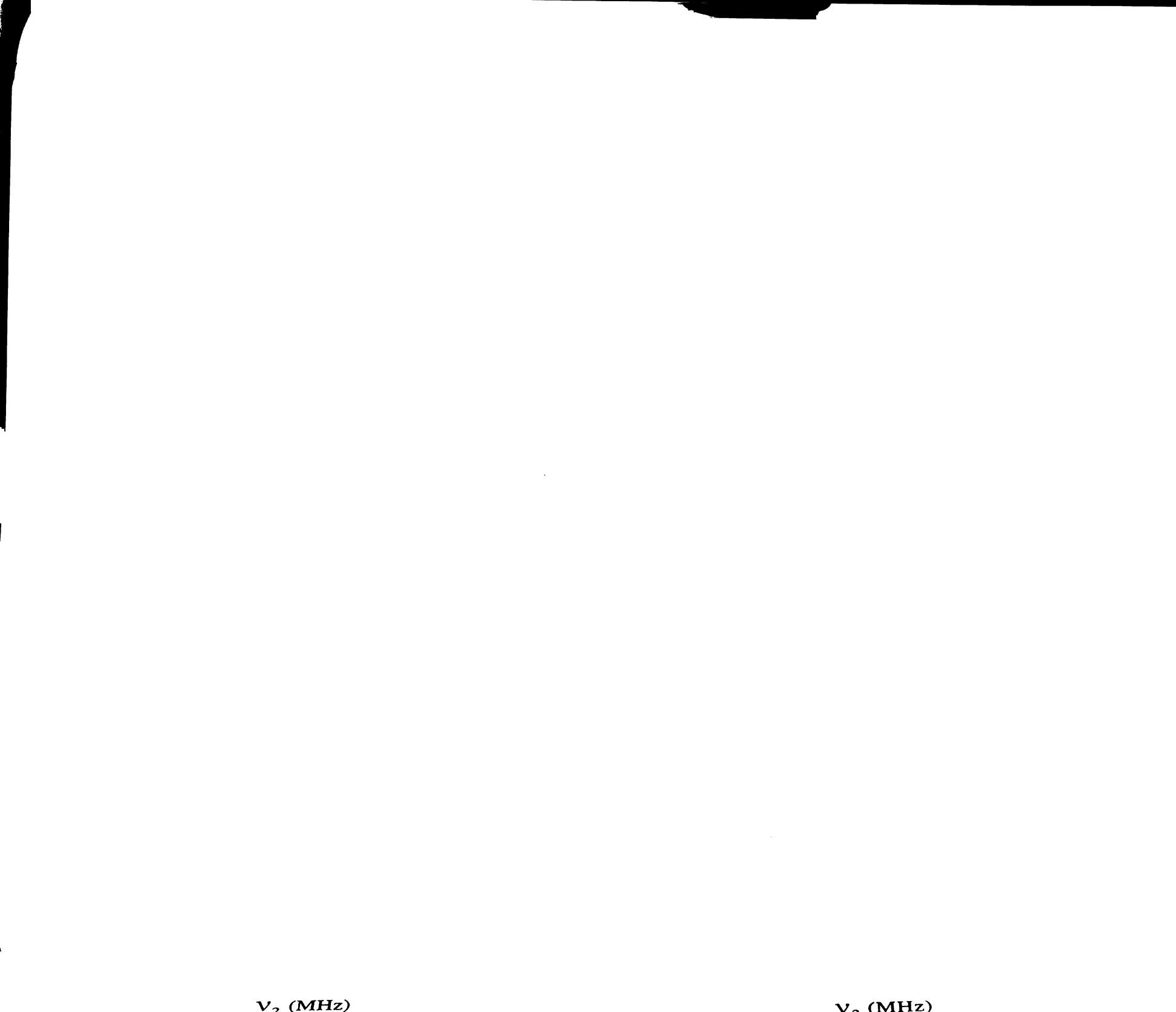
ν_2 (MHz)
ν_3 (MHz)

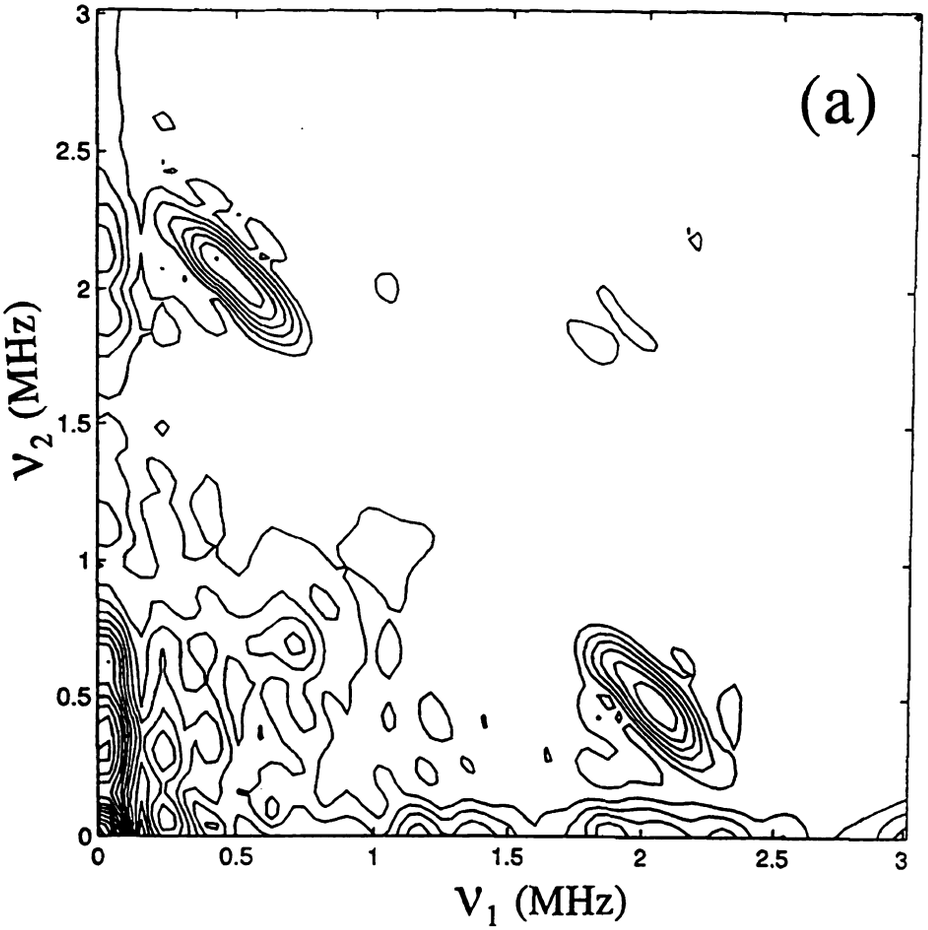
(a)
ν_2 (MHz)
ν_1 (MHz)
0
0.5
1
1.5
2
2.5
3

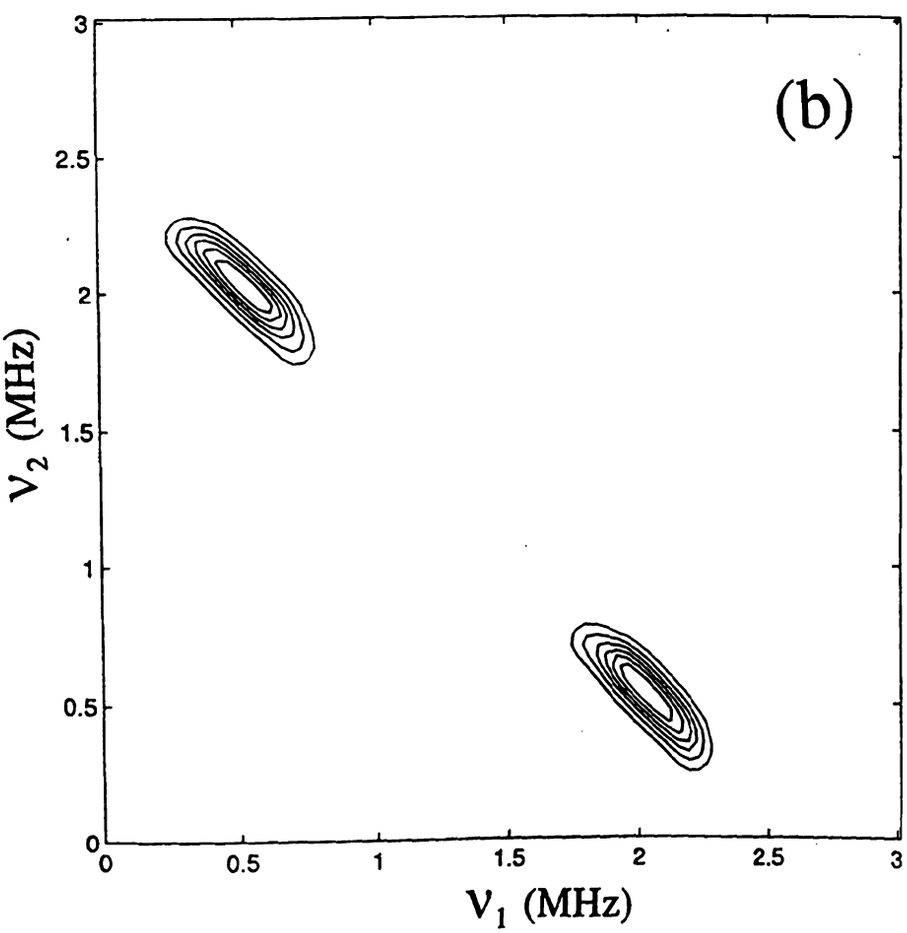
(b)
ν_2 (MHz)
ν_1 (MHz)
0
0.5
1
1.5
2
2.5
3


ν_2 (MHz)
ν_2 (MHz)

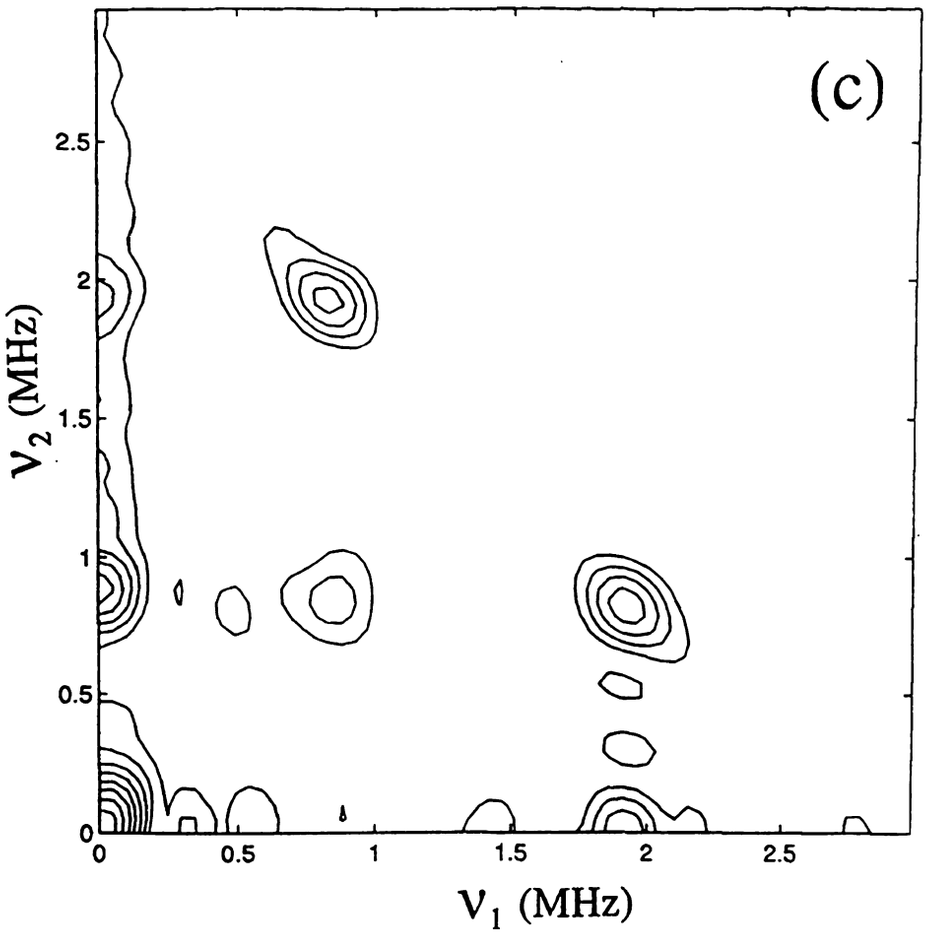
(c)
2.5
2
1.5
1
0.5
0
0
0.5
1
1.5
2
2.5
ν_2 (MHz)
ν_1 (MHz)

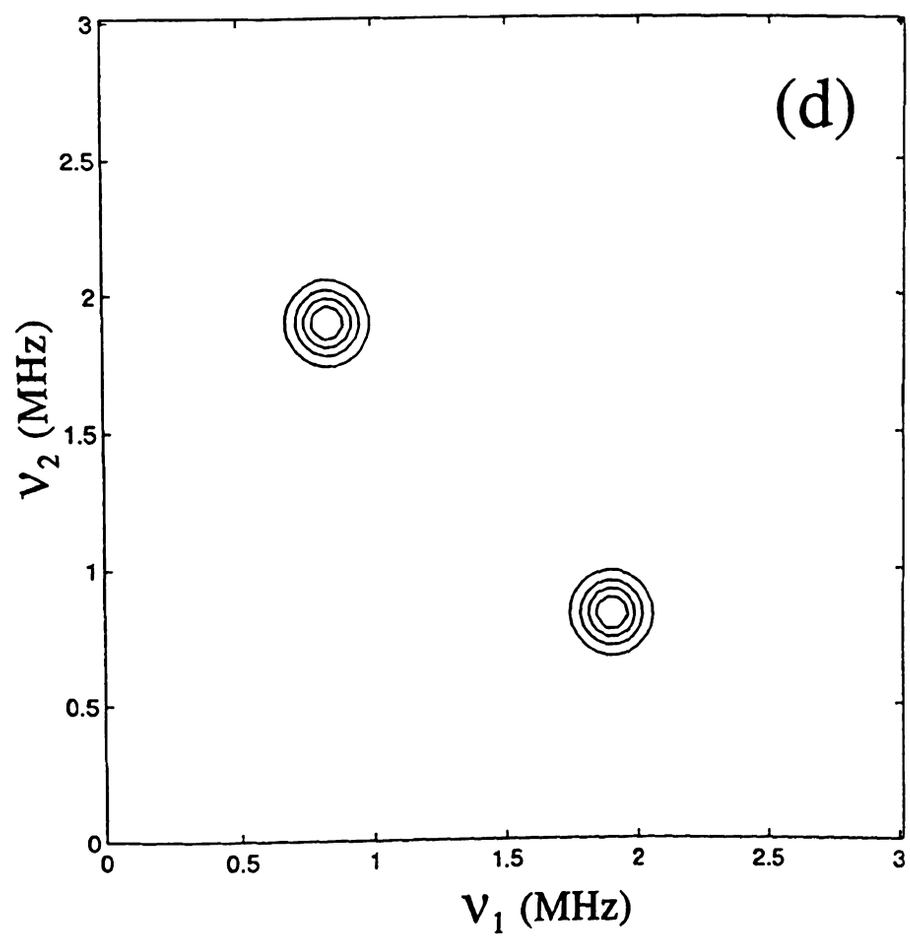
(d)
3
2.5
2
1.5
1
0.5
0
0
0.5
1
1.5
2
2.5
3
ν_2 (MHz)
ν_1 (MHz)

paramete

dipole ap

is shown

Nu

into the e

paramete

coupling

angles of

principal

the electr

paramete

nitrogen

taken at

^{15}N-ESEE

Fig. VI-4.

study we

the ratio

Ni(III)(CN

axis of th

found to

Th

MHz, wh

parameters at A_{iso}=±1.35 MHz and T=±0.29 MHz. According to the point-dipole approximation T corresponds to r_{eff}=3.10 Å. The simulated contour plot is shown in Fig. VI-3d.

Nuclear Quadrupole Interaction (NQI) parameters provide an insight into the electronic distribution about quadrupolar nuclei (e.g. ^{14}N) (30). The parameters that fully describe the NQI tensor are $e^2q_{zz}Q$, the quadrupole coupling constant, η, the asymmetry parameter, and a,b,c, the three Euler angles of the rotation matrix, which transforms the NQI tensor into the principal axis system (PAS) of the g-tensor.The q_{ii} are the principal values of the electric field gradient tensor, i=x, y, z with $\Sigma q_{ii}=0$. The asymmetry parameter is defined as $\eta=(q_{xx}-q_{yy})/q_{zz}$. The NQI parameters of the CN^- nitrogen were obtained by simulation of a series of 3-pulse ESEEM spectra taken at various fields and τ-values (separation of the first two pulses). Two ^{14}N-ESEEM spectra together with the corresponding simulations are shown in Fig. VI-4. The hyperfine coupling parameters obtained in the $C^{15}N^-$ HYSCORE study were used for the ^{14}N-ESEEM simulations after appropriate scaling by the ratio of the nuclear g-factors. The NQI parameters determined for the $Ni(III)(CN)_4(H_2O)_2^-$ were $e^2q_{zz}Q$=3.67 MHz, η=0.09 and a,b,c = 0, $\pi/2$, $\pi/2$. The z-axis of the NQI tensor (direction of the largest electric field gradient) was found to be along the C-N bond.

The NQI constants of the organic nitriles are in the range of 3.70-4.27 MHz, while the asymmetry parameters fall between 0.0046 and 0.183 (30).

Figure VI-4. (a) 3-pulse ESEEM spectra of $Ni(III)(CN)_4(H_2O)_2^-$ at $g_\perp$. Experimental conditions: $\mathbf{B_0}$=2866 G; τ=164 ns; ν_0=8.838 GHz; (b) Result of the corresponding numerical simulation using the following parameters: A_{iso}=0.90 MHz (scaled for ^{14}N from A_{iso}=1.35 MHz of ^{15}N by the ratio of the nuclear g-values); r_{eff}=3.10 Å; polar and azimuthal angles specifying the orientation of the principal axis of the axial HFI tensor with respect to the $g_{||}$ axis, $\pi/2$, 0; $e^2q_{zz}Q$=3.67 MHz; η=0.09; Euler angles that rotate the principal axis system (PAS) of the NQI tensor into the PAS of the g-tensor, 0, $\pi/2$, $\pi/2$. (c) 3-pulse ESEEM spectra of $Ni(III)(CN)_4(H_2O)_2^-$ at $g_{||}$. Experimental conditions: $\mathbf{B_0}$=3135 G; ν_0=8.838 GHz; τ=149 ns. (d) Simulated spectrum. Simulation parameters for HFI and NQI are the same as for (b).

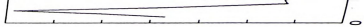

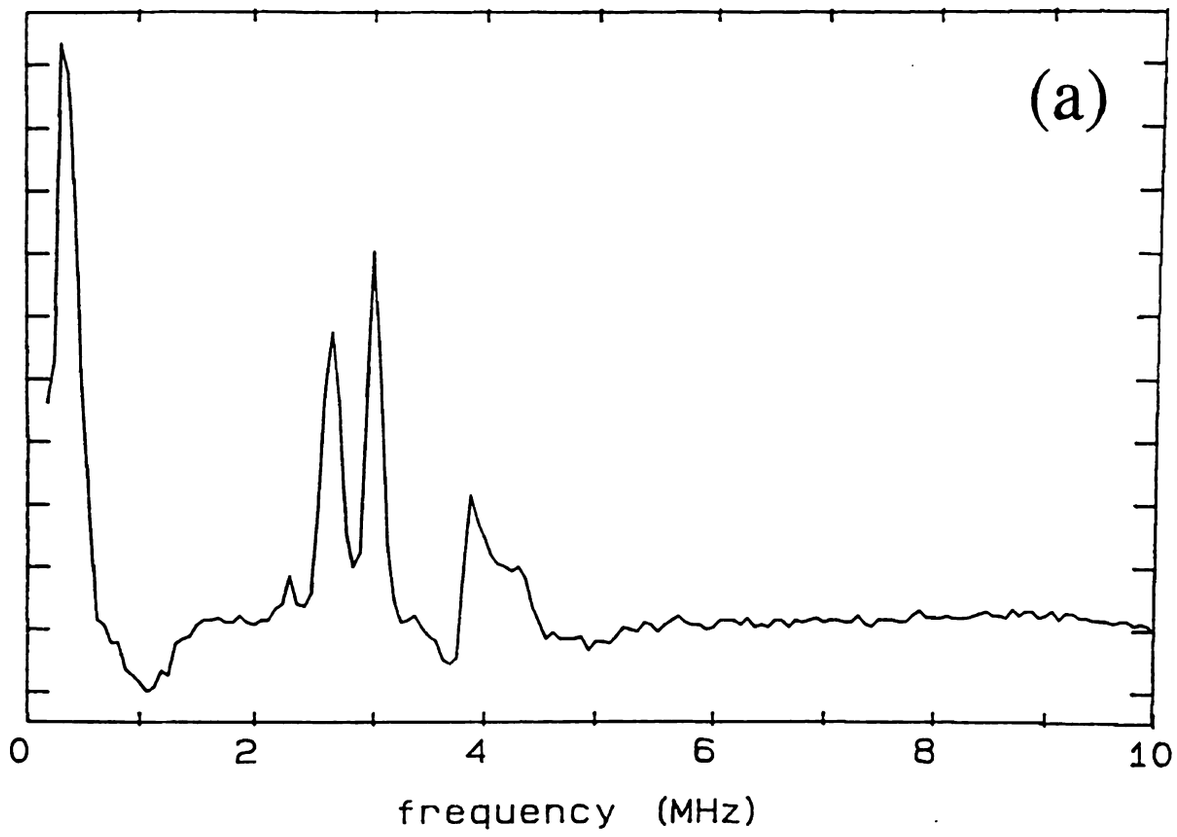
(a)
0
2
4
6
8
10
frequency (MHz)

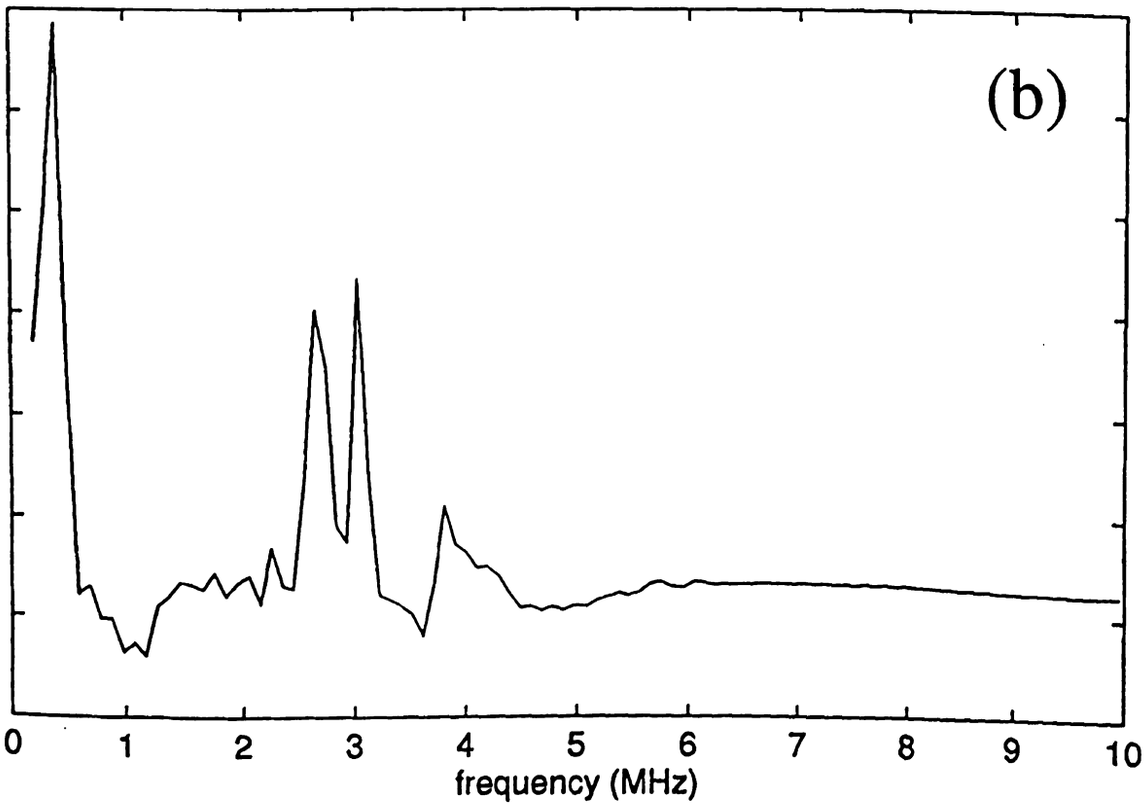
(b)
0
1
2
3
4
5
6
7
8
9
10
frequency (MHz)

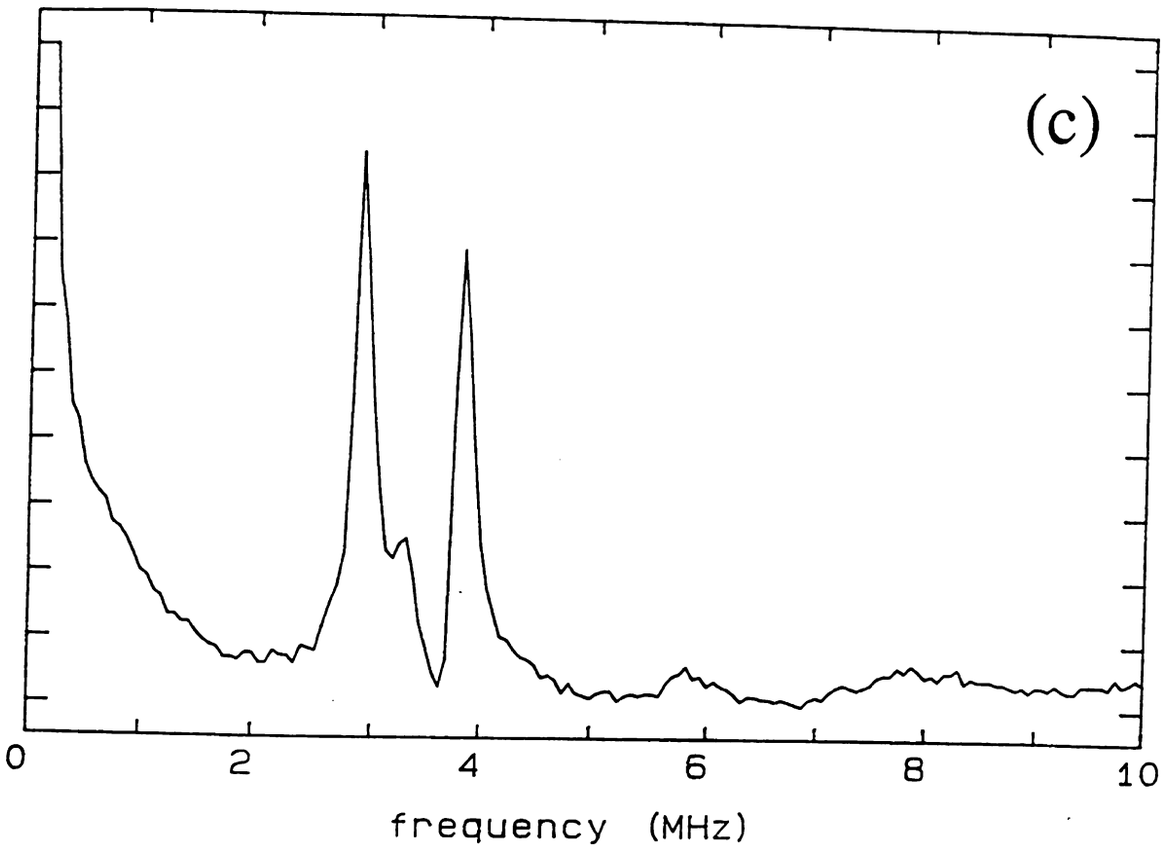
(c)
0
2
4
6
8
10
frequency (MHz)

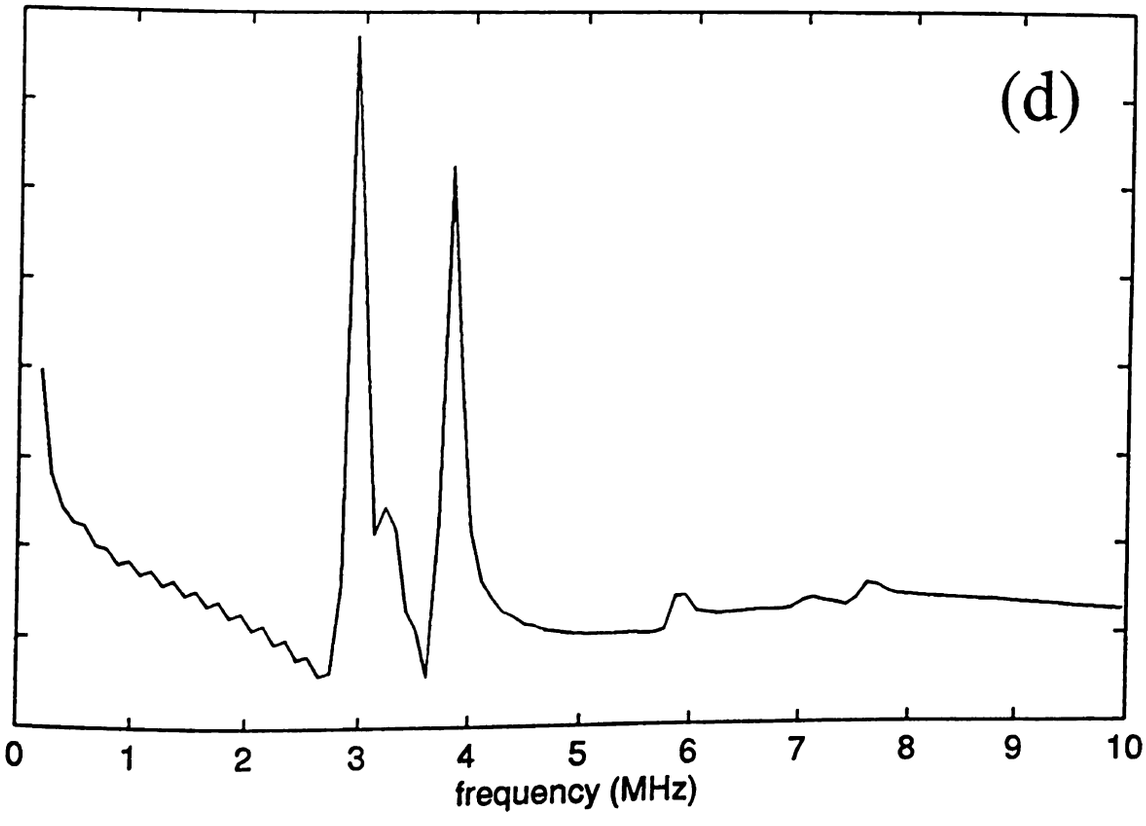
(d)
0
1
2
3
4
5
6
7
8
9
10
frequency (MHz)

For exar

MHz an

expected

NQI par

electron

$e^2q_{zz}Q=3$

the five-

distribut

symmetr

sample,

located i

asymme

VI.5. Co

This wor

large g-t

ESEEM r

determir

orientatio

allows o

insight ir

from the

For example, the parameters for HCN in the solid state at 77 K, are $e^2q_{zz}Q$=4.02 MHz and η=0.0085 (31). Due to the axial symmetry of HCN the value of η is expected to be close to 0. Wang and de Boer have determined the HFI and NQI parameters of coordinated CN^- in $Fe(CN)_6^{3-}$, using pulsed EPR and electron nuclear double resonance (ENDOR) techniques (32). They obtained $e^2q_{zz}Q$=3.84 MHz, η=0.00. $Fe(CN)_6^{3-}$ is a low-spin $3d^5$ complex (S=1/2), where the five-electron configuration can be treated as a positive hole equally distributed between d_{xz}, d_{yz}, and $d_{x^2-y^2}$ orbitals. These orbitals are located symmetrically with respect to the CN^- ligands, thus η=0 is expected. In our sample, however, the presence of the Ni(III) ion with the unpaired electron located in the d_{z^2} orbital breaks this axiality, resulting in a relatively large asymmetry parameter for cyanide (33).

VI.5. Conclusion

This work details the application of HYSCORE to a disordered sample with large g-tensor anisotropy. The results demonstrated the power of this 2-D ESEEM method in that the HFI coupling constants could be accurately determined without numerical simulation. For $Ni(III)(CN)_4(H_2O)_2^-$ the orientation selection of the pulsed experiment due to the Ni(III) g-anisotropy allows one to make unambiguous assignment of the HFI parameters. Further insight into the electronic structure of the Ni(III) complex may be obtained from the Nuclear Quadrupole Interaction (NQI) tensor. The ^{14}N NQI

parame

an e^2q_{zz}

distribu

parameters determined by numerical simulation of 3-pulse ESEEM data show an $e^2q_{zz}Q$ value typical for CN^- and an asymmetry parameter that reflects the distribution of electrons in the d-orbitals of the Ni ion.

1. I
M
2. F
3. F
4. F
5. F
6. B
B
7. M
R
8. C
F
9. V
Fo
10. H
D
26
11. Ei
J.;
19
12. So
13. Pa
14. Ko
H.
15. All
16. Mo
Du
Le

References

1. Lancaster, J. R., Jr., Ed. *The Bioinorganic Chemistry of Nickel*; VCH: New York, 1988.

2. Kolodziej, A. F. *Prog. Inorg. Chem.* **1994**, *41*, 493.

3. Kovács, J. A. *Adv. Inorg. Biochem.* **1994**, *9*, 173.

4. Hausinger, R. P. *Biochemistry of Nickel*; Plenum: New York, 1993.

5. Halcrow, M. A.; Christou, G. *Chem. Rev.* **1994**, *94*, 2421.

6. Benemann, J. R. *Proc. 10th World Hydrogen Energy Conf.* (Cocoa Beach, Florida; 1994).

7. Moura, J. J. G.; Moura, I.; Teixeira, M.; Xavier, A. V. in Nickel and its Role in Biology; *Met. Ions Biol. Systems* **1988**, *23*, 285.

8. Chapman, A.; Cammack, R.; Hatchikian, C. E.; McCracken, J.; Peisach, J. *FEBS Lett.* **1988**, *242*, 134.

9. Volbeda, A.; Charon, M-H.; Piras, C.; Hatchikian, E. C.; Frey, M.; Fontecilla-Camps, J. C. *Nature* **1995**, *373*, 580.

10. He, S. H.; Teixeira, M.; LeGall, J.; Patil, D. S.; Moura, I.; Moura, J. J. G.; DerVartanian, D. V.; Huynh, B. H.; Peck, H. D., Jr. *J. Biol. Chem.* **1989**, *264*, 2678.

11. Eidsness, M. K.; Scott, R. A.; Prickril, B. C.; DerVartanian, D. V.; LeGall, J.; Moura, I.; Moura, J. J. G.; Peck, H. D., Jr. *Proc. Natn. Acad. Sci. U. S. A.* **1989**, *86*, 147.

12. Sorgenfrei, O.; Klein, A.; Albracht, S. P. J. *FEBS Lett.* **1993**, *332*, 291.

13. Pappenhagen, T. L.; Margerum, D. W. *J. Am. Chem. Soc.* **1985**,*107*, 4576.

14. Kojima, N.; Fox, J. A.; Hausinger, R. P.; Daniels, L.; Orme-Johnson, W. H.; Walsh, C. *Proc. Natl. Acad. Sci. U. S. A.* **1983**, *80*, 378.

15. Albracht, S. P. J.; Graf, E. G.; Thauer, R. K. *FEBS Lett.* **1982**, *140*, 311.

16. Moura, J. J. G.; Moura, I.; Huynh, B. K.; Krüger, H. J.; Teixeira, M.; DuVarney, R. C.; DerVartanian, D. V.; Xavier, A. V.; Peck, H. D., Jr.; LeGall, J. *Biochem. Biopys. Res. Commun.* **1982**, *408*, 1388.

17. L
18. M
19. W
C
20. M
21. H
19
22. G
8
23. S
9
24. H
25. D
26. H
E
P
27. M
28. H
1
29. P
2
30. L
P
31. N
32. W
33. T

17. Lee, H-I.; McCracken, J. *J. Phys. Chem.* **1994**, *98*, 12861.

18. McCracken, J.; Friedenberg, S. *J. Phys. Chem.* **1994**, *98*, 467.

19. Wang, Y. L.; Beach, M. W.; Pappenhagen, T. L.; Margerum, D. W. *Inorg. Chem.* **1988**, *27*, 4464.

20. McCracken, J.; Shin, D. H.; Dye, J. L. *Appl. Magn. Reson.* **1992**, *3*, 305.

21. Höfer, P.; Grupp, A.; Nebenführ, H.; Mehring, M. *Chem. Phys. Lett.* **1986**, *132*, 279.

22. Gemperle, C.; Aebli, G.; Schweiger, A.; Ernst, R. R. *J. Magn. Reson.* **1990**, *88*, 241.

23. Shane, J. J.; Höfer, P.; Reijerse, E. J.; DeBoer, E. J. *J. Magn. Reson.* **1992**, *99*, 596.

24. Höfer, P. *J. Magn. Reson.*, **1994**, *Series A 111*, 77.

25. Dikanov, S. A.; Bowman, M. K. *J. Magn. Reson.* **1995**, *Series A 116*, 125.

26. Höfer, P. In *Electron Magnetic Resonance of Disordered Systems EMARDIS-91*; Yordanov, N. D., Ed.; World Scientific: Singapore, 1991; pp. 1-15.

27. Mims, W. B. *J. Magn. Reson.* **1984**, *59*, 291.

28. Hoffman, B. M.; Martinsen, J.; Venters R. A. *J. Magn. Reson.* **1984**, *59*, 110.

29. Pöppl, A.; Böttcher, R.; Völkel, G. *J. Magn. Reson.* **1996**, *Series A 120*, 214.

30. Lucken, E. A. C. *Nuclear Quadrupole Coupling Constants*, Academic Press: New York, 1969.

31. Negita, H.; Casabella, P. A.; Bray, P. J. *J. Chem. Phys.* **1960**, *32*, 314.

32. Wang, D. M.; deBoer, E. *J. Chem. Phys.* **1990**, *92*, 4698.

33. Townes, C. H.; Dailey, B. P. *J. Chem. Phys.* **1949**, *17*, 782.

VII.1. A

The ver

example

because

limitatio

data poi

Gd^{3+} to

HYSCO

Bowmar

(-0.8, -3.

Warncke

the appl

Th

HYSCO

brief intr

which is

Then a r

we prese

Chapter VII

HYSCORE Study on a Tyrosyl Model System

VII.1. Abstract

The very slow relaxation of tyrosyl radicals at low temperatures (4.2 K, for example) makes pulsed EPR experiments on them rather difficult to perform, because usually we cannot use sampling rate higher than ca. 10 Hz. This limitation makes HYSCORE impossible to use, due to the large number of data points to be collected. We have overcome this problem by adding 5 mM Gd^{3+} to the sample.

HYSCORE data were analyzed using the graphical method of Dikanov and Bowman [Ref. (33)]. The principal values of the HFI tensor are found to be (-0.8, -3.1, -3.6) (MHz), which are reasonably close to the values found by Warncke and McCracken using 1D ESEEM [Ref. (31)]. The work demonstrates the applicability of the 2D ESEEM to cases of rhombic hyperfine interactions.

The work presented in this Chapter presents an application of HYSCORE to a randomly oriented sample with *rhombic HFI tensor*. First, a brief introduction to the biologically essential tyrosyl radicals is presented, which is followed by a summary of the general properties of *radical enzymes*. Then a review of the most relevant EPR spectroscopic studies is given. Lastly, we present the results and discussion of our HYSCORE study.

VII.2. In

Amino a

growing

variety

(PS II) (3

and in a

oxidize.

NHE (7

catalysis

thiyl rac

to oxidi

to have

been fou

R

non-spe

radicals

has beer

aging p

to be th

biologic

class fla

primari

VII.2. Introduction

Amino acid radicals are known as essential participants in the reactions of a growing number of enzymes (1, 17). Tyrosyl radicals have been found in a variety of enzymes: in Ribonucleotide Reductase (RNR) (2), Photosystem II (PS II) (3), Prostaglandin H Synthase (PGHS) (4), Galactose Oxidase (GOase) (5) and in amine oxidases (6). Of the 20 amino acids, tyrosine is the easiest to oxidize. In aqueous solution at pH 7 it has a redox potential of +930 mV vs. NHE (7); this may partially account for its widespread occurrence in enzyme catalysis. Cysteine has a similar redox potential (8). It can be oxidized to its thiyl radical form but is rapidly oxidized further by O_2. Tryptophan is also easy to oxidize; it has a redox potential of +1.05 V vs. NHE (7) and has been shown to have an important function in cytochrome c peroxidase (9). Glycine has been found to give rise to a radical in pyruvate formate lyase (10).

Radicals in biology can be classified in two groups: radicals involved in non-specific chemistry (which is ultimately deleterious to the cell) and radicals that are *essential* for certain enzymes. Destructive radical chemistry has been recognized for a considerable time and has been associated with the aging process and cell death (11). Radicals originating from O_2 are considered to be the principal reactants in these processes. Radicals essential for proper biological function have been recognized somewhat more recently. In this class flavin, quinone and chlorophyll radicals have been discovered first (12), primarily because they are relatively stable due to their low redox potentials

1.F

- C

exa

del

- B

exa

-O

exa

2.F

- N

su

- N

3.I

Figure

Metallo-Radical Enzymes

1.Families

- Glycyl/Thiyl radical enzymes

examples: pyruvate formate lyase, anaerobic RNR, clostridial diol dehydratase;

- B_{12}-dependent radical enzymes

examples: glutamate mutase, ethanolamine ammonia lyase;

-O_2-dependent radical enzymes

examples: galactose oxidase, RNR;

2.Functional and Structural Principles

- Metal catalyzes radical formation, radical abstracts H atom from substrate
- Metal cluster/radical/substrate usually in close physical proximity

3.Example: O_2-dependent radical enzymes

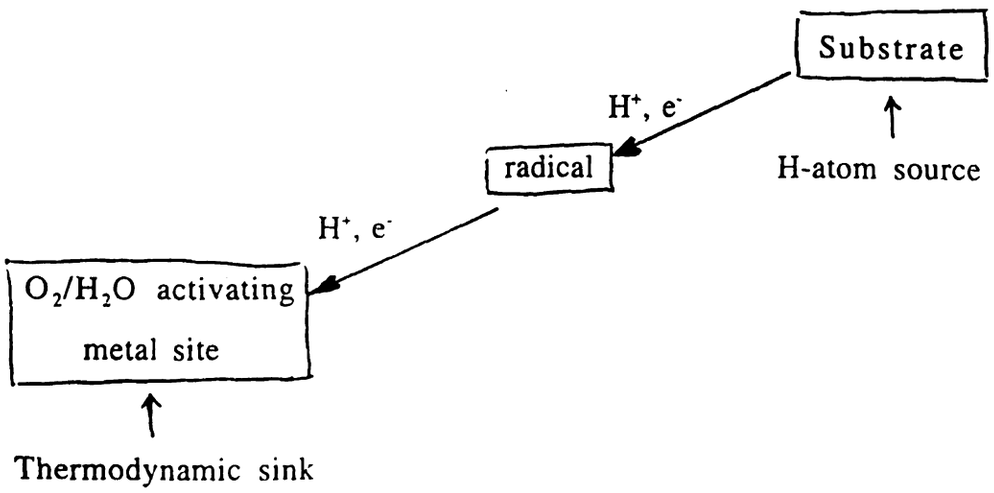

Figure VII-1. Summary of various properties of metallo-radical enzymes.

(-200 to

spectro

the RN

their de

during

trappin

excepti

radicals

VII.3. I

Figure

enzyme

Cu, Co

active c

to that

referred

divided

depend

commo

Functio

in turn

Though

(-200 to +400 mV vs. NHE) and thus can be detected by conventional spectroscopic methods.

The first catalytically essential amino acid radical, the tyrosyl radical in the RNR from *E. coli* , was only discovered in the 1970s (13). The reason for their delayed discovery lies in that they typically occur as transient species during the catalytic cycle and more sophisticated spectroscopic and/or trapping methods are required to detect and characterize them. There are exceptions, such as the Y_{122} in RNR or Y_D in PS II, both of which are stable radicals.

VII.3. Functional and Structural Properties of Radical Enzymes

Figure VII-1 summarizes some generalizations of the properties of radical enzymes (1). Firstly, these enzymes generally contain a metal - typically Fe, Cu, Co or Mn (14). When the metal does not occur it is replaced by redox active cofactors such as S-adenosyl methionine, whose function is analogous to that of the metal. In spite of these exceptions, radical proteins are also referred to as "metallo-radical enzymes". Secondly, these enzymes can be divided into three different families, namely the glycyl/thiyl group, the B_{12}-dependent group and the O_2-dependent group. Thirdly, these enzymes have common structural and functional principles across these families. Functionally the metal center acts to generate the amino-acid radical, which in turn initiates catalysis by abstracting a hydrogen atom from the substrate. Though there are modifications to this principle, the general scheme *"metal*

generat

valid.

scheme

channe

metallo

and ge

thermo

radical

in initi

VII.4. E

Galacto

fungal

aldehyd

reaction

copper

water c

tyrosin

position

active,

antiferr

generates radical and radical initiates catalysis by H-atom abstraction" remains valid. This functional generalization is accompanied by a related structural scheme: the metal, the redox-active side chain and the substrate-binding channel all are physically close in the enzyme structure.

Figure VII-1 gives one example of the operation of the O_2-dependent metallo-radical enzymes. In this family the role of the metal site is to bind O_2 and generate activated metal-bound oxygen species, which serve as a thermodynamic sink to provide oxidizing power to generate the amino acid radical. Once generated, the radical then uses the substrate as a H-atom source in initiating the catalysis.

VII.4. Example: Galactose Oxidase (GOase)

Galactose Oxidase (GOase) is an extracellular, type II copper protein (68 kDa) of fungal origin (15). It catalyzes the oxidation of several primary alcohols to aldehydes with the concomitant reduction of O_2 to H_2O_2, via a two-electron reaction. The crystal structure of GOase (16) reveals a unique mononuclear copper site with two histidine imidazoles, two tyrosines, and an exogenous water or acetate in a *distorted square-pyramidal* coordination. The equatorial tyrosine is covalently linked to a cysteine residue by a C-S bond at the *ortho* position from the OH group (Figure VII-2).

The enzyme exists in three well defined and stable oxidation states: the active, oxidized form is EPR silent, suggesting that the Cu^{2+} ion is *antiferromagnetically coupled* to the free radical. The intermediate form of

the en

center:

The en

forms

specifi

molecu

removi

Figure

radical

oxidati

mechar

conditi

VII.5. E

EPR ha

radical

effective

which

inhomo

ENDO

are usu

the enzyme shows a Cu^{2+} EPR signal, while the reduced form contains a Cu^{+} center:

$$Cu^{2+}\text{-}Tyr^{\cdot+} \overset{e^-}{\Leftrightarrow} Cu^{2+}\text{-}Tyr \overset{e^-}{\Leftrightarrow} Cu^{+}\text{-}Tyr$$

The enzyme can readily be interconverted between the active and the inactive forms in a redox titration using ferri/ferrocyanide solution (5, 15). The specificity of the enzyme for primary alcohols is low, ranging from small molecules to polysaccharides (18). On the other hand, GOase is stereospecific removing the pro-S methylene hydrogen of the C-6 alcohol in galactose.

The mechanistic scheme for the catalytic cycle of GOase is shown in Figure VII-3. Two electrons are transferred from the substrate, one to the free radical and one to the cupric ion. The O_2 then restores the active form by oxidation of the cuprous center and the modified tyrosine. In the proposed mechanism, the aldehyde release precedes O_2 reduction. Under anaerobic conditions, galactose is oxidized into aldehyde and the Cu(I) state is stable.

VII.5. EPR Spectroscopic studies of tyrosyl radicals

EPR has proven to be the most informative spectroscopy to study the tyrosyl radical in both biological and model systems. Since the tyrosyl radicals are *effectively immobilized* in proteins, they give rise to powder EPR spectra, in which small hyperfine couplings are not resolved, due to the inhomogeneous line broadening. As a result, besides the customary CW-EPR, ENDOR and pulsed EPR spectroscopies together with specific isotopic labeling are usually necessary to obtain hyperfine information.

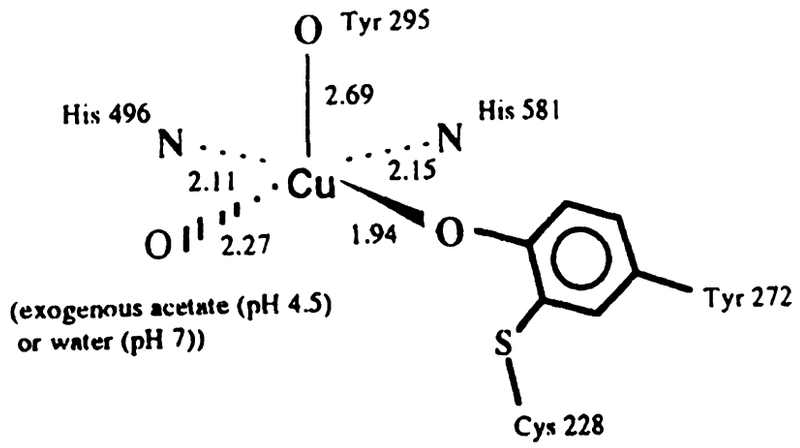

Figure VII-2. The active site of Galactose Oxidase [from Ref. (17)].

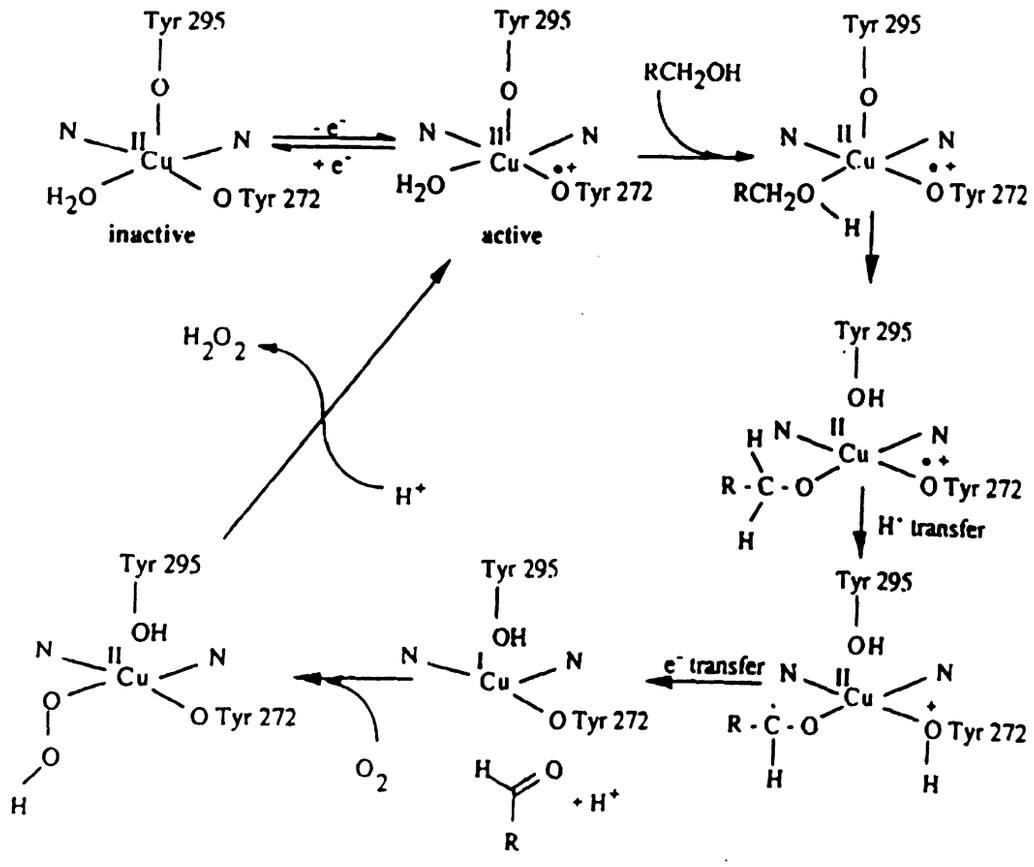

Figure VII-3. A proposed catalytic cycle of Galactose Oxidase

[from Ref. (17)].

ENDO

hyperfi

and 3,5

CH_2 pr

electron

bonds v

relation

where

unpair

dihedra

(19).

various

2,6 pro

positio

all tyro

been fo

the phe

ENDOR has been found to be particularly useful in determining the hyperfine tensor components for various hydrogens. The α-protons at the 2,6 and 3,5 ring positions are characterized by rhombic HFI tensors, while each β-CH_2 proton is characterized by an axial tensor, which reports on the unpaired electron spin density on Carbon-1 as well as on the *dihedral angle of the C-H bonds* with respect to the p_z orbital of C-1, in accordance with the well-known relation,

$$A_\beta=\rho_{C\text{-}1}(B_0+B_2\cos^2\theta),$$

where A_β is the isotropic hyperfine coupling to the β-proton, $\rho_{C\text{-}1}$ is the unpaired electron density at Carbon-1, $B_0 \cong 0$ MHz, B_2 = 162 MHz, θ is the dihedral angle of the C-H bond of the β-proton relative to the p_z orbital of C-1 (19).

TABLE VII-1 summarizes the hyperfine tensors for tyrosyl radicals in various enzymes and in two model systems. In general, the coupling to the 2,6 protons is relatively weak, reflecting low unpaired spin density at these positions. The 3,5 and the methylene protons are more strongly coupled. For all tyrosyl radicals studied thus far, the same basic pattern of spin densities has been found (Fig. VII-4).

ENDOR can also be valuable in characterizing *the hydrogen bonding to the phenol oxygen* (20, 27). It has been shown that in the Y_D tyrosine of PS II

TABLE V

Atom/Pos
H 3,5 x
H 3,5 y
H 3,5 z
H 2,6 x
H 2,6 y
H 2,6 z
H meth ∥
H meth ⊥
H meth ∥
H meth ⊥
H bond ∥
H bond ⊥
O ∥ (z)
Reference:

a) Hyper

b) Shi, W
G., Ts

ABLE VII-1. Hyperfine tensors of tyrosyl radicals.

Atom/Position	RNR	GO	Y_D (PSII)	Y_Z (PSII)	PGHS	Aqueous Glass
H 3,5 x	–26.7		–26.4	–26.8	–25.7	–25.4
H 3,5 y	–8.4	–8.4	–7.9	–8.4		–7.2
H 3,5 z	–19.6	–21.6	–19.5	–19.5	–19.5	–19.5
H 2,6 x	5.0	4.8	4.2	5.0	4.9	
H 2,6 y	7.6	6.8	7.1	7.5	7.1	6.5
H 2,6 z	2.1	2.4		1.3		
H meth ‖	61.2	43.4	31.5	35.4	69	3.0
H meth ⊥	53.7	39.8	27.2	29	58.2	2.3
H meth ‖	2.1	11.4	9.8	7.9		
H meth ⊥	–4.5		4.4	1.4		
H bond ‖	n.a.					
H bond ⊥	n.a.	3.1	3.0			
O ‖ (z)	–125					–111
References	20,21	22	23-26	27	b)	21,28,29,31

a) Hyperfine tensor components given in MHz.

b) Shi, W., Hoganson, C. W., Espe, M., Bender, C. J., Babcock, G. T., Kulmacz, R. J., Palmer, G., Tsai, A.-L., unpublished

and i

bonde

(PGH

confir

intera

concl

spectr

dihedr

distri

as we

invest

about

rotati

accor

dispe

quant

the rc

Warn

proto

and in the tyrosyl of apo-galactose oxidase the phenol oxygen is hydrogen bonded, while in the case of Y_{122} in RNR and Y_{385} in prostaglandin H synthase (PGHS) it is not. For the Y_D and Y_{122} radicals these findings have been confirmed by high-field EPR (30). It has also been shown that H-bonding interactions perturb the basic spin-density pattern only slightly, leading to the conclusion: *the striking variation of lineshapes observed in the CW-EPR spectra of tyrosyl radical enzymes and models is attributed to variations in the dihedral angles of the β-CH_2 bonds, not to variations in the spin-density distribution.*

β-CD_2- labeled tyrosyl radicals show *unexpected ^{2}H-ESEEM lineshapes* as well as anomalous CW-EPR and ENDOR linewidths (23, 27, 28). A detailed investigation has shown that the rotation mobility of the phenol head group about the C_1-C_β bond can account for this phenomenon. As the barrier to this rotation decreases, the heterogeneity in the dihedral angles increases, and accordingly, the magnitude of the isotropic coupling, A_β, will show increased dispersion. An analysis of ^{2}H-ESEEM spectra has provided a detailed quantitative picture: both the rotational barrier and relative populations of the rotamers can be deduced (28, 29).

Utilizing the advantages of the ^{2}H-ESEEM technique over ^{1}H-ENDOR, Warncke and McCracken have characterized the coupling of the 3,5 α-protons, using tyrosine specifically ^{2}H-labeled at these positions (31).

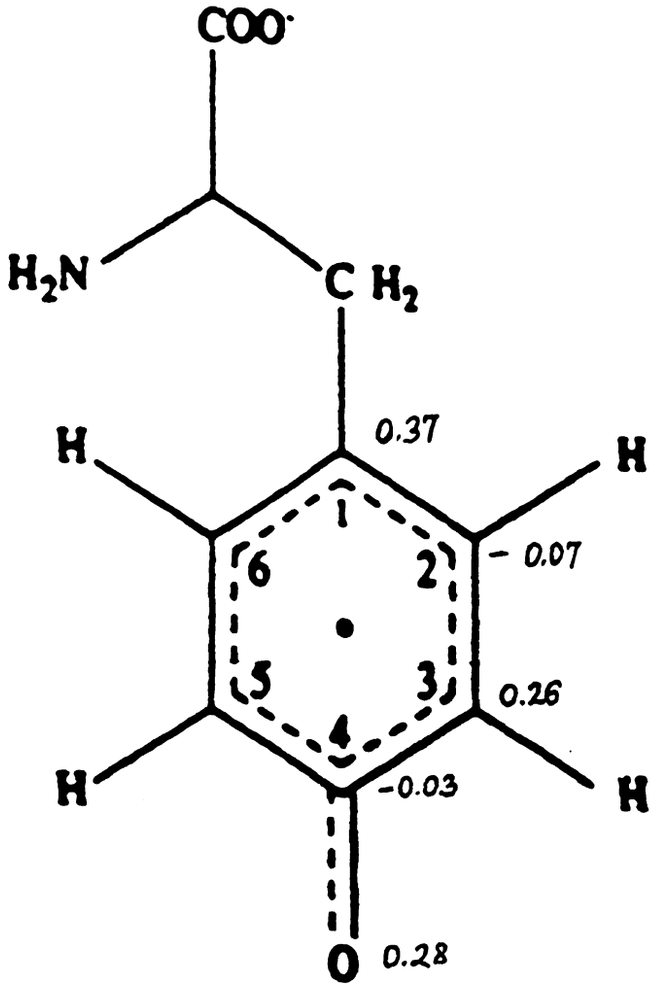

Figure VII-4. Spin-density distribution of tyrosyl radicals.

VII.6.

0.1 M

mL be

mater

NaOH

and m

obtair

0.1M

in 10

12 M

mL w

Prepa

soluti

magn

3,5-^{2}D

then

aliqu

rapid

5mM

descr

the U

VII.6. Sample Preparation

0.1 M Na_2H_2EDTA stock solution: Weigh 5.84 g (20 mmol) H_4EDTA into a 250 mL beaker, then add 100 mL water. Solubility of H_4EDTA is small, most of the material will not dissolve. Prepare 0.4 M NaOH solution by dissolving 1.6 g of NaOH pellets in 100 mL of H_2O. Combine this solution with the H_4EDTA; stir and mildly heat the mixture until a clear solution (0.1 M Na_2H_2EDTA) is obtained.

0.1M $GdCl_3$ stock solution: Dissolve 372 mg of $GdCl_3.6H_2O$ (FW=371.70 $gmol^{-1}$) in 10 mL of H_2O. The pH of the solution will be ca. 5.8.

12 M LiCl stock solution: Weigh out 5.09 g of LiCl (FW=42.4 $gmol^{-1}$). Add 5-6 mL water. Stir until the crystals dissolve. Dilute with water to 10 mL.

Preparation of tyrosyl radicals by UV irradiation: Mix 250 µL $GdCl_3$ stock solution with 260 µL Na_2H_2EDTA stock solution in a vial equipped with a magnetic stirrer. Add 500 µL H_2O and 3.4 mL 12 M LiCl solution. Add 5 mg 3,5-^{2}D tyrosine (Cambridge Isotopes, FW=183 $gmol^{-1}$). 20µL of 40 % NaOH is then added to increase the pH and to cause the tyrosine to dissolve. An aliquot of this solution is introduced into an EPR sample tube, then frozen rapidly with liquid N_2, which results in glass formation. This sample contains 5mM Gd(EDTA) and 5mM tyrosine. Tyrosine radicals were generated as described in Ref. (31), using a 950 W Hg lamp with no filtering. The time of the UV irradiation was 90 s, while the sample was immersed in liquid N_2.

VII.7.

Figur

above

limite

parar

very

Figur

of 10

relax

canno

point

clear

expe

two

whic

when

HFI

posit

prob

VII.7. Results and Discussion

Figure VII-5 shows the CW-EPR spectrum of the sample prepared as described above. It is identical with those published in the literature (32) and provides limited information due to the inhomogeneous broadening. Gd^{3+} is a strongly paramagnetic ion, containing 7 unpaired electrons (S=7/2). It gives rise to a very broad EPR signal, which is hardly observable in derivative EPR spectra.

The echo-detected EPR spectrum of the same sample is shown in Figure VII-6. The data for this spectrum were collected with a repetition rate of 100 Hz, at 4.2 K temperature. A strong radical signal emerges owing to *rapid relaxation* made possible by Gd^{3+} (in contrast, in the absence of Gd^{3+}, echoes cannot be observed at repetition rates higher than 10 Hz).

Figure VII-7 shows the HYSCORE time-domain data set (128x128 points) (a), and the corresponding contour plot (b). The contour pattern is clearly different from the axial case (cf. Chapter VI). Rhombic HFI tensors are expected to give rise to horn-shaped contour lines, so we can assume that the two clearly resolved arcs (designated by 1 and 2) are the two *limiting arcs*, which form the boundary of the horn. They correspond to $\Phi=0^0$ and $\Phi=90^0$, where Φ is the azimuthal angle specifying the position of $\vec{\mathbf{B}}_0$ in the PAS of the HFI tensor (Figure VII-8). In a randomly oriented sample $\vec{\mathbf{B}}_0$ spans all possible positions (Φ and Θ take all values between 0 and 90 degrees) with equal probability. If we fix Φ and let $\vec{\mathbf{B}}_0$ sweep Θ from 0 to 90 degrees, we have a

= 100 Ω | 0.40 sec Time Constant | ±(125) Ω Modulation Amplitude | (670) Receiver Gain | 0.5 mW Microwave Power | Photo. r Detector

WCV 5FR CHART A

VARIAN ASSOCIATES, INC.
PALO ALTO, CALIFORNIA
U.S.A.

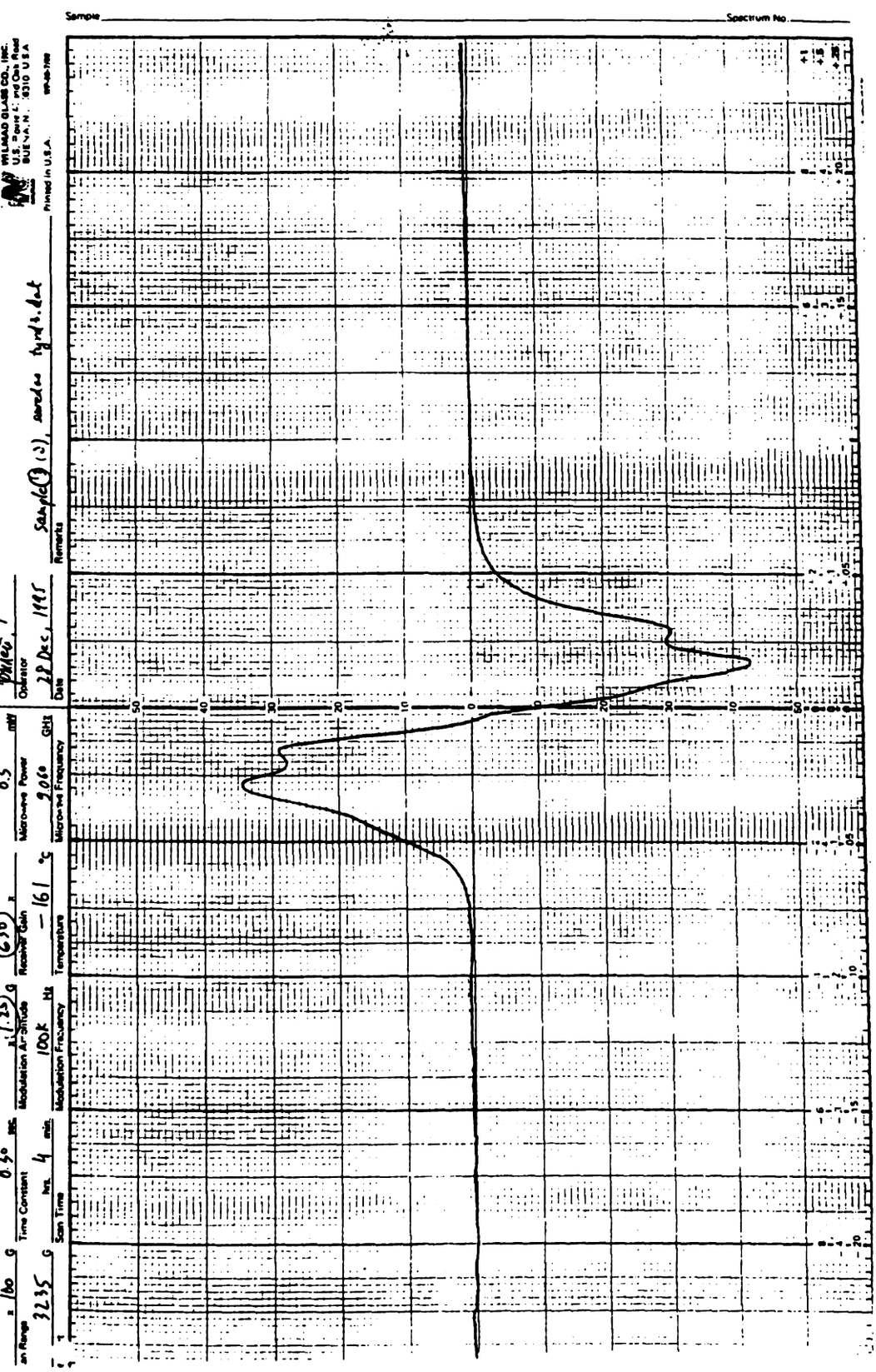

Figure VII-5. CW-EPR spectrum of the 3,5 ^{2}H-tyrosyl radical generated by UV irradiation in a 12 M LiCl frozen solution, with 5 mM Gd^{3+} added.

file: D2tyr.esr2
comment: ese-epr of sample I (w/ 5mM Gd);

freq.: 8.9100 GHz
power: 46.0 dBm

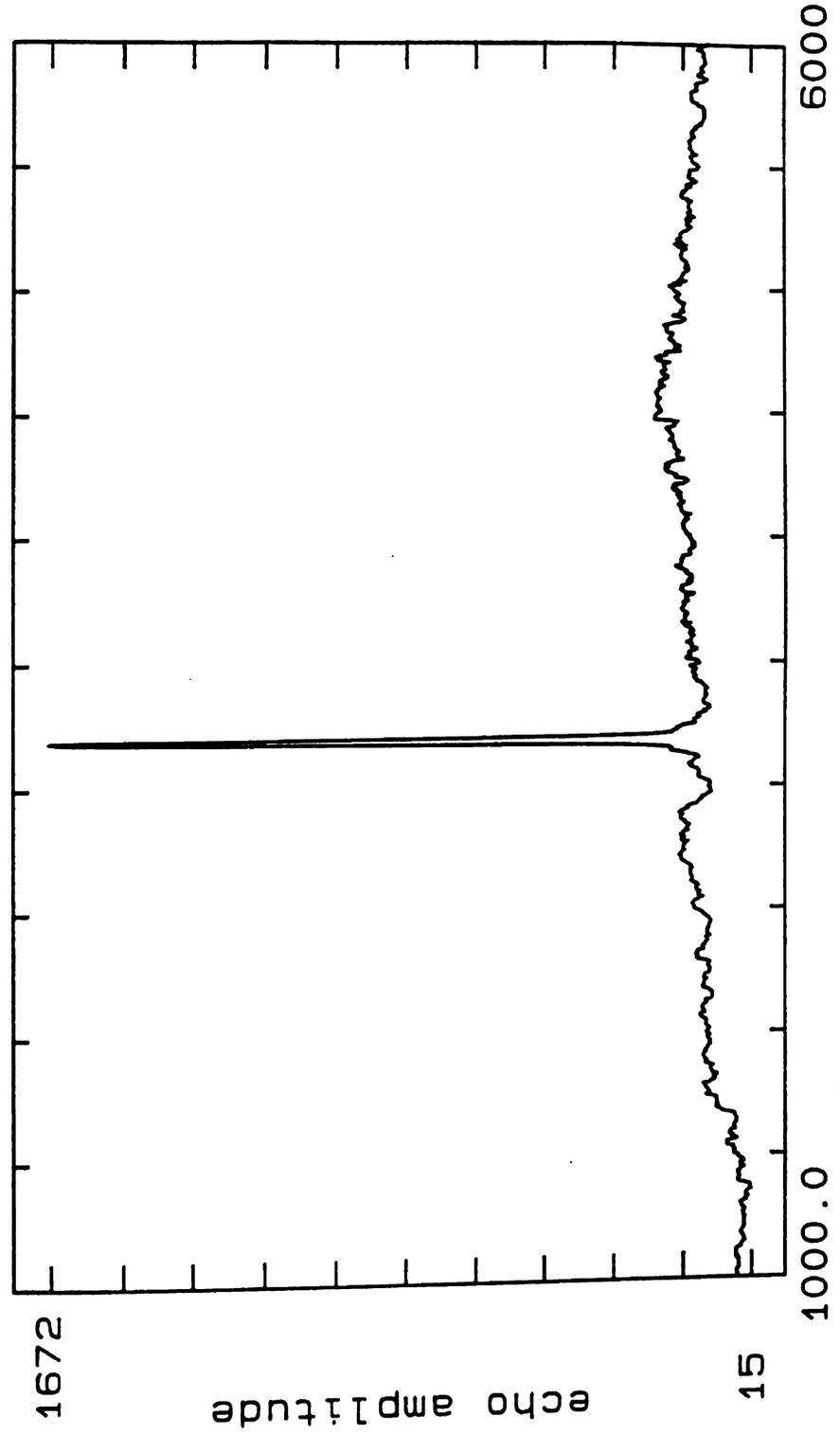

Figure VII-6. Spin-echo detected EPR of the 3,5 ^{2}H-tyrosyl sample, containing 5 mM Gd^{3+}.

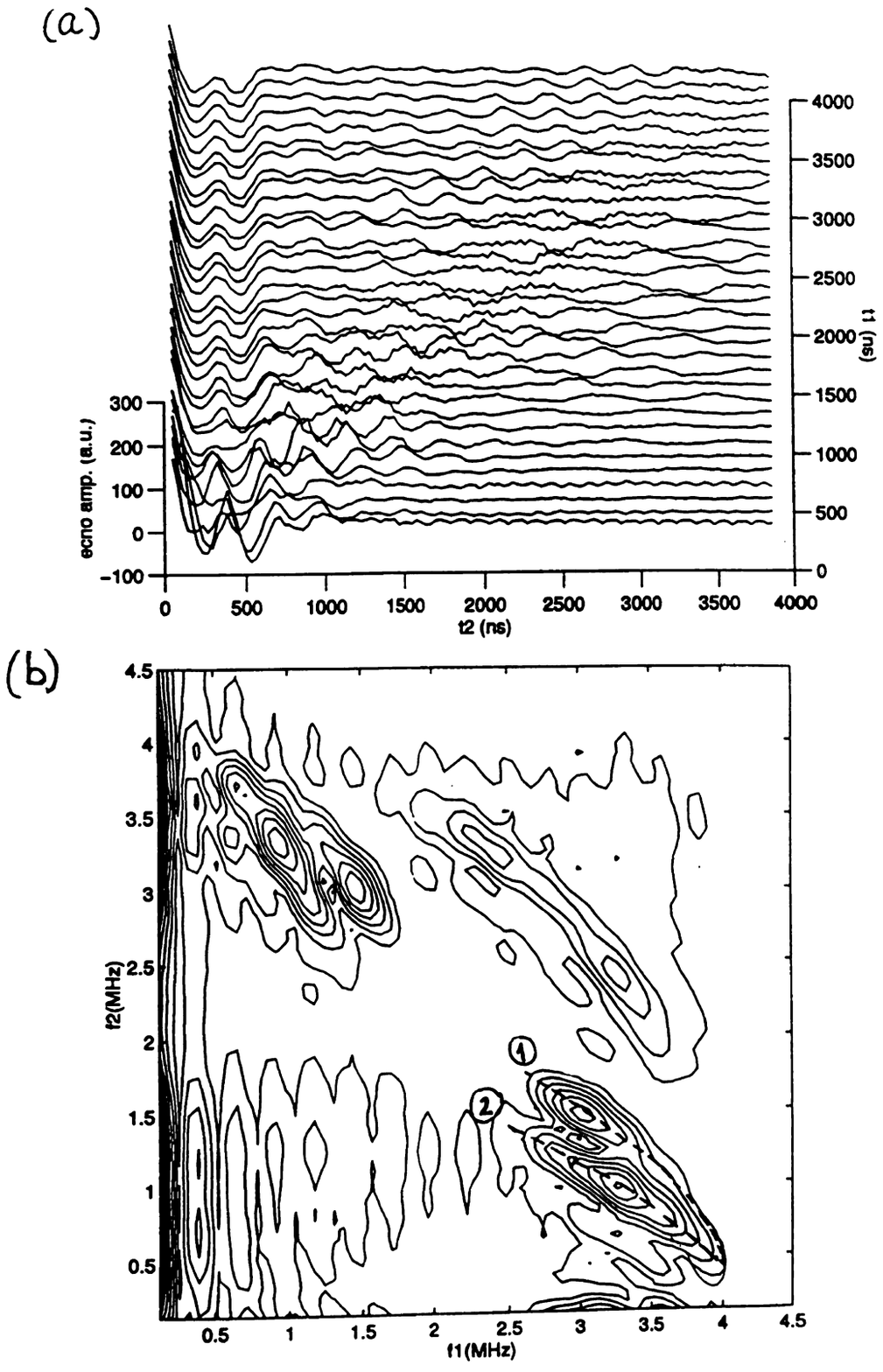

Figure VII-7. (a) Time-domain HYSCORE data (128x128 data points) from 3,5 ^{2}H-tyrosyl, with τ=200 ns; (b) the corresponding HYSCORE frequency-domain contour plot. B_0=3129 G, ν=8.910 GHz.

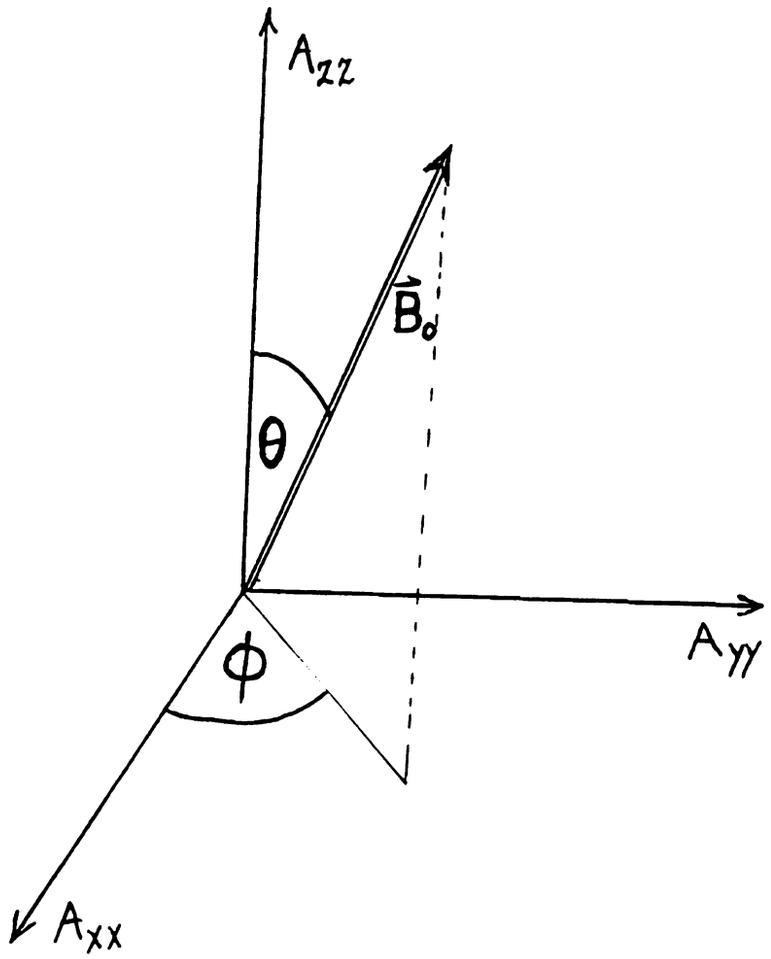

Figure VII-8. Definition of the position of the external magnetic field vector (B_0) in the Principal Axis System of the (rhombic) hyperfine tensor.

situa

such

A_{-} =

$A_{||}$ =

prin

follo

hype

whil

Com

HYS

coup

Furt

nega

to th

situation same as the axial tensor, which results in a pair of arcs. There is one such pair for each Φ and the ensemble of these arcs creates the horn.

When $\Phi=0^0$, the two principal values of this hyperfine tensor will be $A_\perp=A_{xx}$ and $A_{||}=A_{zz}$. When $\Phi=90^0$ these parameters will be $A_\perp=A_{yy}$ and $A_{||}=A_{zz}$. Thus, evaluating these boundary arcs can, in principle, yield all three principal values of the rhombic hyperfine tensor. Analysis of arc 1 ($\Phi=90^0$) following the method of Dikanov and Bowman (33) leads to the axial hyperfine matrix

$$\mathbf{A}(90^0)=\begin{pmatrix}\pm0.8 & 0 & 0\\ 0 & \pm0.8 & 0\\ 0 & 0 & \pm3.6\end{pmatrix} \quad \text{(MHz)}, \qquad \text{[VI-1]}$$

while for arc 2 ($\Phi=0^0$) we obtain

$$\mathbf{A}(0^0)=\begin{pmatrix}\pm3.1 & 0 & 0\\ 0 & \pm3.1 & 0\\ 0 & 0 & \pm3.6\end{pmatrix} \quad \text{(MHz)}. \qquad \text{[VI-2]}$$

Combination of these leads to the *rhombic hyperfine matrix,*

$$\mathbf{A}=\begin{pmatrix}\pm0.8 & 0 & 0\\ 0 & \pm3.1 & 0\\ 0 & 0 & \pm3.6\end{pmatrix} \quad \text{(MHz)}. \qquad \text{[VI-3]}$$

HYSCORE cannot provide direct information on the *sign of the hyperfine coupling;* however, it reports on the relative sign of A_{iso} and T (33). Furthermore, it is known that $A_{iso}<0$ for α-protons, which is expressed in the negative value of the McConnell constant ($\mathbf{Q}(^2H)$=-10.7 MHz) (19). This leads to the hyperfine tensor

$$\mathbf{A} = \begin{pmatrix} -0.8 & 0 & 0 \\ 0 & -3.1 & 0 \\ 0 & 0 & -3.6 \end{pmatrix} \quad \text{(MHz)}. \qquad \text{[VI-4]}$$

These principal values fall in the range of other tyrosyl 3,5, α-proton values (cf. TABLE VII-1; note that ^{1}H coupling parameters are obtained by multiplying the corresponding ^{2}H values by 6.5, i.e. by the ratio of the gyromagnetic ratios of proton and deuteron, $\gamma(^1H)/\gamma(^2H)$).

The validity of the above hyperfine parameters has been checked by performing 1D 3-pulse ESEEM at various τ values. Numerical simulation has been done with the FORTRAN program "sedeut", using the above principal values as input parameters. The simulations show good agreement with the experiment (Figure VII-9).

The result of our study is close to the hyperfine tensor determined by Warncke and McCracken (31) for a tyrosyl model trapped in 40% NaOH glass matrix. The difference between the hyperfine values is expected considering the significantly different media in the two experiments. The assignment has also been confirmed by a numerical simulation of the HYSCORE contour map performed with the MATLAB routine "hyslineRom.m" (Appendix). The simulated and experimental spectra are shown in Figure VII-10. The agreement is satisfactory with significant discrepancy in the intensities at certain parts of the contour lines (e.g. the tail of arc 1). This can be understood considering that the intensities were calculated using the formulae of Gemperle et al. (34) derived for S=1/2, I=1/2. While the frequencies can safely

Figure VII-9. 3-pulse ESEEM spectra of 3,5 ^{2}H-tyrosyl radical with the corresponding simulations; (a) experimental, τ=293 ns. (b) simulated; (c) experimental, τ=438 ns. (d) simulated. Simulation parameters: the principal values of the HFI tensor (MHz), A_{xx}=0.8, A_{yy}=3.1, A_{zz}=3.6; nuclear Larmor frequency, ν_L=2.1 MHz.

(a)

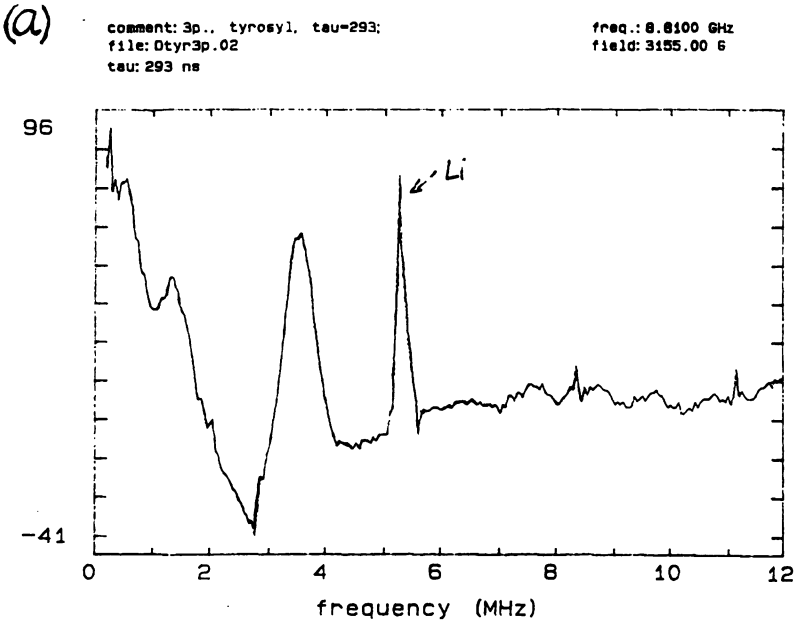
comment: 3p., tyrosyl, tau=293;
file: Dtyr3p.02
tau: 293 ns
freq.: 8.8100 GHz
field: 3155.00 G
96
-41
Li
0
2
4
6
8
10
12
frequency (MHz)

(b)

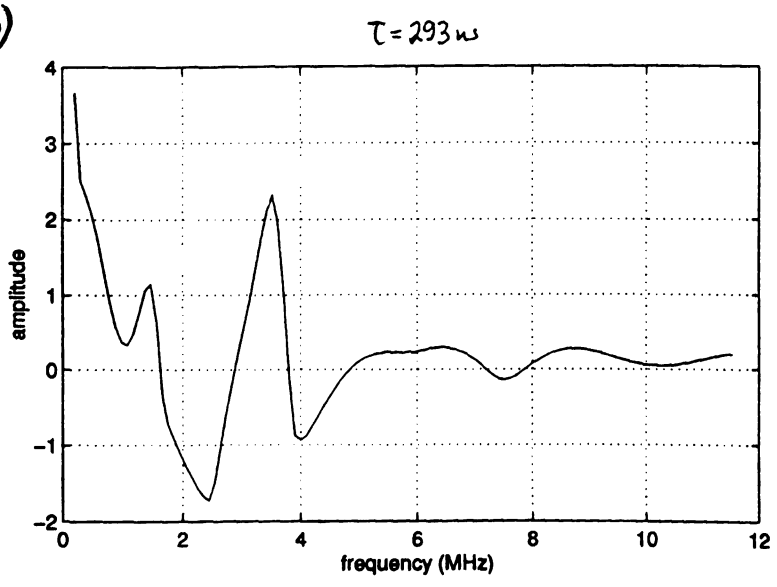
τ = 293 ns
4
3
2
1
0
-1
-2
amplitude
0
2
4
6
8
10
12
frequency (MHz)

(c)

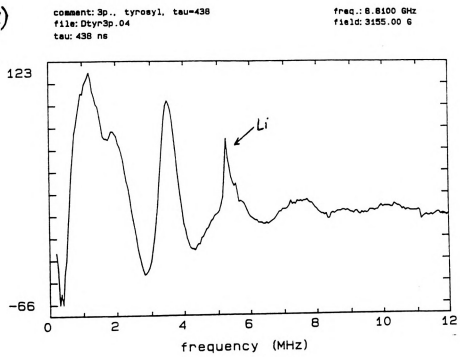
comment: 3p., tyrosyl, tau=438
file: Dtyr3p.04
tau: 438 ns
freq.: 8.8100 GHz
field: 3155.00 G
123
-66
Li
0
2
4
6
8
10
12
frequency (MHz)

(d)

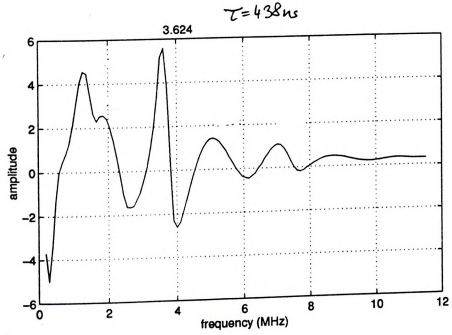
τ=438ns
3.624
amplitude
6
4
2
0
-2
-4
-6
0
2
4
6
8
10
12
frequency (MHz)

Figure VII-10. (a) HYSCORE contour plot of 3,5 ^{2}H-tyrosyl (same as Figure VI-7b); (b) the corresponding frequency-domain simulation performed with the MATLAB program "hyslineRom.m" using the following parameters: nuclear Larmor frequency, ν_L=2.1 MHz; A_{iso}=2.6 MHz, T=0.80 MHz, asymmetry parameter of HFI tensor, δ=0.53; tau-value, τ=200 ns.

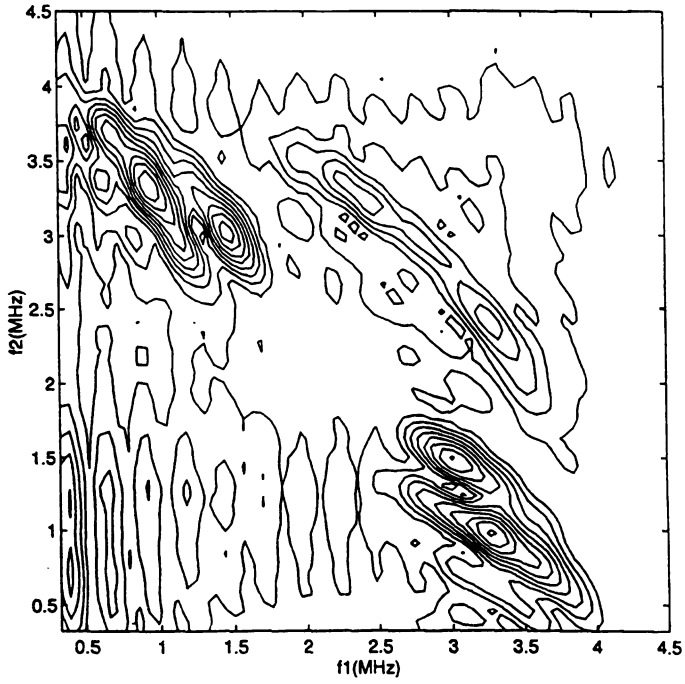
4.5
4
3.5
3
2.5
2
1.5
1
0.5
f2(MHz)
0.5
1
1.5
2
2.5
3
3.5
4
4.5
f1(MHz)

(a)

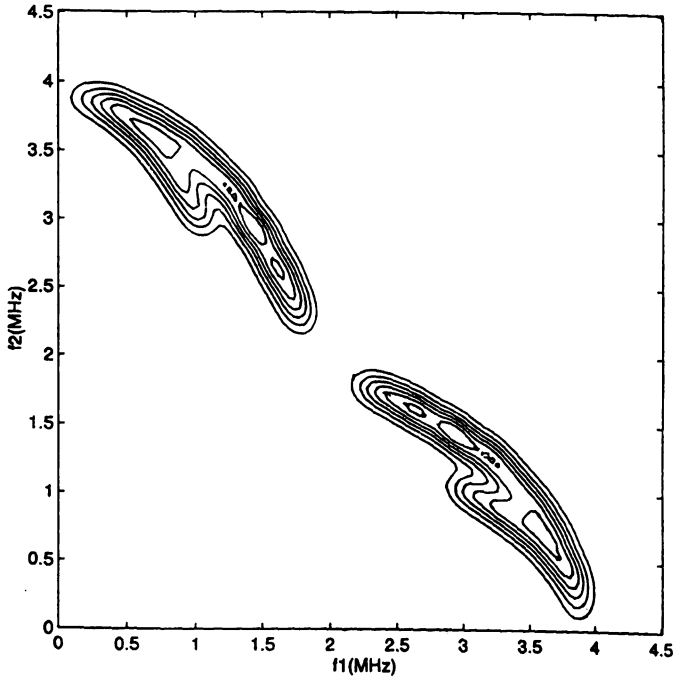
4.5
4
3.5
3
2.5
2
1.5
1
0.5
0
f2(MHz)
0
0.5
1
1.5
2
2.5
3
3.5
4
4.5
f1(MHz)

(b)

be c

the

inte

qua

On

cer

this

of

con

ter

ser

of

sp

su

Eg

st

st

E

d

ca

be calculated with this formula (the small nuclear quadrupole interaction of the deuterium does not alter the ENDOR frequencies substantially), *the intensities of the cross peaks* may be more significantly affected by the quadrupole interaction.

The τ-suppression effect in HYSCORE has been discussed in Chapter II. One can easily infer from Eq. [II-11c] that at a certain τ-value the intensity of certain cross-peaks becomes zero (blind spots). In randomly oriented samples this leads to a distortion of the lineshape, which makes the lineshape analysis of the 1D ESEEM very involved. In HYSCORE, however, partially suppressed contour lines still provide sufficient information to deduce the hyperfine tensor parameters without spectral simulation (33). Figure VII-11 shows a series of HYSCORE contour plots obtained at different τ-values. Suppression of various parts of the lineshape depending on τ can be observed. These spectra also demonstrate that the shortest τ-value (200 ns) has yielded the least suppressed features, in agreement with Höfer's analysis (35).

In conclusion: this work presents an example of the application of ^{2}H-ESEEM, which is an alternative method to ^{1}H-ENDOR to obtain detailed structural information on organic radicals. It shows that a low-temperature study of slowly-relaxing radicals is possible if rare earth ions (such as Gd^{3+}, Eu^{3+}) are added to the sample in sufficient concentration. This study demonstrates that the contour lineshape analysis of Dikanov and Bowman can be applied to the tyrosyl radical as well; it yields the parameters of the

rhot

rhombic hyperfine matrix without lengthy spectral simulation.

Figure VII-11. The τ-suppression effect in our experiments. HYSCORE spectra of the 3,5 ^{2}H-tyrosyl radical taken at various values of τ: (a) 200 ns; (b) 300 ns; (c) 400 ns; (d) 500 ns; (e) 600 ns.

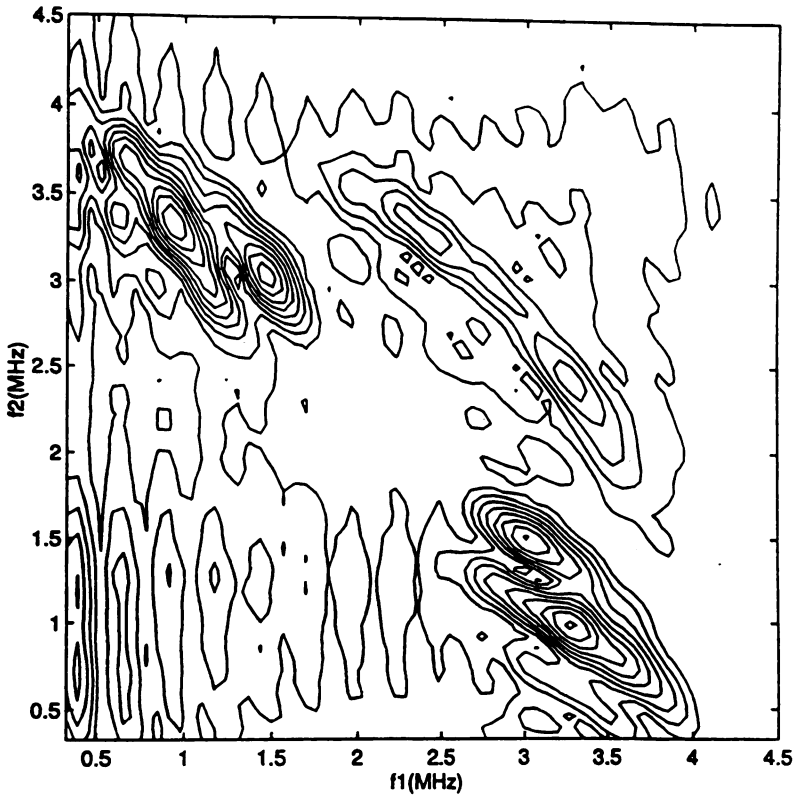
4.5
4
3.5
3
2.5
2
1.5
1
0.5
f2(MHz)
0.5
1
1.5
2
2.5
3
3.5
4
4.5
f1(MHz)

(a)

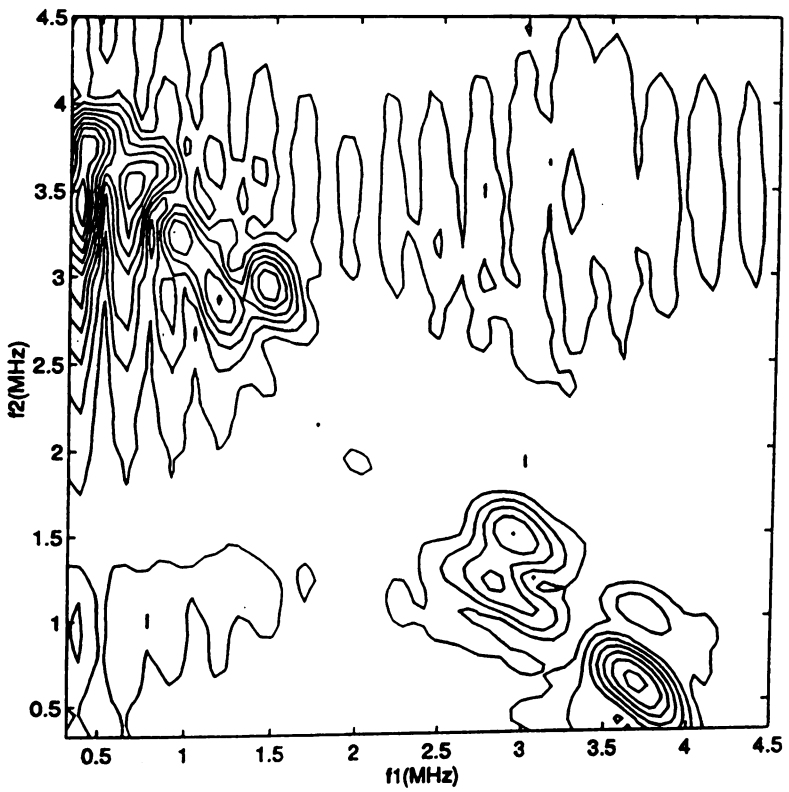
4.5
4
3.5
3
2.5
2
1.5
1
0.5
f2(MHz)
0.5
1
1.5
2
2.5
3
3.5
4
4.5
f1(MHz)

(b)

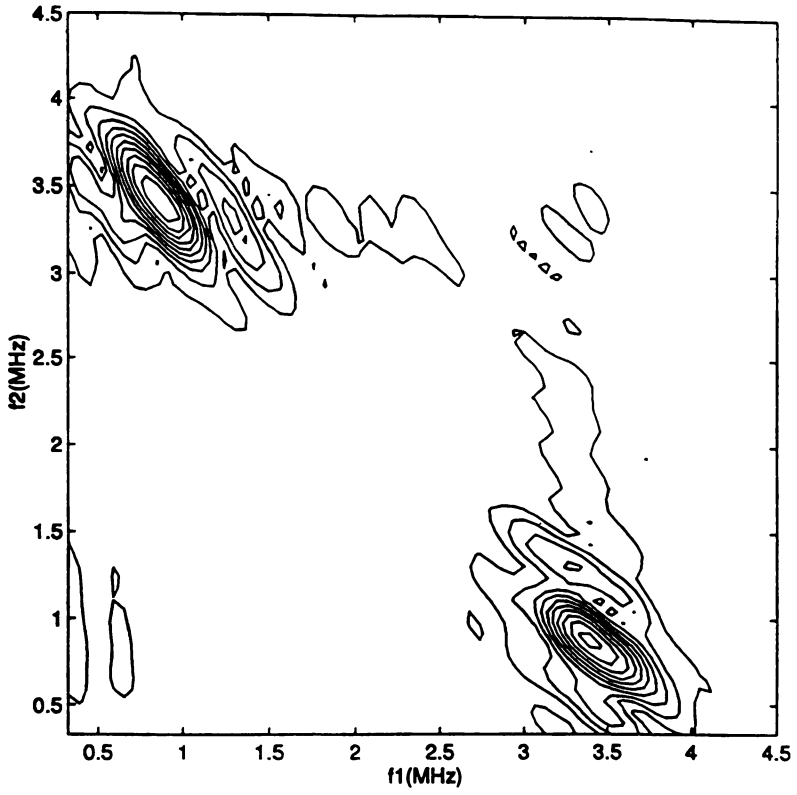
4.5
4
3.5
3
2.5
2
1.5
1
0.5
f2(MHz)
0.5
1
1.5
2
2.5
3
3.5
4
4.5
f1(MHz)

(c)

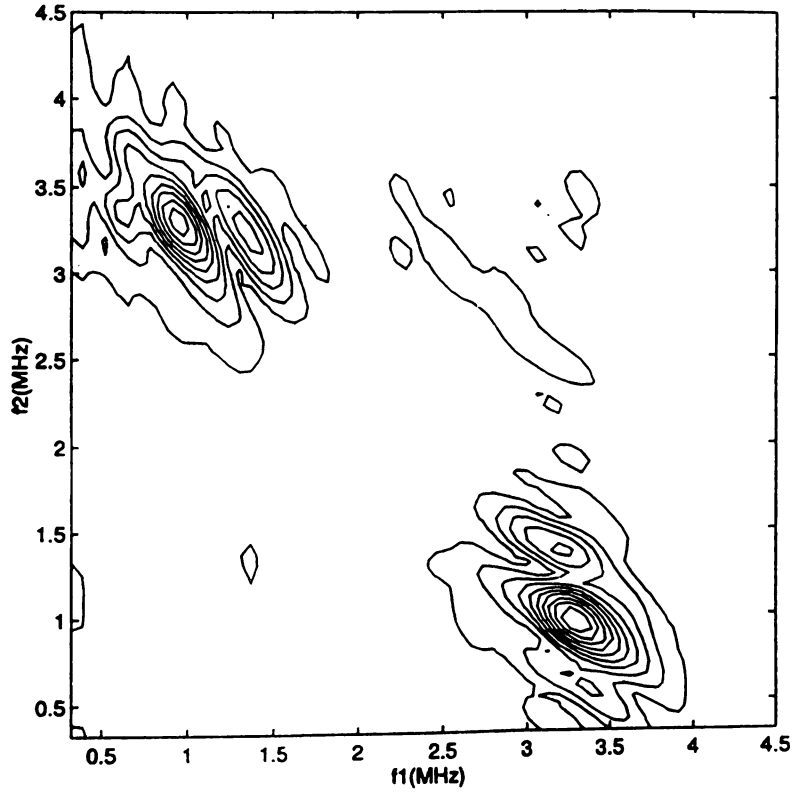
4.5
4
3.5
3
2.5
2
1.5
1
0.5
f2(MHz)
0.5
1
1.5
2
2.5
3
3.5
4
4.5
f1(MHz)

(d)

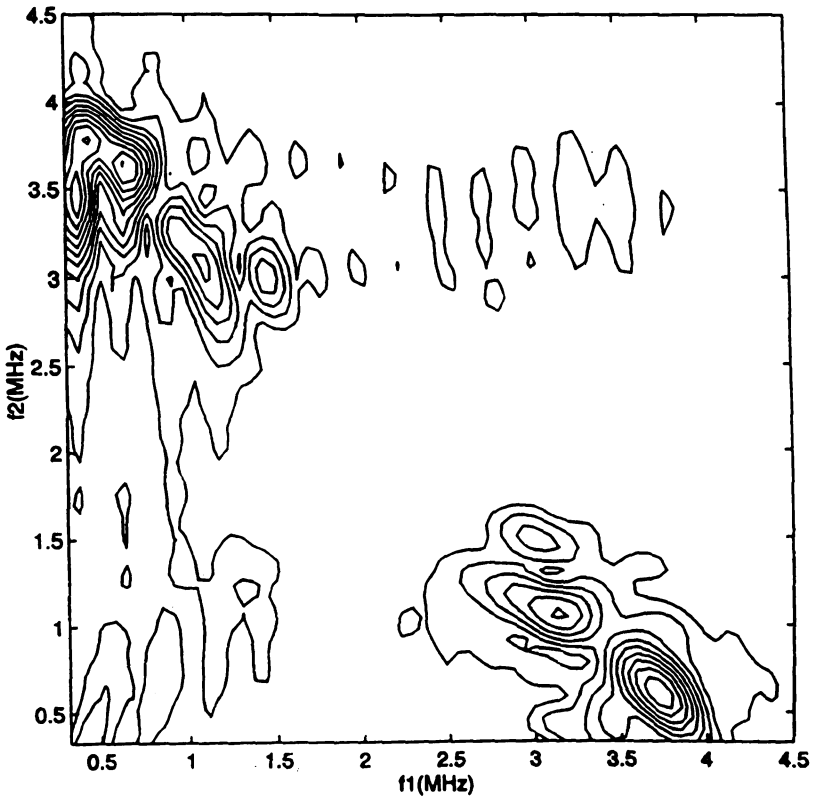

(e)

References

1. Sigel, H.; Sigel, A., Eds. *Metal Ions in Biological Systems, Vol 30.*; Marcel Dekker: New York, 1994.

2. Sjöberg, B.-M.; Gräslund, A. *Adv. Inorg. Biochem.* **1983**, *5*, 87.

3. Barry, B. A.; Babcock, G. T. *Proc. Natl. Acad. Sci. U.S.A.* **1987**, *84*, 7099.

4. Smith, W. L.; Eling, T. E.; Kulmacz, R. J.; Marnett, L. J.; Tsai, A. L. *Biochemistry* **1992**, *31*, 3.

5. Whittaker, M. M.; Whittaker, J. W. *J. Biol. Chem.* **1990**, *265*, 9610.

6. Jones, S. M.; Mu, D.; Wemmes, D.; Smith, A. J.; Kaus, S.; Maltby, D.; Burlingname, A. L.; Klinman, J. P. *Science* **1990**, *248*, 981.

7. DeFillipis, M. R.; Murthy, C. P.; Faraggi, M.; Klapper, M. H. *Biochemistry* **1989**, *28*, 4847.

8. Prütz, W. A.; Butler, J.; Land, E. J.; Swallow, A. J. *Free Radical Res. Commun.* **1986**, *2*, 69.

9. Sivaraja, M.; Goodin, D. B.; Smith, M.; Hoffman, B. M. *Science* **1989**, *245*, 738.

10. Wagner, A. F. V.; Frey, M.; Neugebauer, F. A.; Schäfer, W.; Knappe, J. *Proc. Natl. Acad. Sci. U.S.A.* **1992**, *89*, 996.

11. Weindruch, R. *Scientific American* **1996**, *January*, 46.

12. Shinkarev, V. P.; Wraight, C. in *The Photosynthetic Reaction Center, Vol I.*; Deisenhofer, J.; Norris, J. R., Eds.; Academic Press: San Diego, 1993.

13. Reichard, P.; Ehrenberg, A. *Science* **1983**, *221*, 514.

14. Frey, P. A. *Chem. Rev.* **1990**, *90*, 1343.

15. Whittaker in Ref (1), pp. 315-360.

16. Ito, N.; Phillips, S. E. V.; Yad, K. D. S.; Knowles, P. F. *J. Mol. Biol.* **1994**, *238*, 794.

17. Fontecave, M.; Pierre, J.-L. *Bull. Soc. Chim. Fr.* **1996**, *133*, 653.

18. Johnson, J. M.; Halsall, H. B.; Heineman, W. R. *Biochemistry* **1985**, *24*, 1579.

19. Gordy, W. in *Techniques in Chemistry, Vol. XV: Theory and Applications of Electron Spin Resonance;* West, W., Ed.; Wiley: New York, 1980.

20. Bender, C. J.; Sahlin, M.; Babcock, G. T.; Barry, B. A.; Chandrashekar, T. K.; Salowe, S. P.; Stubbe, J.; Lindström, B.; Petersson, L.; Ehrenberg, A.; Sjöberg, B.-M. *J. Am. Chem. Soc.* **1989**, *111*, 8076.

21. Hoganson, C. W.; Sahlin, M.; Sjöberg, B.-M.; Babcock, G. T. *J. Am. Chem. Soc.* **1996**, *118*, 4672.

22. Babcock, G. T.; El-Deeb, M. K.; Sandusky, P. O.; Whittaker, M. M.; Whittaker, J. W. *J. Am. Chem. Soc.* **1992**, *114*, 3727.

23. Warncke, K.; McCracken, J.; Babcock, G. T. *J. Am. Chem. Soc.* **1994**, *114*, 7332.

24. Rigby, S. E.; Nugent, J. H. A.; O'Malley, P. *J. Biochem.* **1994**, *33*, 1734.

25. Hoganson, C. W.; Babcock, G. T.; *Biochemistry* **1992**, *31*, 11874.

26. Tommos, C.; Madsen, C.; Styring, S.; Vermaas, W. *Biochemistry* **1994**, *33*, 11805.

27. Tommos, C.; Tang, X.-S.; Warncke, K.; Hoganson, C. W.; Styring, S.; McCracken, J.; Diner, B. A.; Babcock, G. T. *J. Am. Chem. Soc.* **1995**, *117*, 10325.

28. Warncke, K.; McCracken, J. *J. Chem. Phys.* **1995**, *103*, 6829.

29. Warncke, K.; Babcock, G. T. McCracken, J. *J. Phys. Chem.* **1996**, *100*, 4654.

30. Un, S.; Atta, M.; Fontecave, M.; Rutherford, A. W. *J. Am. Chem. Soc.* **1995**, *117*, 10713.

31. Warncke, K.; McCracken, J. *J. Chem. Phys.* **1994**, *101*, 1832.

32. Barry, B. A.; El-Deeb, M. K.; Sandusky, P. O.; Babcock, G. T. *J. Biol. Chem.* **1990**, *265*, 20139.

33. Dikanov, S. A.; Bowman, M. K. *J. Magn. Reson.* **1995**, *Series A 116*, 125.

34. Gemperle, C.; Aebli, G.; Schweiger, A.; Ernst, R. R. *J. Magn. Reson.* **1990**, *88*, 241.

35. Höfer, P. *J. Magn. Reson.*, **1994**, *Series A 111*, 77.

Appendix

This Appendix contains the printouts of MATLAB programs that are necessary to run HYSCORE experiments. It also has two MATLAB scripts which are capable of simulating HYSCORE contour plots (hysline1 and hyslineRom). The function of these programs is briefly described at the beginning of each script file. The operation of the program can easily be followed by reading the notes embedded in the script.

```
%hyscore_read.m
%       This m-file reads data output by the 4-pulse hyscore
%       data collection program
%
%       The data will be placed in a square matrix of dimension
%       cval(8), npts by npts of the format data(t1,t2)
%
fname=input('enter hyscore data file name:','s');
fp=fopen(fname);
%
%       set up floating point parameters
%
freq=fscanf(fp,'%lf',1);
field=fscanf(fp,'%lf',1);
power=fscanf(fp,'%lf',1);
temp=fscanf(fp,'%lf',1);
%
%       get integer control parameters
%
cval=fscanf(fp,'%d',8);
tau=cval(1);
npts=cval(8);
t1start=cval(2);
tincr=cval(3);
%
%       read in the date of expt
%
date=fscanf(fp,'%d',3);
%
%       read in the data array
%
data=fscanf(fp,'%d');
%
```

```
%hyscore_plot2.m
%   This m-file uses the time domain data array created by the
%  program  "hyscore_read.m" and transforms it into a matrix
%  of dimension npts x npts; then it creates a 3-D plot

%hyscore_read;

%create the data-matrix (D) using the data array "data" created by
%       "hyscore_read;

for i=1:npts
   for j=1:npts
      D(i,j)=data((i-1)*npts+j);
        end
  end
%run "baseline" to get the baseline corrected data matrix DBC
%
baseline;
%
%to save memory space delete D and B and b
%
clear D;
clear B;
clear b;
%
k=1:npts;
T(k)=tincr*(k-1)+t1start;
mesh(T,T,DBC)
xlabel('t2 (ns)');
ylabel('t1 (ns)');
zlabel('echo amp. (a.u.)');

%
% call tdplot to plot the time-domain in 3-D (using the mesh routine);
%tdplot;
```

```
%tdplot.m plot the time-domain in 3-D using the plot3 routine
%
%
N=input('enter the # of slices you wish to see : ');
  num=round(npts/N);
    E=eye(npts);
for i=2:npts
  if rem(i,num)==0
     E(i,i)=1;
   else
     E(i,i)=0;
   end
 end
SH=DBC'*E;
%  plot using the plot3 function
%  first generate the matrices needed for the plot3 routine

for i=1:npts
  for j=1:npts
    X(i,j)=T(i);
  end
end
Xm=X*E;
Y=X';
Ym=Y*E;
plot3(Xm,Ym,SH)
xlabel('t2 (ns)')
ylabel('t1 (ns)')
zlabel('echo amp. (a.u.)')


ans=input('do you want to change the # of slices ? (y/n) ','s');
if ans=='y',
tdplot;
end
clear X;
clear Xm;
clear Y;
clear Ym;
clear SH;
clear T;
clear E;

return;
```

```
%frplot512.m
% this script creates a 3-D plot of the (++) quadrant of the hyscore
 % the matrix obtained by the 2-D FT of the time domain data matrix, DBC.
%
%
np=512;
YY=fft2(DBC',np,np);
SPEC=abs(YY);
clear YY;

disp512

end
```

```
%   disp512.m  this file displays the desired  portion of the 2-D spectrum,
      by the file frplot512;

frinc=1000./(tincr*(np-1));
f=(0:(np-1))*frinc;

frmin=input('enter fmin:  ');
frmax=input('enter fmax:  ');

lmin=round(frmin/frinc)+1;
lmax=round(frmax/frinc)+1;

x=lmin:lmax;
mesh(f(x),f(x),SPEC(lmin:lmax,lmin:lmax));
xlabel('f1(MHz)');
ylabel('f2(MHz)');
zlabel('ampl.(a.u.)');
PL=SPEC(lmin:lmax,lmin:lmax);
ans=input('would you like to see another frequency range ? (y/n): ','s');
if ans=='y',
disp512
end
```

```
%  DQ2.m
% this script creates a 3-D plot of the (-+) quadrant of the hyscore
 % the matrix obtained by the 2-D FT of the time domain data matrix, DBC.
%
%
np=512;
YY=fft2(DBC',np,np);
SPEC=abs(YY);
clear YY;
frinc=1000./(tincr*(np-1));
f=(0:(np-1))*frinc;

frmin=input('enter fmin:  ');
frmax=input('enter fmax:  ');

lmin=round(frmin/frinc)+1;
lmax=round(frmax/frinc)+1;

x=lmin+1:lmax+1;

Lma=np-lmin+1;
Lmi=np-lmax+1;


mesh(f(x),f(x),SPEC(lmin:lmax,Lma:-1:Lmi));
PL=SPEC(lmin:lmax,Lma:-1:Lmi);

xlabel('-f1(MHz)');
ylabel('f2(MHz)');
zlabel('ampl.(a.u.)');
ans=input('would you like to see another frequency range ? (y/n): ','s');
if ans=='y',
DQ2;
end
return;
```

```
%  hysline.m  this script generates 2-D frequency correlation maps for dis-
%ordered systems with axial hfi tensor;
%

vi=input('enter the nuclear Larmor frequency (MHz): ');
 a=input('enter the isotropic hyperfine constant (MHz): ');
 T=input('enter the anisotropic HFI constant (T), in MHz : ');
 tau=input('enter the tau value of the experiment, in ns : ');
   del =input('enter the time increment of the exp., in ns: ');
wd= input('enter the gaussian linewidth (MHz): ');
np= input('enter the # of "data-points":  ');


fmax=1000/del;


%
%  define the limiting (principal) values of the HyperFine Interaction
%  along the two principal axes of the HFI tensor (i.e. along and perpen-
%  dicular to the external magnetic field
%

VAP=-vi+(a+2*T)/2;
VBP=-vi-(a+2*T)/2;
VAM=-vi+(a-T)/2;
VBM=-vi-(a-T)/2;

%  generate nmr frequency array;

dt=pi/120;
%t=(pi/2-dt*20):dt:pi/2;
t=0:dt:pi/2;
c=cos(t);
csq=c.*c;
s=sin(t);
ssq=s.*s;
VAN=VAM*VAM;
VAA=VAP*VAP-VAN;
va=sqrt((VAA*csq)+VAN);
VBN=VBM*VBM;
VBA=VBP*VBP-VBN;
vb=sqrt((VBA*csq)+VBN);
SS=abs(vi^2-((va+vb).^2)/4);
SS=SS./(va.*vb);
CS=abs(vi^2-((va-vb).^2)/4);
CS=CS./(va.*vb);
k=4*SS.*CS;
%
%
tau=tau/1000;
sa=sin(va*2*pi*tau/2);
sb=sin(vb*2*pi*tau/2);

amp=(k/4).*abs(sa.*sb).*sqrt(2*(CS.^2+SS.^2));
%
%   generate the 2-D frequency-domain data matrix, SPEC
%

%r=[VAM,VBM,VAP,VBP];
%fmax=max(abs(r))*1.1;
```

```
frinc=fmax/(np-1);
f=(0:(np-1))*frinc;
SPEC=zeros(np,np);
for i=1:61
  nchana=round(va(i)/frinc)+1;
  nchanb=round(vb(i)/frinc)+1;
    SPEC(nchana,nchanb)=amp(i);
    SPEC(nchanb,nchana)=amp(i);
      end

%  perform the convolution in 2 steps along the matrix SPEC;
%
  %  set up Gaussian line-shape function for convolution
%
Gauss;


for i=1:np
L(i,:)=conv(SPEC(i,:),fg);
end
SP=zeros(np+40,np+40);
   for i=1:(np+40)
  SP(:,i)=conv(L(:,i),fg);
end

%  we have to account for the size differnce between the matrices before
%  and after the convolution

DS=zeros(np,np);
for i=1:np
    for j=1:np
          DS(i,j)=SP(i+20,j+20);
        end
    end

hysplot1



% hysplot1.m  this routine displays the desired frequency range of the matrix
% generated by 'hysline1.m ...


frmin=input('enter fmin:  ');
frmax=input('enter fmax:  ');

lmin=round(frmin/frinc)+1;
lmax=round(frmax/frinc)+1;

x=lmin:lmax;
mesh(f(x),f(x),DS(lmin:lmax,lmin:lmax));
xlabel('f1(MHz)');
ylabel('f2(MHz)');
zlabel('ampl.(a.u.)');
PL=DS(lmin:lmax,lmin:lmax);

ans= input('would you like to see another frequency range ? (y/n):','s');
if ans=='y',
hysplot1;
end
```

```
%  hyslineRom.m  this script generates 2-D frequency correlation maps for
%        systems with rhombic hfi tensor;
%

vi=input('enter the nuclear Larmor frequency (MHz): ');
 a=input('enter the isotropic hyperfine constant (MHz): ');
 T=input('enter the anisotropic HFI constant (T), in MHz : ');
 D=input('enter the rhombicity parameter of the HFI tensor : ');
 tau=input('enter the tau value of the experiment, in ns : ');
   del =input('enter the time increment of the exp., in ns: ');
wd= input('enter the gaussian linewidth (MHz): ');
np= input('enter the # of "data-points":  ');


fmax=1000/del;


%
%  define the limiting (principal) values of the HyperFine Interaction
%  along the two principal axes of the HFI tensor (i.e. along and perpen-
%  dicular to the external magnetic field
%

Vza=-vi+(a+2*T)/2;
Vzb=-vi-(a+2*T)/2;
%
Vxa=-vi+(a-T*(1-D))/2;
Vxb=-vi-(a-T*(1-D))/2;
%
Vya=-vi+(a-T*(1+D))/2;
Vyb=-vi-(a-T*(1+D))/2;
%
V2za=Vza*Vza;
V2zb=Vzb*Vzb;
V2xa=Vxa*Vxa;
V2xb=Vxb*Vxb;
V2ya=Vya*Vya;
V2yb=Vyb*Vyb;

%  generate nmr frequency array;

dt=pi/120;
t=0:dt:pi/2;
c=cos(t);
csq=c.*c;
s=sin(t);
ssq=s.*s;
V2xya=V2ya-(V2ya-V2xa)*csq;
V2xyb=V2yb-(V2yb-V2xb)*csq;
tau=tau/1000;
SPEC=zeros(np,np);

for i=1:61
VA=sqrt((V2za-V2xya(i))*csq+V2xya(i));
VB=sqrt((V2zb-V2xyb(i))*csq+V2xyb(i));

SS=abs(vi^2-((VA+VB).^2)/4);
SS=SS./(VA.*VB);
CS=abs(vi^2-((VA-VB).^2)/4);
CS=CS./(VA.*VB);
```

```
k=4*SS.*CS;

sa=sin(VA*2*pi*tau/2);
sb=sin(VB*2*pi*tau/2);

amp=(k/4).*abs(sa.*sb).*sqrt(2*(CS.^2+SS.^2));
%
%    generate the 2-D frequency-domain data matrix, SPEC
%
frinc=fmax/(np-1);
f=(0:(np-1))*frinc;

for i=1:61
  nchana=round(VA(i)/frinc)+1;
  nchanb=round(VB(i)/frinc)+1;
    SPEC(nchana,nchanb)=amp(i)+SPEC(nchana,nchanb);
    SPEC(nchanb,nchana)=amp(i)+SPEC(nchanb,nchana);
      end
end

%  perform the convolution in 2 steps along the matrix SPEC;
%
 %  set up Gaussian line-shape function for convolution
%
Gauss;


for i=1:np
L(i,:)=conv(SPEC(i,:),fg);
end
SP=zeros(np+40,np+40);
  for i=1:(np+40)
  SP(:,i)=conv(L(:,i),fg);
end

%  we have to account for the size differnce between the matrices


DS=zeros(np,np);
for i=1:np
    for j=1:np
          DS(i,j)=SP(i+20,j+20);
        end
    end

hysplot1
```